

EFFECTS OF COOLING RATE AND SUPERCOOLING
ON THE FORMATION OF ICE IN A CELL POPULATION

by

MAURY DAVID COSMAN

B.S., Cornell University
(1976)

S.M.M.E., Massachusetts Institute of Technology
(1978)

SUBMITTED TO THE DEPARTMENT OF
MECHANICAL ENGINEERING IN PARTIAL
FULFILLMENT OF THE
REQUIREMENTS FOR THE
DEGREE OF

DOCTOR OF PHILOSOPHY

at the

MASSACHUSETTS INSTITUTE OF TECHNOLOGY

FEBRUARY 1983

© Massachusetts Institute of Technology 1983

Signature of Author _____
Department of Mechanical Engineering
January 11, 1983

Certified by _____
Ernest G. Cravalho
Thesis Supervisor

Accepted by _____
Warren M. Rohsenow
Chairman, Department Committee

Archives
MASSACHUSETTS INSTITUTE
OF TECHNOLOGY

APR 20 1983

LIBRARIES

EFFECTS OF COOLING RATE AND SUPERCOOLING
ON THE FORMATION OF ICE IN A CELL POPULATION

by

MAURY D. COSMAN

Submitted to the Department of Mechanical Engineering
on January 11, 1983 in partial fulfillment of the
requirements for the Degree of Doctor of Philosophy in
Mechanical Engineering

ABSTRACT

The distribution of water content in a cell population exposed to cooling at specified rates is calculated using a two-dimensional histogram of properties representing the full range of cell surface area, initial water content, reference water permeability and permeability activation energy. Statistical techniques for combining the first 3 distributed properties into a single distributed parameter are described. Criteria for observable intracellular freezing are defined in terms of a minimum required cell water content and in terms of internal supercooling or temperature, based on hypothesized spontaneous or assisted internal freezing mechanisms. The latter criteria are shown to reduce to the single criterion of cell freezing temperature. The distribution of this property is inferred from reported experiments involving rapid cooling to subzero temperatures with immediate slow warming, conditions favoring intracellular ice formation and lethal recrystallization. An argument is presented showing how the distribution of cell freezing temperatures can be obtained, alternately, from low cooling rate experiments performed with varying amounts of extracellular supercooling. The fraction of a red cell population expected to undergo observable intracellular freezing (OIF) is calculated as a function of cooling rate and extracellular supercooling using the distributed water transport results and plausible values for the water content and freezing temperature criteria. The fraction OIF surface above the cooling rate-extracellular supercooling plane slopes upward from zero fraction at cooling rates less than 1000 K/min with supercoolings less than 4 K, to 1 at cooling rates above ~8000 K/min and with supercoolings above 6 K. Qualitatively similar results are obtained for lymphocytes but with more than an order of magnitude lower cooling rates for the transition from 0 to 1 fraction OIF. Cryomicroscope observations of intracellular freezing are described for both red cells and lymphocytes with cooling rates over the range 10-1600 K/min and 10-1200 K/min respectively, and with supercoolings between 0 and 20 K. Good agreement exists between the analytical and experimental results. The present observations support the assisted, membrane penetra-

tion hypothesis of cell freezing. Efforts during the freezing investigations to improve and expand the capabilities of the cryomicroscope included: addition of digital reference signal generators capable of reproducing nonlinear and high rate of temperature change protocols, analysis of the thermal control system and design of a lead compensating network and additional hardware, providing an order of magnitude bandwidth increase over the previous 3 hz system, addition of extracellular supercooling control, and addition of a video interface capable of superimposing temperature numerics at the frame rate on the video camera signal.

Thesis Supervisor: Ernest G. Cravalho
Title: Matsushita Professor of Mechanical
Engineering in Medicine

ACKNOWLEDGEMENTS

This work was supported in part by the National Heart and Lung Institute, by the National Institute of General Medical Sciences in the form of a one-year fellowship, and by the Matsushita Electric Industrial Company, Ltd., of Osaka, Japan.

I am grateful to my thesis committee, Professor Ernest G. Cravalho, Dr. Charles E. Huggins, Professor Borivoje Mikić and Professor William C. Unkel for their support, suggestions and congeniality through the years. I have been privileged to work with them in this research and hope that opportunities arise for future interaction.

I would like to thank Professor Joseph L. Smith for his hospitality in providing working space and access to facilities at the Cryogenic Engineering Laboratory and also for his advice and numerous anecdotes.

I am indebted to several others who have assisted during various phases of this work including: Joel Kandel who helped develop and debug the instrumentation, Phil Shapiro who also aided with several aspects of the instrumentation development as well as aiding in the distributed water transport analysis, Phil Mandel who provided design guidance for the video interface, Darius Thabit who engaged in useful discussions of the distributed analysis technique, Dr. Thomas Fuller and the staff of the MGH Histocompatibility Laboratory who prepared the lymphocyte samples and performed the flow cytometry studies, Judy Marcot and other members of the MGH Blood Bank and Transfusion Service staff who collected the red cell samples, Jack Darnell and Vincent Giannusa who prepared the ACD collection tubes and helped in setting up the darkroom for a number of projects, Irwin Deutsch of Atlantex and Zieler, Dedham, Mass. who taught me how to use the Zeiss microscope, Bob Gertsen, Karl Benner and Howard Lunn who loaned their expertise in metal-working many times in the Cryogenic Engineering Laboratory shop, present and former students at the Cryogenic Engineering Laboratory including Larry Sobel and John McGrath who provided technical advice, interesting discussions and encouragement, and Dr. T.C. Hua who carefully read this thesis and offered many suggestions for its improvement.

The drawings in this thesis were skillfully executed by Paul Halloran of the Charles Stark Draper Laboratory, Cambridge, Massachusetts. The rough manuscript was transformed into a finished document through the patient typing of Sandra Williams Tepper of the Mechanical Engineering Graduate Office. I owe her many thanks as do legions of graduate students for her friendly and efficient assistance in handling administrative difficulties.

Finally, I would like to thank my family, particularly my parents, to whom this thesis is dedicated, for their wisdom, unfailing support, and humor which have made these years pass lightly.

TABLE OF CONTENTS

	<u>PAGE</u>
ABSTRACT	2
ACKNOWLEDGEMENTS	4
TABLE OF CONTENTS	5
LIST OF TABLES	7
LIST OF FIGURES	9
NOMENCLATURE	15
CHAPTER 1 - INTRODUCTION	27
1.1 Background	27
1.2 Analyses of Intracellular Freezing	35
1.3 Scope of the Present Work	37
CHAPTER 2 - THEORY	42
2.1 Water Transport in Individual Cells	42
2.2 Water Transport in a Cell Population	47
2.3 Mechanisms of Ice Formation in Cells	66
2.4 Criteria for Intracellular Freezing	76
2.5 Fraction of Cells with Internal Freezing: Dependence on Cooling Rate	85
2.6 Fraction of Cells with Internal Freezing: Dependence on Extracellular Supercooling	91
2.7 Summary	98
CHAPTER 3 - EXPERIMENTAL METHODS	101
3.1 Cryomicroscope	101
3.2 Sample Preparation	107
3.3 Cryomicroscope Operation	107
CHAPTER 4 - EXPERIMENTAL RESULTS	113
4.1 Human Red Cells	113
4.2 Human Lymphocytes	120

	<u>PAGE</u>
CHAPTER 5 - DISCUSSION	130
5.1 Correlation of Theory with Experimental Results for Red Cells	130
5.2 Correlation of Theory with Experimental Results for Lymphocytes	135
5.3 Summary	141
5.4 Suggestions for Future Research	146
APPENDICES	
A Distribution of a Function of Random Variables	148
B Approximations for the First and Second Statistical Moments of a Function of Random Variables Using Series Expansions	157
C Flowchart for Distributed Water Transport Analysis	162
D Flowchart of Algorithm for Finding Fraction of Cells that Undergo Observable Internal Freezing	163
E Video Interface	164
F Supercooling Controller	171
G Reference Signal Generation	176
H Bandwidth Required for the Thermal Control System	187
I Coolant Supply	190
J Specimen Viewing Stage	203
K Power Amplifier Characteristics	226
L Thermocouple Amplification	236
M Lead Compensating Controller	242
N Thermal Control Loop Performance	248
O Human Lymphocyte Volume	264
REFERENCES	273

LIST OF TABLES

<u>NUMBER</u>	<u>TITLE</u>	<u>PAGE</u>
2.1	Assumptions in Water Transport Model and Likely Magnitude of Error Introduced	46
2.2	Human Red Blood Cell Properties	48
2.3	Comparison of Moments of the Distribution of α/V_W	52
2.4	Assumptions in the Distributed Water Transport Analysis	65
2.5	Intracellular Freezing Temperatures With and Without External Ice Present	67
2.6	Depression of Freezing Point for Solution in a Membrane Pore, $(T_e - T)$ [K]	75
3.1	Cryomicroscope System Functions and Performance Specifications	108
3.2	Lymphocyte Separation Protocol	110
4.1	Red Cell Size Comparison	121
5.1	Human Lymphocyte Properties	136
A.1	Contributing Distribution Properties	153
A.2	Comparison of Moments Calculated from p_{y3} to Values Calculated from y_3 Directly	156
E.1	Observer Reaction Time Measurements	166
E.2	Thermocouple Linearization End Points	170
G.1	Binary and Voltage Equivalents of Temperature	178
I.1	Densities and Viscosities of Nitrogen Gas Between 100 and 300 K	193
J.1	Summary of Measured Heat Transfer Coefficients	210

<u>NUMBER</u>	<u>TITLE</u>	<u>PAGE</u>
J.2	Estimated Thermal Mass of the Heater Window	214
J.3	Expected Range of Window Time Constant	215
N.1	Summary of Thermal Control Loop Component Transfer Functions	250
N.2	Typical Values of Transfer Function Constants	251
O.1	Summary of Lymphocyte Volume Measurements	265
O.2	Optical Microscopy and Flow Cytometry Measurements	272

LIST OF FIGURES

<u>NUMBER</u>	<u>TITLE</u>	<u>PAGE</u>
1.1	Dependence of survival on cooling rate for several cell types cooled to -196°C and thawed rapidly (from Mazur et al. [9])	28
1.2	Measured survival of yeast as a function of warming rate, [5]	29
1.3	Effect of glycerol concentration on the survival of marrow stem cells cooled to -196°C and warmed rapidly [7]	31
1.4	Schematic summary of the freeze-thaw process	32
1.5	Transition cooling rates for intracellular freezing on the cryomicroscope compared to survival	34
2.1	Comparison of probability density functions for α/V_W	54
2.2	Histogram and probability distribution function for α	56
2.3	2-D joint probability distribution and part of corresponding 2-D histogram	57
2.4	Distributed red cell water content with cooling at 10^4 K/min	60
2.5	Distributed internal osmolalities for red cells cooled at 10^4 K/min	63
2.6	Distributed water transport analysis flow-chart	64
2.7	Relative nucleation rate as a function of temperature and supercooling	71
2.8	Equilibrium contact angle at solution-ice-channel interface	73
2.9	Criteria for observable intracellular freezing in the water content domain	79

<u>FIGURE</u>	<u>TITLE</u>	<u>PAGE</u>
2.10	Criteria for observable intracellular freezing in the osmolality domain	80
2.11	Fraction of cells with observable intracellular freezing in a cell group cooled rapidly to -6°C	82
2.12	Cumulative distribution functions for normally distributed cell freezing temperatures compared to experimentally determined lethalities for mouse ova and hamster fibroblasts cooled rapidly to subzero ($^{\circ}\text{C}$) final temperatures prior to slow warming	84
2.13	Fraction of a red cell population with observable intracellular freezing (OIF) as a function of cooling rate and final temperature of cooling	89
2.14	Final fraction of a red cell population with observable intracellular freezing as a function of cooling rate and standard deviation of freezing temperature	90
2.15	External supercooling and nucleation in the water content domain	92
2.16	External supercooling and nucleation in the osmolality domain	93
2.17	Fraction of a red cell population with observable internal freezing as a function of extracellular supercooling and cooling rate	96
2.18	Fraction intracellular freezing surface above the cooling rate-extracellular supercooling plane for the red cell	97
2.19	Schematic overview of the analysis of intracellular freezing	99
3.1	Cryomicroscope system elements	102
3.2	Cryomicroscope thermal control system components	104

<u>FIGURE</u>	<u>TITLE</u>	<u>PAGE</u>
3.3	Cryomicroscope system operation	111
4.1	Human red cells, pre-freeze	114
4.2	Red cells at 233 K after cooling at 8 K/min, $\Delta T^{\circ} = 1.5$ K, Type 1	114
4.3	Red cells at 233 K after cooling at 260 K/min, $\Delta T^{\circ} = 2.5$ K, Type 2	115
4.4	Red cells at 213 K after 84 K/min cooling, $\Delta T^{\circ} = 5$ K, Types 2, 3, 4	115
4.5a	Red cells at 233 K after 250 K/min cooling, $\Delta T^{\circ} = 8.5$ K, Type 4	116
4.5b	Red cells at 233 K after 260 K/min cooling, $\Delta T^{\circ} = 20.5$ K, Type 4	116
4.6	Summary of red cell types	118
4.7	Summary of cryomicroscope red cell observations	119
4.8a	Lymphocytes pre-freeze	122
4.8b	Lymphocytes of Fig. 4.8a at 233 K after cooling at 374 K/min, $\Delta T^{\circ} = 3.5$ K, Type 3	122
4.8c	Lymphocytes of Figs. 4.8a and 4.8b at 261 K during warming at 5 K/min	123
4.9a	'Dark' lymphocytes pre-freeze	124
4.9b	Lymphocytes of Fig. 4.9a at 233 K after cooling at 1240 K/min, $\Delta T^{\circ} = 8.5$ K, Type 4	124
4.10a	Lymphocytes pre-freeze	126
4.10b	Lymphocytes of Fig. 4.10a at 233 K after cooling at 12 K/min, $\Delta T^{\circ} = .5$ K, Type 1	126
4.11	Summary of lymphocyte types	128
4.12	Summary of cryomicroscope lymphocyte observa- tions	129

<u>FIGURE</u>	<u>TITLE</u>	<u>PAGE</u>
5.1	Comparison of red cell analytical and experimental results for effect of cooling rate on the cell fraction with observable internal freezing	131
5.2	Comparison of red cell analytical and experimental results for effect of extracellular supercooling	134
5.3	Comparison of lymphocyte analytical and experimental results for effect of cooling rate on the cell fraction with observable internal freezing	138
5.4	Fraction of lymphocytes with observable internal freezing: dependence on extracellular supercooling	140
5.5	Fraction internal freezing surface above the cooling rate-extracellular supercooling plane for lymphocytes	142
5.6	Comparison of lymphocyte analytical and experimental results for effect of extracellular supercooling	143
5.7	Schematic overview of the present work	144
E.1	Observer reaction time measurement	165
E.2	Block diagram of video interface	168
F.1	Extracellular supercooling controller	172
F.2	Extracellular supercooling controller circuitry	173
F.3	Supercooling controller operating voltages	175
G.1	Block diagram of hard-wired digital reference signal generator	179
G.2	Digital reference clock period dependence on timing resistance and capacitance	182
G.3	Circuit schematic for digital reference signal generator	183

<u>FIGURE</u>	<u>TITLE</u>	<u>PAGE</u>
G.4	Program flowchart for microcomputer reference signal generation	185
H.1	Control system error for a ramp reference input	188
H.2	Error for a ramp reference input: dependence on bandwidth and temperature change rate	189
I.1	Coolant supply flow schematic	191
I.2	Flow dependence on regulator outlet pressure	192
I.3	Flow dependence on control valve position	196
I.4	Stream temperature dependence on mass flow	197
I.5	Ratio of flow without heat exchanger to flow with heat exchanger: dependence on valve position	200
J.1	Specimen viewing stage	204
J.2	Heater window cross section and corresponding lumped parameter heat transfer model	206
J.3	Heater power dependence on window-stream temperature difference for an ambient temperature stream	208
J.4	Heater power dependence on window-stream temperature difference for cold streams	209
J.5	Dependence of Nusselt number on Reynolds number	211
J.6	Block diagram of heater window	212
J.7	Heater window frequency response	217
J.8	Fin approximation of the viewing window	219
J.9	Radial temperature distribution in the viewing window	222

<u>FIGURE</u>	<u>TITLE</u>	<u>PAGE</u>
J.10	Maximum cooling rate capability of the viewing stage	224
K.1	Power amplifier circuit schematic	227
K.2	Heater power and transistor dissipation: dependence on resistance and supply voltage	230
K.3	Power amplifier frequency response	235
L.1	Thermocouple signal conditioning module schematic	237
L.2	Copper-constantan thermoelectric voltage	238
L.3	Frequency response of the chart recorder and signal conditioning module	240
M.1	Controller circuit schematic	243
M.2	Controller frequency response	247
N.1	Thermal control system steady-state error dependence on reference and stream temperatures	253
N.2	Open and closed loop frequency response of previous thermal control system	256
N.3	Open and closed loop frequency response of present thermal control system	257
N.4	Slew rate limits on allowable input voltage swing to the thermal control loop	262
O.1a	Laser flow cytometry histogram of forward-scattered light, lymphocytes in .290 osm saline	267
O.1b	Ortho Spectrum 111 computer report	267
O.2	Osmometric behavior of human lymphocytes	269
O.3	Flow cytometer forward scattered light dependence on lymphocyte volume	270

NOMENCLATURE

A	Surface area [cm^2]
\bar{A}	Mean of the surface area distribution [cm^2]
A_F	Flow-passage area [ft^2]
A_w	Effective window area for convective heat transfer [cm^2]
a_w	Activity of water
B	Cooling rate [K/s] or [K/min]
B_{max}	Maximum cooling rate attainable with heater power switched off [K/s]
B_{ult}	Ultimate cooling rate attained for an infinitesimal temperature drop [K/s]
b	Membrane permeability temperature coefficient [1/K]
b_R	Ramp reference input to control loop [K/min]
C_1	Supercooling controller timing capacitance [μF]
C_D	Clock duty cycle timing capacitance [μF]
C_d	Input capacitance for controller compensation circuit [μF]
C_i	Feedback capacitance in controller compensation leg [μF]
C_p	Clock period timing capacitance [μF]
CPA	Cryoprotective agent
C_{TA}	Offset added by thermocouple amplifier, [volts]
DAC	Digital-to-analog converter
D_C	Cell diameter [μ]
\bar{D}_C	Mean cell diameter [μ]

D_F	Flow passage diameter [cm]
D_{RBC}	Red cell diameter [μ]
E	Membrane permeability activation energy [Kcal/mole]
E_j	Property, E , of the j^{th} subpopulation [kcal/mole]
Ex	Expectation
F	Frequency [hz]
F_n	Natural frequency of thermal control loop in Appendix H assuming second order response; also natural frequency of chart recorder [hz]
F_v	Standard volume flow rate [SCFM]
\hat{F}_v	Volume flow normalized to the max flow at a particular regulator outlet pressure
F_{-3db}	Frequency at which the magnitude of response is attenuated by 3db ($1/\sqrt{2}$) [hz]
f	Friction factor
f_{Ej}	Fraction of the population with property E_j
f_{OF}	Fraction of the population with observable intra-cellular freezing
$f_{Tf\ell}$	Fraction of population with property $T_{f\ell}$
$f_{\alpha i}$	Fraction of population with property α_i
$f_{\theta k}$	Fraction of population satisfying the condition: $\theta_{min} + (k-1)\Delta\theta \leq \theta_{ij} \leq \theta_{min} + k\Delta\theta$
$f_{\phi k}$	Fraction of the population satisfying the condition: $\phi_{min} + (k-1)\Delta\phi \leq \phi_{ij} \leq \phi_{min} + k\Delta\phi$
$f_{\phi > .5}$	Fraction of population for which water content exceeds 50% of initial water content
G_C	Controller transfer function [volts/volt]

G_{C1}	Transfer function of first controller subsection [v/v]
G_{C2}	Transfer function of second controller subsection [v/v]
G_{C3}	Transfer function of third controller subsection [v/v]
G_{CL}	Control system closed loop transfer function [v/v]
G_{MT}	Transfer function relating window temperature to heater power [K/watt]
G_{OL}	Control system open loop transfer function [v/v]
G'_{OL}	Steady-state magnitude of the open loop control system transfer function [v/v]
G_P	Power amplifier transfer function [watt/volt]
G_{TA}	Thermocouple amplifier transfer function [volts/volt]
G_{TC}	Thermocouple transfer function [volts/K]
G_W	Heater window transfer function [volts/watt]
ΔG_C	Free energy of solidification per length of capillary [dyne-cm/cm]
ΔG_{LS}	Free energy change of solidification [dyne-cm/mole]
ΔG_N	Free energy change of solidification [dyne-cm/mole]
ΔG_N^*	Free energy of formation of a stable nucleus of solid phase [dyne-cm]
ΔG_S	Free energy of formation of a nucleus on a substrate [dyne-cm]
g_θ	geometry factor
H_I	Molar enthalpy of ice [dyne-cm/mole]
H_W	Partial molar enthalpy of water [dyne-cm/mole]
ΔH_{LS}	Enthalpy change of solidification [dyne-cm/mole] [6.01×10^{10} dyne-cm/mole for water]
h	Heat transfer coefficient [watts/cm ² K]

h_{FE}	Current gain of Darlington transistor pair [amps/amp]
I	Rate of formation of stable nuclei [nuclei/s]
I_0	Modified Bessel function of order zero
I_{REF}	Rate of formation of stable nuclei with $\Delta T = 10$ K, $T = 263.16$ K, $T_e = 273.16$ K [nuclei/s]
i_1	Op-amp source current in power amplifier circuit schematic, [amps] also used in Appendix M
i_2	Current flowing in heater, controlled by Darlington pair in power amplifier, also used in Appendix M [amps]
$i_{2,max}$	Maximum heater current [amps]
i_3	Current used in analysis of compensator transfer function, [amps] Appendix M
i_4	Current used in analysis of compensator transfer function, [amps] Appendix M
J_W	Water flux [mole/s]
K_0	Modified Bessel function of order zero
K_{C1}	Magnitude of controller first stage transfer function [v/v]
K_P	Membrane water permeability [$cm^3/dyne-s$]
K_{Pi}	Power amplifier incremental output power change with input voltage [watts/volt]
K_{PR}	Reference membrane water permeability [$cm^3/dyne-s$]
\bar{K}_{PR}	Mean of the membrane reference permeability distribution [$cm^3/dyne-s$]
K_{TA}	Thermocouple amplifier gain, steady-state, 688 [v/v]
K_{TC}	Slope of thermocouple voltage in the vicinity of $0^\circ C$ [v/K]
K_{TS}	Thermal conductivity of stream [watt/cm-s]
K_{VP}	Power amplifier voltage gain, v_H/v_C

K_w	Thermal conductivity of viewing window 8.8×10^{-3} [watt/cm-K]
k_B	Boltzman's constant [1.381×10^{-16} dyne-cm/K]
L	Flow passage length [cm]
L_w	Latent heat of fusion of water [6.01×10^{10} dyne-cm/mole]
M_n	Statistical moment of order n
M_T	Thermal mass [joules/K]
m	No. segments in the histogram approximation of the distribution of α
\dot{m}	Mass flow rate [lb/hr][Kg/hr]
\dot{m}'	Mass flow rate corrected for low temperature stream [lb/hr][Kg/hr]
m_1	$\dot{Q}_R / A_w K_w \delta$ [K/cm ²]
m_2	$\sqrt{h / K_w \delta}$, 8.18 [1/cm]
N_s	No. moles solute [moles]
N_w	No. moles water [moles]
N_{wi}	Initial no. moles water in cell [moles]
\bar{N}_{wi}	Mean of the initial no. moles cell water distribution [moles]
NSTPS	Number of 1/2°C steps used to approximate a given linear segment of a thermal protocol
n	No. segments in the histogram approximation of the distribution of E
θ	Osmolality [osmoles/Kg]
θ_{ij}	Osmolality of intracellular solution for subpopulation with properties α_i , E_j [osm/Kg]
θ_{max}	Maximum value of θ_{ij} [osm/Kg]

θ_{\min}	Minimum value of θ_{ij} [osm/Kg]
$\Delta\theta$	Width of θ -histogram segments: $(\theta_{\max} - \theta_{\min})/q$ [osm/Kg]
OIF	Observable Intracellular Freezing
P	Pressure [lb/in ² , dynes/cm ²]
P_R	Regulator outlet pressure [psig]
P_T	Power dissipated in main Darlington transistor [watts]
ΔP	Pressure drop [psi]
ΔP_a	General pressure drop associated with ambient temperature streams [psi]
ΔP_c	Pressure drop, general, associated with a cold stream [psi]
ΔP_{HE}	Pressure drop across heat exchanger [psi]
$\Delta P'_{HE}$	Pressure drop in heat exchanger corrected for a cold stream [psi]
PEG	Polyethylene glycol
PVP	Polyvinylpyrrolidone
P_A	Distribution function for surface area [1/cm ²]
P_E	Distribution function of membrane permeability activation energy [moles/kcal]
P_K	Distribution function of membrane reference permeability [dyne-s/cm ³]
P_{NWi}	Distribution function of initial cell water content [1/mole]
P_{Tf}	Probability distribution for cell freezing temperatures [1/K]
P_α	Probability distribution function, or density function of α [dyne-s-moles/cm ⁵]
P_ϕ	Probability distribution of normalized cell water content

\dot{Q}_R	Electrical power dissipated in heater [watts]
$\dot{Q}_{R,max}$	Maximum power that can be dissipated in heater [watts]
\dot{Q}_S	Convective heat transferred to stream [watts]
q	No. of ϕ -histogram segments
R	Gas constant [8.307×10^7 dyne-cm/mole-K], [1.986×10^{-3} Kcal/mole-K]
R_1	Supercooling controller timing resistance, also used in Appendix K [ohms]
R_{2-4}	Resistances in Appendix K; power amplifier schematic [ohms]
R_B	Ballast resistance, see power amplifier circuit schematic [ohms]
R_d	Feedback resistance in controller compensation leg [ohms]
R_G	Gain-setting resistor in controller first stage [ohms]
R_H	Electrical resistance of tin-oxide heater layer [ohms]
R_p	Clock period timing resistance [ohms]
Re	Reynolds number
r	Radius [cm]
r_C	Capillary radius [cm]
r_N	Radius of solid phase nucleus [cm]
r_N^*	Radius of critical cluster of molecules, or nucleus [cm]
r_w	Radius of viewing window, 1.25 [cm]
S_A	Standard deviation of surface area distribution [cm^2]
S_D	Standard deviation of the cell diameter distribution [μ]

S_K	Standard deviation of membrane reference permeability distribution [cm ³ /dyne-s]
S_{NWi}	Standard deviation of the cell volume distribution [cm ³]
S_{Tf}	Standard deviation of cell freezing temperature distribution [K]
S_V	Standard deviation of the volume distribution [cm ³] or [μ ³]
\hat{S}_V	Normalized standard deviation of the volume distribution, S_V/V
S_α	Standard deviation of α distribution [cm ⁵ /dyne-s-mole]
SGTM	Time allowed for a linear segment of thermal protocol [s]
SPTM	Time required for each 1/2°C step in a linear segment approximation for a thermal protocol
ΔS_{LS}	Entropy change of solidification [dyne-cm/mole-K]
s	Laplace transform variable
T	Temperature [K]
\hat{T}	Local viewing-window stream temperature difference [K]
T_0	Equilibrium freezing temperature of pure water [273.15 K]
T_a	Ambient temperature [~298 K]
T_E	Temperature error [K]
T_e	Equilibrium freezing temperature [K]
T_f	Freezing temperature of intracellular solution (non-equilibrium) [K]
\bar{T}_f	Mean cell freezing temperature [K]
T_i	Initial temperature [K]
T_R	Reference temperature [298.16 K, 25°C]

T_S	Coolant stream temperature [K]
T_w	Heater window temperature [K]
T_{wf}	Final lumped window temperature [K]
T_{wi}	Initial lumped window temperature [K]
ΔT	Difference between actual temperature at which phase change begins and T_e . Supercooling prior to phase change $T_e - T$, [K]
ΔT_f	Supercooling required for intracellular freezing by assisted or spontaneous mechanisms [K]
ΔT^i	Supercooling of intracellular solution $T_e - T$, [K]
ΔT^o	Supercooling of extracellular solution [K]
t	Time [s]
t_C	Clock period [s]
t_f	Final time [s]
t_p	Supercooling controller pulse period [s]
u	Number of elements in the histogram approximation of the distribution of cell freezing temperatures
u'	Number of freezing temperature histogram elements that must be considered during cooling to a temperature within the range of cell freezing temperatures
V	Flow velocity [ft/s]
\bar{V}	Mean cell volume [μ^3]
V_b	Osmotically inactive volume [cm^3]
V_i	Initial cell volume [cm^3]
V_{OF}	Cell volume at time intracellular freezing is observed [cm^3]
V_{RBC}	Red cell volume [μ^3]
V_w	Molar volume of water [$18.0 \text{ cm}^3/\text{mole}$]

V_{wi}	Initial volume of cell water [cm^3]
v_l	Supercooling controller temperature-equivalent firing voltage
v_{BE}	Overall Darlington pair, base to emitter voltage
v_C	Controller output voltage
V_{C1}	Output of first controller subsection [volts]
v_{CE}	Collector to emitter voltage of primary current carrying transistor of power amplifier [volts]
$v_{C\ell}$	Output of controller compensation leg [volts]
v_{Cp}	Output of proportional leg of second controller subsection [volts]
v_E	Emitter voltage appears across power amplifier ballast resistor
$v_{E,max}$	Maximum power amplifier emitter voltage
v_e	Control system error
$v_{e,ss}$	Steady-state control system error [volts]
v_F	Supercooling controller pulse period adjust voltage
v_H	Voltage across heater; power amplifier output voltage
$v_{H,max}$	Maximum voltage that can be applied to the heater
v_{OA}	Operational amplifier output voltage
$v_{OA,max}$	Maximum op-amp output voltage
v_R	Output of reference signal generator [volts]
$v_{R,pp}$	Peak-to-peak amplitude of a sinusoidal reference [volts]
v_S	Power amplifier DC supply voltage
v_{Tw}	Window temperature-equivalent voltage; output of thermocouple amplifier

v_w	Window thermocouple output voltage
$\Delta v/\Delta T$	Thermocouple-amplifier voltage sensitivity [v/K]
x_w^i	Mole fraction water inside cell
x_w^o	Mole fraction water outside cell

Greek Symbols

α	Ensemble of distributed cell properties, $K_{PR}A/N_{wi}$ [cm ⁵ /dyne-s-moles]
α_i	Property, α , of the i^{th} subpopulation [cm ⁵ /dyne-s-mole]
$\bar{\alpha}$	Mean of the α distribution [cm ⁵ /dyne-s-mole]
β	Dummy variable
γ	Initial ratio of no. moles salt to water in cell
δ	Thickness of viewing window, .051 [cm]
ζ	Damping ratio of 2nd order hypothetical thermal control loop
θ	Contact angle of solid on capillary wall [degrees]
θ_v	Valve position [turns open]
μ	Viscosity, Appends. I, J [lb/hr-ft]
μ_a	Viscosity of an ambient temperature stream [lb/hr-ft]
μ_c	Viscosity of a cold stream [lb/hr-ft]
μ_I	Chemical potential of ice [dyne-cm/mole]
μ_w^i	Chemical potential of water inside cell [dyne-cm/mole]
μ_w^o	Chemical potential of water outside cell [dyne-cm/mole]
μ_w^r	Reference chemical potential of water, a function of temperature and pressure only [dyne-cm/mole]

ρ	Density [lb/ft ³]
ρ_a	Density of an ambient temperature stream [lb/ft ³]
ρ_c	Density of a cold stream [lb/ft ³]
σ_{LC}	Liquid-capillary wall interfacial energy [dyne-cm/cm ²]
σ_{LS}	Liquid-solid interfacial energy [dyne-cm/cm ²]
σ_{SC}	Solid-capillary wall interfacial energy [dyne-cm/cm ²]
τ_{TA}	Thermocouple amplifier time constant, 6.37×10^{-4} [s]
τ_{TC}	Thermocouple time constant [s]
τ_w	Window time constant [s]
ϕ_c	Controller phase shift [degrees]
ϕ_{C1}	Phase shift of first controller subsection [degrees]
ϕ_{CL}	Closed loop phase shift of the thermal control system [degrees]
ϕ_{OL}	Closed loop phase shift of the thermal control system [degrees]
ϕ_p	Phase shift of power amplifier transfer function [degrees]
ϕ_{TA}	Phase shift of thermocouple amplifier transfer function [degrees]
ϕ_w	Phase shift of the heater window transfer function [degrees]
ϕ	Nondimensional cell water content, $[N_w/N_{wi}]$
ϕ_{ij}	Nondimensional water content of subpopulation with properties α_i, E_j
ϕ_{max}	Maximum value of ϕ_{ij}
ϕ_{min}	Minimum value of ϕ_{ij}
$\Delta\phi$	Width of ϕ -histogram segments: $(\phi_{max} - \phi_{min})/q$

CHAPTER 1
INTRODUCTION

1.1 Background

Low temperature preservation of biological materials is an emerging technology with important applications in medicine, agriculture, and biological research. Notable successes include clinical preservation of blood [1, 2], cornea, spermatozoa and skin [3] as well as mammalian embryos including those of mice and cattle [4]. Although attempts to preserve large volumes of tissue, or organs for transplantation have as yet been unsuccessful, there are no fundamental reasons to prevent this in the future; the primary obstacle is lack of sufficient understanding of the mechanisms of freezing damage.

Several factors have been determined through experimental studies to affect survival of cells exposed to freezing and thawing: the dependence of survival on cooling rate is shown for several types of cells in Fig. 1.1. Although the range of rates for peak survival and the peak height are cell-specific, the curves are qualitatively similar. The influence of warming rate on the survival of yeast [5] is shown in Fig. 1.2. The survival of cells cooled at supraoptimal rates is increased by rapid warming while cells cooled at suboptimal rates are little affected. Similar observations have been made for hamster tissue culture cells [6], marrow stem cells [7] and red cells [8]. The effects of storage temperature and time, important down to $\sim -60^{\circ}\text{C}$, become less significant at lower

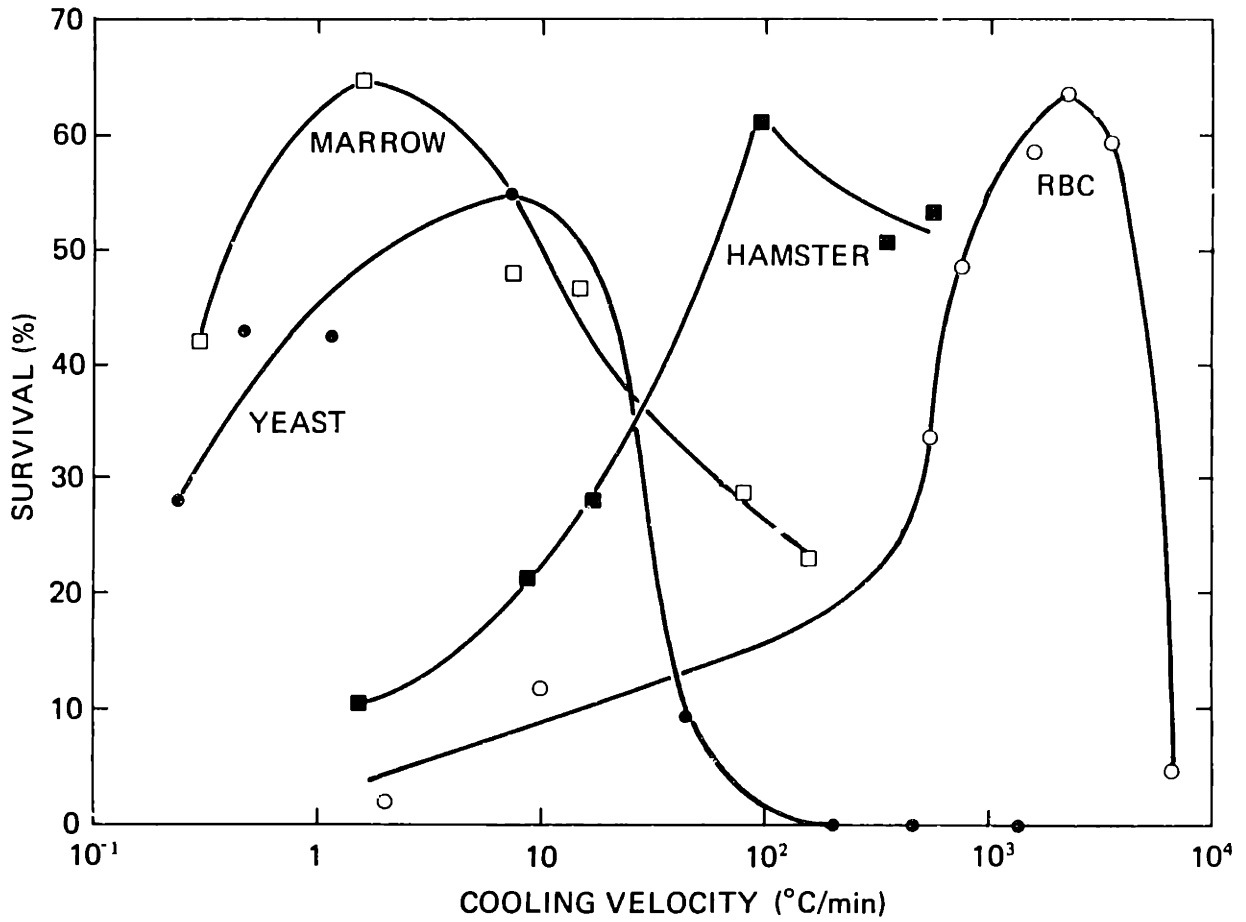


FIGURE 1.1 Dependence of survival on cooling rate for several cell types cooled to -196°C and thawed rapidly (from Mazur et al. [9])

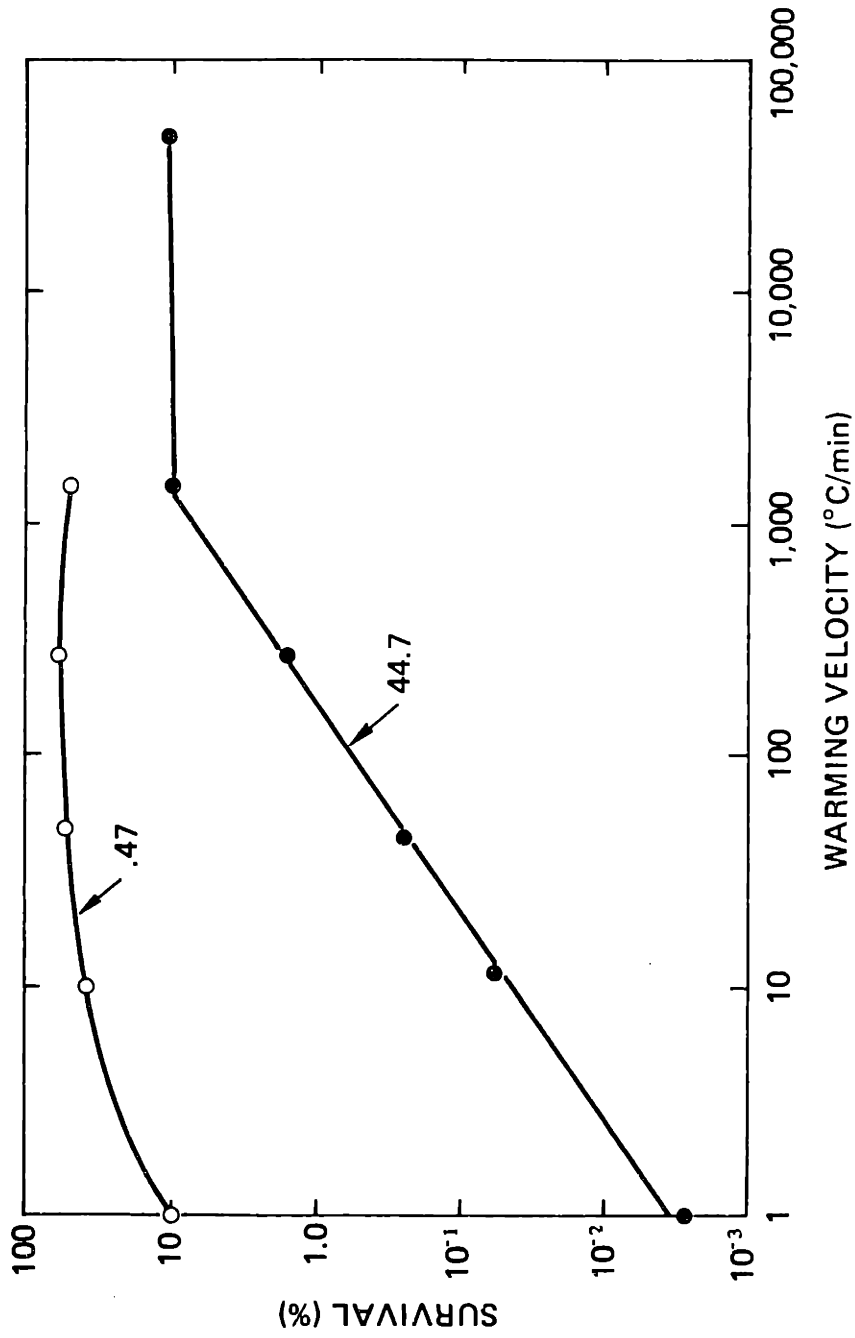


FIGURE 1.2 Measured survival of yeast as a function of warming rate, [5]: numbers next to curves are cooling rates that preceded warming

temperatures [3,10], and can therefore be eliminated from consideration. Dramatic improvement of post-thaw viability has been obtained with chemical additives in several types of cells. Low-molecular weight permeating additives such as glycerol and dimethyl sulfoxide and non-permeating polymers including PVP and PEG have provided protection under appropriate conditions [11]. Figure 1.3 shows survival of marrow stem cells suspended in Tyrode balanced salt solution with varied glycerol concentrations [7]. The presence of 1.25 M glycerol results in nearly two orders of magnitude reduction in the optimal cooling rate and a factor of 3 increase in survival. Similar effects have been seen in cryoprotected red cells [12].

Many of the observed phenomena can be accommodated by the two-factor hypothesis of freezing injury proposed originally by Mazur [13,10,14]. The major features of this model are summarized schematically in Fig. 1.4. The hypothesized combination of intracellular ice and solution effect damage during cooling produces an inverted U-shaped dependence of survival on cooling rate. Poor viabilities at suboptimal cooling rates are attributed to solution effects. The phase relationship between pure ice and increasingly concentrated extracellular solution provides the osmotic driving force for cellular dehydration; low cooling rates allow sufficient dehydration to maintain equilibrium between intra- and extracellular solutions. Exposure to these hypertonic solutions can produce substantial time-dependent damage even at ambient temperatures. Additionally, hypertonic solutions are implicated in the thermal shock [15] and dilution shock damage phenomena [16]. A single mechanism of damage, membrane component

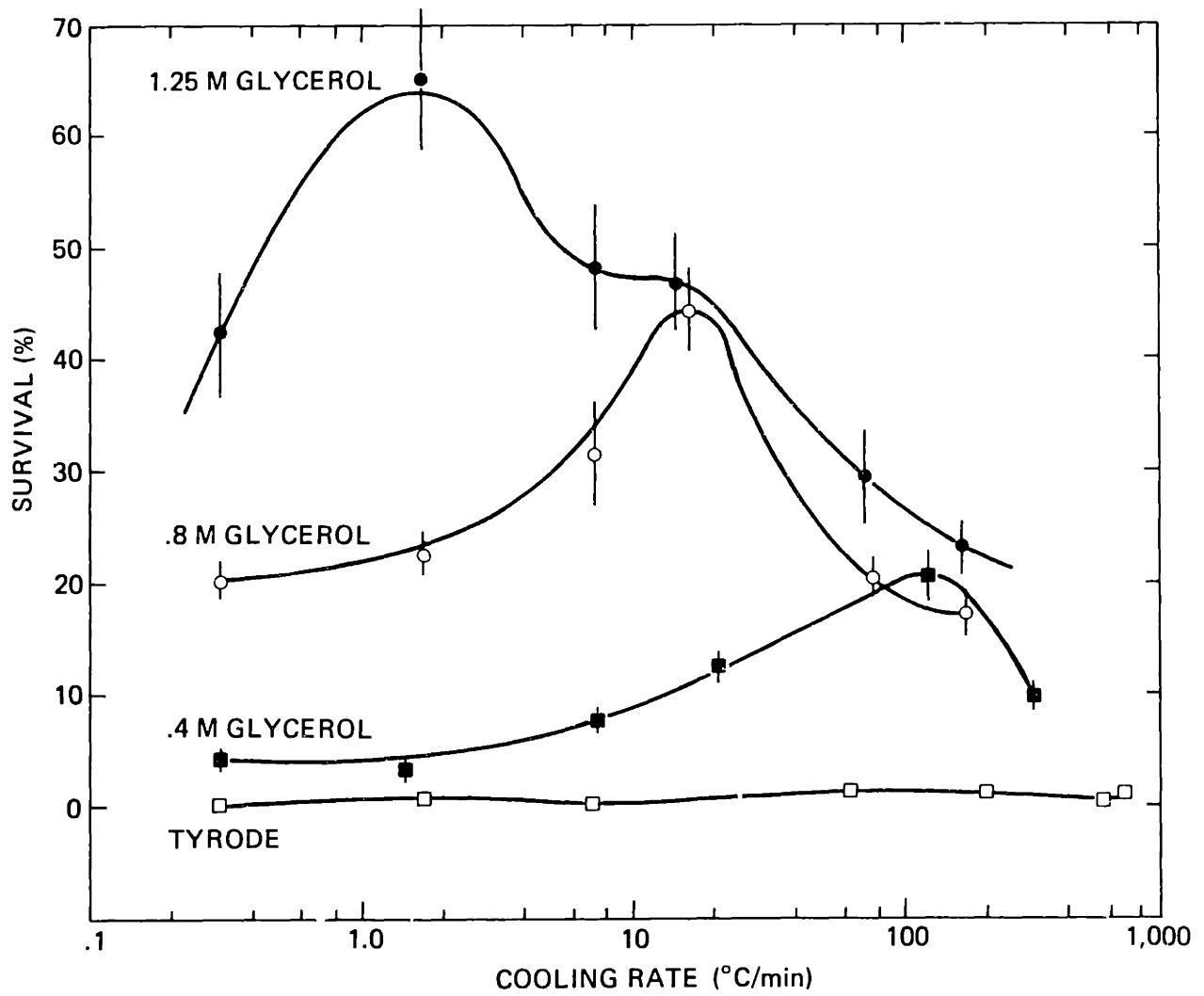


FIGURE 1.3 Effect of glycerol concentration on the survival of marrow stem cells cooled to -196 °C and warmed rapidly [7]

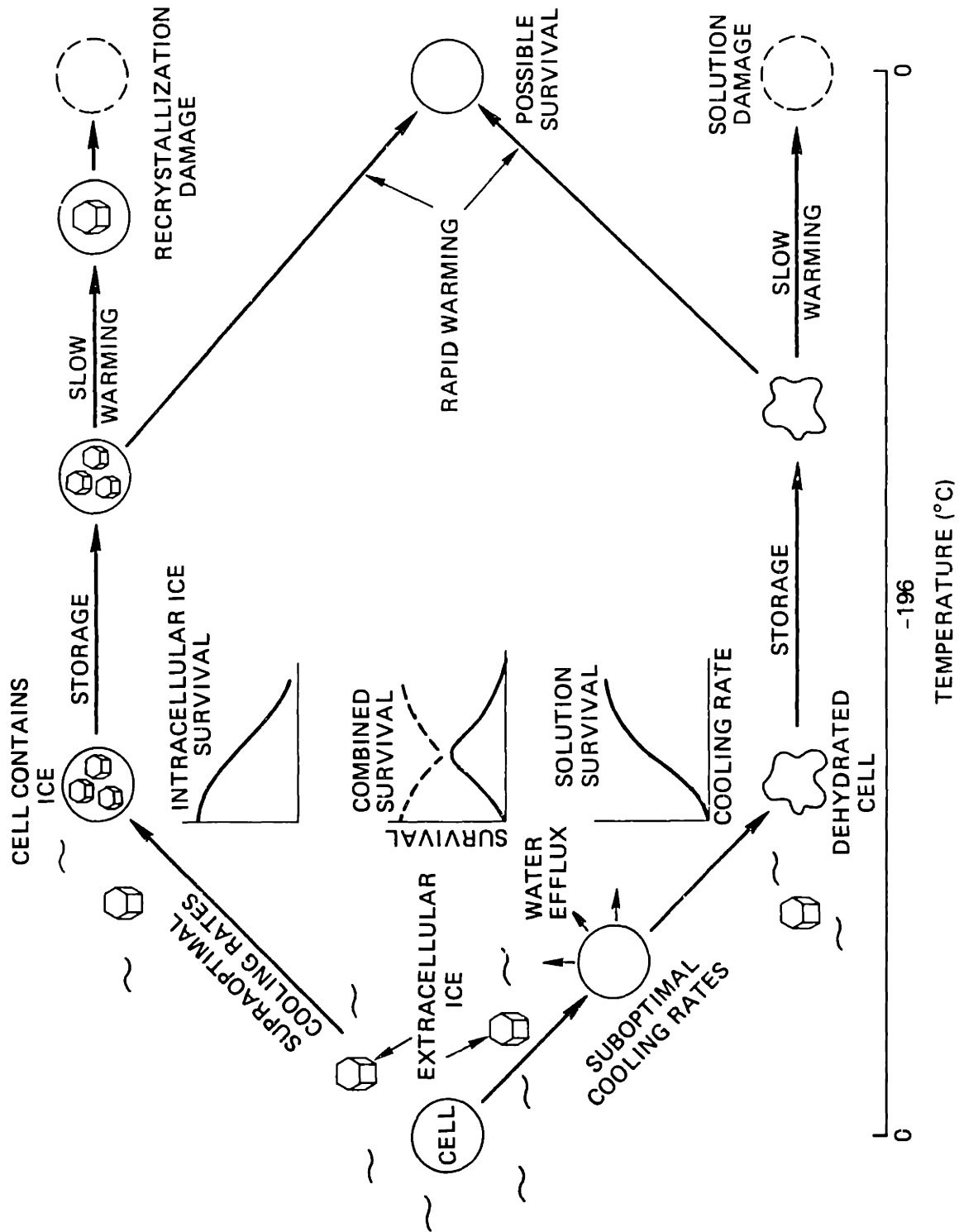


FIGURE 1.4 Schematic summary of the freeze-thaw process

desorption, may underlie the solution effects [17].

The two-factor hypothesis associates cellular injury at high cooling rates with formation of intracellular ice. At these rates, water transport is insufficient to maintain transmembrane osmotic equilibrium resulting in supercooling and ultimate crystallization of water internally. The transition cooling rates for observed intracellular freezing on the cryomicroscope are shown for mouse ova, HeLa and red cells in Fig. 1.5 compared to survival data [18,19,20,12]. With the exception of anomalously low cooling rates for observed intracellular freezing in human red cells, the evidence supports the connection between high cooling rate damage and internal freezing; see review in [21]. Recrystallization of internal ice crystals is clearly a factor in the strong warming rate dependence of survival for cells cooled at supraoptimal rates.

Cryoprotective agents affect many of the processes that occur during freezing and thawing. Permeating agents reduce membrane water conductivity thereby reducing the cooling rate at which transmembrane osmotic equilibrium can be maintained. This effect, which taken alone reduces the cooling rates for observed intracellular freezing, is partially offset by substantial increases in the capability of the cell contents to supercool, providing more time for osmotic equilibration. Protection is conferred primarily at sub-optimal cooling rates for permeating CPA's and seems to result from the ability of the CPA to reduce the ionic salt concentration by partially substituting for solvent water.

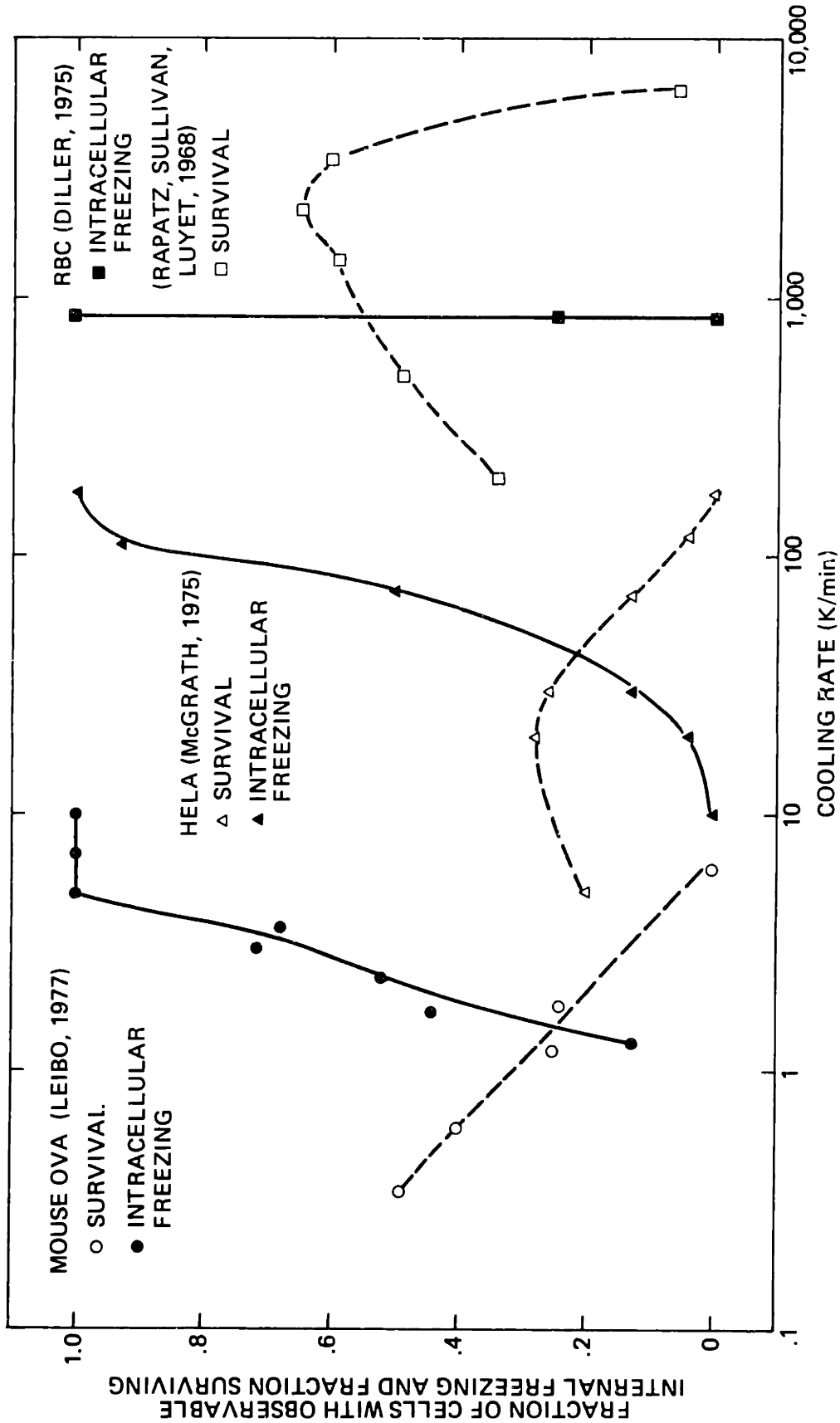


FIGURE 1.5 Transition cooling rates for intracellular freezing on the cryomicroscope compared to survival

1.2 Analyses of Intracellular Freezing

The pivotal role of water transport in determining the freeze-thaw behavior of cells has led to numerous analyses of the problem [22] through [35]. Some authors consider the critical phenomenon of intracellular freezing and attempt to predict cooling rates at which it occurs. The approaches usually involve combining water transport results with criteria for internal freezing based on varied mechanisms of internal ice formation: Toscano et al. perform a parameter study of the effectiveness of internal nucleants in precipitating solidification of an average red cell assuming spontaneous freezing by heterogeneous nucleation. Solidification by this hypothetical mechanism occurs over a range of temperatures and with internal concentrations between physiological and NaCl eutectic. A sharp cooling-rate transition separates cells solidifying at higher temperatures, with substantial retained water, from those that dehydrate and solidify below the eutectic temperature. For a specific nucleator geometry, cell solidification occurs at a constant level of internal supercooling. This is to be expected from the strong supercooling dependence of the nucleation phenomenon. Toscano et al. imply that solidification of the red cell in the higher temperature regime corresponds to observable freezing on the cryomicroscope; the water quantity required for observable freezing is not discussed.

A supercooling criterion was used by Cosman et al. [35] to establish the transition cooling rate for observable internal freezing in a generalized cell. If internal supercooling exceeded a hypothetical value the

cell was said to be internally frozen. At all cooling rates below the transition value the cell was defined as unfrozen even though solidification ultimately occurs. This analysis suffers from the same ambiguity as that of Toscano et al.; the connection between freezing in the analysis and experimentally observed internal freezing is not well defined.

Mazur [21] uses two approaches to calculate the probability of intracellular freezing as a function of cooling rate: in the first, probability is assumed proportional to the extent of internal supercooling evaluated at the cell freezing temperature; this assumes an assisted mechanism of internal freezing in which the membrane prevents external ice from seeding the internal solution until a particular temperature is reached during cooling. If this temperature were hypothetically -10°C and cooling proceeded rapidly enough to prevent dehydration, the internal solution would be supercooled roughly 9.5°C , allowing for $.5^{\circ}\text{C}$ equilibrium freezing point depression. Such a cell would have an internal freezing probability of 1. A similar cell cooled at very low rates would have zero probability of internal freezing. These probabilities have been implied in the cited article to represent fractions of a cell population that have undergone observable internal freezing. The calculations do not show the response of a cell population but actually show quantity of water relative to the equilibrium amount inside a single cell when the freezing temperature is reached. Two issues are thus confused in this approach: the quantity of water that must solidify internally to have observable internal freezing and the fraction of the population that meets the water quantity condition when the freezing temperature is reached. Similar confusion exists in

analysis of intracellular freezing by Leibo [18].

In the second approach taken by Mazur, probability of intracellular freezing is zero for internal supercooling below 2°C and with volume less than 10% of the pre-freeze volume and probability is assumed 1 for supercooling and volume greater than 2°C and 10%. The transition from zero probability to 1 should occur with infinite slope at a specific cooling rate if properties of a single cell are used in the water transport analysis. The finite slopes actually shown are inconsistent with the stated criteria of freezing; distributed cell properties are not mentioned. Again, the issue of criteria for observable freezing in a single cell is confused with the issue of the fraction of the population that meets the conditions for observable freezing.

1.3 Scope of the Present Work

Some of the issues raised in the preceding review are considered in the present work: 1) Can 'intracellular freezing' be defined unambiguously in terms of cell water content? Confusion results at present from the lack of consensus on the meaning of this phrase; some authors imply an observable, detectable, or damaging solidification of 'substantial' quantities of water inside the cell. Others have used the phrase to refer to solidification of dehydrated cells containing little or no ice. Definition of internal freezing is a necessary step in analyzing cellular response to cooling at supraoptimal rates. 2) What are the likely mechanisms of internal freezing? Can a common denominator be found for all of these? 3) Can predictions of 'probability of intracellular freezing' as

a function of cooling rate be placed on a rigorous mathematical foundation? If deterministic criteria can be defined for freezing in an individual cell, what distributed cell properties must be considered for these predictions? A mathematical protocol for this calculation would help eliminate the current confusion between freezing in individual cells and in whole populations. 4) Can the very narrow transition cooling rate range for observable freezing in unprotected red cells [20] (Fig. 1.5) be understood in terms of narrow distributions of the appropriate red cell properties?

Experimental investigations of issues 2) and 4), using a cryomicroscope, were accompanied by random and often large values of extracellular supercooling. The effects of supercooling, recognized analytically by Silveiras et al. [24,31] and in cryomicroscopy by Diller [20], include dramatic reduction of the cooling rates required to produce observable internal freezing. This effect was studied further, providing an additional test of the analytical methods developed in addressing issue 3). Some of the difficulties encountered during these investigations, particularly at cooling rates greater than 1000 K/min, were neutralized through improvement of the microscope thermal control system; others necessitated new hardware development. The high cooling rate problems were avoided in a parallel study of human lymphocytes which undergo observable intracellular freezing at much lower cooling rates than red cells.

The overall analytical and experimental effort is documented here in five chapters: General background and brief reviews of intracellular freez-

ing analyses have been discussed in Chapter 1. Chapter 2 begins with a short review of water transport in individual cells to establish the basic equations and standard assumptions. Water transport in a cell population is considered next by solving the transport equation using a two-dimensional histogram of properties representing the full range of possible values of cell surface area, initial water content, reference water permeability, and activation energy for water permeability. Statistical methods are established in Section 2.2 for combining the first three properties into a single distributed property. The advantages of solving the water transport equation for n^2 rather than n^4 histogram values, where n is the number of elements in each independent histogram, are obvious. To the author's knowledge, the analysis of Section 2.2 is the first attempt to consider water transport in a cell population rather than in individual cells. Section 2.3 is a review and discussion of the most plausible mechanisms of ice formation in cells: spontaneous nucleation, and seeding by external ice through the cell membrane. Depending on the mechanism, one criterion for intracellular freezing is shown to be internal supercooling or absolute temperature. A second criterion, that cell water content exceed a specified fraction of the initial water content, is established in Section 2.4. Justification is provided to combine the spontaneous nucleation and assisted criteria for internal freezing into a single criterion; temperature must be below the cell 'freezing' temperature. A class of experiments involving rapid cooling to specified high subzero °C temperatures with subsequent slow re-

warming to room temperature is invoked to establish the shape of the distribution of these cell freezing temperatures. The details of this class of experiments had not previously been explained within an analytical framework.

The distributed water transport analysis of Section 2.2 is combined in Section 2.5 with the criteria for intracellular freezing. The 'probability' of intracellular freezing in red cells is described rigorously as the fraction of the population with observable internal freezing. This again, may be the first attempt to consider distributed properties of the cell population in an analysis of intracellular freezing. Extracellular supercooling is introduced in Section 2.6 adding an extra dimension to the cell freezing problem. All of the analytical results are presented compactly in a surface representing the fraction of the population with observable freezing above a plane defined by the cooling rate and extracellular supercooling.

Chapter 3 contains a short description of the current cryomicroscope system, sample preparations and cryomicroscope operating procedures. The chapter refers to appendices which document the analyses performed to improve the thermal control loop as well as detailed design information for other system elements. These are provided to support further development of the experimental system, and to facilitate operation and maintenance of the existing system.

Observations of intracellular freezing are described in Chapter 4 for human red cells and lymphocytes over wide ranges of cooling rate and extra-

cellular supercooling. Interpretation rules for deciding whether or not a cell has undergone intracellular freezing are discussed.

The analytical predictions of Chapter 2 are compared to the experimental results for red cells in Section 5.1. Analysis and experimental results for lymphocytes are compared in Section 5.2. The major findings of the present work are summarized in Section 5.3. Suggested future research, Section 5.4, is the last topic addressed.

CHAPTER 2

THEORY

2.1 Water Transport in Individual Cells

The quantity of water transferred across a cell membrane, and its dependence on cell properties as well as the thermal history, is a crucial factor in assessing nature and extent of cryoinjury. A model for water transport in biological cells cooled without protective agents is briefly derived here following the assumptions of Mazur [22], but with notation similar to that of Levin [25], Pushkar et al. [29] and Lynch and Diller [30]. Equation (2.1) expresses positive cell water efflux in terms of the transmembrane chemical potential difference [36,37]:

$$J_W = \frac{K_p A}{V_W^2} (\mu_W^i - \mu_W^o) \quad (2.1)$$

The chemical potential of water in Eq. (2.1) is expressed below as a function of temperature, pressure and activity [38]:

$$\mu_W = \mu_W^i(T,P) + RT \ln a_W \quad (2.2)$$

Solution ideality or Raoult's law, Eq. (2.3), equates activity and mole fraction, defined in Eq. (2.4). The number of moles of solute, N_s , is twice the nominal amount for ionic salts such as NaCl:

$$a_W = X_W \quad (2.3)$$

$$X_W = \frac{N_W}{N_W + N_S} \quad (2.4)$$

Considering the cell and its suspension isothermal, isobaric, and ideal, Eqs. (2.1), (2.2) and (2.3) combine to yield Eq. (2.5):

$$J_W = \frac{K_P A RT}{V_W^2} (\ln X_W^i - \ln X_W^o) \quad (2.5)$$

Equilibrium between pure ice and aqueous extracellular solution can be expressed using Eqs. (2.2) and (2.3) as:

$$\mu_I = \mu_W^i(T,P) + RT \ln X_W \quad (2.6)$$

This can be rearranged to obtain

$$\ln X_W = \frac{\mu_I}{RT} - \frac{\mu_W^i(T,P)}{RT} \quad (2.7)$$

The temperature dependence of $\ln X_W$ can be found at constant pressure by differentiating Eq. (2.7) with respect to T [38]:

$$\begin{aligned} \left. \frac{\partial \ln X_W}{\partial T} \right|_P &= \frac{1}{R} \frac{\partial \mu_I / T}{\partial T} - \frac{1}{R} \frac{\partial \mu_W^i / T}{\partial T} \\ &= \frac{-H_I + H_W}{RT^2} \\ &= \frac{L_W}{RT^2} \end{aligned} \quad (2.8)$$

Equation (2.8) is integrated assuming constant L_W from the equilibrium freezing temperature of pure water to the solution temperature, T , giving an expression for the solution-ice two phase equilibrium states in the extracellular medium:

$$\ln x_W = \frac{L_W}{R} \left(\frac{1}{T_0} - \frac{1}{T} \right) \quad (2.9)$$

The cell membrane water permeability temperature dependence is usually expressed in either the exponential form of Eq. (2.10) or the Arrhenius form in Eq. (2.11):

$$K_p = K_{PR} e^{b(T-T_R)} \quad (2.10)$$

$$K_p = K_{PR} e^{-E/R \left(\frac{1}{T} - \frac{1}{T_R} \right)} \quad (2.11)$$

Both forms adequately describe the observed membrane permeability temperature dependence over the limited temperature ranges that have been reported. The arguments advanced by Levin [26] support the Arrhenius form as a more logical choice, hence Eq. (2.11) will be used here.

Equations (2.5), (2.9) and (2.11) combine to give Eq. (2.12) for the cell water flux:

$$-\frac{dN_W}{dt} = J_W = \frac{K_{PR} A RT}{V_W^2} \left[e^{-\frac{E}{R} \left(\frac{1}{T} - \frac{1}{T_R} \right)} \right] \left[\ln \left(-\frac{N_W}{N_W + N_s} \right) - \frac{L_W}{R} \left(\frac{1}{T_0} - \frac{1}{T} \right) \right] \quad (2.12)$$

The definitions for the cooling rate, B , and the nondimensional cell water content, ϕ , in Eqs. (2.13) and (2.14) are introduced into Eq. (2.12) to obtain Eq. (2.15):

$$B = - dT/dt \quad (2.13)$$

$$\phi = \frac{N_W}{N_{Wi}} \quad (2.14)$$

$$\frac{d\phi}{dT} = \frac{K_{PR} A RT}{V_W^2 N_{Wi} B} \left[e^{-\frac{E}{R} \left(\frac{1}{T} - \frac{1}{T_R} \right)} \right] \left[\ln \left(\frac{\phi}{\phi + \gamma} \right) - \frac{L_W}{R} \left(\frac{1}{T_0} - \frac{1}{T} \right) \right] \quad (2.15)$$

This equation is subject to the initial condition:

$$\phi = 1 \quad \text{at} \quad T = T_i \quad (2.16)$$

There are many assumptions inherent in the development of Eq. (2.15), some of which have been discussed in detail in the literature. Table 2.1, reproduced with changes from Mazur [21], summarizes the assumptions, the likely magnitude of the errors introduced, and references. The assumptions with the greatest potential impact are items 5, 8 and 9. The case for extrapolating above 0°C permeability measurements to subzero temperatures using Eq. (2.11) is supported by Papanek's human red cell results [39] in the +25 to -10°C range. Introducing permeability osmolality dependence of the form found by Rich et al. [40] and

TABLE 2.1
 ASSUMPTIONS IN WATER TRANSPORT MODEL
 AND LIKELY MAGNITUDE OF ERROR INTRODUCED

ASSUMPTION	ERROR MAGNITUDE	REFERENCES
1. Intra- & Extracellular Solution Ideality	Small	22,23,24,28
2. Extracellular equilibrium between ice and solution once extracell. nucleation has occurred.	Negligible	22
3. Constant latent heat, L_W	Negligible	22,24
4. Constant number of moles of intracellular solute	Small	22,31
5. Above 0°C permeability temperature dependence extrapolates to below 0°C	Major	22,24,26
6. Thermal equilibrium between the cell and suspending medium	Negligible	22,23,32
7. Constant cell surface area	Small	22,23
8. Permeability osmolality independence	Moderate	24
9. Intracellular chemical potential equilibrium	Small to Moderate	27,29
10. Transmembrane pressure equilibrium	Negligible	41

Blum and Forster [42] may be premature in light of the osmotic flow, rectification interpretation of Farmer and Macey [43]. Papanek's results for RBC exosmosis in hypertonic saline solutions do not show permeability osmolality dependence. Finally, the assumption of intracellular chemical potential equilibrium does not significantly affect the calculated cell water content for cooling rates below ~5000 K/min (in RBC's) [27].

2.2 Water Transport in a Cell Population

The importance of the cell water content has led many authors to pursue solutions to equations similar to Eq. (2.15). Although analytical solutions are possible for limited cases [33], numerical techniques have been used by all authors referenced in Table 2.1, due to the nonlinearity of the problem. Solutions have been obtained for a variety of cell types and thermal protocols but in all cases for a single cell at a time, with specified properties. The response of the entire cell population is inferred from the analyzed response of the "mean" cell. More realistic simulations of cell freezing should include the effects of intrinsic distributions of cell properties.

The properties whose distributions are required in analyzing water transport for a cell population, referring to Eq. (2.15), are area, reference permeability, initial water content and activation energy. Table 2.2 summarizes the statistics of these properties for the human red blood cell. The red cell was chosen for study because of its role as a model cryobiological system, which results from its relatively simple

TABLE 2.2
HUMAN RED BLOOD CELL PROPERTIES

PROPERTY	MEAN	STANDARD DEVIATION	SCALING & UNITS	REFERENCES
K_{PR}	1.45	~.3	$\times 10^{-11} \frac{\text{cm}^3}{\text{dyne-s}}$	40,42,43,44
A	135	16	$\times 10^{-8} \text{ cm}^2$	45
N_{Wi}	3.72	.78	$\times 10^{-12} \text{ moles}$	45, see text
E	3.3	.33	Kcal/mole	44

internal structure, abundance of biophysical data and ready availability for experiments.

The value listed for the mean reference permeability was representative of the literature values [40,42,43]. The standard deviation was estimated from scatter shown in [44]. The mean initial number of moles of water was computed from the mean initial volume of $94 \mu^3$ quoted in [45], and the water volume ratio of $.717 \pm .005$ reported by Savitz et al. [46], using the relation:

$$\begin{aligned} N_{Wi} &= [V_i \left(\frac{V_{Wi}}{V_i} \right)] / V_W \\ &= [V_i (.717)] / V_W \end{aligned} \tag{2.17}$$

The standard deviation of the initial number of moles of water is estimated by assuming that all of the observed cell volume variation is due to variations in water content such that:

$$S_{NWi} = S_V / V_W \tag{2.18}$$

The values listed for the mean and standard deviation of the membrane permeability activation energy are similar to those reported by Vieira et al. [44].

A significant question concerning measurement statistics, such as those in Table 2.2, is whether the variations observed represent in-

intrinsic distributions of properties or scatter in the measurements. The area and water content values represent, unequivocally, the intrinsic distributions. The membrane permeability and activation energy values, however, more likely result from experimental uncertainty, particularly because the stop-flow technique used to obtain these values observes the mean averaged volume change of many cells simultaneously and should therefore give the mean permeability. The values listed can certainly provide a starting point for analysis.

Simplification of the water transport analysis for a cell population results from grouping the distributed properties and finding the distribution of the ensemble. One such group is readily apparent in Eq. (2.15) and is defined below:

$$\alpha \equiv \frac{K_{PR} A}{N_{Wi}} \quad (2.19)$$

Mathematical techniques for finding the distribution of a function of distributed variables are discussed by Wozencraft [47]. The application of these techniques to Eq. (2.19) is pursued in detail in Appendix A assuming independent, normally distributed, contributing variables. The moments of the resulting distribution can be computed using two methods whose comparison serves as a check on the calculated distribution. Definitions of the moments for the first method are listed in Eqs. (2.20) through (2.22), from Appendix A. Notation essentially follows that of Papoulis [48] and Wozencraft [47].

$$M_0 \equiv \int p_\alpha(\beta) d\beta \equiv 1 \quad (2.20)$$

$$M_1 \equiv \text{Ex}(\alpha) = \bar{\alpha} = \int \beta p_\alpha(\beta) d\beta \quad (2.21)$$

$$\begin{aligned} M_2 \equiv S_\alpha^2 &= \text{Ex}(\alpha^2) - \text{Ex}^2(\alpha) \\ &= \int \beta^2 p_\alpha(\beta) d\beta - \bar{\alpha}^2 \end{aligned} \quad (2.22)$$

The integrals in the above equations must be evaluated numerically over a suitably large range of the dummy variable, β . The moments can also be found without first computing p_α using Eqs. (2.23) and (2.24), which are derived in Appendix A:

$$\begin{aligned} M_1 \equiv \text{Ex}(\alpha) = \bar{\alpha} &= \bar{K}_{PR} \bar{A} \left(\frac{\bar{I}}{N_{Wi}} \right) \\ &= \bar{K}_{PR} \bar{A} \int \frac{1}{\beta} p_{NWi} d\beta \end{aligned} \quad (2.23)$$

$$\begin{aligned} M_2 \equiv S_\alpha^2 &= (S_K^2 + \bar{K}_{PR}^2)(S_A^2 + \bar{A}^2) \left(\int \left(\frac{1}{\beta} \right) p_{NWi} d\beta \right) \\ &\quad - \left[\bar{K}_{PR} \bar{A} \left(\frac{\bar{I}}{N_{Wi}} \right) \right]^2 \end{aligned} \quad (2.24)$$

Again, numerical integrations are required to evaluate the moments. The results obtained by these methods, listed in the first two lines of Table 2.3, compare favorably, corroborating the calculated distribution.

TABLE 2.3
 COMPARISON OF MOMENTS
 OF THE DISTRIBUTION OF α/V_W

METHOD, SOURCE	M_0 [DIMENSIONLESS]	M_1 [cm ² /dyne-s]	M_2 [(cm ² /dyne-s) ²]
Appendix A Eqs. (A.21)-(A.23), Text Eqs. (2.20)-(2.22)	.999	2.990×10^{-7}	$.7545 \times 10^{-14}$
Appendix A Eqs. (A.24), (A.25)	1	2.991×10^{-7}	$.7597 \times 10^{-14}$
Appendix B Eqs. (B.17), (B.18)	1	2.989×10^{-7}	$.6754 \times 10^{-14}$

Contributing distribution statistics:

$$[\text{cm}^3/\text{dyne-s}] \bar{K}_{PR} = 1.45 \times 10^{-11} \qquad S_K = .3 \times 10^{-11}$$

$$[\text{cm}^2] \bar{A} = 135 \times 10^{-8} \qquad S_A = 16 \times 10^{-8}$$

$$[\text{cm}^3] \bar{N}_{Wi} V_W = 67 \times 10^{-12} \qquad S_{NWi} V_W = 10 \times 10^{-12}$$

Note: A smaller value of S_{NWi} ($.56 \times 10^{-12}$ moles) than that listed in Table 2.2 was used in calculating the above moments.

Figure 2.1 shows the distribution, p_α , compared to a Gaussian with moments M_1 and M_2 from Table 2.3, line 2. Substitution of the Gaussian for p_α is justified by the close correspondence between the two curves. The simplification resulting from this substitution can be extended further by using a third method for computing the mean and variance which does not require numerical integration. A power series expansion of the function α is obtained in the vicinity of the contributing means, \bar{K}_{PR} , \bar{A} and \bar{N}_{Wi} , and then integrated term-by-term using the definition for the mean:

$$M_1 \equiv \text{Ex}(\alpha) = \bar{\alpha} = \int \int \int \alpha p_K p_A p_{N_{Wi}} dK dA dN \quad (2.25)$$

A complete derivation of the power series expansion and moment evaluation is performed in Appendix B. The closed form, truncated expressions for the first and second moments are given below in Eqs. (2.26) and (2.27) with numerical results in Table 2.3, line 3 for comparison to the first two methods considered

$$M_1 \equiv \bar{\alpha} = \frac{\bar{K}_{PR} \bar{A}}{\bar{N}_{Wi}} + \frac{\bar{K}_{PR} \bar{A}}{\bar{N}_{Wi}^3} S_{N_{Wi}}^2 \quad (2.26)$$

$$M_2 \equiv S_\alpha^2 = S_K^2 \left(\frac{\bar{A}}{\bar{N}_{Wi}} \right)^2 + S_A^2 \left(\frac{\bar{K}_{PR}}{\bar{N}_{Wi}} \right)^2 + S_{N_{Wi}}^2 \left(\frac{\bar{K}_{PR} \bar{A}}{\bar{N}_{Wi}^2} \right)^2 \quad (2.27)$$

The series approach yields moments for the distribution of α that are reasonably close to those obtained by more precise methods, with the sub-

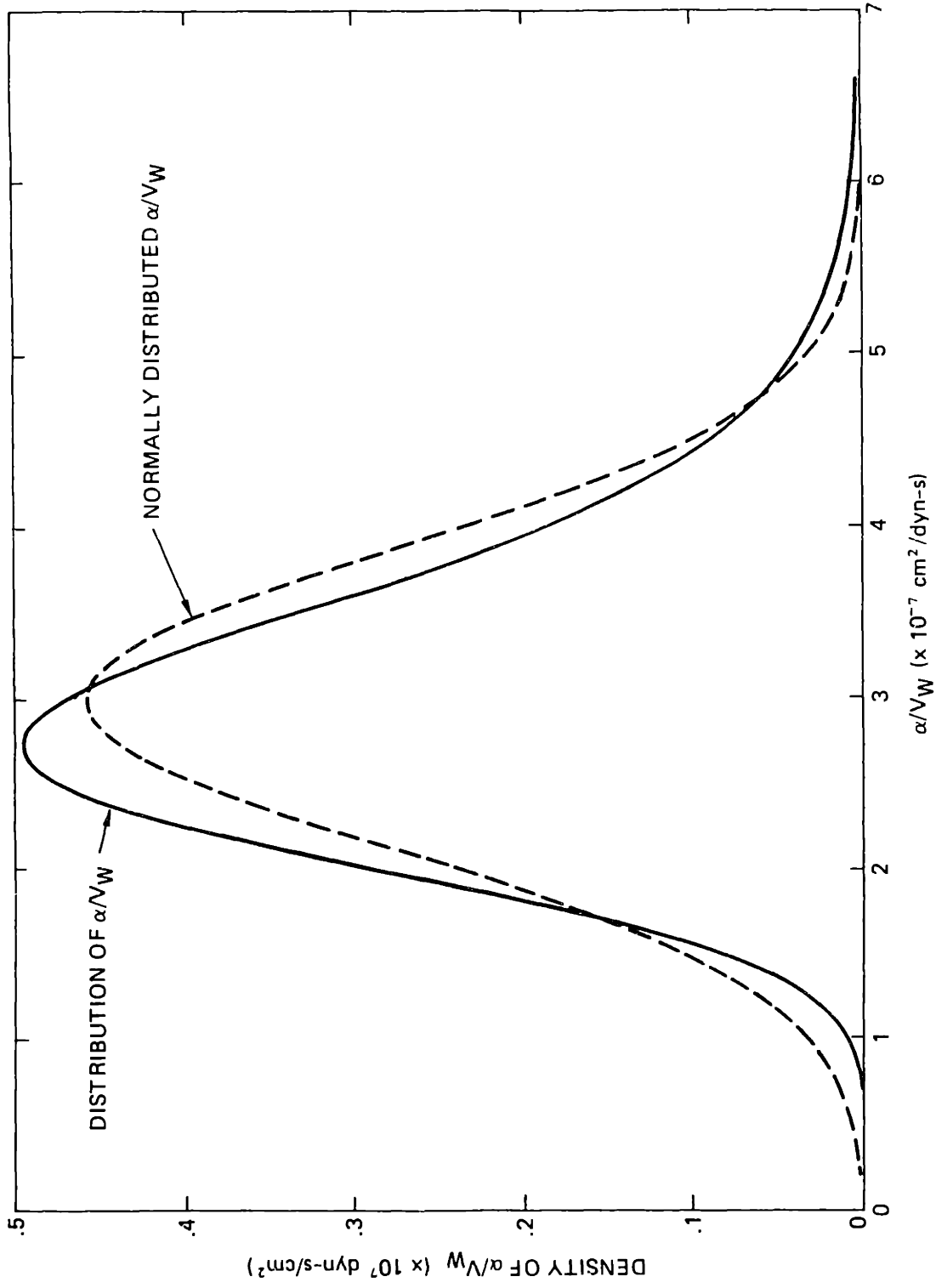


FIGURE 2.1 Comparison of probability density functions for α/V_W

stantial advantage of requiring no numerical integrations. This approach is used in subsequent analysis.

The number of independent distributions that must be considered in a water transport analysis for a cell population has been reduced in the preceding discussion from 4 to 2. The distributed cell water content can be found by creating a 2-dimensional histogram for the cell population by value of α and E and then solving Eq. (2.15) numerically for each histogram group. The 2-dimensional histogram is built from 1-dimensional histograms such as the one illustrated for α in Fig. 2.2. The histogram plateaus representing the fractions of the population with properties α_i , are calculated from the distribution function of α where the number of plateaus, m , is 12:

$$f_{\alpha i} = p_{\alpha}(\alpha_i) \cdot \frac{6S_{\alpha}}{m} \quad (2.28)$$

The normal distribution for α in Fig. 2.2 is given by Eq. (2.29):

$$p_{\alpha}(\alpha_i) = \frac{1}{\sqrt{2\pi} S_{\alpha}} e^{-\frac{1}{2S_{\alpha}^2} (\alpha_i - \bar{\alpha})^2} \quad (2.29)$$

Each element of the histogram can be expanded in an orthogonal histogram by sorting the cells by value of E . Figure 2.3 shows the correspondence between the 2-dimensional joint probability distribution surface and the approximating facets of the resulting 2-dimensional histogram. The height of a particular facet above the α - E plane represents the fraction of the cells with properties α_i, E_j . The sum of all of

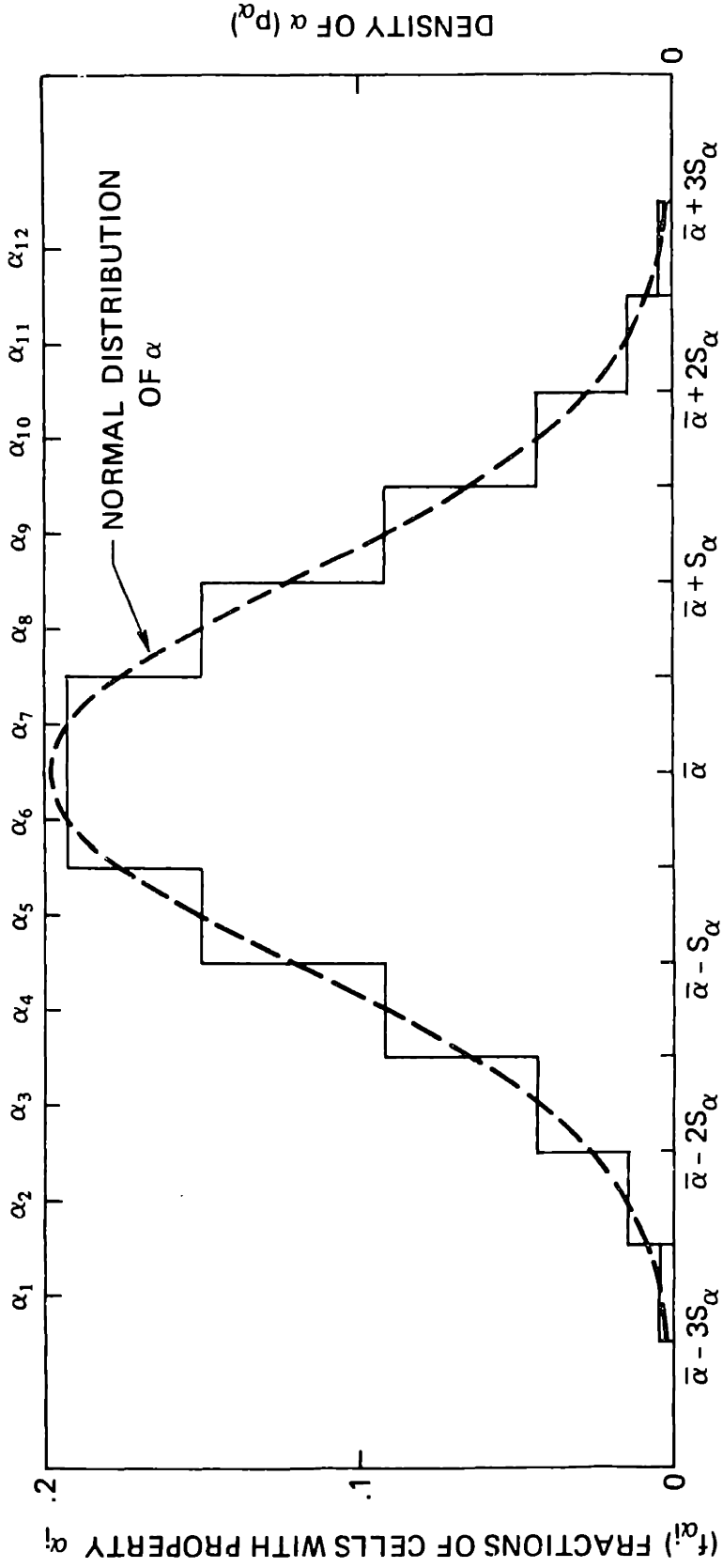


FIGURE 2.2 Histogram and probability distribution function for α

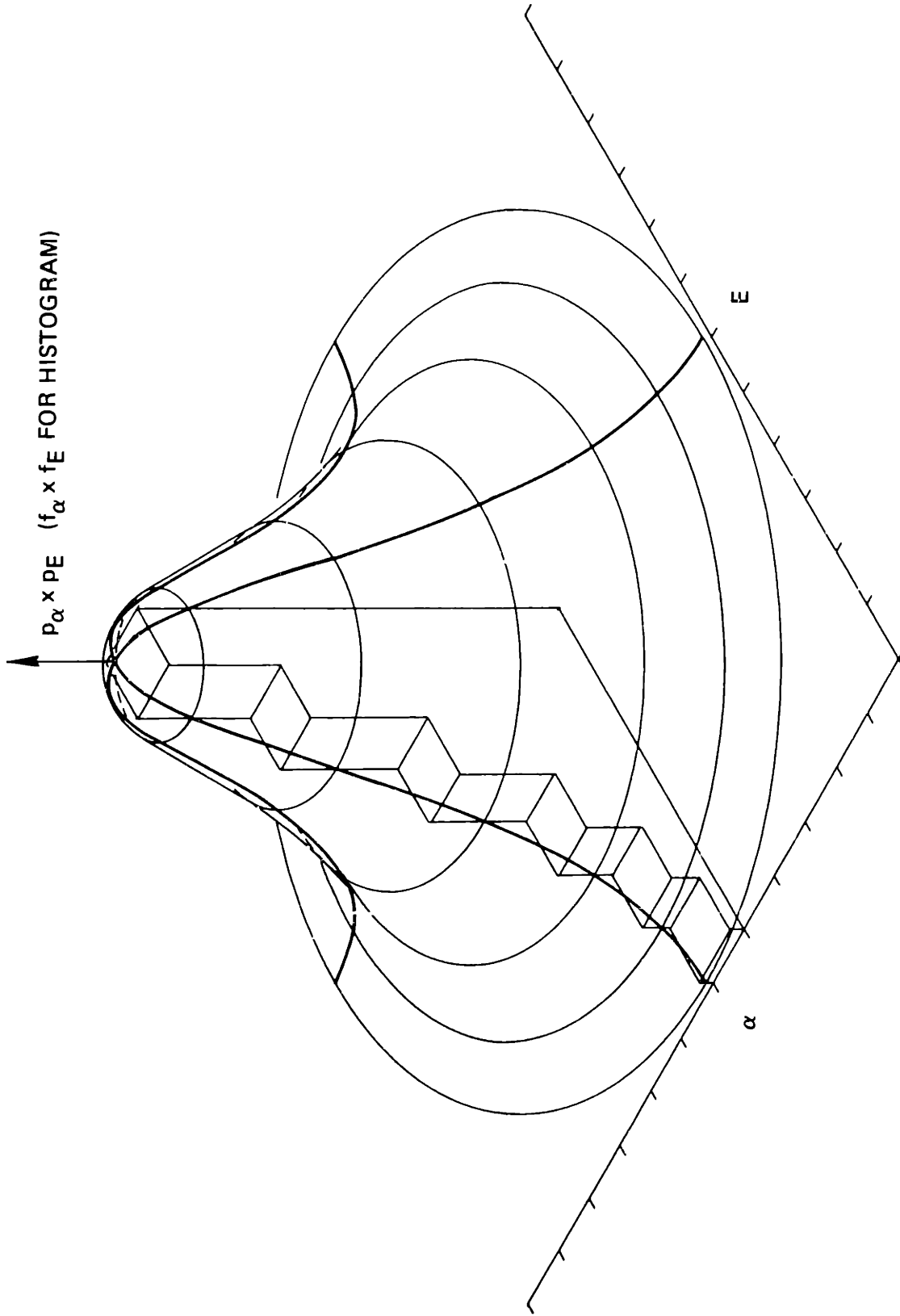


FIGURE 2.3 2-D joint probability distribution and part of corresponding 2-D histogram

the fractions must add to 1 ; m and n are the numbers of segments of the contributing histograms of α and E :

$$\sum_{i=1}^m \sum_{j=1}^n f_{\alpha i} \cdot f_{Ej} = 1 \quad (2.30)$$

Equation (2.15) is rewritten below in terms of the cell properties α_i , E_j corresponding to the fraction of the cells, $f_{\alpha i} \cdot f_{Ej}$:

$$\frac{d\phi_{ij}}{dT} = \frac{\alpha_i RT}{V_W^2 B} \left[e^{\frac{E_j}{R} \left(\frac{1}{T} - \frac{1}{T_R} \right)} \right] \left[\ln \left(\frac{\phi}{\phi + \gamma} \right) - \frac{L_W}{R} \left(\frac{1}{T_0} - \frac{1}{T} \right) \right] \quad (2.31)$$

Numerical integration of $m \times n$ variants of Eq. (2.31) gives at any temperature, $m \times n$ values of ϕ .

Histograms of ϕ can be found at a particular temperature by dividing the total range of ϕ into q segments and then summing the contributing cell fractions for each segment. This is expressed for the k^{th} ϕ segment in Eq. (2.33) while noting that the segment width is defined as:

$$\Delta\phi = (\phi_{\max} - \phi_{\min})/q \quad (2.32)$$

$$\sum f_{\alpha i} \cdot f_{Ej} = f_{\phi k} \quad (2.33)$$

$$\forall \phi_{ij} \ni [\phi_{\min} + (k-1)\Delta\phi \leq \phi_{ij} \leq \phi_{\min} + k\Delta\phi]$$

Since all of the ϕ_{ij} are, by definition, within the total range of ϕ , the total fraction of cells in q segments of ϕ must be 1:

$$\sum_{k=1}^q f_{\phi k} = 1 \quad (2.34)$$

Solutions to Eq. (2.31) for red cells with $m, n = 20$, $\bar{\alpha} = 5.49 \times 10^{-6}$ $\text{cm}^5/\text{dyne-s-mole}$, $S_{\alpha} = 1.67 \times 10^{-6}$ $\text{cm}^5/\text{dyne-s-mole}$, and $B = 10^4$ K/min , are shown in Fig. 2.4 using the histogram form discussed above with $q = 15$. A flowchart for the algorithm used to obtain these solutions is provided in Appendix C. The curve labeled equilibrium reflects Eq. (2.9) and results for all cells when cooling proceeds at infinitesimal rates. The curve labeled mean is obtained when mean values of all cell properties are used in Eq. (2.15). Substantial divergence of the water content occurs at the lower temperatures shown in the figure. The implications of this divergence will become apparent later, in the discussions of intracellular ice formation.

The driving force for osmotic equilibration appears indirectly in Fig. 2.4 as the difference between the water content of a particular cell group and the equilibrium water content. The results can be shown more directly in terms of driving force by using osmolality as a measure of cell water content. The relationship between freezing point depression and osmolality is given in Eq. (2.35):

$$\theta \equiv (T_0 - T)/1.858 \quad (2.35)$$

Freezing point depression and mole fraction are related by Eq. (2.9) for an ideal solution:

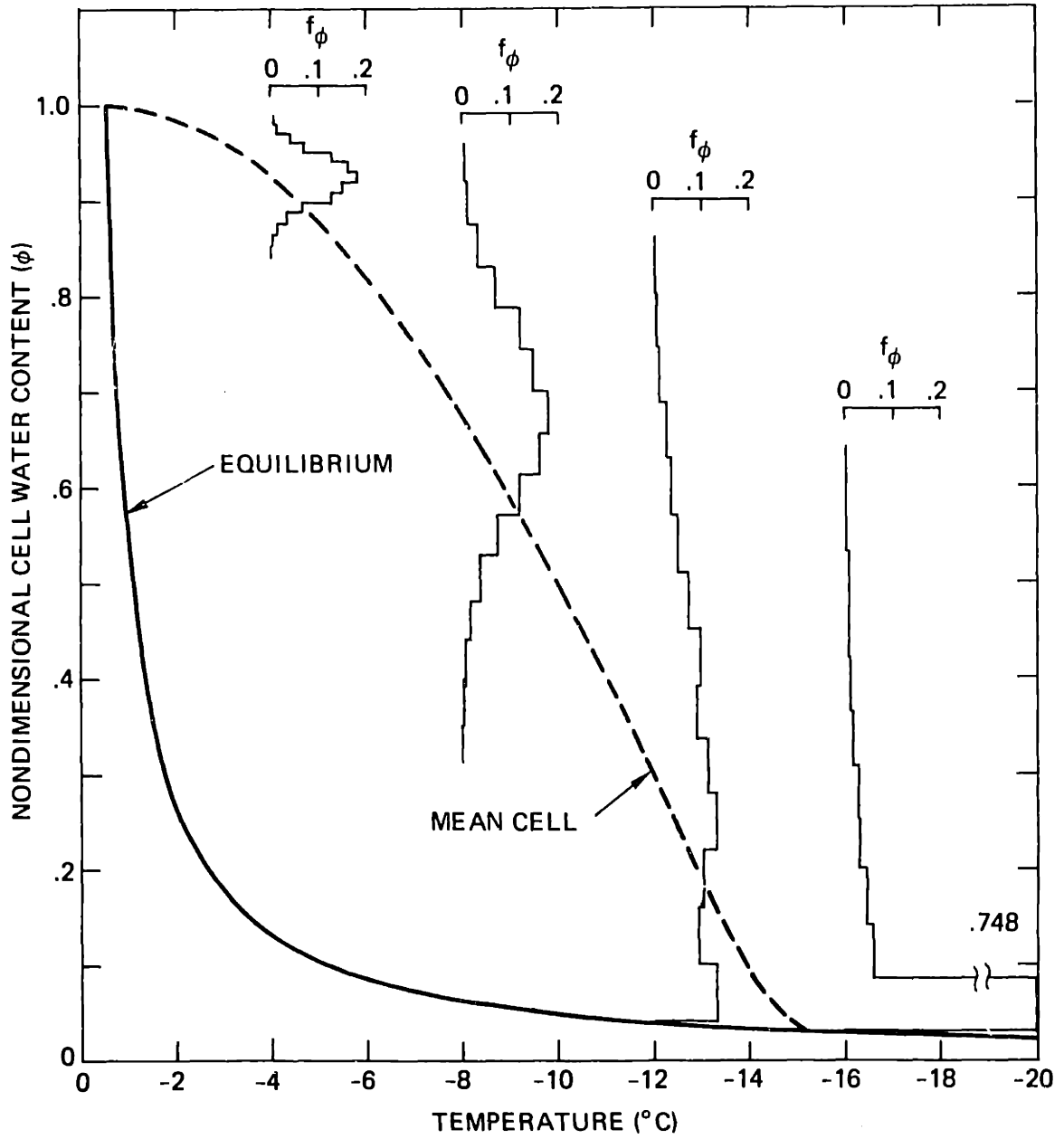


FIGURE 2.4 Distributed red cell water content with cooling at 10^4 K/min

$$\ln X_W = - \frac{L_W}{R} \left(\frac{T_0 - T}{T_0 T} \right) \quad (2.36)$$

Eliminating $(T_0 - T)$ from Eqs. (2.35) and (2.36) effectively relates the osmolality to the chemical potential of water, recalling Eq. (2.2):

$$\theta = - \ln X_W \left(\frac{RT T_0}{1.858 L_W} \right) \quad (2.37)$$

Since mole fraction expressed in terms of ϕ is already available in the solution process for Eq. (2.31), little additional manipulation provides the results in osmolality form. Histograms of the cell population osmolalities are obtained by dividing the total osmolality range into segments, sorting the $m \times n$ osmolalities into these segments and summing fractions for each segment as was done for the ϕ histograms. Equation (2.38), for the fraction of cells in the k^{th} osmolality segment, is analogous to Eq. (2.33):

$$\sum f_{\alpha i} f_{Ej} = f_{\theta k} \quad (2.38)$$

$$\forall \theta_{ij} \ni [\theta_{\min} + (k-1) \Delta\theta \leq \theta_{ij} \leq \theta_{\min} + k\Delta\theta]$$

Equation (2.39) expresses the same requirement as Eq. (2.34), that the q fractions of the population must sum to 1:

$$\sum_{k=1}^q f_{\theta k} = 1 \quad (2.39)$$

Osmolality histograms with $q=15$, for red cells cooled at 10^4 K/min are shown in Fig. 2.5. The curve labeled equilibrium, Eq. (2.35), represents extracellular ice-solution phase equilibrium as well as transmembrane osmotic equilibrium, as in Fig. 2.4. The osmolality of the mean cell shown in Fig. 2.5 corresponds also, to the curve shown for the mean cell in Fig. 2.4. A noteworthy difference between the two presentations, aside from the compression of the high water content histograms in the osmolality domain, is the temperature at which the maximum departure from equilibrium occurs. In Fig. 2.4 the maximum difference between the mean cell and equilibrium curves occurs at $\sim -4^\circ\text{C}$, whereas in Fig. 2.5 the maximum difference occurs at $\sim -13^\circ\text{C}$. Misleading in representing the underlying thermodynamics, the water content presentation has the advantage of correspondence to cell volume, which, unlike osmolality, is readily observed in the laboratory. Both presentations adequately depict the metastable condition of the intracellular solution resulting from subcooling or incomplete dehydration.

The steps taken to obtain the distributed response of a cell population to the osmotic changes accompanying freezing in suspension, are summarized in the flowchart of Fig. 2.6. The assumptions made during the analysis are listed in Table 2.4 by number, according to the associated flowchart step. Assumptions that have not been discussed previously in this chapter are 2a, 2c and 7.

The distributed cell properties are considered independent for the following reasons: there is no a priori reason for linking the permeability

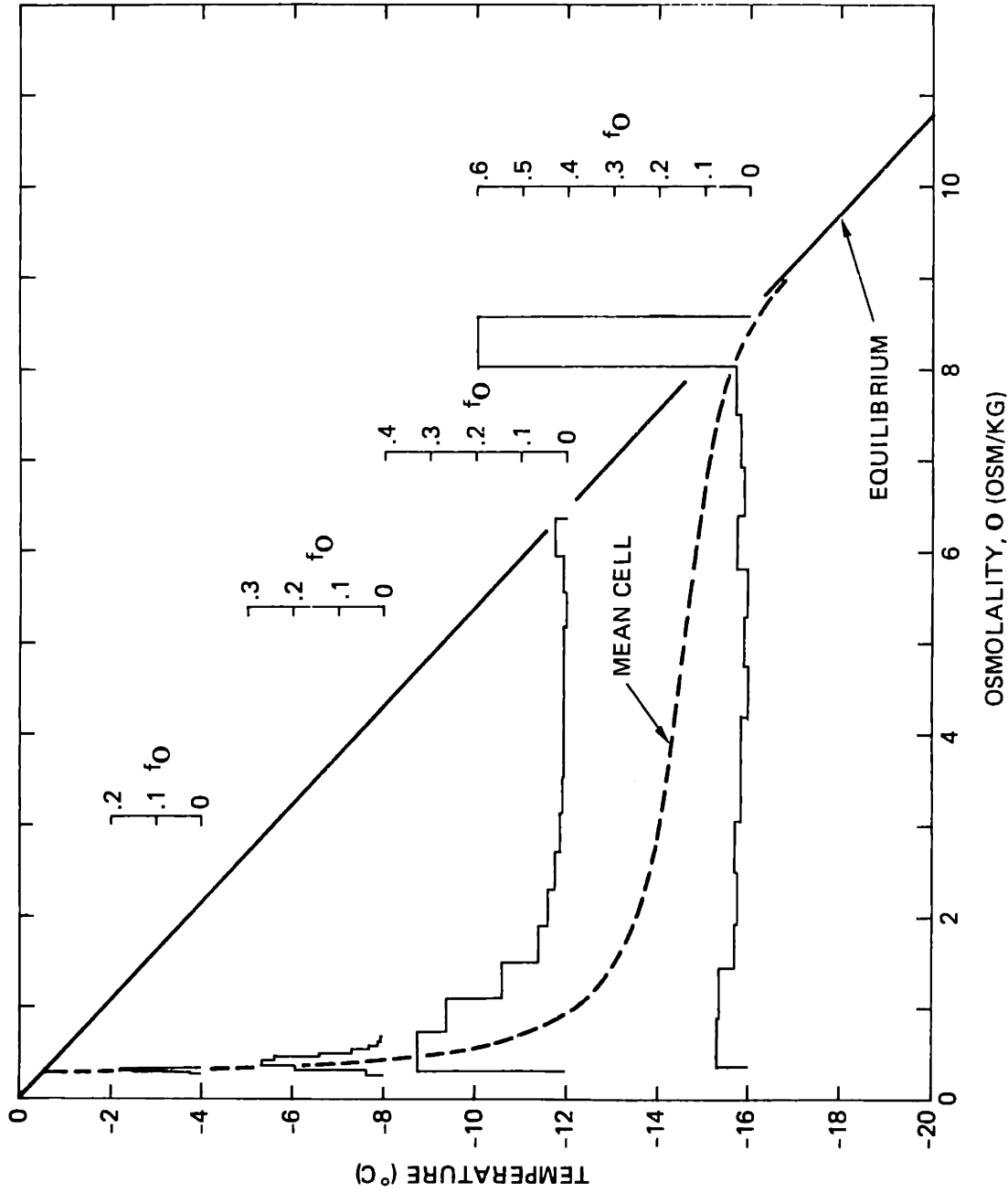


FIGURE 2.5 Distributed internal osmolalities for red cells cooled at 10^4 K/min

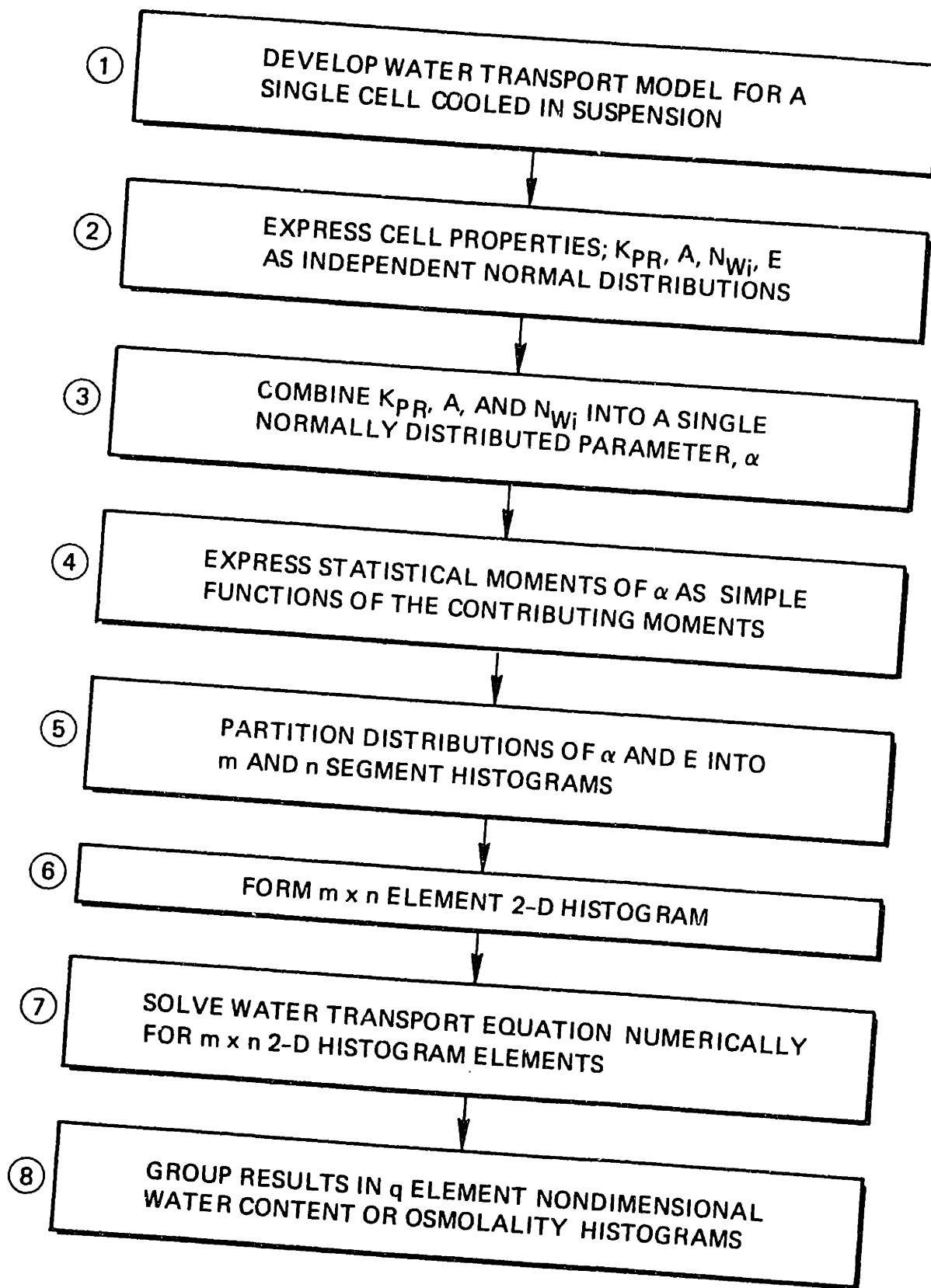


FIGURE 2.6 Distributed water transport analysis flowchart

TABLE 2.4
ASSUMPTIONS IN THE
DISTRIBUTED WATER TRANSPORT ANALYSIS

FLOWCHART STEP	ASSUMPTION
(1)	See Table 2.1
(2)	(a) Distributed properties are independent (b) Literature values for property statistics reflect intrinsic distributions and not measurement uncertainties (c) Properties are distributed normally
(3)	Combined parameter α is distributed normally
(4)	Simple expressions for moments of α are adequate
(7)	Finite number of 2-D histogram elements does not bias results

parameters K_{pR} and E to the other properties or to each other in the absence of a predictive, mechanistic model for the cell membrane. Geometrical relationships between area and volume do not extend to area and water content due to the decoupling effects of the distributed osmotically inactive fraction of the cell volume, V_b , and the existence of membrane folds in some cell types.

Normal distributions are assumed for the cell properties for the following reasons: many characteristics of biological systems are normally distributed, measured red cell geometrical properties [45] match these distributions well, and mathematical manipulations are simplified. Finally, there are no compelling arguments in favor of any other distribution for the properties. The last assumption, that a finite number of histogram elements does not distort the results, is difficult to justify in general. This question was addressed specifically for red cells by reducing the number of 2-D histogram elements from 400 to 144. Results similar to those presented in Figs. 2.4 and 2.5 were obtained. Alternate simulation techniques that assign values of the properties cell by cell using random number generation can serve to check the current method, but again, the number of simulation points required, cannot be determined in advance.

2.3 Mechanisms of Ice Formation in Cells

The formation of ice in biological cells during low temperature exposure has been observed over a range of temperatures and is influenced by the presence of ice in the suspending medium. Table 2.5 summarizes the observed freezing conditions by cell type. Internal freezing in most of the

TABLE 2.5
 INTRACELLULAR FREEZING TEMPERATURES
 WITH AND WITHOUT EXTERNAL ICE PRESENT

CELL TYPE	INTERNAL FREEZING TEMP.		METHOD OF ELIMINATING EXTERNAL ICE	REF./REMARK
	EXTERNAL ICE PRESENT	EXTERNAL ICE NOT PRESENT		
Sea Urchin Eggs	-4 - -8°C	Lower than -8°C	Suspension in Silicone Oil	49
Spirogyra	- 7.7°C	Lower than -12.4°C	Supercooling of Suspension	50
HeLa	-13°C			
Mouse Ova	-45°C			51, (in 1 M DMSO)
Yeast	-10 - -15°C	-40 - -47°C	Safflower Oil Emulsions	52,53,54

cells listed occurs at $\sim -10^{\circ}\text{C}$ in the presence of external ice and at significantly lower temperatures in the absence of external ice. It is reasonable to conclude from these observations that external ice plays an important role in intracellular freezing. A significant exception is that of mouse ova, which undergo internal freezing, even in the presence of external ice, at -45°C . This is in the range where spontaneous freezing of water has been observed in small samples [55,56]. Although no single mechanism is capable of explaining all of the observed phenomena, only a few mechanisms are required to account for the majority of the observations, and are marked by substantial similarities. These mechanisms are reviewed here to establish criteria for use in simulations of freezing in a cell population.

Hypothesized mechanisms for internal freezing can be categorized as spontaneous or assisted. Two related mechanisms for spontaneous ice formation are homogeneous and heterogeneous nucleation. Homogeneous nucleation involves random accretions of molecules or nuclei which serve as substrates for subsequent growth to macroscopic size. The accretion process is aided in heterogeneous nucleation by the presence of surfaces which promote ice structure in the surrounding liquid.

The free energy of formation of a spherical cluster of molecules of the solid phase with radius, r_N , consists of a contribution from the release of latent heat as well as a term for the energy required to increase the surface area of the cluster [57]:

$$\Delta G_N = - \frac{4\pi r_N^3 \Delta G_{LS}}{3 V_W} + 4\pi r_N^2 \sigma_{LS} \quad (2.40)$$

A critical radius, such that further growth of the cluster is thermodynamically favored, can be found by setting the derivative of ΔG_N with respect to r_N , from Eq. (2.40), to zero. The size of the critical cluster and the free energy of its formation are given in Eqs. (2.41) and (2.42) respectively:

$$r_N^* = 2 \sigma_{LS} V_W / \Delta G_{LS} \quad (2.41)$$

$$\Delta G_N^* = \Delta G_N |_{r_N^*} = \frac{16\pi}{3} \frac{\sigma_{LS}^3 V_W^2}{\Delta G_{LS}^2} \quad (2.42)$$

The bulk free energy change for the liquid to solid transformation can be derived by noting first, that by definition:

$$\Delta G_{LS} = \Delta H_{LS} - T \Delta S_{LS} \quad (2.43)$$

If ΔH_{LS} and ΔS_{LS} are considered constant with temperature, and with ΔS_{LS} defined as $\Delta H_{LS}/T_e$, then ΔG_{LS} becomes:

$$\Delta G_{LS} \cong \Delta H_{LS} \Delta T / T_e \quad (2.44)$$

The assumption of constant ΔH_{LS} and ΔS_{LS} leads to significant error if the departure from equilibrium is large enough. Hoffman [58] considers the temperature dependence of these terms and proposes the simplified expression of Eq. (2.45) to replace Eq. (2.44):

$$\Delta G_{LS} = \Delta H_{LS} \frac{\Delta T}{T_e} \left(\frac{T}{T_e} \right) \quad (2.45)$$

The rate of formation of stable clusters is highly dependent on the energy barrier, according to Eq. (2.46):

$$I \propto e^{-\left(\Delta G_N^*/k_B T\right)} \quad (2.46)$$

The energy barrier in heterogeneous nucleation is reduced by a factor, g_θ , which depends on the shape of the substrate [59,60]:

$$\Delta G_S = g_\theta \Delta G_N^* \quad (2.47)$$

Thus, for both homogeneous and heterogeneous nucleation, the rate of appearance of stable clusters goes as Eq. (2.48), which combines Eqs. (2.42) (2.45) and (2.46):

$$I \propto e^{-g_\theta \left(\frac{16\pi}{3} \frac{\sigma_{LS}^3}{\Delta H_{LS}^2} \frac{V_W^2}{k_B} \frac{T_e^4}{\Delta T^2 T^3} \right)} \quad (2.48)$$

The relative magnitude of the nucleation rate is illustrated in Fig. 2.7 as a function of temperature for constant supercoolings of 10.0 and 10.1°C. The shape factor, g_θ , was set equal to 1; the interfacial energy, σ_{LS} was assumed constant at 22 ergs/cm² [56] and the equilibrium freezing temperature, supercooling and absolute temperature are related by the definition: $\Delta T \equiv T_e - T$. The reference value of I was calculated

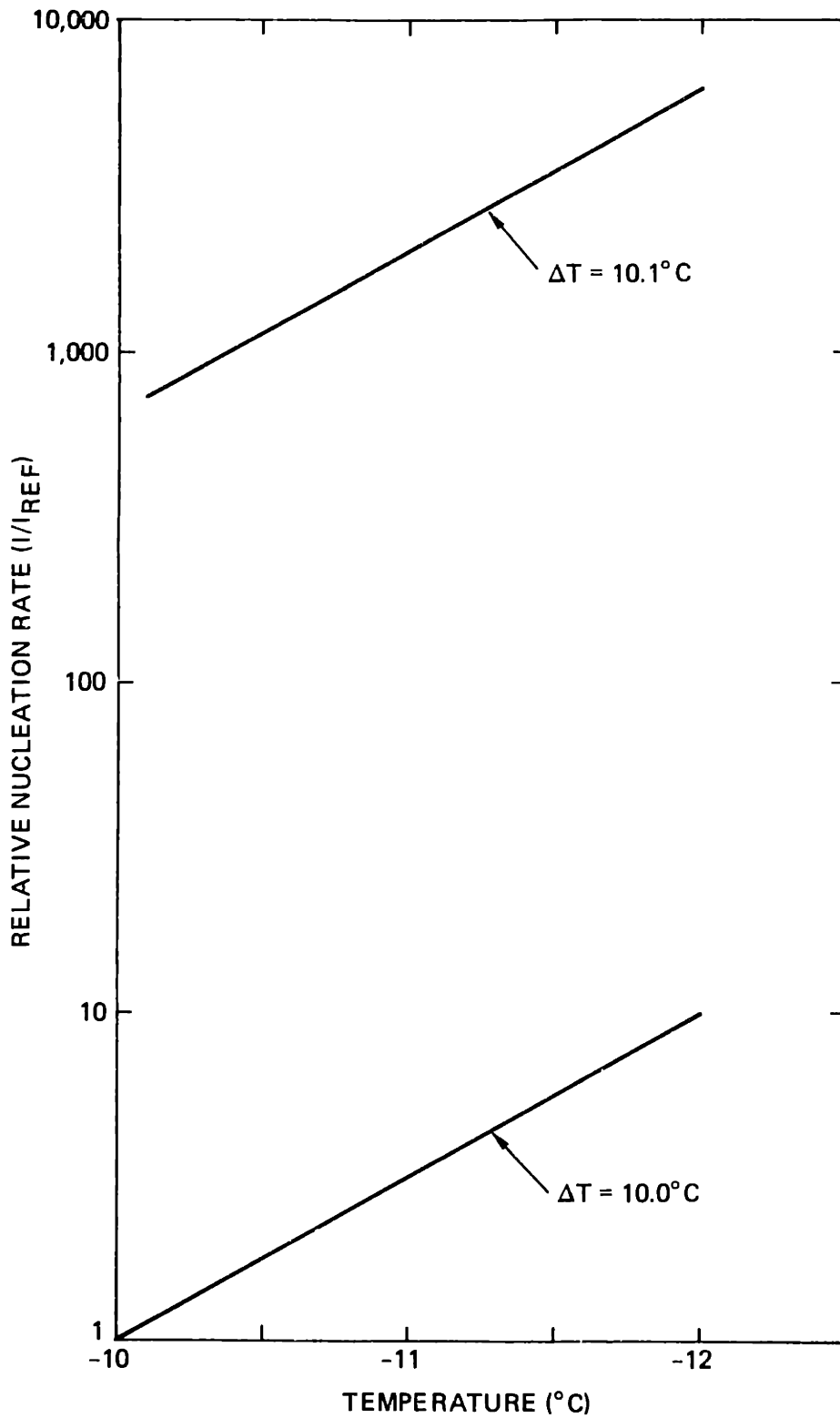


FIGURE 2.7 Relative nucleation rate as a function of temperature and supercooling

using $\Delta T = 10.0^\circ\text{C}$, $T = 263.15\text{ K}$ and $T_e = 273.15\text{ K}$. The tremendous sensitivity of the nucleation rate to supercooling compared to temperature is clearly evident: rate increases 2000 times as much per degree of supercooling as per degree of absolute temperature. If intracellular freezing were to occur, therefore, by heterogeneous or homogeneous nucleation, strong dependence on internal supercooling should be observed.

A plausible assisted mechanism of intracellular ice formation, proposed by Mazur [53,10], involves seeding of the internal solution by external ice through 'pores' or channels in the cell membrane. Arguments for the existence of the pores are presented by Solomon [61], who calculates equivalent pore radii from semiempirical models combined with tracer diffusive and osmotically driven, water flow measurements.

The Gibbs free energy change associated with solidification in a capillary [62] is analogous to that for a cluster of molecules in homogeneous nucleation in that the process is driven by release of latent heat, and surface free energy changes. The free energy of solidification per unit length of capillary is given in Eq. (2.49):

$$\Delta G_C = \frac{-\pi r_c^2 \Delta G_{LS}}{V_W} + 2\pi r_c (\sigma_{LC} - \sigma_{SC}) \quad (2.49)$$

The equilibrium contact angle, θ , shown in Fig. 2.8 is related to the interfacial energies in Eq. (2.50):

$$\sigma_{LS} \cos\theta = \sigma_{LC} - \sigma_{SC} \quad (2.50)$$

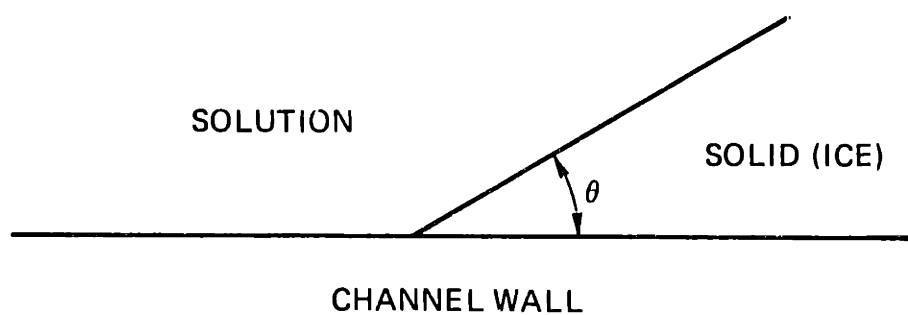


FIGURE 2.8 Equilibrium contact angle at solution-ice-channel interface

The propagation temperature, T , for ice in a capillary can be found by substituting Eqs. (2.44) and (2.50) into Eq. (2.49) while noting that $\Delta G = 0$ at equilibrium between the solid and liquid phases:

$$T_e - T = \frac{2\sigma_{LS} \cos\theta T_e V_w}{\Delta H_{LS} r_c} \quad (2.51)$$

The membrane channels could conceivably contain pure water driven from the cell by osmotic forces, intracellular solution, or extracellular solution. In the first case, the equilibrium freezing temperature is a fixed value and internal seeding would depend on absolute temperature rather than internal supercooling. If the channels contain internal solution, the equilibrium freezing temperature changes with cellular dehydration and seeding would therefore depend on the supercooling of the internal solution. Seeding of the internal solution by external ice would not be possible if the membrane channels contained extracellular solution.

Values of $T_e - T$ are listed in Table 2.6 for contact angles between 0° and 75° and pore radii between 4 and 28 \AA . The equivalent pore radius of 4.5 \AA calculated for the human RBC [61] in conjunction with expected contact angles of $0-25^\circ$ give ice-solution interface equilibrium temperatures substantially lower than values of about -10°C observed for intracellular ice formation, listed in Table 2.5. Larger contact angles and/or larger pore sizes are needed to account for the observations.

The existence of a distribution of pore sizes with some pores substantially larger than the others is not excluded by the equivalent

TABLE 2.6
DEPRESSION OF FREEZING POINT
FOR SOLUTION IN A MEMBRANE PORE, $(T_e - T)$ [K]

PORE RADIUS [\AA]	CONTACT ANGLE, θ [DEGREES]			
	0	30	60	75
4	89.8	77.8	44.9	23.3
12	30.0	25.9	15.0	7.8
20	18.0	15.6	9.0	4.7
28	12.8	11.1	6.4	3.3

pore model. Only one large pore is required to seed each cell; cell-to-cell variations of the largest pore size would lead to variations in freezing temperature within the population. The question of larger contact angles in the pore hinges on the possibility of a more ordered liquid in the channels than is seen in bulk. These issues as well as the more fundamental question of the validity of using bulk properties to describe the behavior of matter on a submicroscopic scale have yet to be resolved.

Criteria for intracellular freezing that are apparent from the preceding discussion include: internal supercooling must exceed that required for nucleation by heterogeneous or homogeneous mechanisms, or absolute temperature must be below or internal supercooling exceed that required for growth of ice through a membrane channel.

2.4 Criteria for Intracellular Freezing

The water transport results of Section 2.2 provide a starting point for analysis of freezing in a cell population, and its dependence on the thermal history. Some of the questions that remain to be considered are: what fraction of a cell's initial water content must freeze internally in order to produce a lethal or damaging condition, and how does this fraction relate to that required for cryomicroscopic observability as 'flashing' or darkening. How is nucleation temperature or supercooling required for internal ice formation distributed in the cell population? The first question is complicated by the additional factor of crystal size. Growth of small crystals into larger crystals during the warming has been

shown directly, or by implication [21,63,5] to increase the lethality of a particular quantity of ice inside a cell. The amount of ice required before lethal recrystallization can occur has not specifically been established. The first question can be approached indirectly by considering the established connection between intracellular freezing and decreased viability observed on the cryomicroscope, [Review in 21,19,51] and the large fractional cell volumes at which observable intracellular freezing (OIF) occurs. Large fractional volumes at the observed moment of intracellular freezing imply large fractional cell water content. The few observations available support the statement that intracellular freezing occurs at volumes, V_{OF}/V_i , greater than $\sim .7$ [64, §4.1]. Since the volume of intracellular water, V_{Wi}/V_i is also $\sim .7$, the requirement for observable freezing in terms of ϕ can be written:

$$\begin{aligned} \phi_{OF} &> \frac{N_{OF}}{N_{Wi}} = \frac{(V_{OF} - V_b)/V_W}{\left(\frac{V_{Wi}}{V_i}\right)\left(\frac{V_i}{V_W}\right)} = \frac{V_{OF} - V_b}{V_{Wi}} && (2.52) \\ &> \sim .5 \end{aligned}$$

A similar condition can be written in terms of osmolality by using Eqs. (2.4), (2.14), (2.35), (2.36) and (2.52):

$$0 < .58 \tag{2.53}$$

The additional requirement for OIF is that temperature be below the freezing temperature, or internal supercooling exceed that required for spontaneous or assisted nucleation in the observed cell:

$$T \leq T_f$$

or

$$\Delta T^i \geq \Delta T_f \quad (2.54)$$

The criteria for OIF in Eqs. (2.52), (2.53) and (2.54) are illustrated for a single cell in Figs. 2.9 and 2.10 which use the nondimensional water content and osmolality representations discussed earlier. The mechanism of cell freezing determines the importance of temperature relative to supercooling of the cell contents. Curves assumed at -6°C freezing temperature, and 5.5°C supercooling for internal nucleation, are drawn for comparison. Additionally, the trajectories of states for similar cells cooled at rates B_1 and B_2 , with $B_1 > B_2$, are shown. The combination of the water content, and temperature or supercooling conditions, produces a region in which observable intracellular freezing is expected. The curve labeled B_1 passes into this region hence the cell cooled at this rate forms OIF. Dehydration of the cell cooled at B_2 returns the cell to equilibrium before the criteria for OIF are satisfied.

An important feature of the region of OIF in Figs. 2.9 and 2.10 is its relative insensitivity to the mechanism of internal ice formation. Equivalent cells cooled at B_1 , differing only in assumed mechanism of ice

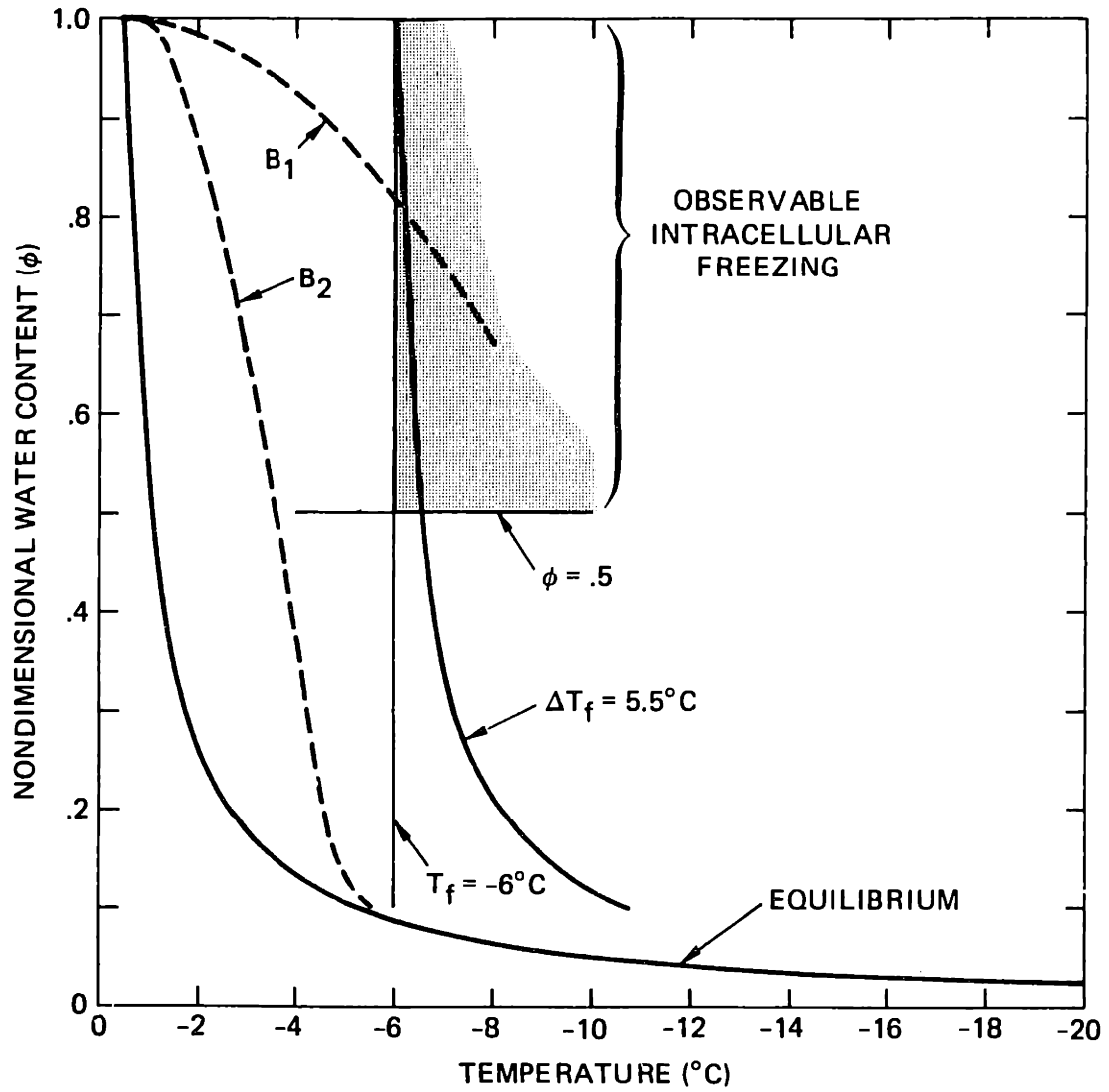


FIGURE 2.9 Criteria for observable intracellular freezing in the water content domain

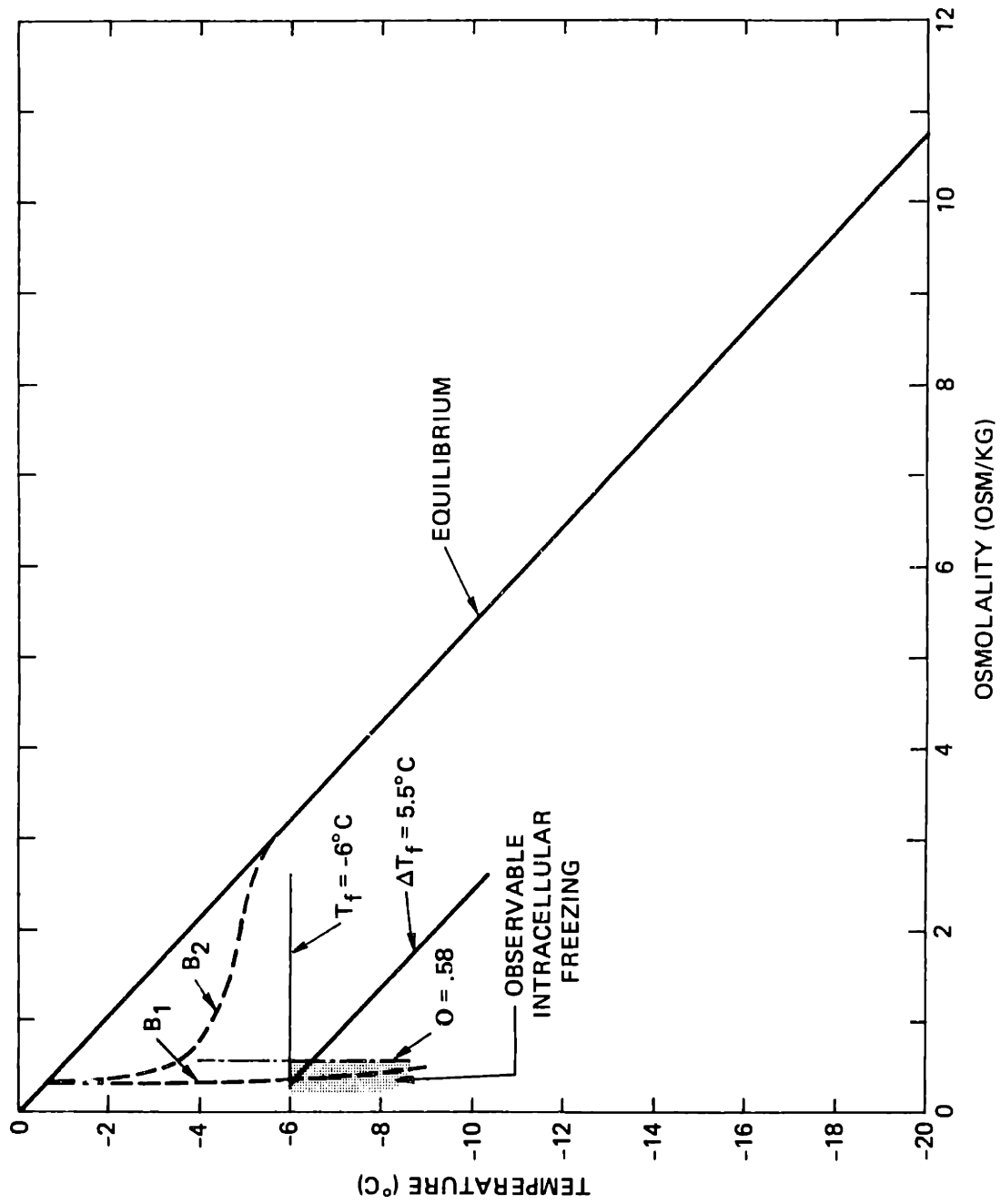


FIGURE 2.10 Criteria for observable intracellular freezing in the osmolality domain

formation with $T_f = -6^\circ\text{C}$ for one and $\Delta T_f = 5.5^\circ\text{C}$ for the other, would be indistinguishable in their observed responses. Indeed, over a range of cooling rates for which OIF is expected, only a minor internal freezing temperature dependence on cooling rate would distinguish cells freezing by a supercooling mechanism from those freezing by a temperature related mechanism. The current state of cryomicroscope instrumentation makes determination of the mechanism of freezing based on freezing temperature cooling-rate dependence unlikely, as this would require reproducible temperature measurements within $\sim .2^\circ\text{C}$.

The similarity of supercooling and temperature criteria for OIF allows significant simplification of cell freezing analyses by allowing use of a cell freezing temperature, T_f , independent of mechanism. The distribution of values of this cell property can be found experimentally without knowledge of other cell properties through the following procedures and reasoning: Groups of cells are cooled at rates well above those known to produce OIF, to a series of subzero $^\circ\text{C}$ temperatures and in each case the percentage with OIF or percentage survival, observed. All cells satisfy the water content criterion for OIF at sufficiently high cooling rates. Internally frozen cells accumulate as the temperature goes below the freezing temperatures of individual cells, resulting, then, in the cumulative distribution of cell freezing temperature. This process is illustrated in Fig. 2.11 for a group of cells cooled rapidly to -6°C . The distributions of properties, affecting the water transport, result in a range of ϕ , but all cells in this range contain sufficient water to manifest OIF. The

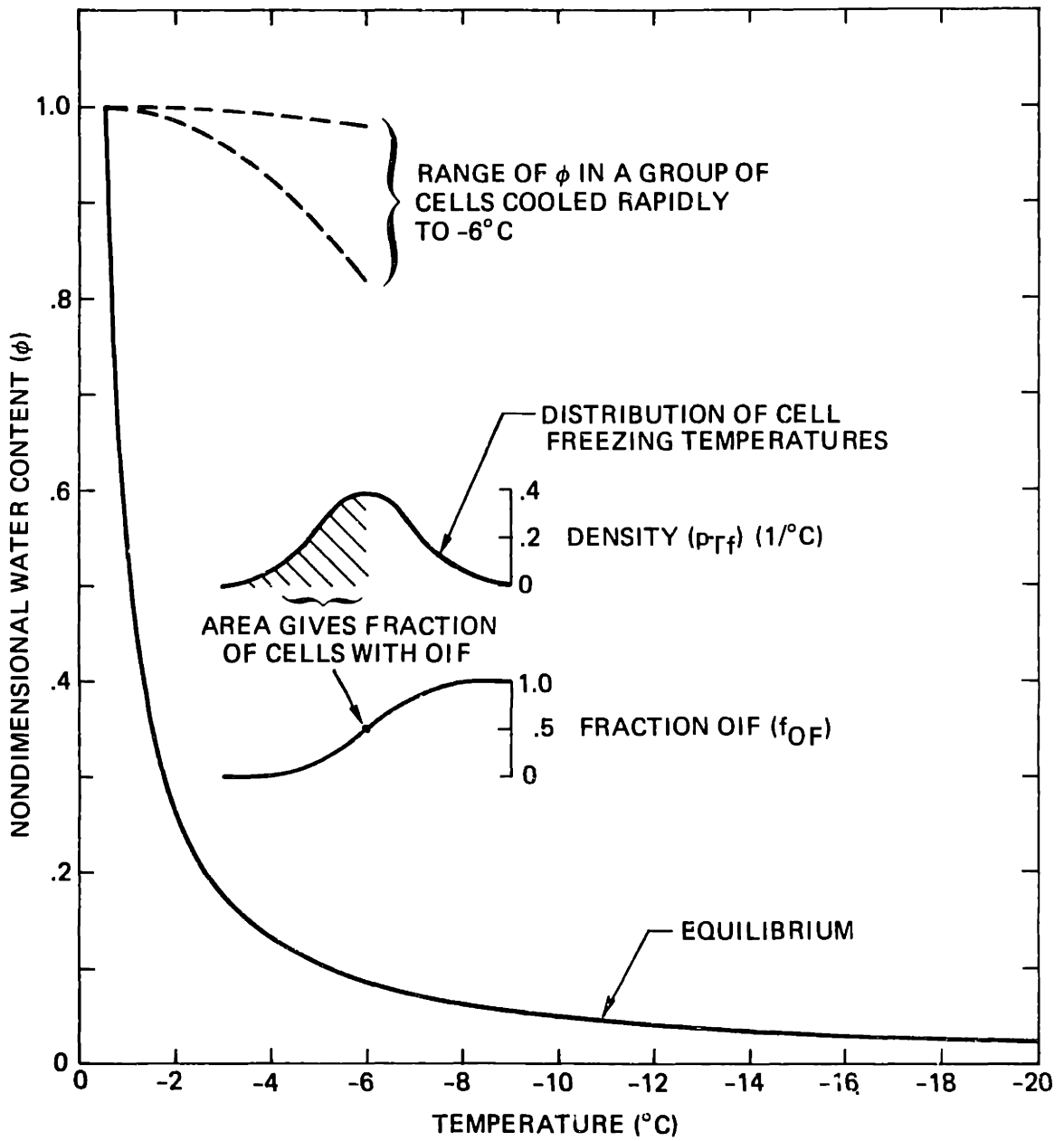


FIGURE 2.11 Fraction of cells with observable intracellular freezing in a cell group cooled rapidly to -6°C

integral of the hypothetical distribution of cell freezing temperatures gives a single point on the cumulative distribution function for the fraction of cells containing OIF. This is stated mathematically for the case shown, in Eq. (2.55):

$$f_{\text{OIF}}|_{-6^{\circ}\text{C}} = \int_{-54^{\circ}\text{C}}^{-6^{\circ}\text{C}} p_{\text{Tf}} dT \quad (2.55)$$

This process must be repeated for different final temperatures to reproduce the entire fraction OIF curve.

Experiments of this type have been reported in the literature, but with no attempt to derive distributions of cell freezing temperature. Figure 2.12 shows experimentally determined lethalities for mouse ova in saline [18], and hamster fibroblasts [65] in 5% V/V DMSO, cooled rapidly to various final temperatures and warmed slowly. Similar data have been reported for ova in glycerol and DMSO [18], for *P. tularensis* in gelatin saline [66] and for yeast in distilled water [52]. The solid curves in each figure are the cumulative distribution functions obtained by integrating assumed normal distributions of cell freezing temperature. The means and variances of the assumed distributions were chosen casually to provide a reasonable fit after integration, to the experimentally determined points. The primary assumption required in inferring the distributions of freezing temperatures from the lethality observations, is that lethality results from observable intracellular ice formation and/or related events such as bubble formation [50] and recrystallization during slow

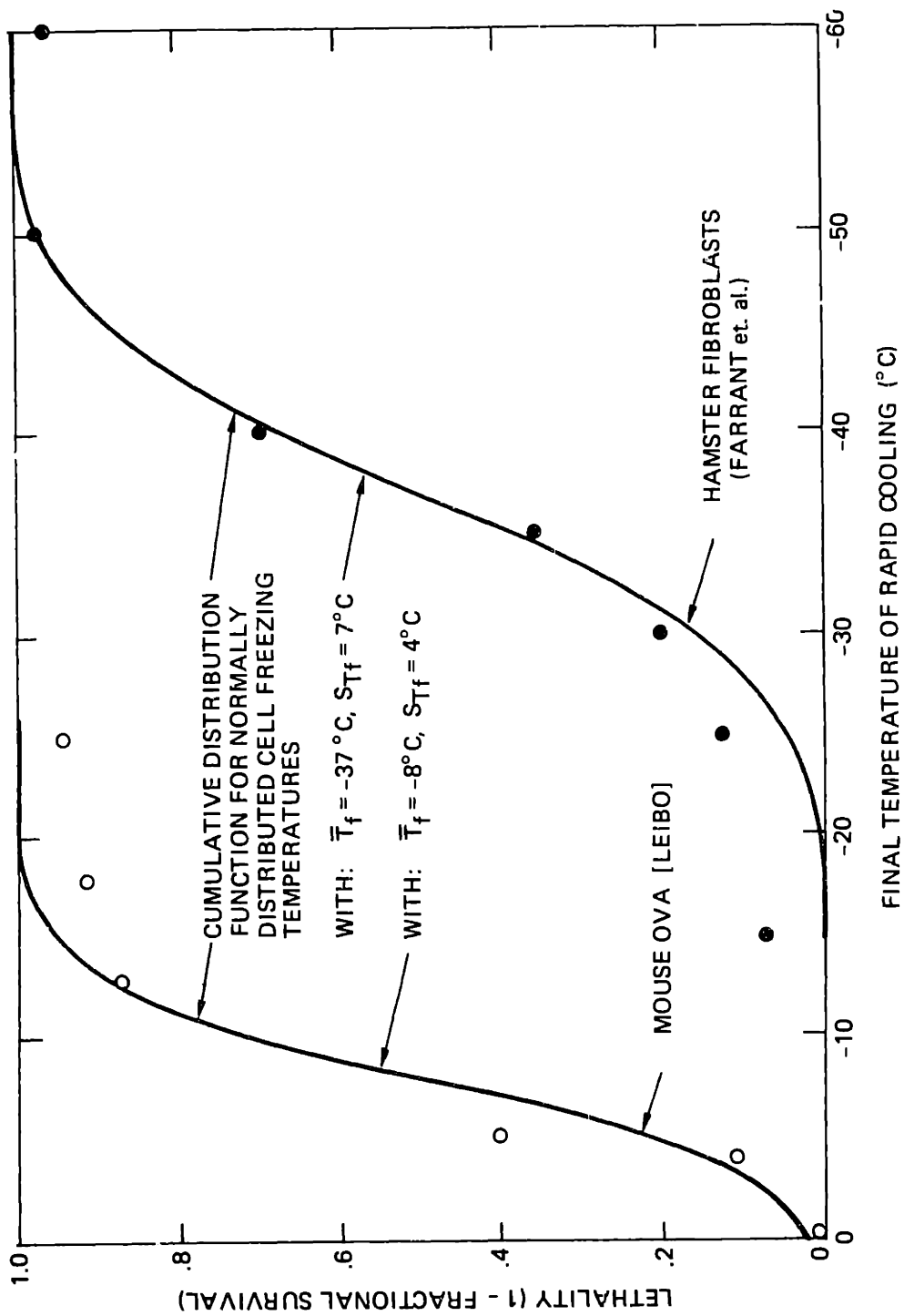


FIGURE 2.12 Cumulative distribution functions for normally distributed cell freezing temperatures compared to experimentally determined lethality for mouse ova and hamster fibroblasts cooled rapidly to subzero ($^{\circ}\text{C}$) final temperatures prior to slow warming

warming. The lethality-OIF connection was discussed earlier and has been directly established for several cell types including mouse ova.

A brief summary of this discussion includes the following salient points: (1) Observable intracellular freezing and lethality are closely related. (2) One condition for OIF is the presence of at least 50% of the initial water in the cell. (3) The second condition for OIF is that temperature be below the nucleation temperature or supercooling exceed that required for nucleation. (4) Supercooling and absolute temperature conditions for internal ice formation can be combined into a single criterion to replace item (3), namely that temperature be below the cell freezing temperature. (5) Distributions of freezing temperature in a cell population can be determined indirectly from experiments that involve rapid cooling to subzero ($^{\circ}\text{C}$) temperatures. (6) Cell freezing temperatures are normally distributed.

2.5 Fraction of Cells with Internal Freezing: Dependence on Cooling Rate

The fraction of a cell population that undergoes observable intracellular freezing during low temperature exposure can be determined by combining the criteria for ice formation, discussed in Section 2.4, with the distributed water transport analysis of Section 2.2. The incremental fraction of cells that forms OIF at a temperature within dT of T in the range of cell freezing temperatures, is given by the product of the fraction of cells that freeze at T , $p_{Tf}|_T dT$, and the fraction that meets the water content criterion, defined in Eq. (2.56):

$$f_{\phi > .5} \equiv \int_{.5}^{1.0} p_{\phi} d\phi \quad (2.56)$$

The incremental fractions with OIF must be summed over temperature to find the total fraction, expressed in Eq. (2.57):

$$f_{OF}|_T = \int_{-.54}^T (p_{Tf} \cdot f_{\phi>.5}) dT \quad (2.57)$$

The integral of Eq. (2.56) must be evaluated continuously during the temperature integration of Eq. (2.57) since the cell fraction meeting the water content criterion changes with time as dehydration proceeds. The probability density function for cell freezing temperature can be assumed Gaussian, based on the discussion in Section 2.4:

$$p_{Tf} = \frac{1}{\sqrt{2\pi} S_{Tf}} e^{-\frac{(T_f - \bar{T}_f)^2}{2S_{Tf}^2}} \quad (2.58)$$

Solutions for f_{OF} are immediately available for 2 cases: at high relative cooling rates, Eq. (2.56) is always 1 and the problem reduces to evaluating Eq. (2.55). In this instance, distributed water transport has no effect on the fraction of cells with observable internal freezing. In the slow cooling rate extreme, Eq. (2.56) goes to zero before the range of cell freezing temperatures is reached, resulting in $f_{OF} = 0$ in Eq. (2.57).

A numerical approach for finding the fraction of cells with OIF continues the methodology discussed earlier by partitioning the population to obtain a histogram of cell freezing temperatures. The sum of the cell

fractions represented by u histogram elements must always be 1:

$$\sum_{\ell=1}^u f_{T_{f\ell}} = 1 \quad (2.59)$$

A three-dimensional histogram of cell properties results from the independence of the cell freezing temperature distribution. Each of the u freezing temperature groups contain $m \times n$ cells corresponding to the ranges of α and E . The discrete equivalent of Eq. (2.57) for cooling to a temperature within the freezing temperature range is written as:

$$f_{OF_{T_{f u' < T < T_{f(u'+1)}}}} = \sum_{\ell=1}^{u'} f_{T_{f\ell}} (f_{\phi > .5} |_{T_{f\ell}}) \quad (2.60)$$

The discrete equivalent of Eq. (2.56) for the cell fraction meeting the water content criterion becomes:

$$f_{\phi > .5} |_{T_{f\ell}} = \sum_{i,j \forall \phi_{ij} > .5} (f_{\alpha i} \cdot f_{Ej}) |_{T_{f\ell}} \quad (2.61)$$

This summation is performed for all i, j pairs associated with water content greater than .5.

The algorithm used to find f_{OF} in Eq. (2.60) is summarized in the flowchart of Appendix D. The computational steps associated with updating the ϕ matrix, from the distributed water transport analysis, are embedded in the new algorithm. The solution method can be visualized

by considering a stack of u identical distributions of cell water content at temperatures above the first freezing temperature histogram element. The water transport problem for any stack layer remains that of solving for the $m \times n$ elements discussed in Section 2.2. When the highest freezing temperature element is reached, the first stack layer is 'peeled' off and evaluated for the water content criterion of observable freezing. This corresponds to the summation in Eq. (2.61). Dehydration continues for the $u-1$ stack layers until the next freezing temperature histogram element is reached. The second stack layer is then 'peeled' off, evaluated for OIF and the fraction summed with that found for the first stack layer. This summation for u layers corresponds to that of Eq. (2.60).

The fractions of cells with OIF are shown in Fig. 2.13 using red cell properties with $\bar{T}_f = -6^\circ\text{C}$, $S_{Tf} = .5^\circ\text{C}$ and $u = 30$. At the highest cooling rate shown, all cells undergo OIF and the curve reproduces the integral of Eq. (2.60) with Eq. (2.56) always equal to 1. This is the same result as would be expected from the discussion in Section 2.4 for rapid cooling to the indicated final temperatures. The ultimate fractions OIF attained over a range of cooling rates are shown in Fig. 2.14. The wide range of cooling rates over which the fraction of cells with OIF goes from 0 to 1 results primarily from the distribution of ϕ and not from S_{Tf} as demonstrated by the relatively small effect of changed S_{Tf} . These results will be compared to experimental findings and reported analyses in Chapter 5.

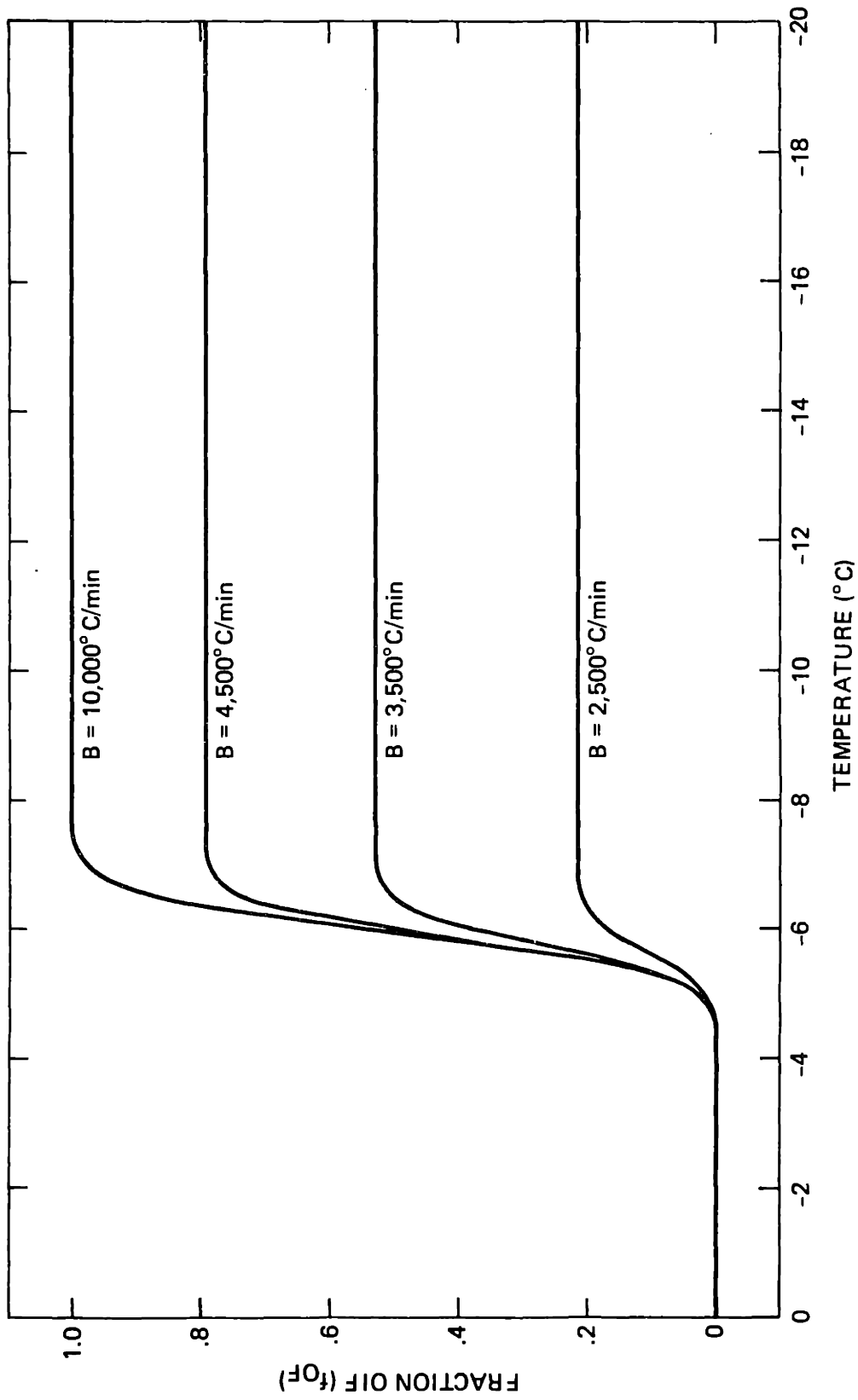


FIGURE 2.13 Fraction of a red cell population with observable intracellular freezing (OIF) as a function of cooling rate and final temperature of cooling

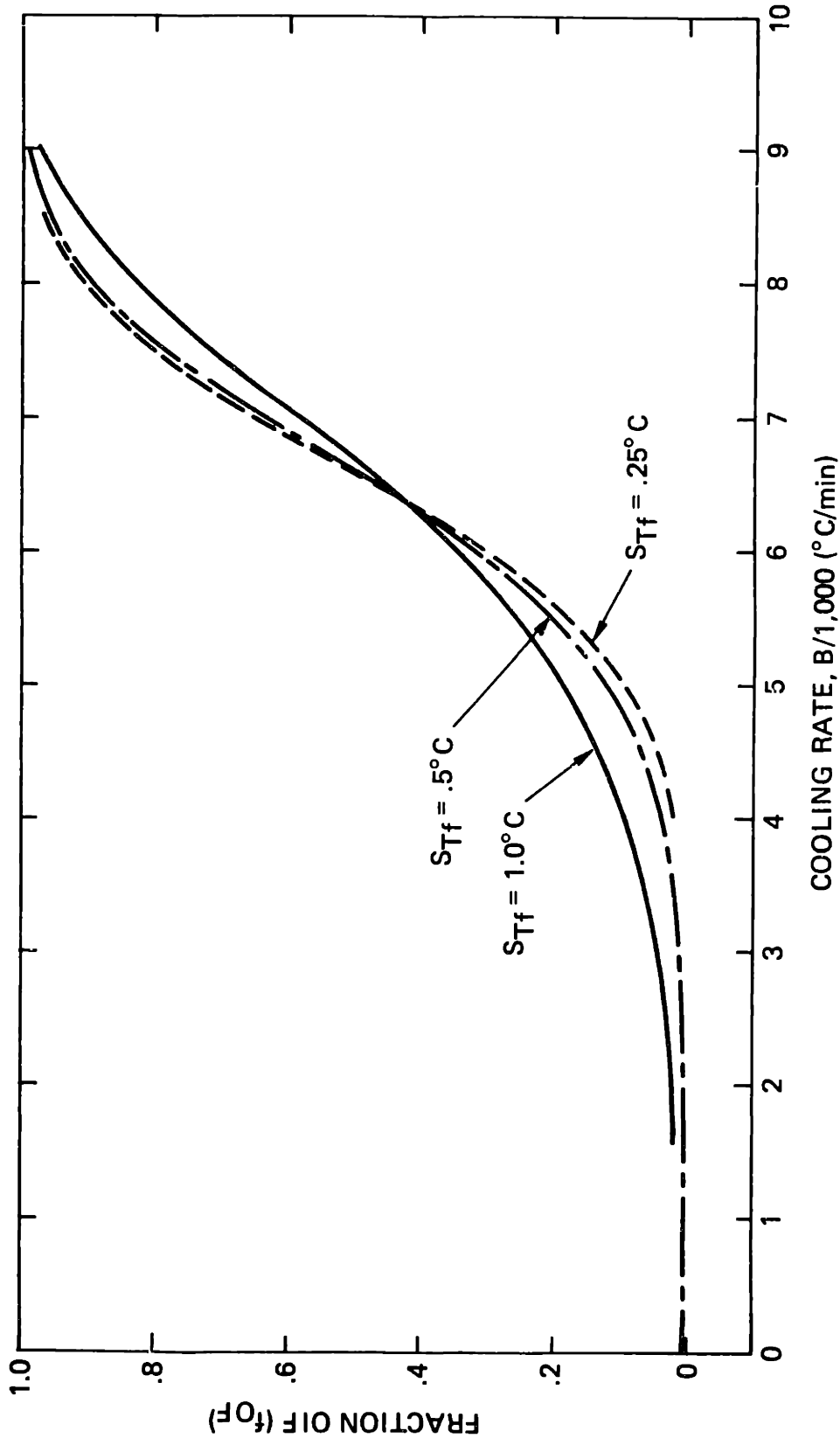


FIGURE 2.14 Final fraction of a red cell population with observable intracellular freezing as a function of cooling rate and standard deviation of freezing temperature

2.6 Fraction of Cells with Internal Freezing: Dependence on Extracellular Supercooling

Supercooling and nucleation of the cell-suspending medium as much as 20 K below the equilibrium freezing point, is common in small sample, freezing studies. Rapid precipitation of pure ice follows nucleation, with ice-solution equilibrium maintained during subsequent cooling. Sufficient cooling power is available, at least in cryomicroscope work, to avoid temperature rebound as the latent heat is removed, thereby allowing uninterrupted linear cooling.

The existence of the supercooling effect and the possibility for its control offer a unique tool for studying intracellular ice formation. Figures 2.15 and 2.16 illustrate the states of the suspending medium and hypothetical cell populations prior to, and after extracellular ice formation at -6°C . Supercooling prevents cellular dehydration until after external nucleation, increasing the fraction of cells meeting the water content criterion for OIF. The fraction of cells that freeze by an internal supercooling-dependent mechanism prior to external nucleation is given by Eq. (2.62):

$$f_{\text{OF}} = \int_{-.54^{\circ}\text{C}}^{-.54^{\circ}\text{C}-\Delta T^{\circ}} p_{\text{Tf}} dT \quad (2.62)$$

This fraction will build during cooling and if external supercooling is great enough, a significant fraction of cells freezes visibly. Equation (2.62) also represents the fraction of cells with observable freezing

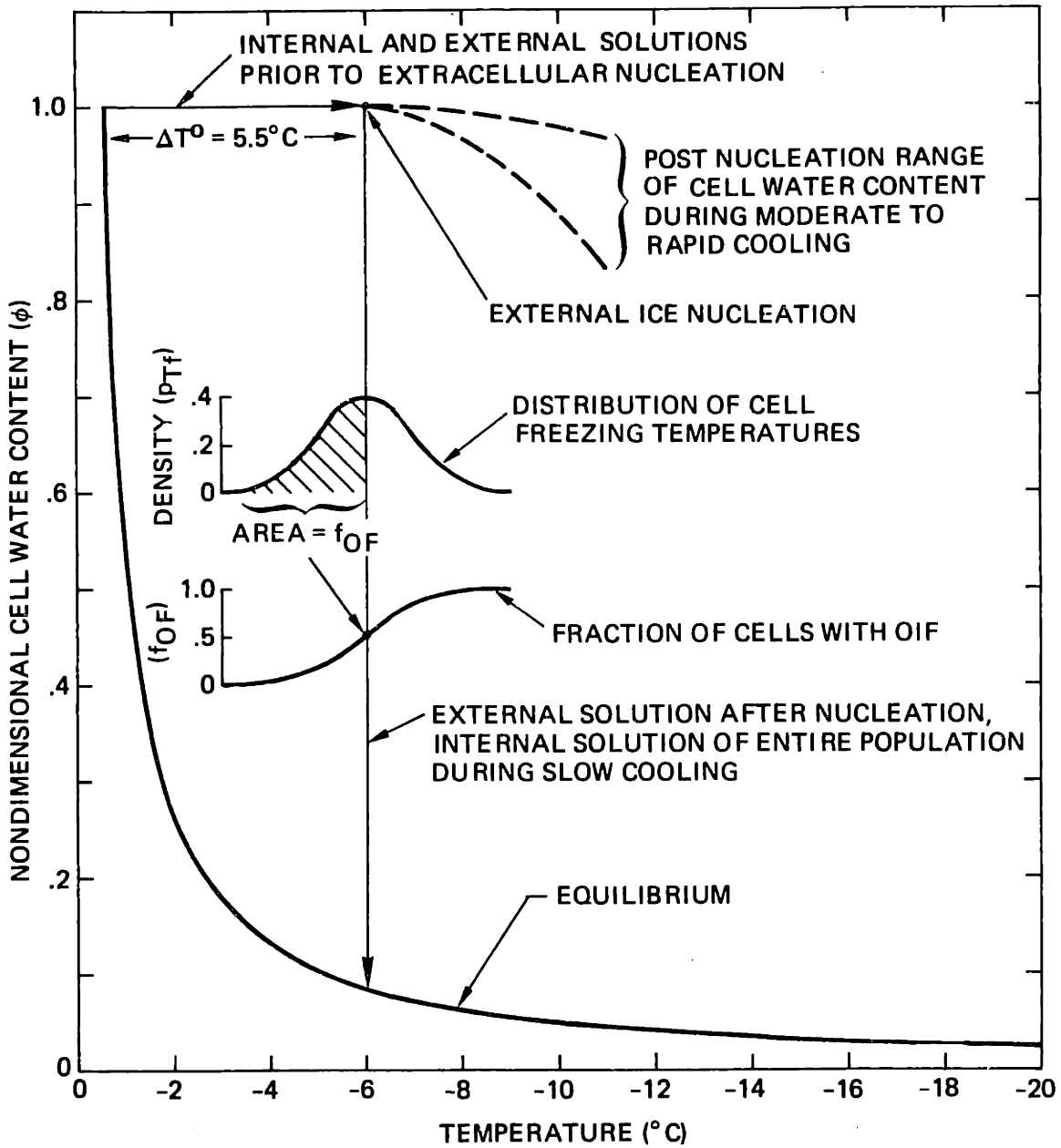


FIGURE 2.15 External supercooling and nucleation in the water content domain

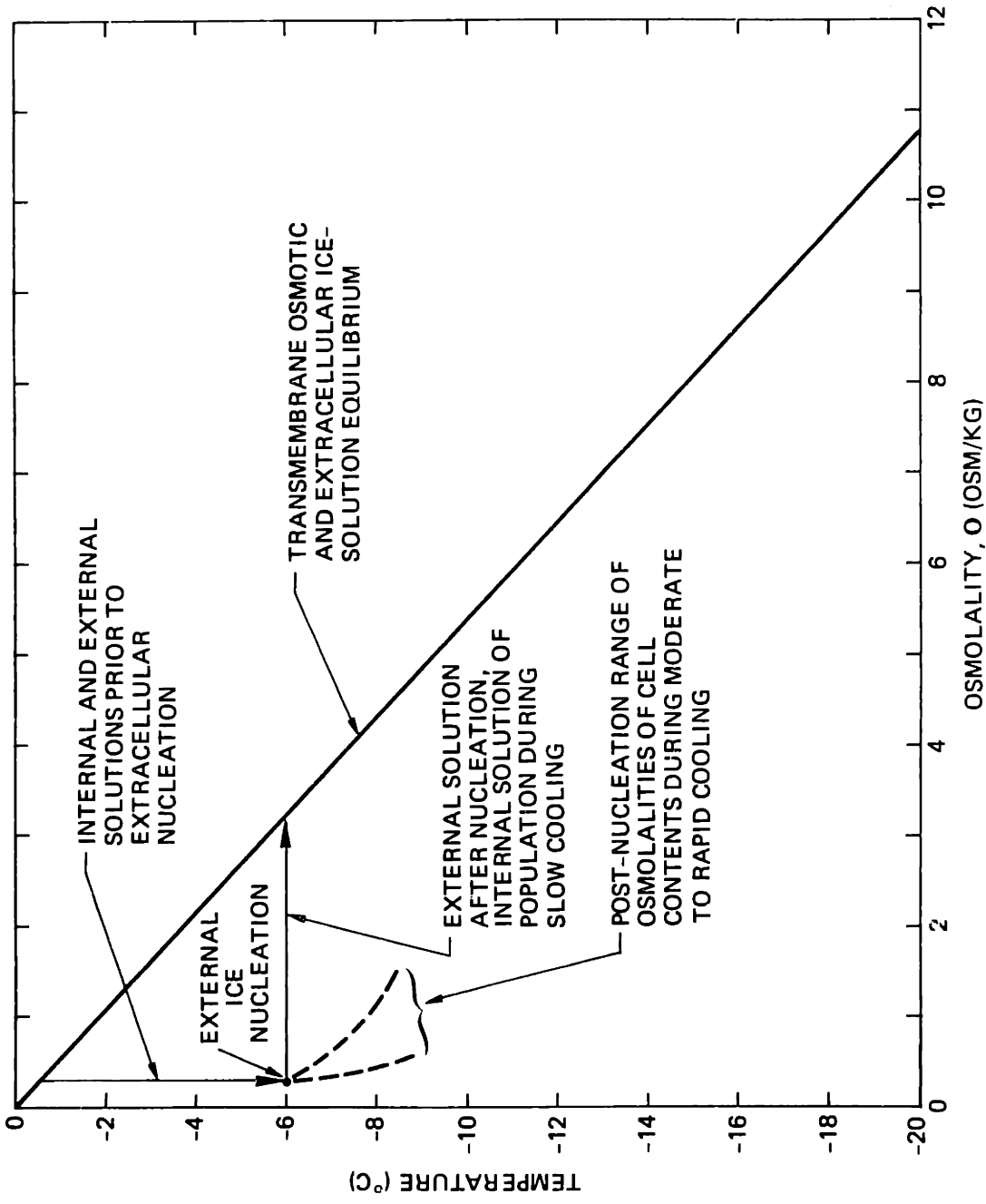


FIGURE 2.16 External supercooling and nucleation in the osmolality domain

just after passage of the external ice front, if internal freezing occurs by an 'assisted' mechanism. External supercooling offers, therefore, a way to distinguish between assisted and spontaneous mechanisms of cell freezing.

After the external nucleation event, the additional fraction of cells that undergoes internal freezing depends on the distributed water transport-cooling rate, as was the case in Section 2.5 with no external supercooling. At moderate to high cooling rates, all of the cells in the population meet the criteria for OIF. Very low cooling rates allow the cells to achieve equilibrium through dehydration such that the fraction OIF does not increase after external nucleation.

Low cooling rates combined with extracellular supercooling provide an alternate method to that of Section 2.4 for finding distributions of cell freezing temperature. In this approach, a series of observations of f_{OF} are performed at a suitably low cooling rate, for a range of external supercooling. Each experiment provides a single value for the cumulative distribution of cell freezing temperatures, as shown for a hypothetical normal distribution of T_f centered at $\bar{T}_f = -6^\circ\text{C}$ in Fig. 2.15. The freezing temperature distribution can be found by differentiating the experimentally determined cumulative distribution. The literature unfortunately contains few data with which to test this hypothesis. Experimental results for human red cells and lymphocytes, obtained as part of the present work and discussed in Sections 5.1 and 5.2 can be used to estimate the freezing temperature distributions by this approach.

The numerical technique for finding f_{OF} as a function of external supercooling and cooling rate uses the same algorithm, shown in Appendix D, as that of Section 2.5. The only change required is to lower the starting temperature of the dehydration analysis to reflect the amount of supercooling. Should this starting temperature fall within the range of cell freezing temperatures, an initial leap in the algorithm performs the summation of Eq. (2.63) which approximates the integral of Eq. (2.62):

$$f_{OF} \Big|_{T_{fu'} < (.54 - \Delta T^0) < T_{f(u'+1)}} = \sum_{\ell=1}^{u'} f_{Tf\ell} \quad (2.63)$$

This equation derives directly from Eq. (2.60) with Eq. (2.61) equal to 1 before dehydration of the population begins. After extracellular nucleation, Eq. (2.60) is used with the lower limit of summation replaced by u' .

The results of Fig. 2.17 were obtained using red cell distributed properties and cooling rates between 10 and 10000 K/min. A normal distribution of cell freezing temperatures with $\bar{T}_f = -6^\circ\text{C}$ and $S_{Tf} = .5^\circ\text{C}$ was assumed. The curves shown for cooling rates between 10 and 100 K/min match the expected cumulative distribution of cell freezing temperatures. At higher cooling rates, progressively less external supercooling is required to produce internal freezing in a given fraction of the population. These results as well as those of Section 2.5 are summarized in the f_{OF} surface above the cooling rate-extracellular supercooling plane in Fig. 2.18. Figure 2.14 appears as the f_{OF} versus cooling rate face of Fig. 2.18. The curves perpendicular to this face representing the supercooling

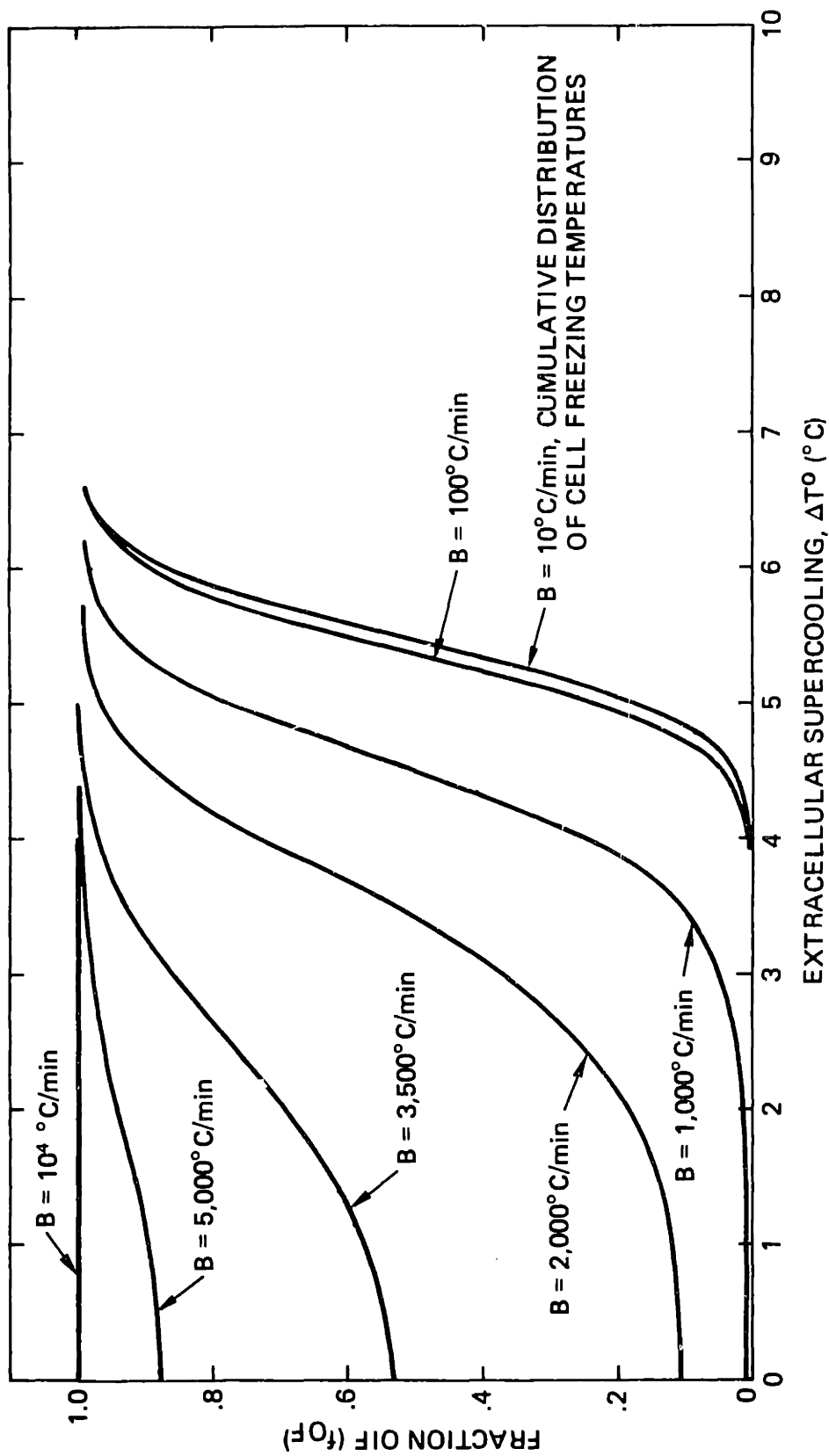


FIGURE 2.17 Fraction of a red cell population with observable internal freezing as a function of extracellular supercooling and cooling rate

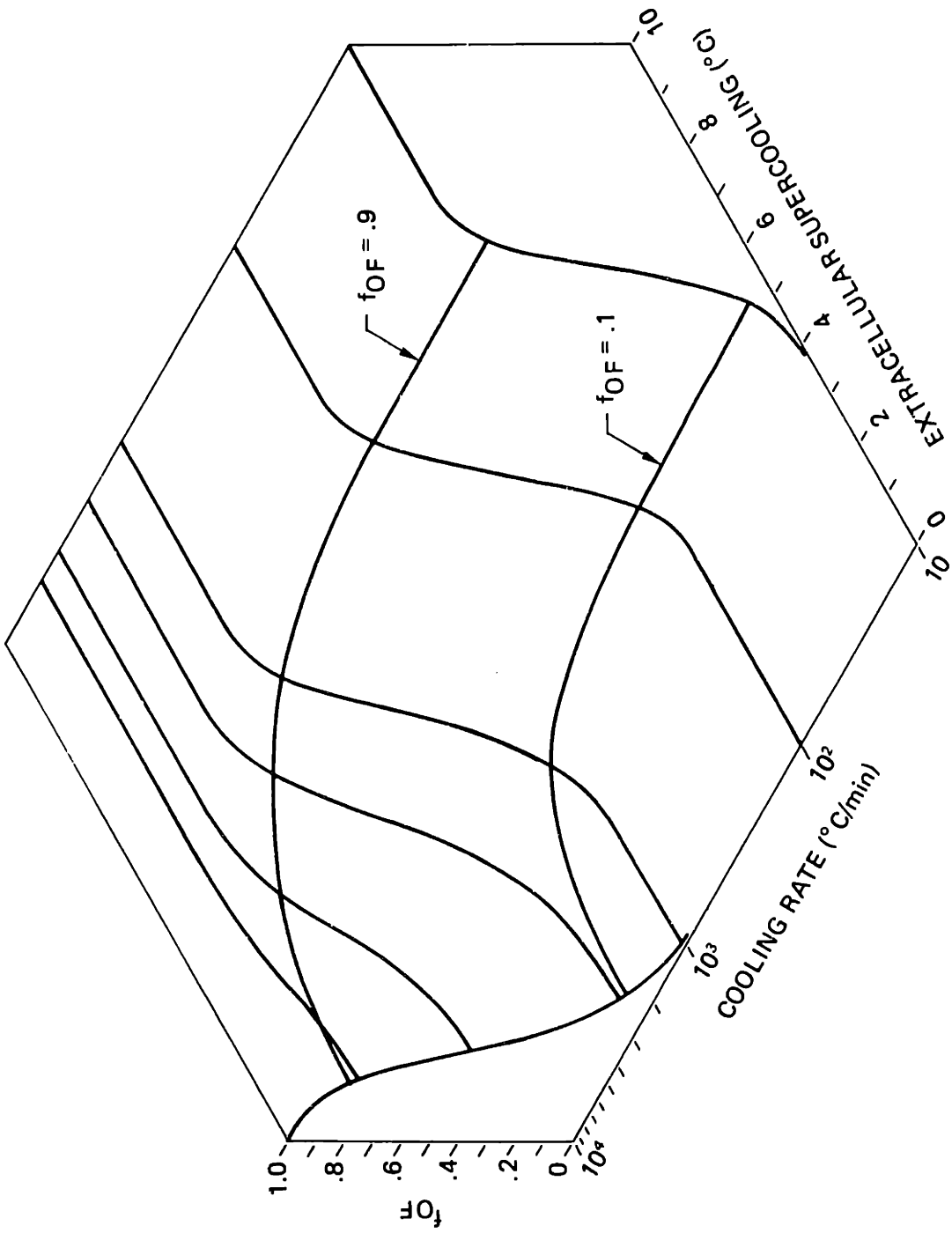


FIGURE 2.18 Fraction intracellular freezing surface above the cooling rate-extracellular supercooling plane for the red cell

dependence of f_{OF} , are redrawn from Fig. 2.17. Contour lines are shown for $f_{OF} = .1$ and $.9$.

2.7 Summary

Theoretical and analytical techniques developed in Chapter 2 to calculate the fraction of a cell population with observable internal freezing are overviewed in Fig. 2.19. Among the inputs to the analysis are the external thermal conditions of cooling rate and supercooling as well as statistics for distributed cell area, initial water content, reference water permeability and permeability activation energy. The distribution of water content in the population is calculated by solving the governing water transport equation for $m \times n$ values of independent cell properties, α and E . The distribution of α is derived from the area, water content and reference permeability distribution. Two criteria are established for observable freezing of a particular cell: water content must be greater than 50% of the initial value and temperature must be below the cell 'freezing' temperature. The latter condition is applicable regardless of whether internal freezing is precipitated by external ice or occurs spontaneously. Distributions of cell freezing temperatures can be determined indirectly from cell survival after rapid cooling to specified temperatures followed by slow warming. These distributions can also be determined from slow cooling observations with varied extracellular supercooling. Each of $m \times n$ groups of cells can be formed into u sub-elements by value of freezing temperature. The water content criterion is applied to each sub-element as temperature goes below the associated freezing temperature during numerical solution of the water transport equation. The

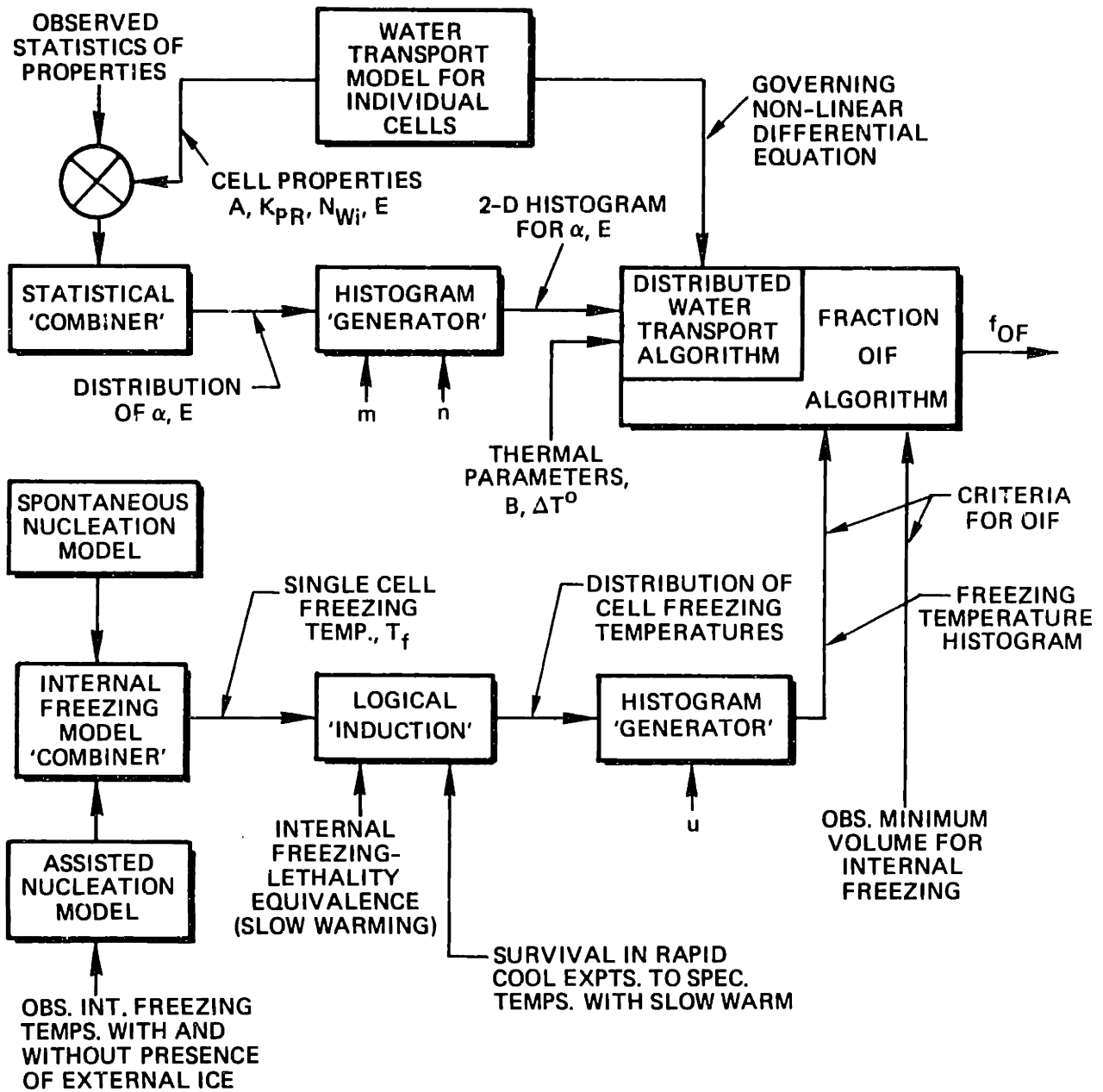


FIGURE 2.19 Schematic overview of the analysis of intracellular freezing

fractions of the $m \times n$ groups that meet the water content condition at each intermediate temperature are summed to form the fraction of cells with observable internal freezing.

CHAPTER 3
EXPERIMENTAL METHODS

3.1 Cryomicroscope

The primary tool used in the experimental program is the cryomicroscope, an instrument enabling observation of biological cells subjected to predetermined temperatures and rates of change of temperature. The present system, diagrammed in Fig. 3.1, incorporates additions and refinements to hardware developed at M.I.T. by Diller [67], Ushiyama [68] and McGrath [69]. A Zeiss Universal Research microscope with 60 watt illuminator, 7 mm working distance condenser with .63 numerical aperture (NA) and .60 NA 25x or .75 NA 40x objectives provide the observer with a 250-800x image of cells on the viewing stage. The image can be recorded for future study by a monochrome video camera or by motor driven Nikon or Zeiss manual, still cameras. A light meter can be switched into the optical path for convenience in setting the still camera exposures.

Timing-temperature uncertainties associated with the use of the chart recorder foot-switch event marker at high temperature change rates resulted in development of the video interface. This device superimposes updated temperature numerics on each video field. Inputs to the system [70] are the video camera signal, amplified thermocouple voltage, horizontal and vertical synchronization signals from a GBC model CTC6000 camera, and field counter reset signal. The output is the video camera signal with 16 superimposed characters in the format: T = ttt.t K; F = fffff, where fffff

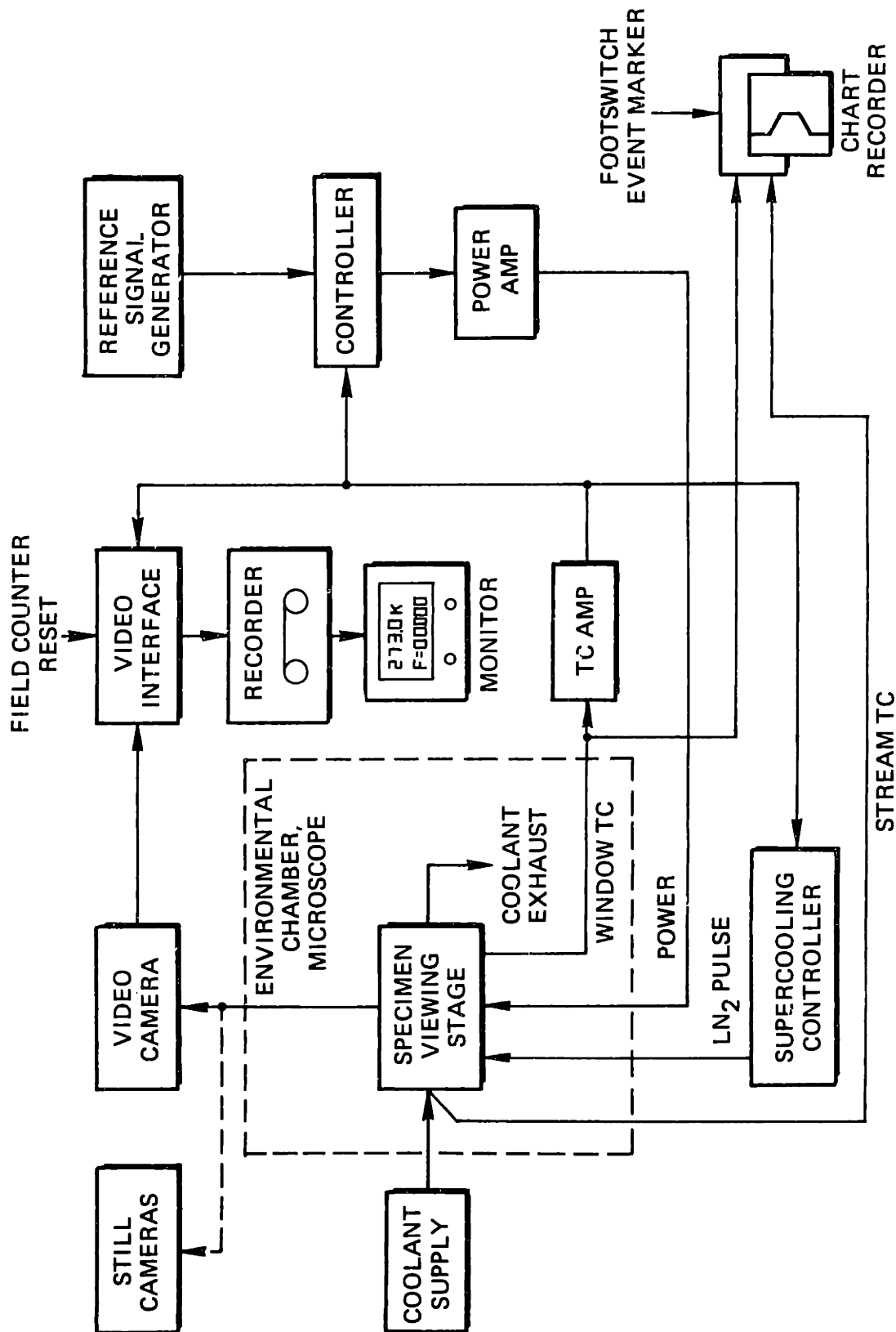


FIGURE 3.1 Cryomicroscope system elements

is the number of video fields since the last counter reset and t is the Kelvin temperature to the nearest .1K, updated at the beginning of each field. The horizontal and vertical position as well as the width of the characters can be adjusted. The video interface is discussed further in Appendix E.

Ice nucleation in the cell suspending medium generally occurs randomly with supercooling as large as 20°C. Some degree of control of the supercooling can be exercised by judicious placement of the cell-retaining coverslip on the viewing stage and by adjustment of coolant flow rate and temperature, all of which affect the thermal gradients within the cell medium. More authoritative control of the degree of extracellular supercooling is afforded by a mechanical device which automatically sprays a small quantity of liquid nitrogen at the edge of the cell sample during a cooling protocol. Supercooling controller design and operation are described in Appendix F.

Thermal control of the specimen is effected by balancing the convective cooling power of a gaseous nitrogen stream with electrical power dissipation in a transparent coating on the window of the viewing stage. A feedback control loop incorporating thermocouple, control, and power amplifiers, shown in Fig. 3.2, adjusts the heater power to drive the window temperature close to the reference signal equivalent temperature. The reference signal can currently be produced by three techniques, each with unique strengths and weaknesses: analog, hardwired digital and micro-processor. All of the reference generators provide a 0-10V output, corres-

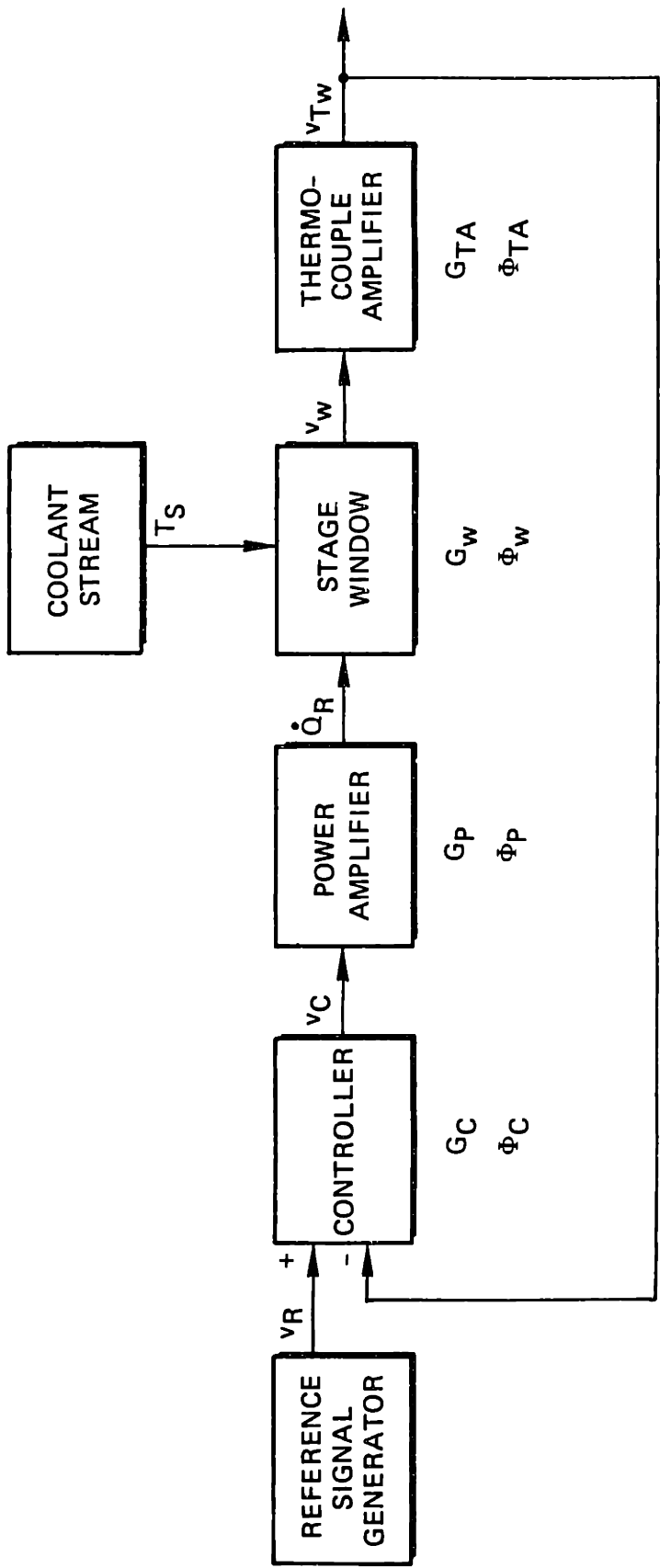


FIGURE 3.2 Cryomicroscope thermal control system components

ponding nominally to a temperature range of -200 to +200°C. The analog system, adapted from earlier hardware, is based on a Teledyne-Philbrick integrator whose time constant can be changed by switched resistors. Linear cooling and warming have been demonstrated with the analog reference over the range: 10°C/min to 1200°C/min during observations of human lymphocytes. Repeatability and initial setting accuracy were a few percent and 5-10% respectively.

The hardwired digital reference was designed originally to implement high average-rate nonlinear, 'optimal' thermal protocols for the human red cell [71]. The device consists of a 1K by 10 bit digital memory, address logic, output registers, 10 bit digital-to-analog (DAC) converter, clock, and control switches [72]. Protocols are manually entered point-by-point in binary during the program mode and are then clocked at an adjustable rate to the DAC during the run mode. The resolution corresponding to the 10 bit word length is ~.4°C. Linear operation of the unit can be achieved with a single program over a fairly wide range of rates by adjusting the time constant of the clock. Linear rates ranging from 30 K/min to almost 1700 K/min with about 5% repeatability were obtained during human red cell observations.

The third reference generator is a commercially available microcomputer, the TRS-80, combined with a custom analog-digital interface [73] based on Analog Devices RTI-1220 and RTI-1221 circuit boards. Statements for reading clock time from the interface and writing digital information to the interface can be incorporated in BASIC language reference-generation programs. The present, user-friendly, linear-protocol software is limited to

rates below 60°C/min. The microcomputer reference generator was not used during the experimental program. Further details of reference generating hardware and software are provided in Appendix G.

Previous thermal control system dynamic performance was insufficient to accurately reproduce rapidly changing thermal protocols. One index of dynamic performance, bandwidth, is discussed in Appendix H in terms of the error between reference and feedback signals and temperature change rate, assuming a 2-pole system model. Error of 3K was expected for the previous 3 Hz B.W. system at temperature change rates of 2000 K/min. System bandwidth of 10 Hz is required to reduce error from this source to 1K. In order to increase bandwidth and because little design and performance analysis had been done previously, a semi-empirical study of the entire system was undertaken. The results of this study are included in the appendices: Coolant supply flow rates and stream temperatures are discussed in Appendix I. Viewing stage lumped parameter heat transfer model with measured steady-state heat transfer coefficients, predicted and measured frequency response, horizontal thermal gradients and predicted linear cooling capability are provided in Appendix J. Power amplifier transfer characteristics including output dependence on load resistance are considered in Appendix K. Performance of a Hewlett Packard thermocouple amplifier and a new signal conditioning module based on an Analog Devices AD522 hybrid instrumentation amplifier are compared in the frequency domain in Appendix L. Appendix M compares the predicted and measured transfer characteristics of a lead compensating controller which supplanted the previous low gain proportional controller. Performance of

the overall control loop is analyzed in Appendix N in terms of steady-state error and frequency response. Measured thermal slew rate capability is also included.

Functions comprising the cryomicroscope data acquisition system and corresponding performance specifications are summarized in Table 3.1.

3.2 Sample Preparation

Cryomicroscope observations of red cells were performed using whole blood collected from normal donors at the Massachusetts General Hospital (MGH) Blood Bank, each day of the experimental program. Approximately 2 ml of ACD anticoagulant were used in 10 ml collection tubes, which were maintained during a day's observations in an ice bath. Occasionally, blood that had been stored overnight in a refrigerator at $\sim 5^{\circ}\text{C}$, was used.

The human lymphocyte observations required substantially greater preparation than was the case for the RBC's. Cell separations from whole blood were performed by the MGH Histocompatibility Laboratory, generally within 1 day after the blood sample was drawn, using procedures roughly as listed in Table 3.2. Tubes containing the cells were transported and stored during use, in an ice bath.

3.3 Cryomicroscope Operation

Operating procedures for the cryomicroscope are outlined in Fig. 3.3. Power should be applied in the order: $\pm 15\text{V}$, $+ 5\text{V}$, controller and thermocouple amplifier. Details of operation for the reference signal generators are provided in Appendix G. The thermocouple amplifier should be zeroed using procedures in Appendix L allowing 10 minutes for warm-up drift. The chart recorder should be zeroed per operating manual instructions [74] after

TABLE 3.1
CRYOMICROSCOPE SYSTEM FUNCTIONS AND
PERFORMANCE SPECIFICATIONS

Video Interface: Annotates each video field with updated temperature and frame count.

Supercooling Controller: Induces ice nucleation in cell-suspending medium within ~2K of desired value.

Specimen Thermal Control: Temperature and temperature change rate for 1-2 μl cell suspensions.

Reference signal generation: Varied analog and digital methods provide linear and nonlinear thermal histories at nominal rates ranging from .1 K/min to 10^7 K/min (based on hardwired digital system clock rate of 1 Mhz). Resolution: .4 K or better.

Coolant supply: Provides gaseous N_2 stream at rates up to ~18 lb/hr (8.2 Kg/hr) and temperatures between 120 and 298 K.

Thermal control loop: Components: heater window on viewing stage, power and thermocouple amplifiers, lead compensating controller. Bandwidth: > 10 hz. Steady-state error during temperature holds: <.5 K Typ. Expected. Steady error during linear ramp thermal histories <1 K Typ. Expected.

Thermal slew rate: ~3000 K/min demonstrated over several K
7500 K/min theoretical limit for small temperature change.

Error due to gradients in plane of specimen: <.5 K Typ. Expected.

Thermocouple nonlinearity error: <.5 K if nonlinearity is programmed in Reference Generator, <.5 K over 218 K to 278 K range with no linearization. Phase margin: 30°. Gain margin: 12 db.

TABLE 3.1 (Cont'd.)

OPTICS:

Microscope: Zeiss Universal Research, X-Y micrometer platform to support viewing stage, 7 mm working distance condenser, phase contrast dry objectives, 60 watt tungsten illuminator with regulated supply. Resolution: $\sim .4\mu$.

Cameras: Zeiss manual 35 mm, Nikon 35 mm with 5 frame/s drive, GBC CTC6000 monochrome camera with IVC-800 video tape recorder and GBC Model MV-17 monitor.

MISCELLANEOUS:

Chart Recorder:

Hewlett Packard Model 7100B with 2 model 17502A, -200°C - $+200^{\circ}\text{C}$ input modules for copper-constantan thermocouples, footswitch event marker.

Environmental Chamber:

A clear acrylic box which is purged with dry N_2 to prevent condensation on viewing stage.

TABLE 3.2
LYMPHOCYTE SEPARATION PROTOCOL

1. Defibrinate using: 30mm glass beads
50 μ l 20.6% CaCl₂
50 μ l Thrombin
2. Spin @ 1300 g 6-7 minutes.
3. Remove excess plasma.
4. Draw-off remaining plasma and buffy coat (~1 ml) and place in small tube.
5. Add 2-3 ml PBS to small tube.
6. Add diluted buffy's to 2 tubes containing 2 ml Lymphocyte Separation Medium LSM, (Bionetics, Kensington, Md).
7. Spin @ 1300 g, 30 minutes.
8. Remove solution above white bands.
9. Pipette white bands into another small tube.
10. Dilute with PBS to wash-off LSM.
11. Spin @ 1300 g 7 minutes.
12. Aspirate solution above button of cells on bottom of tube.
13. Add ~1 ml medium 199 or Terasaki/Park.

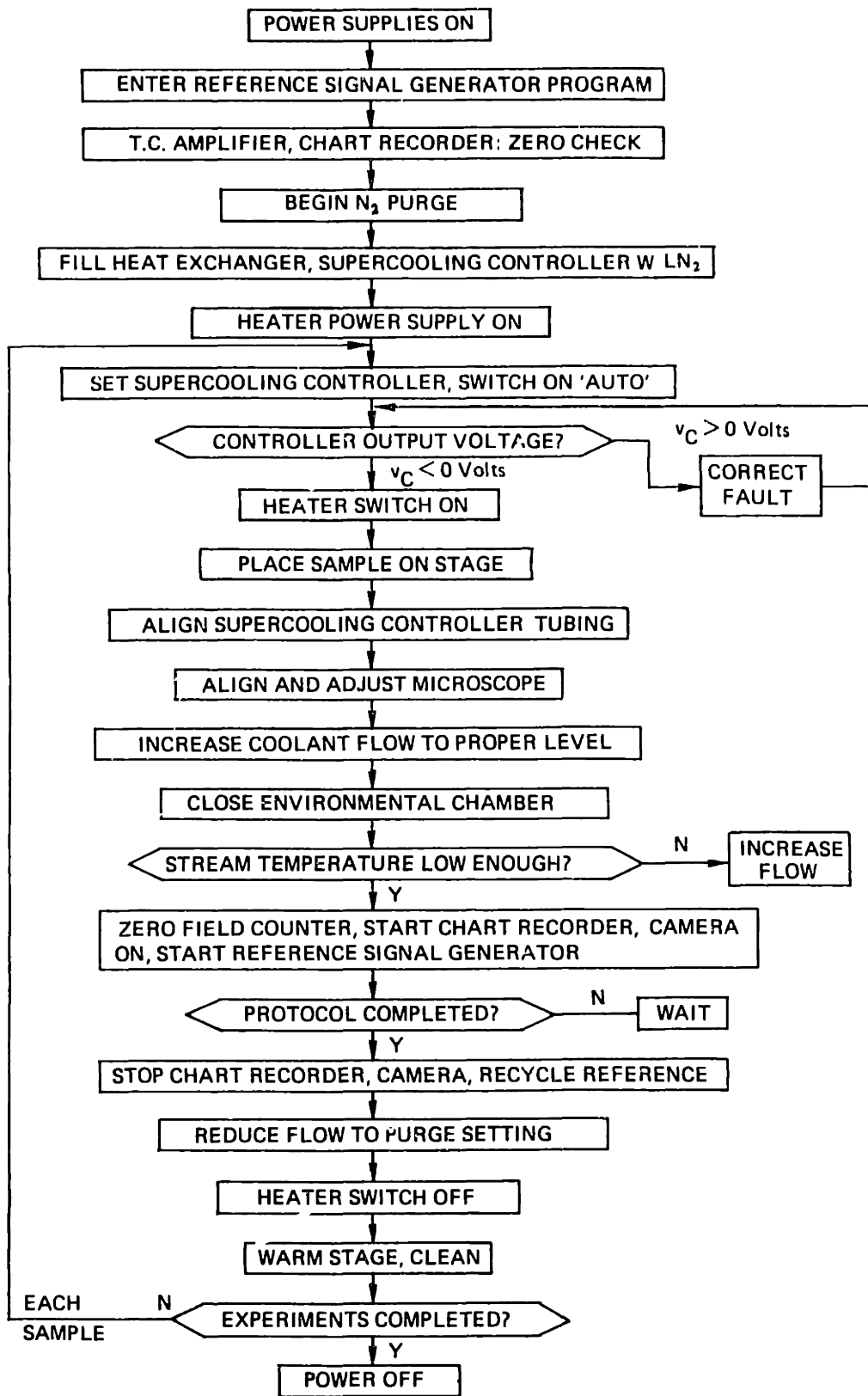


FIGURE 3.3 Cryomicroscope system operation

allowing 30 minutes for stabilization. It is advisable to check for drift every hour or so, particularly on the chart recorder. The dry nitrogen purge at ~1 lb/hr (.5 Kg/hr) is recommended to prevent ice build-up in the heat exchanger. Heater power supply voltage should be chosen using the information of Appendix K, large enough to provide adequate power. A 120 Ω heater resistance, for example, requires 65 V to assure a maximum heating capability of $\dot{Q}_R = 40$ watts. The supercooling controller firing-voltage should be set to a temperature-equivalent above the desired value, to allow for the slight delay between initiation of the LN₂ pulse and nucleation. Appendix F should be consulted for additional information. The controller output voltage is checked prior to switching the heater into the circuit to allow correction of any faults, such as incorrect reference generator output. A micropipette is convenient for placing 1-2 μ l of the cell suspension on the heater window; a 12 mm x 12 mm #1 coverslip retains the sample. Pressure should never be used to seat the coverslip. Microscope optical alignment and settings other than fine focus are done prior to closing the environmental chamber. Sufficient flow should be established to achieve the desired final temperatures, using the results of Appendix I. The programmed thermal protocol is initiated when the coolant stream temperature has dropped below the minimum programmed temperature. If supercooling is to be controlled, this should be ~220 K. The procedures reverse at the completion of a thermal cycle. The stage can be warmed with a heat gun to facilitate cleaning and preparation for the next sample.

CHAPTER 4
EXPERIMENTAL RESULTS

4.1 Human Red Cells

Human red cells were observed using phase contrast microscopy in whole blood cooled at rates ranging from 10 K/min to ~1600 K/min in the presence of 0 K to 20 K supercooling. The pre-freeze appearance of the cells, typified by Fig. 4.1, remained unchanged in all cases, until the external ice front propagated through the field of view. Cells underwent dramatic changes in appearance accompanying the front passage and were classified into four categories: Type 1 cells, shown in Fig. 4.2, are wrinkled and appear to have undergone substantial dehydration. Cells of type 2 have some wrinkling and light internal shading as shown in Fig. 4.3. Cells of the third category have similar light coloring as those of type 2, but do not have a wrinkled appearance, and additionally, contain finger-like internal structures. These structures, quite clear in Fig. 4.4, form patterns with varied fineness and in some instances appear to communicate with the extracellular environment through gaps in the cell surface. The fourth category of cells is characterized by fine internal structure and dark shading. Some of these are shown with type 2 and 3 cells in Fig. 4.4. Progressively finer reticulation of the internal structure of type 4 cells is shown in Figs. 4.5a and 4.5b.

The structures and changes in appearance described above were completed shortly after passage of the external ice front for types 3 and

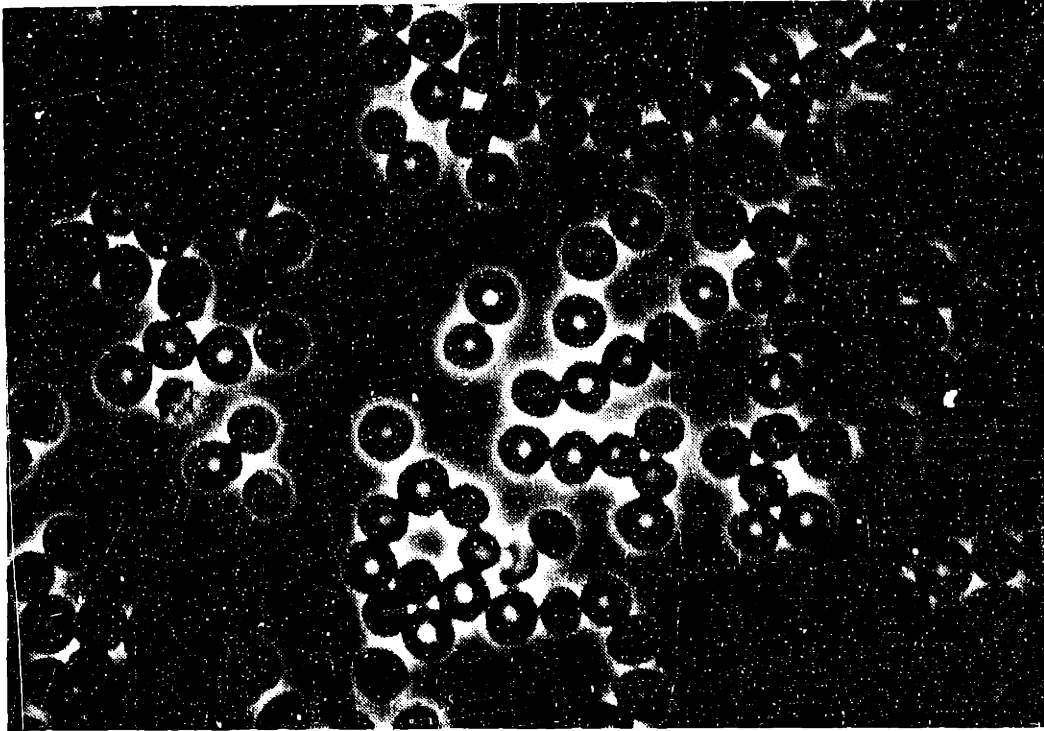
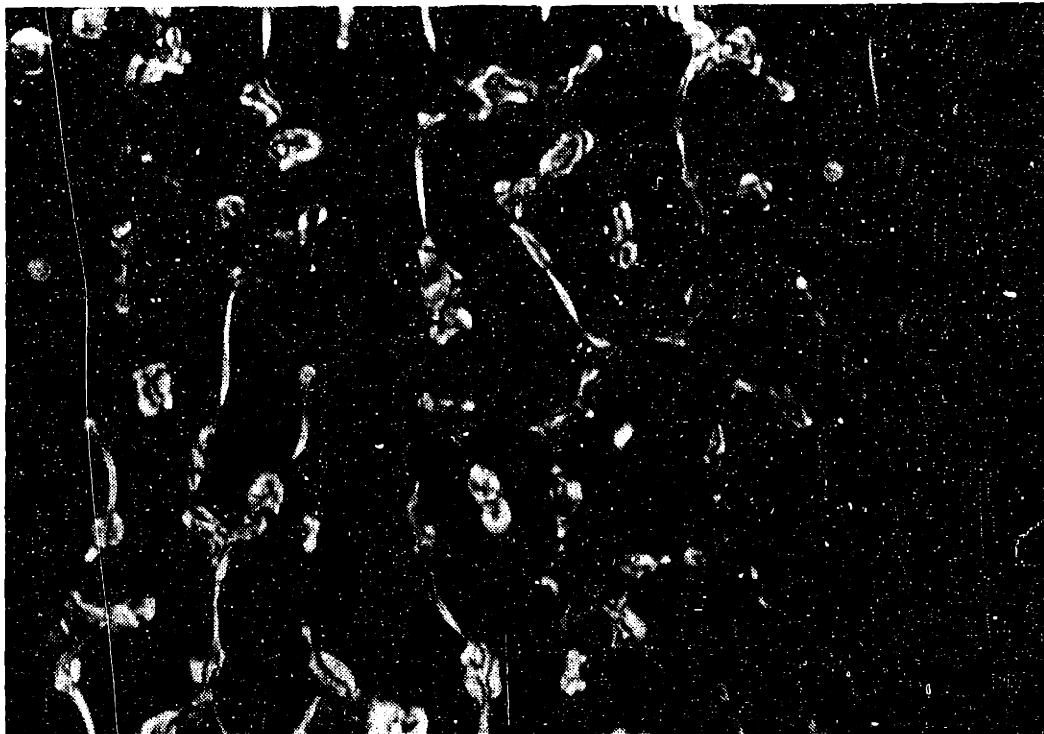


FIGURE 4.1 Human red cells, pre-freeze

FIGURE 4.2 Red cells at 233 K after cooling at 8 K/min, $\Delta T^0=1.5$ K, Type 1



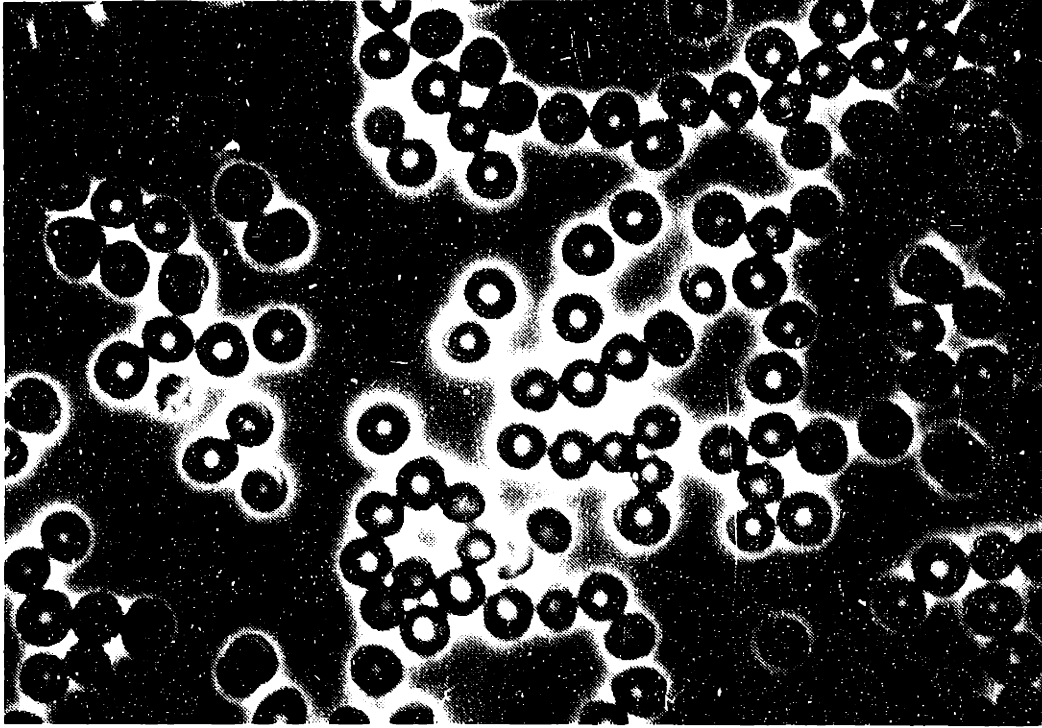
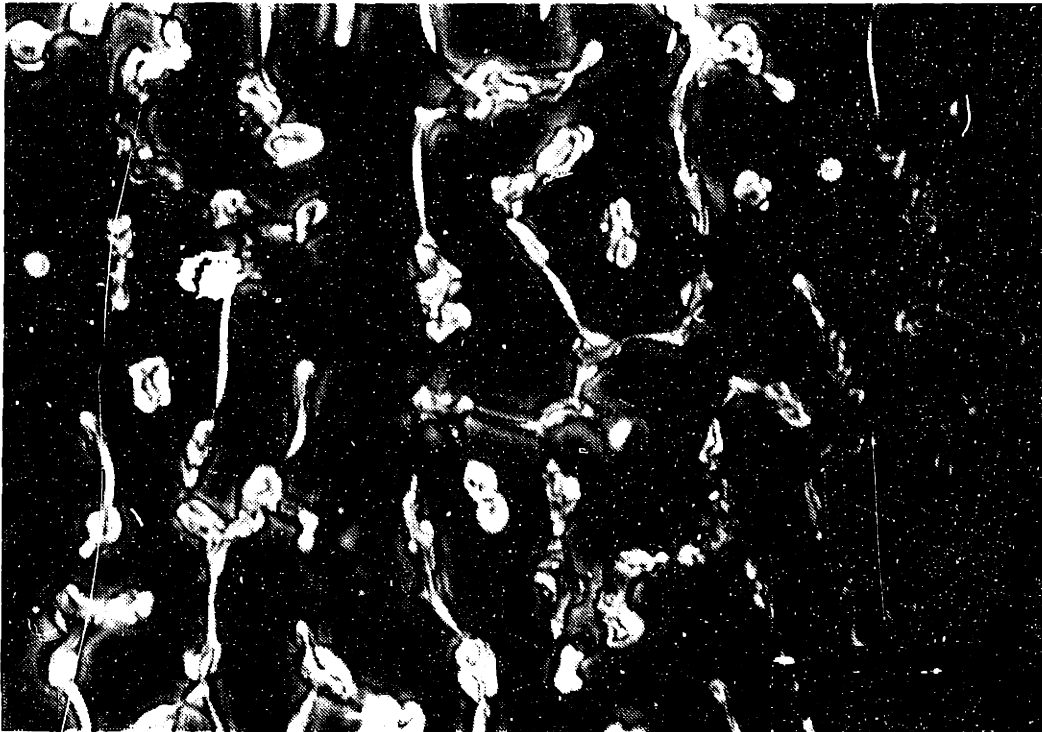


FIGURE 4.1 Human red cells, pre-freeze

FIGURE 4.2 Red cells at 233 K after cooling at 8 K/min, $\Delta T^0=1.5$ K, Type 1



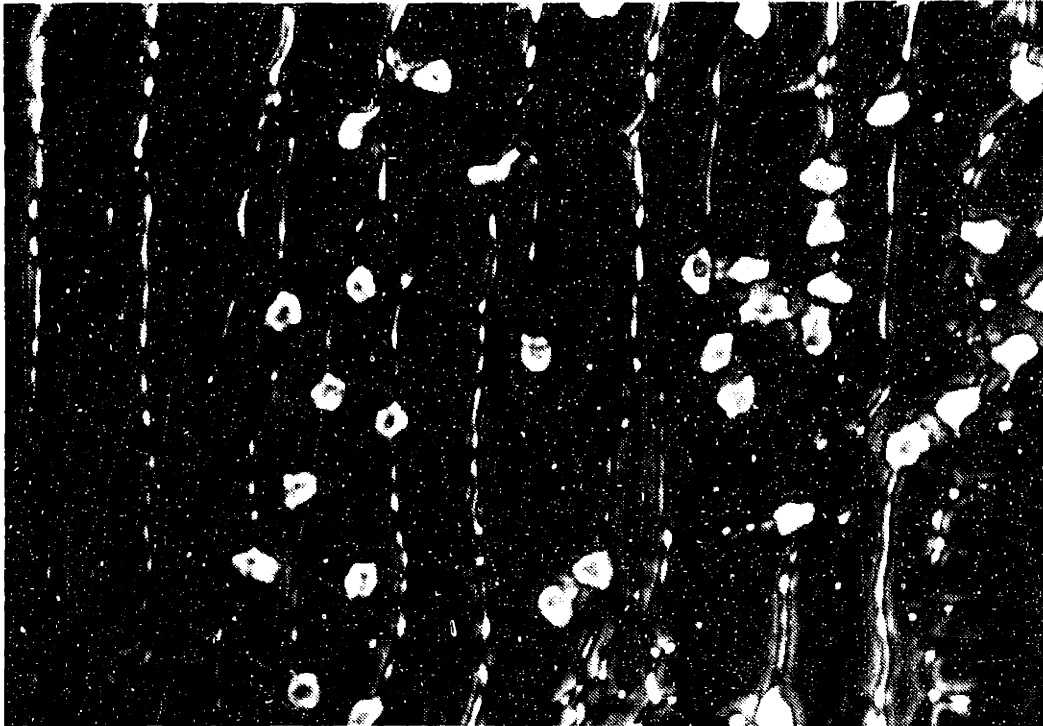
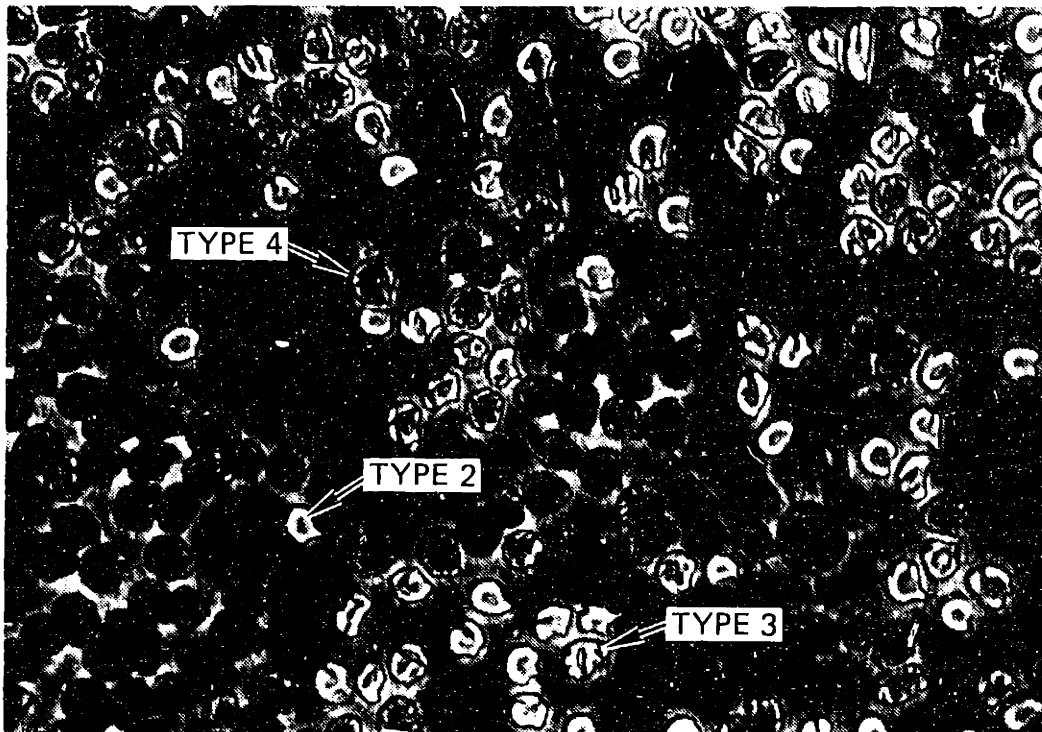


FIGURE 4.3 Red cells at 233 K after cooling at 260 K/min, $\Delta T^0=2.5$ K, Type 2

FIGURE 4.4 Red cells at 213 K after 84 K/min cooling, $\Delta T^0=5$ K, Types 2,3,4



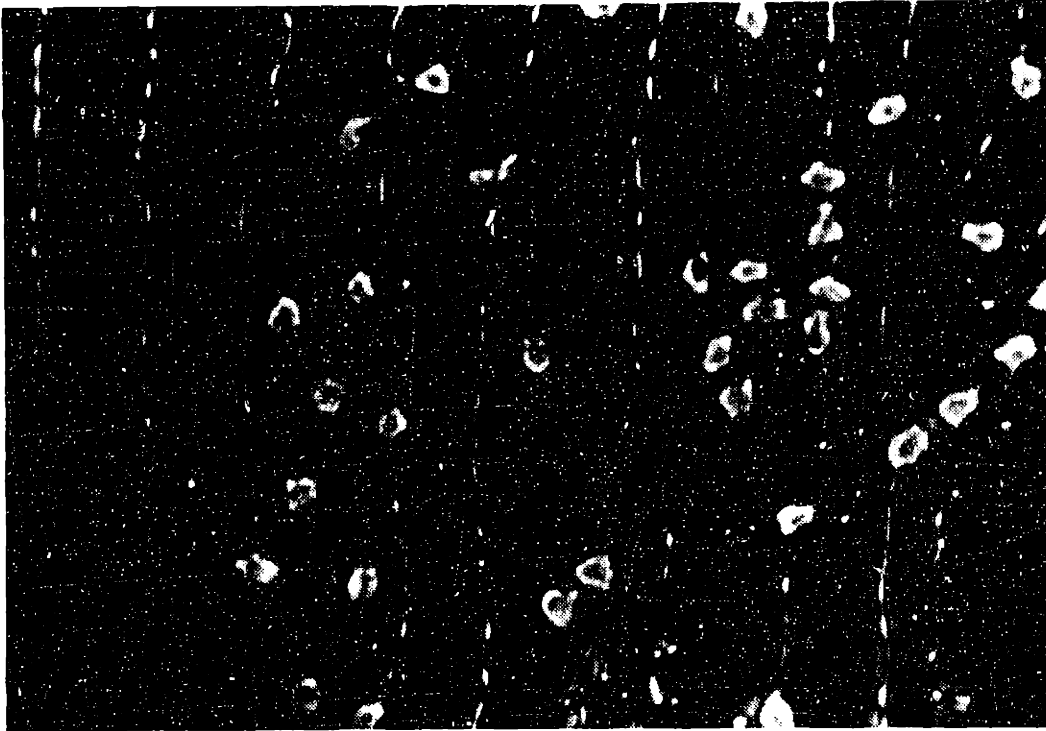
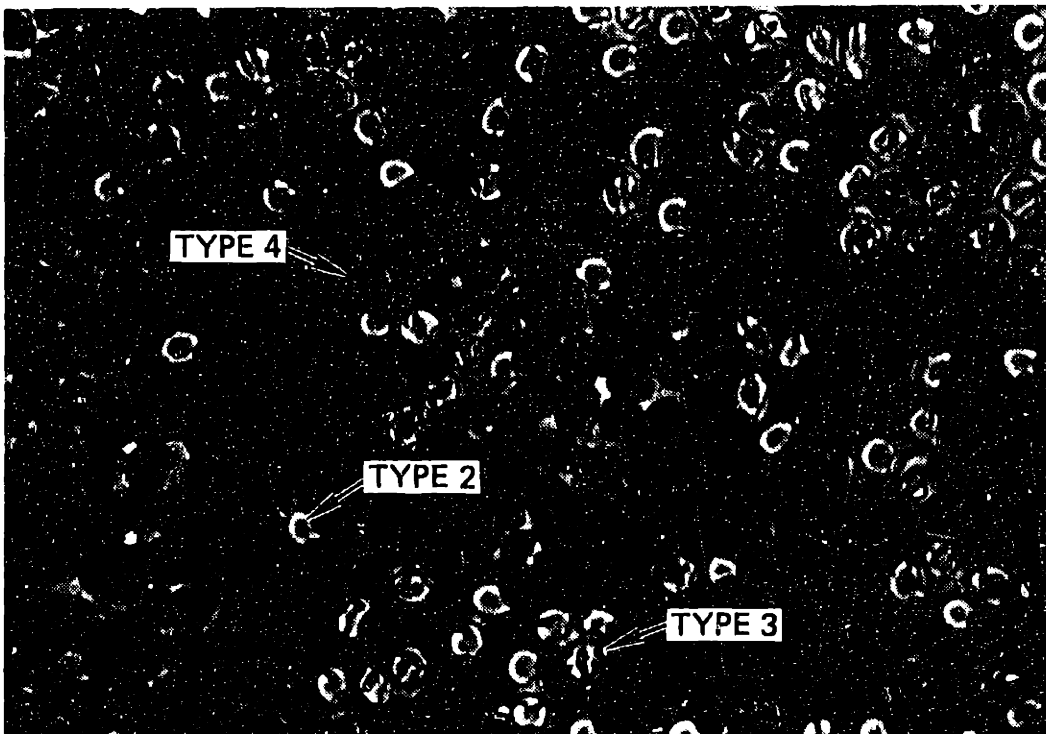


FIGURE 4.3 Red cells at 233 K after cooling at 260 K/min, $\Delta T^0=2.5$ K, Type 2

FIGURE 4.4 Red cells at 213 K after 84 K/min cooling, $\Delta T^0=5$ K, Types 2,3,4



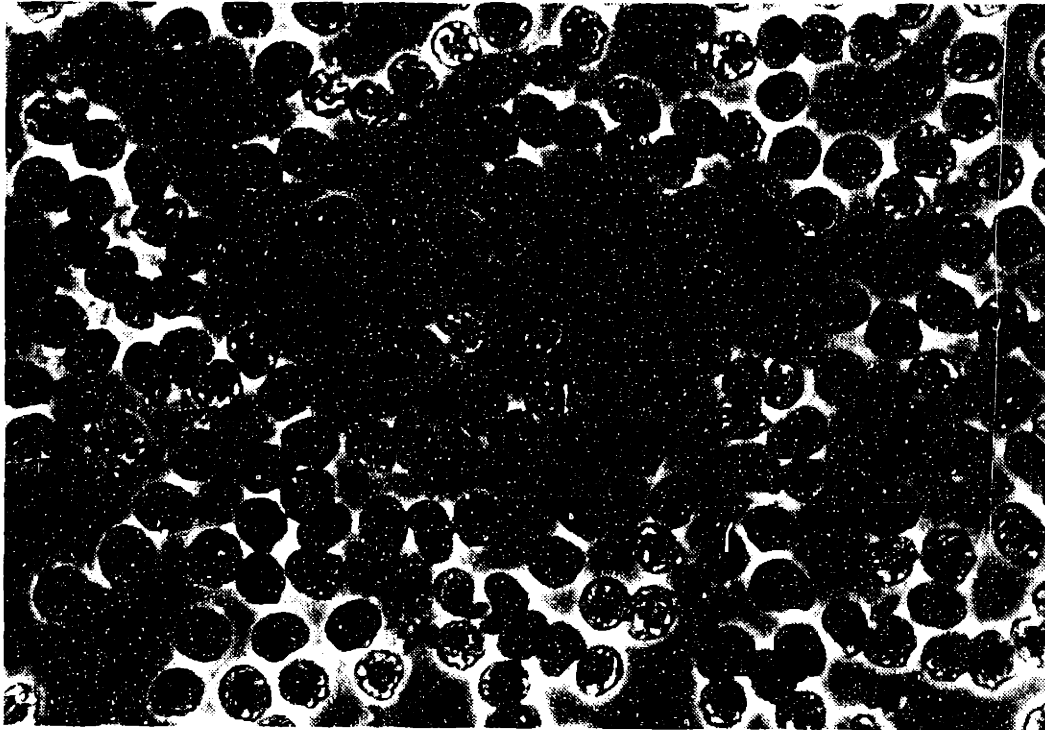
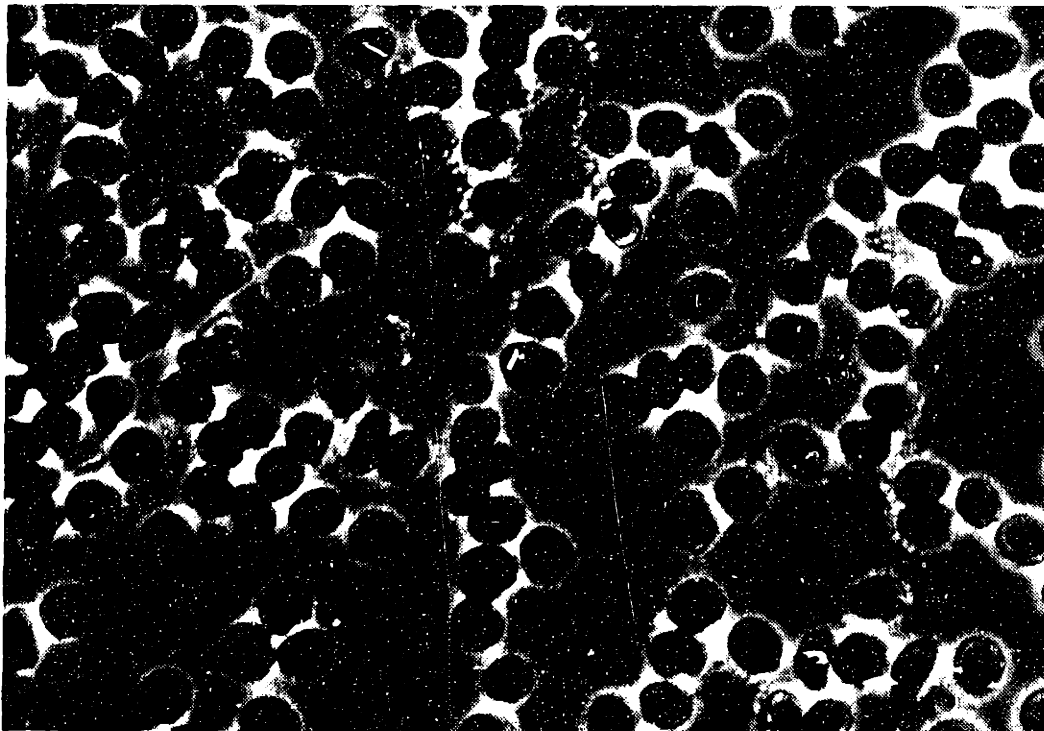


FIGURE 4.5a Red cells at 233 K after 250 K/min cooling, $\Delta T^0=8.5$ K,
Type 4

FIGURE 4.5b Red cells at 233 K after 260 K/min cooling, $\Delta T^0=20.5$ K,
Type 4



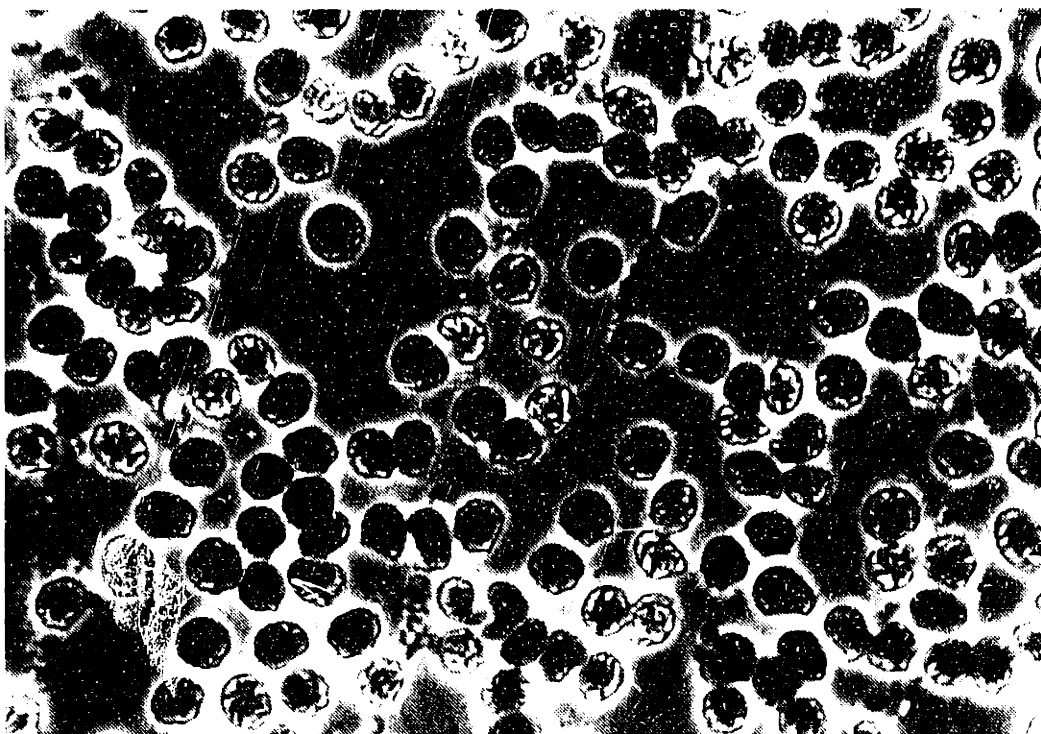
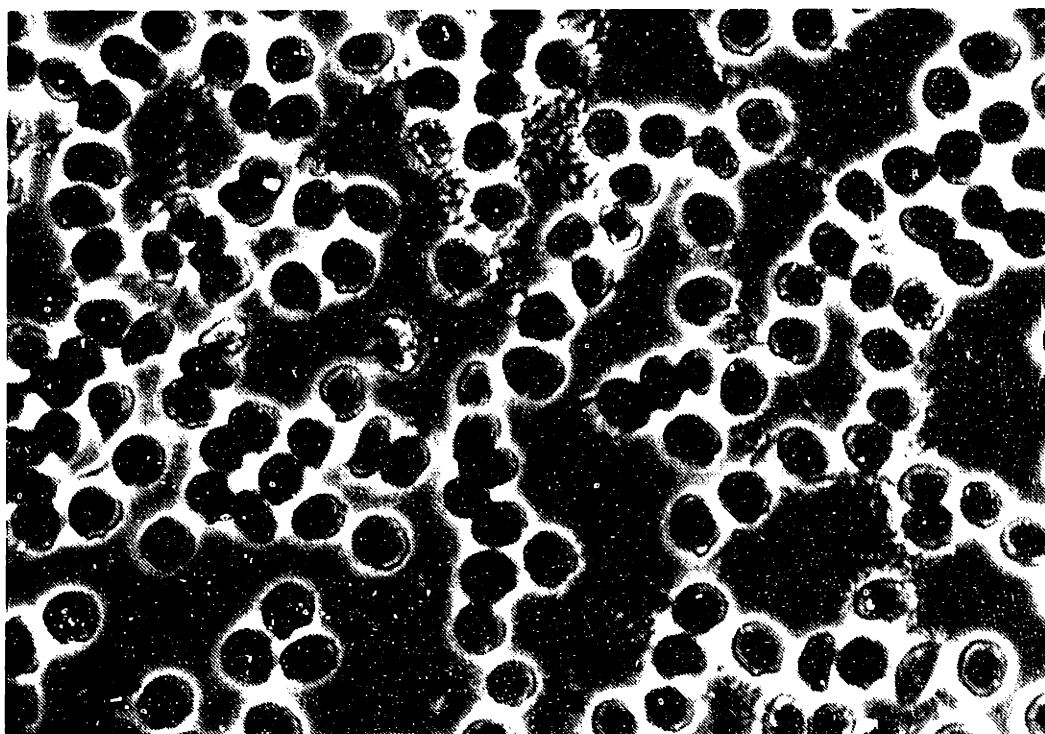


FIGURE 4.5a Red cells at 233 K after 250 K/min cooling, $\Delta T^0=8.5$ K,
Type 4

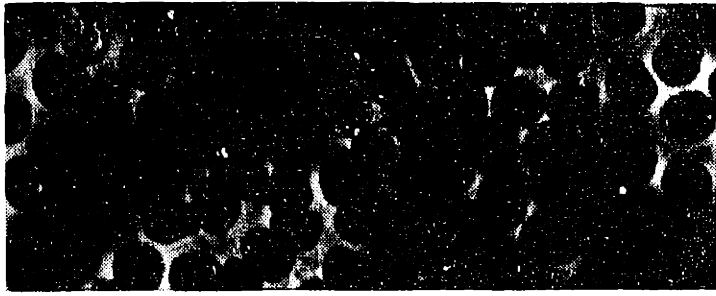
FIGURE 4.5b Red cells at 233 K after 260 K/min cooling, $\Delta T^0=20.5$ K,
Type 4



4 or by ~ 263 K for types 1 and 2. Videotapes showed type 4 internal structure within 2 or 3 video fields after ice front passage at 261 K, for cells cooled at 30 K/min. The transitions from pre-freeze to type 3 or 4 structure are essentially instantaneous to the observer. The transitions to type 1 and 2 appearance occurred over periods as long as several seconds. Once formed, the characteristic appearance of each category remained stable throughout subsequent cooling and holds maintained at 223 K for several minutes.

Slices from the red cell photographs are reproduced in Fig. 4.6 to facilitate comparison. Category 1 and 2 cells were interpreted to contain no observable internal freezing while cells in categories 3 and 4 were interpreted to have undergone observable internal freezing. This interpretation is applied to the observations in Fig. 4.7. Each circle represents an observation of approximately 40 cells; open circles for runs in which fewer than 10% of the cells were types 3 or 4, half-filled circles for runs with 10 - 90% type 3 or 4 cells, and filled circles for runs in which more than 90% of the cells were characterized as types 3 or 4. The cooling rate scale-change in the lower part of the figure was included solely to facilitate presentation of the results.

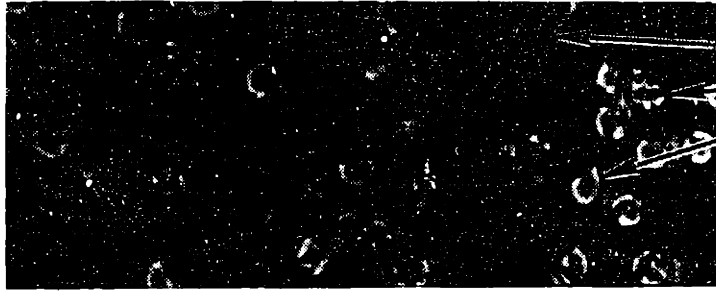
The foot-switch event marker on the chart recorder was used to note the passage of the ice front through the field of view in all of the observations. This necessitated a systematic correction, as discussed in Appendix E, for the observer time delay. The measured standard deviation



TYPE 4

250 K/min

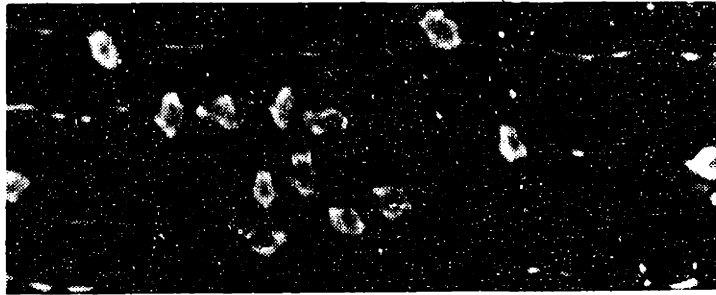
$\Delta T^0 = 8.5 \text{ K}$



TYPES 2, 3, 4

84 K/min

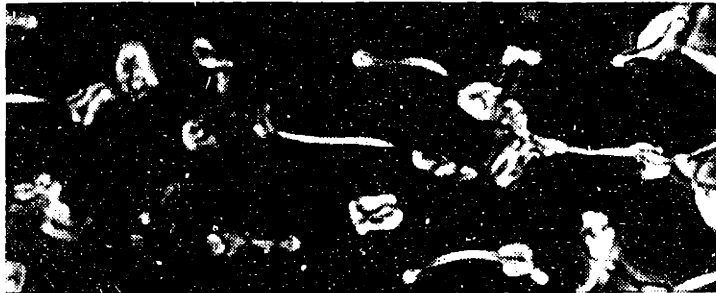
$\Delta T^0 = 5 \text{ K}$



TYPE 2

260 K/min

$\Delta T^0 = 2.5 \text{ K}$



TYPE 1

8 K/min

$\Delta T^0 = 1.5 \text{ K}$



PRE-FREEZE

NO INTERNAL FREEZING

INTERNAL FREEZING, TYPES 3, 4

FIGURE 4.6 Summary of red cell types

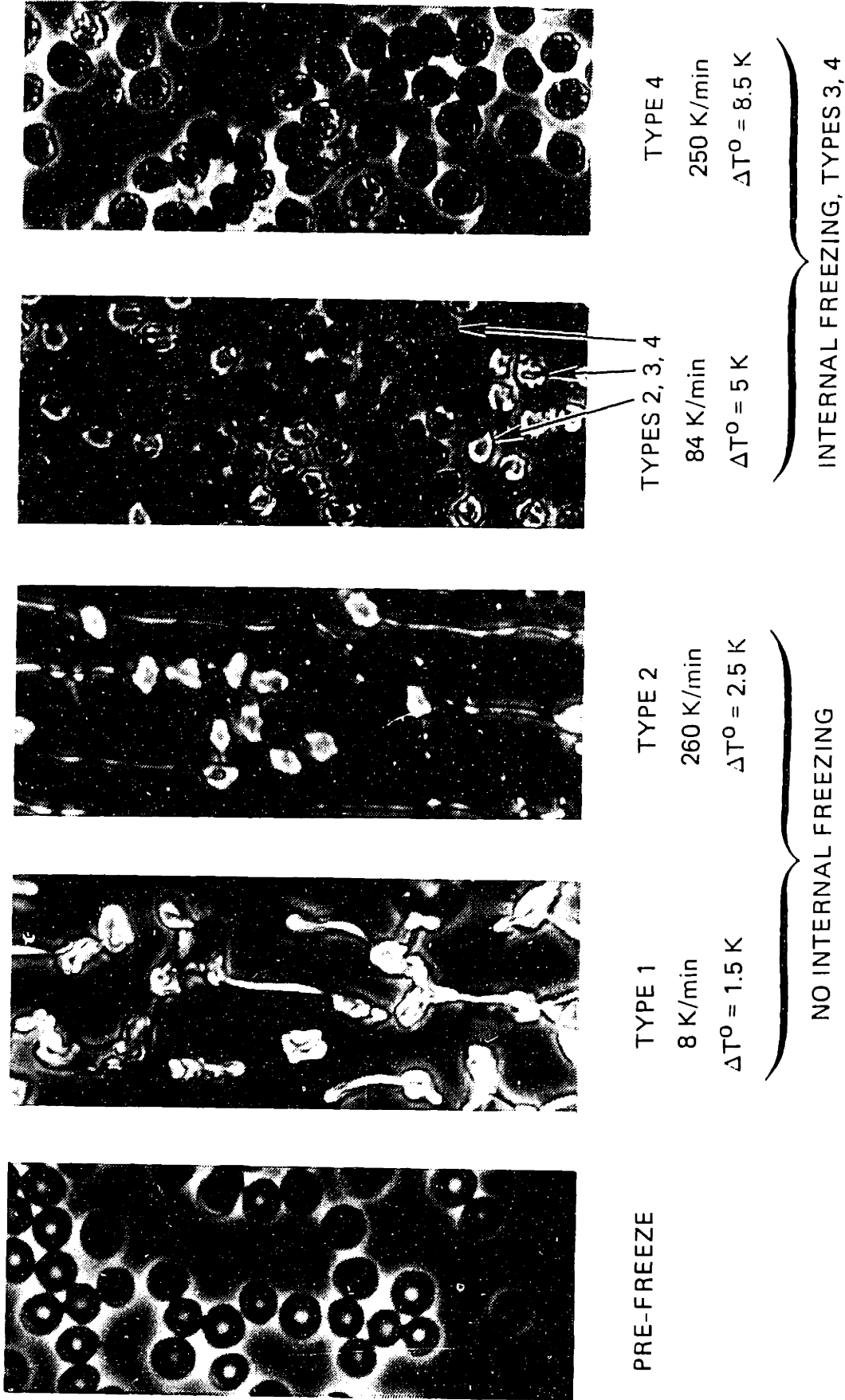


FIGURE 4.6 Summary of red cell types

of the time delay, .03 s, causes scatter of ~.5 K in the observed extracellular supercooling at 1000 K/min, with increasingly serious error at higher rates. Caution must therefore be exercised during additional interpretation of the observations at high cooling rates.

Measurements of cell diameters were performed from photographs such as those in Figs. 4.1 and 4.3 through 4.5, to determine the volume of type 2 cells relative to types 3 and 4. These measurements were normalized to the pre-freeze value and multiplied by the mean diameter for red cells of 7.82 μ [45]. The resulting diameters were used to compute volumes using Eq. (4.1) [75]:

$$V_{RBC} = 29.7 D_{RBC}^3 - 134.6 \quad (4.1)$$

The volumes are summarized in Table 4.1. Type 2 cells alone, or in photographs with types 3 and 4, are substantially smaller than 3, 4 cells.

4.2 Human Lymphocytes

Human lymphocytes suspended in saline were observed using phase contrast microscopy at rates between 12 and 1200 K/min in the presence of up to 14.5 K of supercooling. There were two readily discernable pre-freeze categories: cells with a dark center surrounded by a bright ring, dark membrane and external 'halo', shown in Fig. 4.8a, and a group with more uniform, dark internal shading such as that of Fig. 4.9a, which also exhibits a strong phase contrast halo. The darker group was usually larger in diameter and occasionally resulted when the lighter cells were

TABLE 4.1
RED CELL SIZE COMPARISON

CATEGORY	DIAMETER [μ]	VOLUME [μ^3]	VOLUME/PRE-FREEZE VOLUME
Pre-freeze	7.82 \pm .587	97.7 \pm 17.4	1.00 \pm .18
Type 2 alone	6.37 \pm .704	54.5 \pm 20.9	.56 \pm .21
Type 2 with 3&4	7.12 \pm .500	76.8 \pm 14.8	.79 \pm .15
Types 3 and 4	7.82 \pm .704	97.7 \pm 20.9	1.00 \pm .21

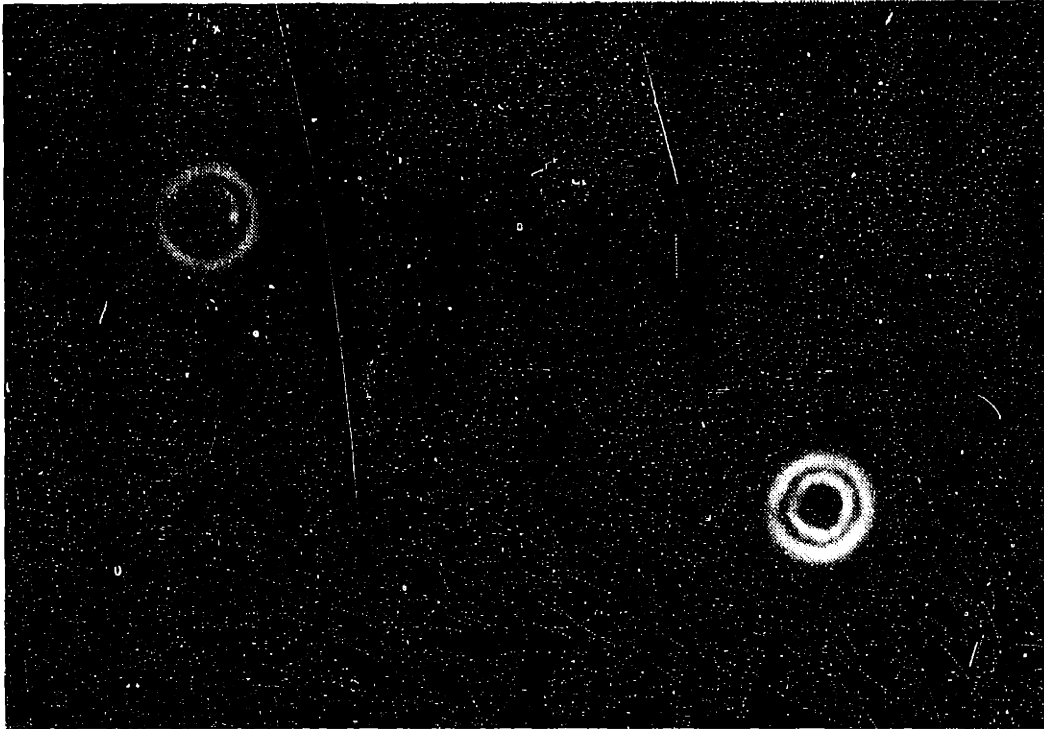
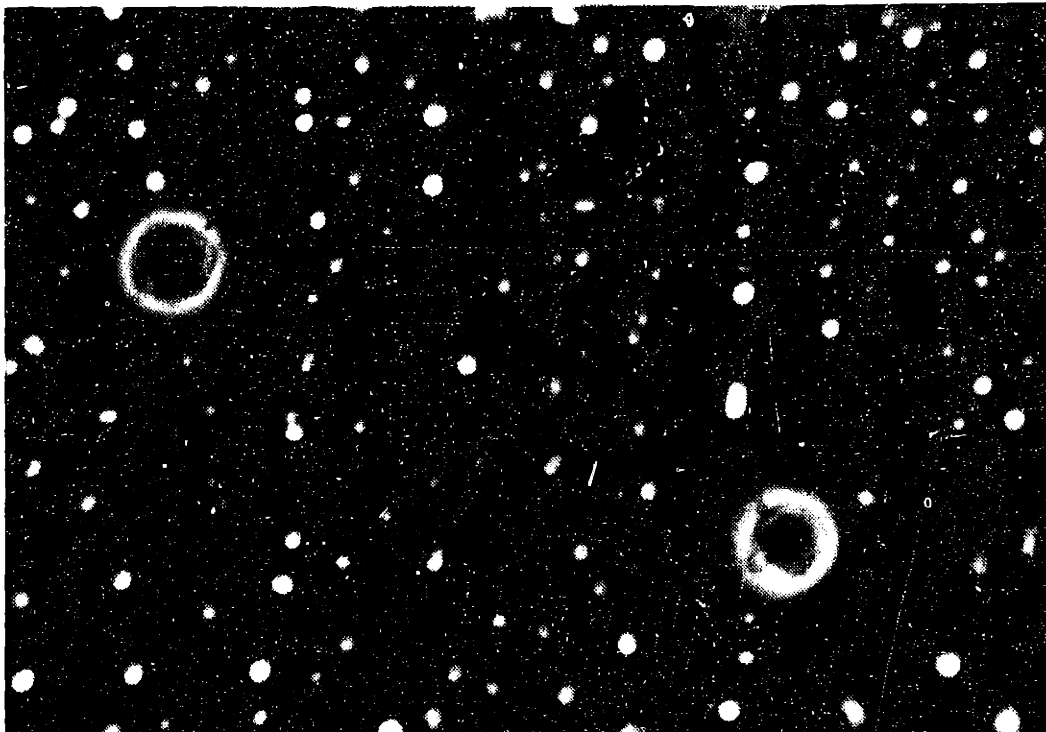


FIGURE 4.8a Lymphocytes pre-freeze

FIGURE 4.8b Lymphocytes of Fig. 4.8a at 233 K after cooling at 374 K/min, $\Delta T^0=3.5$ K, Type 3



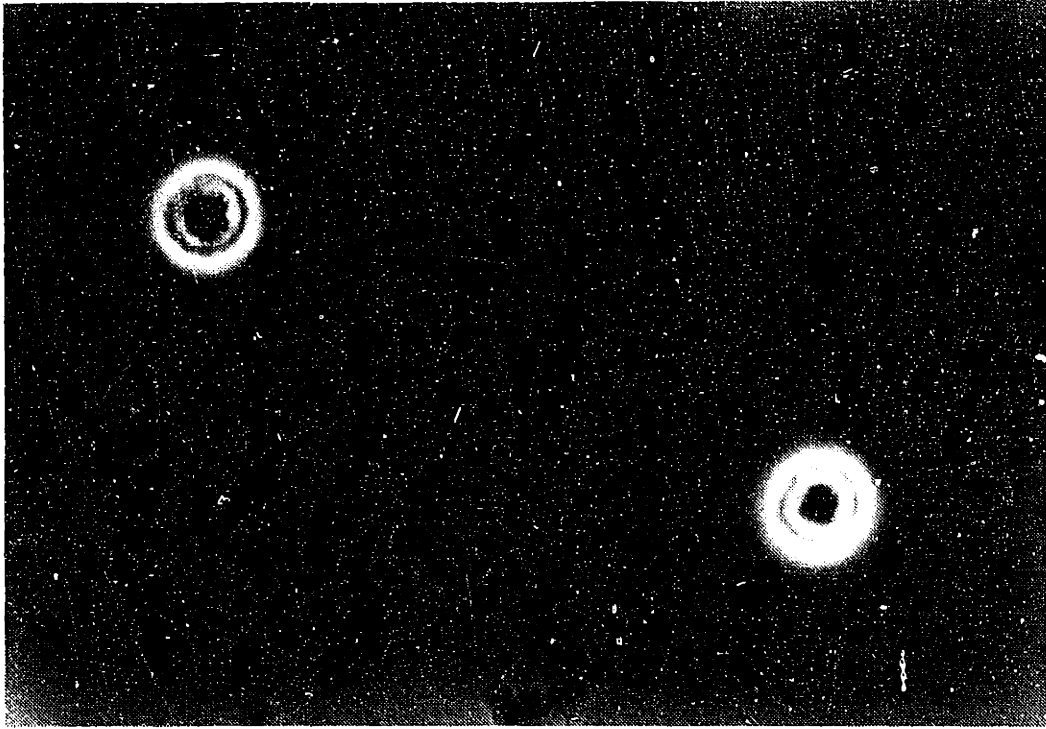
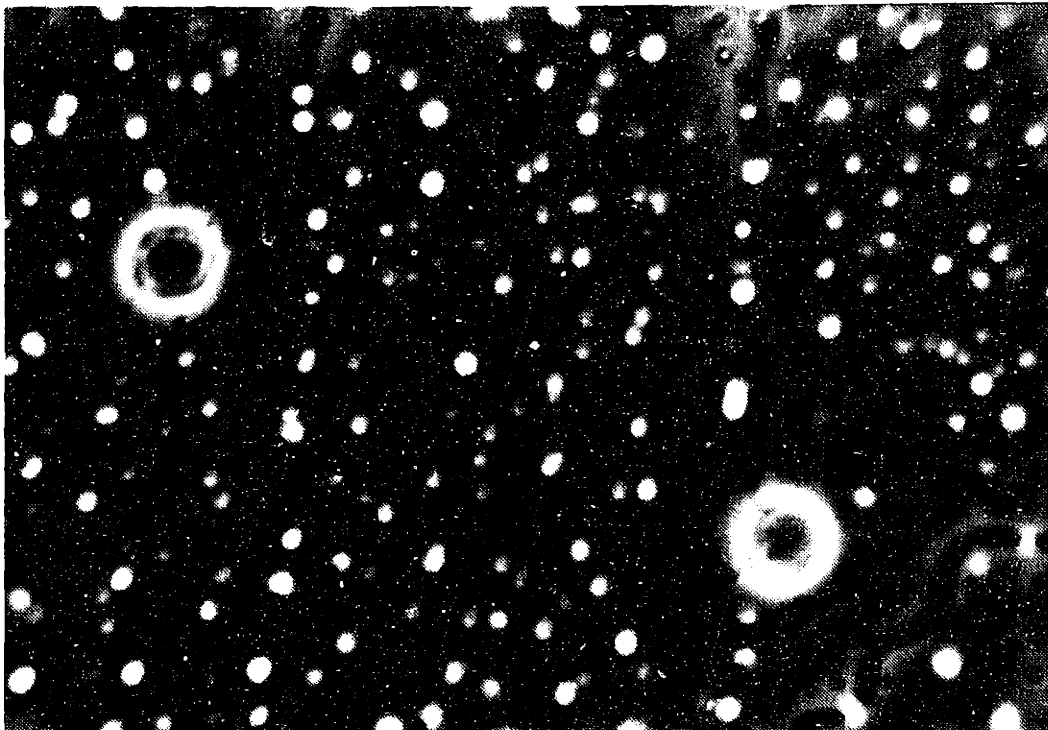


FIGURE 4.8a Lymphocytes pre-freeze

FIGURE 4.8b Lymphocytes of Fig. 4.8a at 233 K after cooling at 374 K/min, $\Delta T^0=3.5$ K, Type 3



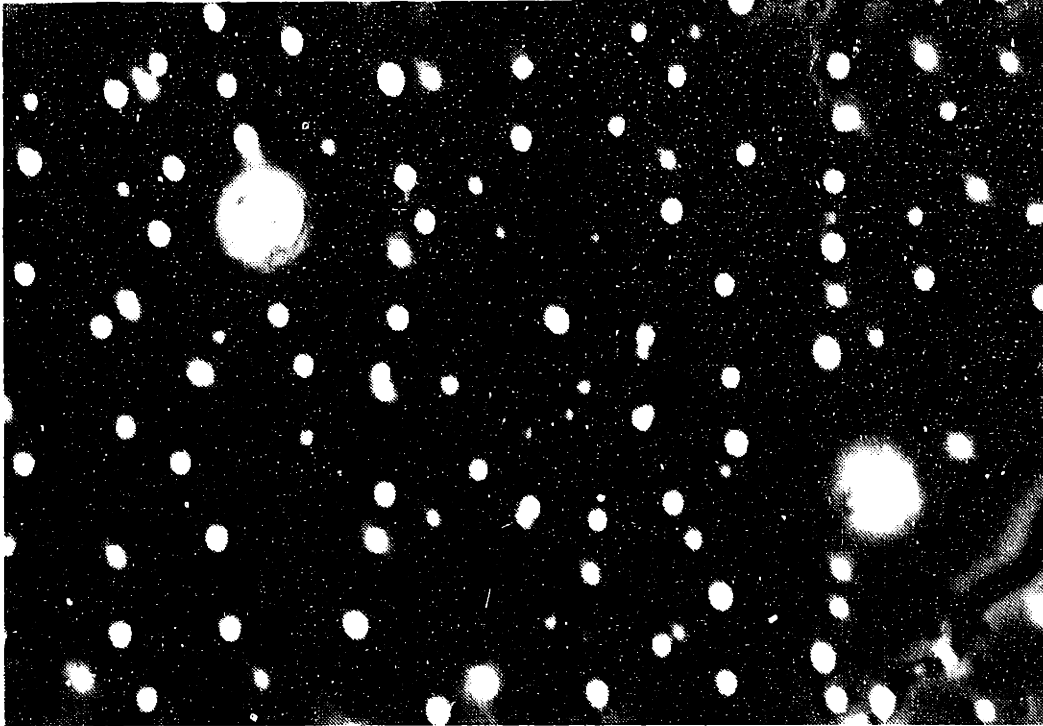


FIGURE 4.8c Lymphocytes of Figs. 4.8a and 4.8b at 261 K during warming at 5 K/min

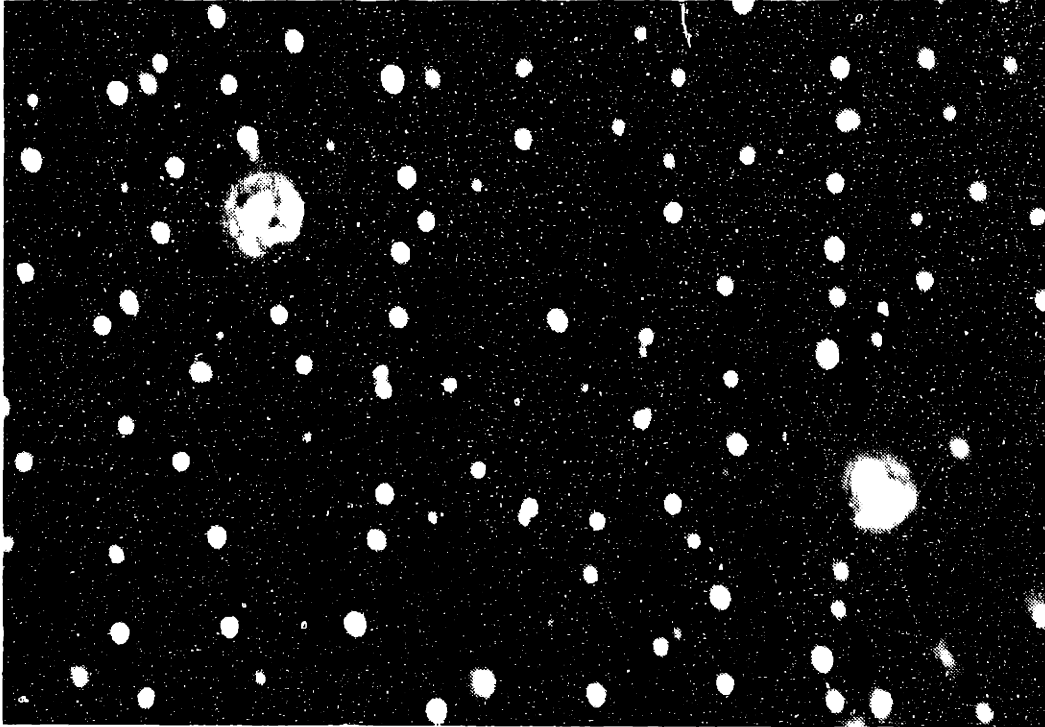


FIGURE 4.8c Lymphocytes of Figs. 4.8a and 4.8b at 261 K during warming at 5 K/min

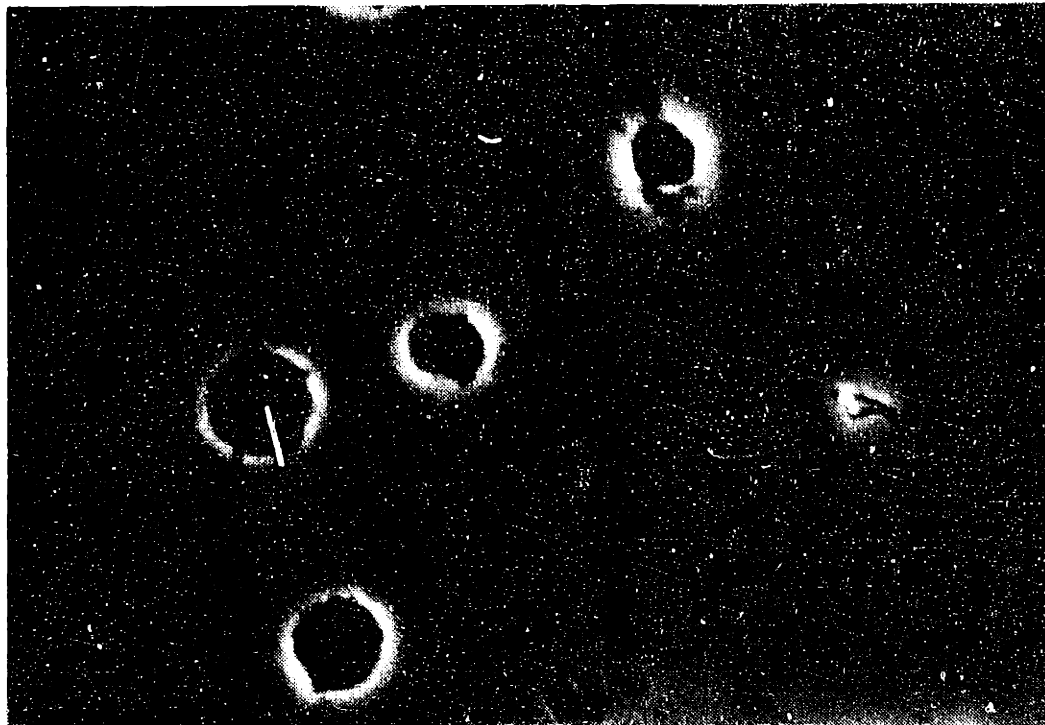
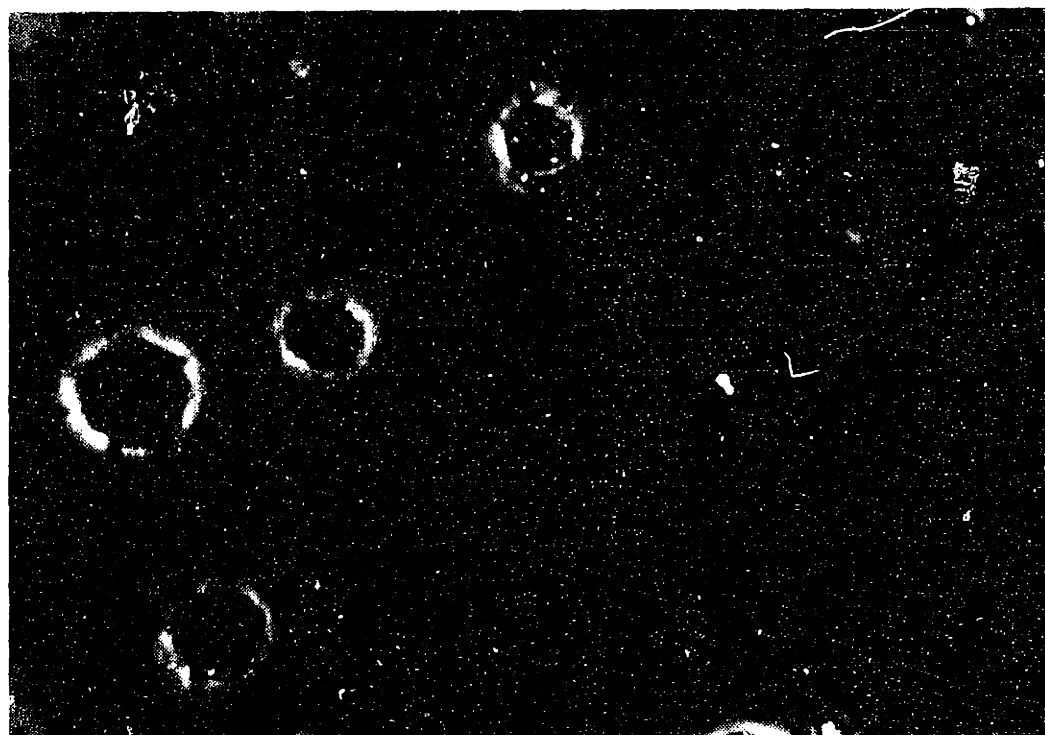


FIGURE 4.9a 'Dark' lymphocytes pre-freeze

FIGURE 4.9b Lymphocytes of Fig. 4.9a at 233 K after cooling at 1240 K/min, $\Delta T^0=8.5$ K, Type 4



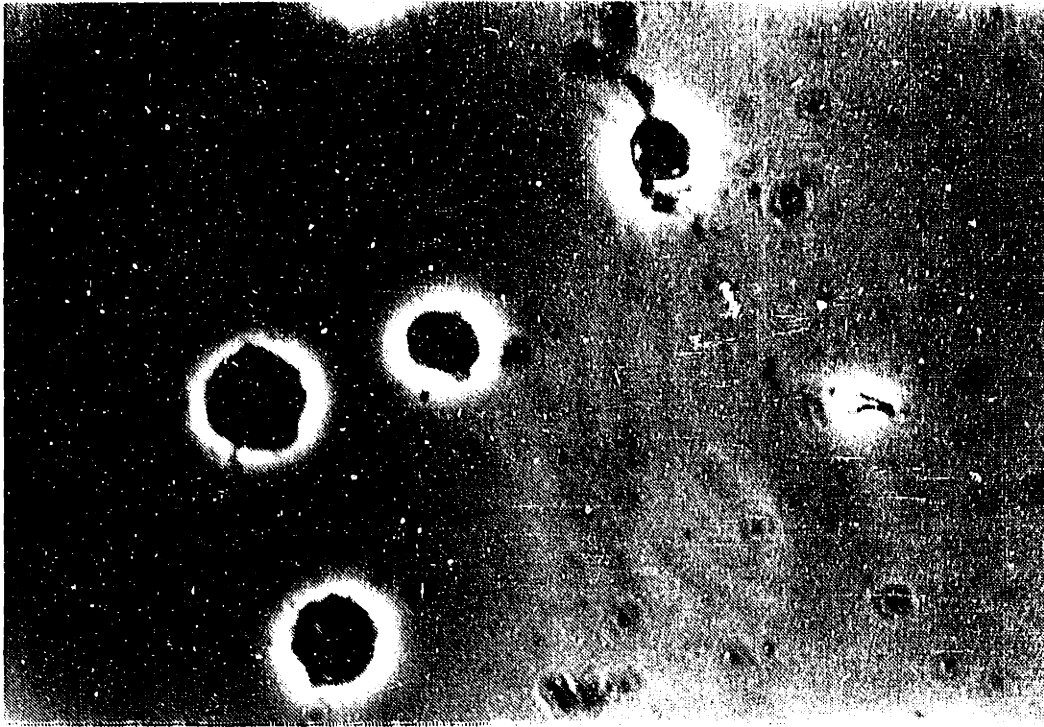
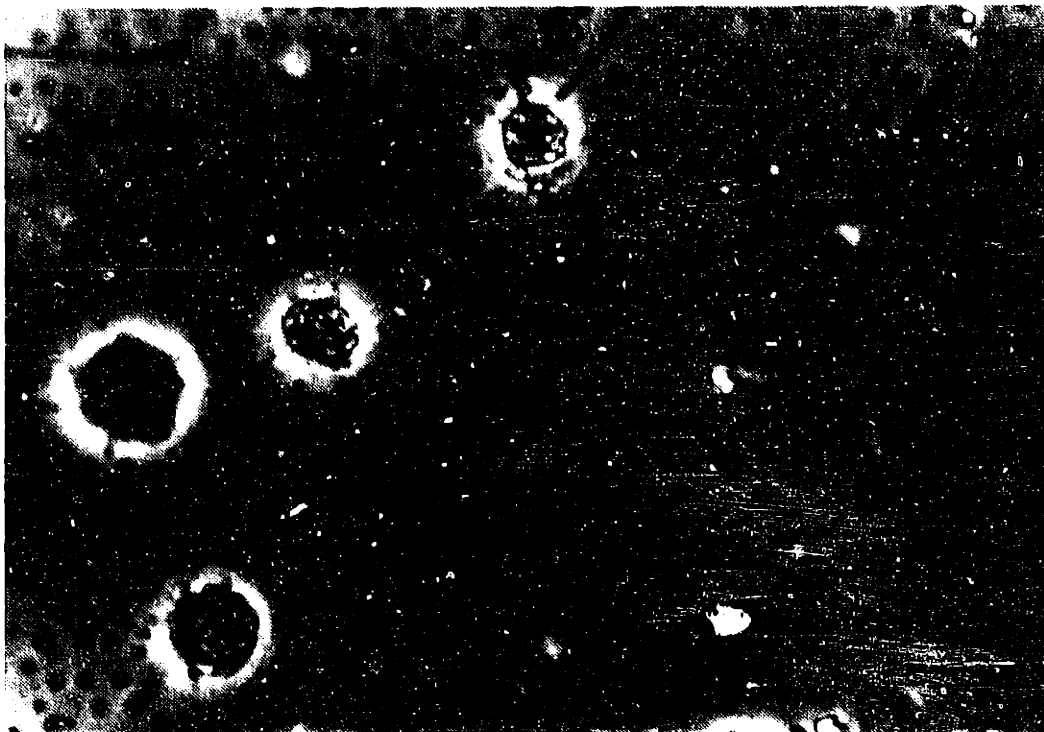


FIGURE 4.9a 'Dark' lymphocytes pre-freeze

FIGURE 4.9b Lymphocytes of Fig. 4.9a at 233 K after cooling at 1240 K/min, $\Delta T^0=8.5$ K, Type 4



maintained on the stage for more than a few minutes prior to freezing. The darker appearance also resulted when any pressure was used to seat the retaining coverslip and occurred with greater frequency for cells that had been in the ice bath longer.

As was the case for red cells, substantial appearance changes marked the passage of the extracellular ice front and again, several cell categories could be defined. The first category, comparable to red cell type 1, includes cells that show evidence of dehydration through reduced size and distorted shape. These are shown in Fig. 4.10b, which should be compared to the pre-freeze appearance of Fig. 4.10a. Another salient characteristic of type 1 lymphocytes is bright internal shading. Type 1 lymphocytes were observed at cooling rates ranging as high as ~ 100 K/min with supercooling generally below 4 K.

The second category of lymphocytes at low temperature, is characterized by relatively light internal appearance and similar size to pre-freeze cells. Fine internal structure is sometimes distinguishable. Type 3 lymphocytes also, are characterized by size similarity to unfrozen cells and fine structure, but are usually darker and more uniform in shading than pre-freeze or type 2 cells. Type 3 cells are shown in Fig. 4.8b with the unfrozen cells in Fig. 4.8a. Occasional difficulty in interpreting the observed cells as types 2 or 3 was resolved by resorting to changes of appearance during thaw, peculiar to type 3 cells. The changes involved formation of white internal regions at $\sim -20^\circ\text{C}$ which increased in size and merged, with complete coalescence by $\sim -4^\circ\text{C}$. The

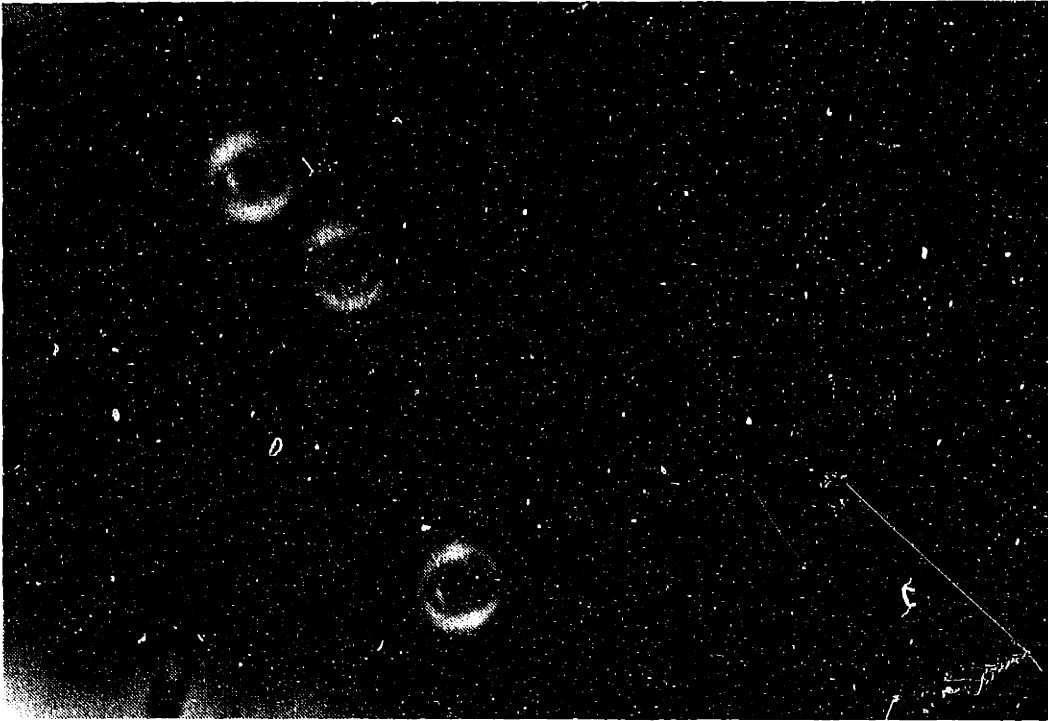
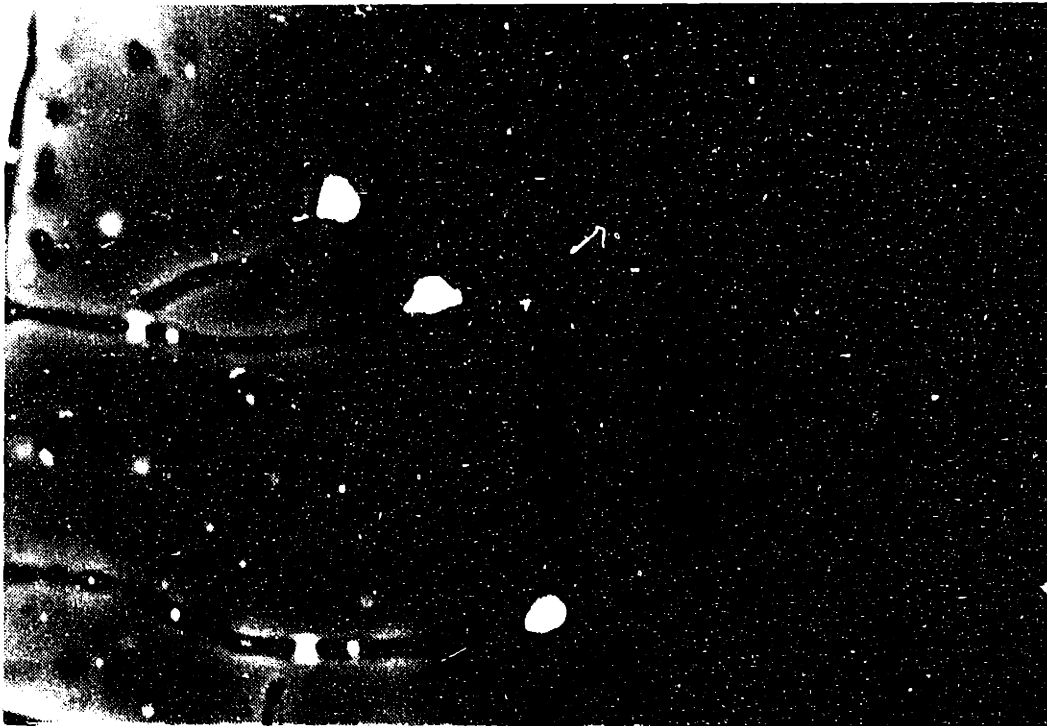


FIGURE 4.10a Lymphocytes pre-freeze

FIGURE 4.10b Lymphocytes of Fig. 4.10a at 233 K after cooling at 12 K/min, $\Delta T^0 = .5$ K, Type 1



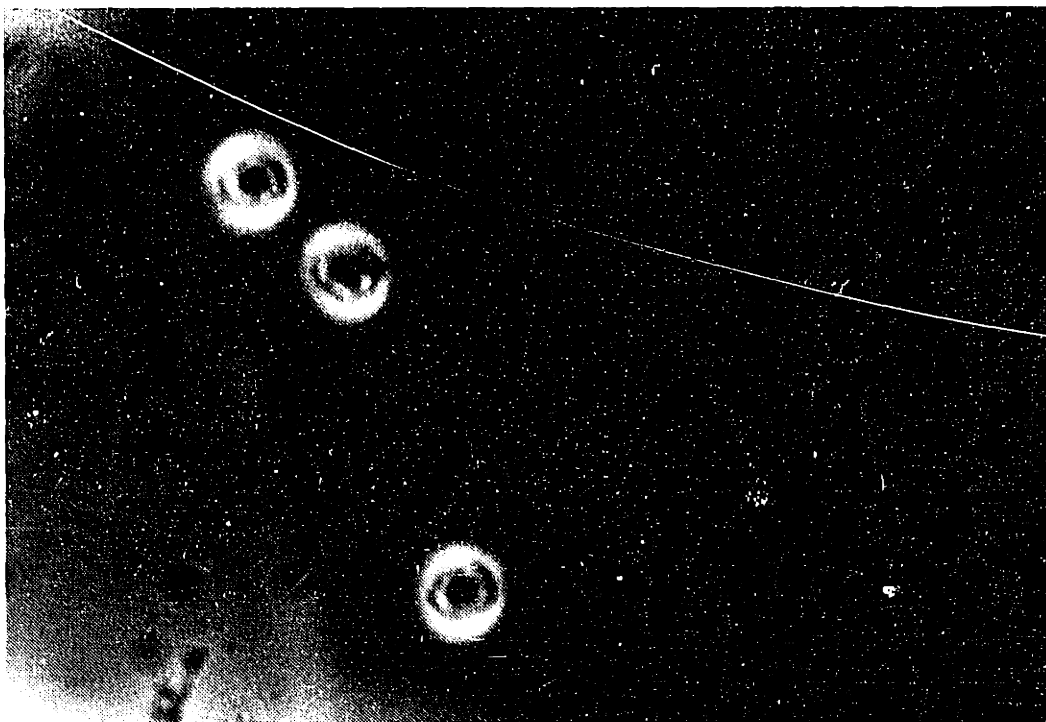
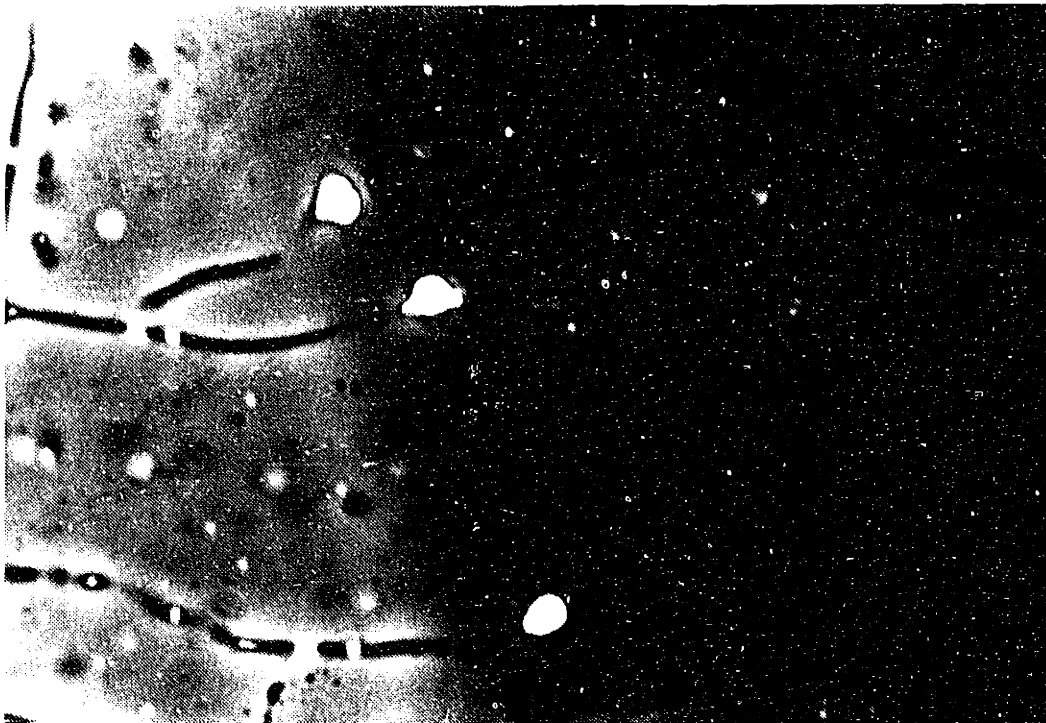


FIGURE 4.10a Lymphocytes pre-freeze

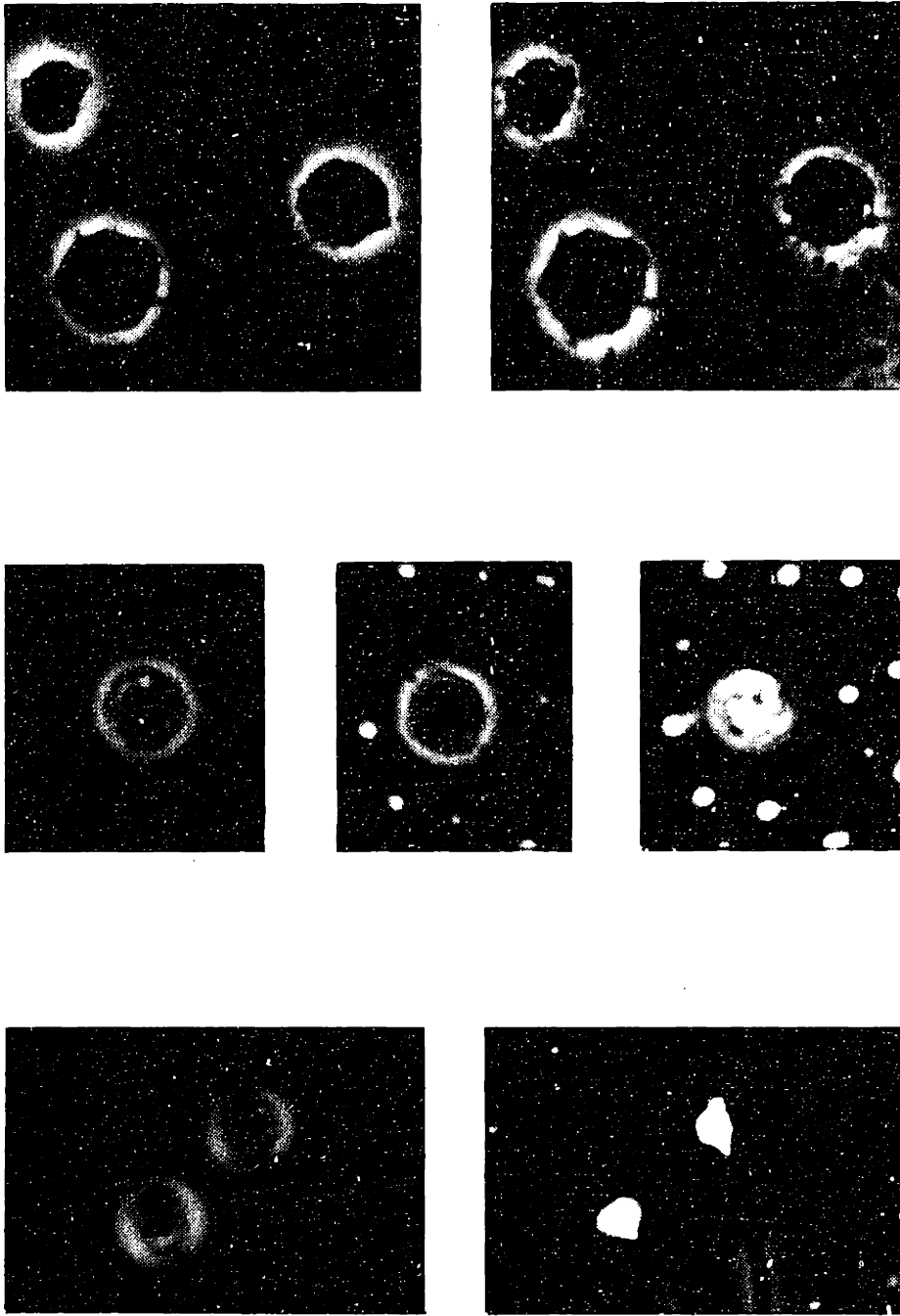
FIGURE 4.10b Lymphocytes of Fig. 4.10a at 233 K after cooling at 12 K/min, $\Delta T^0 = .5$ K, Type 1



coalescence process was usually accompanied at higher subzero °C temperatures by the appearance of a single bright region within the cell boundary, reminiscent of a bubble. These persisted in the remnants of the cell for several seconds after the thaw. Additional observations concerning the coalescence effect include: formation and growth of the white regions during relatively slow cooling at 30 K/min by -16°C, slow growth of the regions during holds of several minutes at -40°C, complete coalescence into a single light region during holds of tens of seconds at -24 to -20°C. Coalescence of internal structure at -12°C during warming at ~5K/min for type 3 cells is shown in Fig. 4.8c. Type 2 cells were observed at cooling rates up to 200 K/min and at supercoolings as large as 9 K but were usually seen at cooling rates below 100 K/min with 2-5 K of supercooling. Type 3 cells usually formed in the presence of more than 4 K of supercooling below 100 K/min and at any supercooling above 100 K/min.

A fourth category of cells is characterized by coarsely-grained internal structure such as that shown in Fig. 4.9b. This structure, similar to that observed in type 3 cells after the beginning of the coalescence process, appeared in cells that were larger and darker, pre-freeze. Conditions likely to produce type 3 cells were also likely to accompany type 4 cell development.

Lymphocyte photographs are compared in Fig. 4.11. Interpretation rules applied to the lymphocyte observations were: cell types 1 and 2 did not undergo observable internal freezing, cell types 3 and 4 did undergo observable internal freezing. The results are summarized in Fig. 4.12.



	PRE-FREEZE	PRE-FREEZE	'DARK' CELLS PRE-FREEZE
TOP:			
MIDDLE:		TYPE 3, 374 K/min, $\Delta T^0 = 3.5$ K	
BOTTOM:	TYPE 1, 12 K/min, $\Delta T^0 = .5$ K	TYPE 3 DURING WARMING AT 5 K/min	TYPE 4, 1240 K/min, $\Delta T^0 = 8.5$ K

FIGURE 4.11 Summary of Lymphocyte types

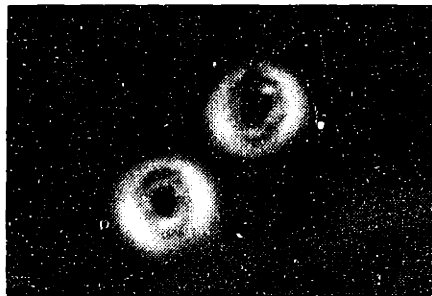
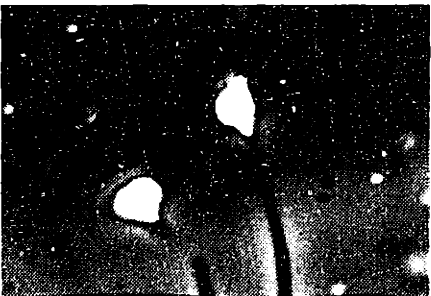
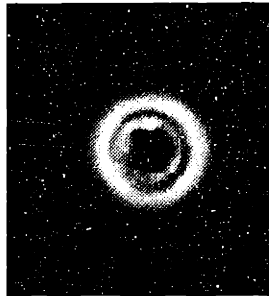


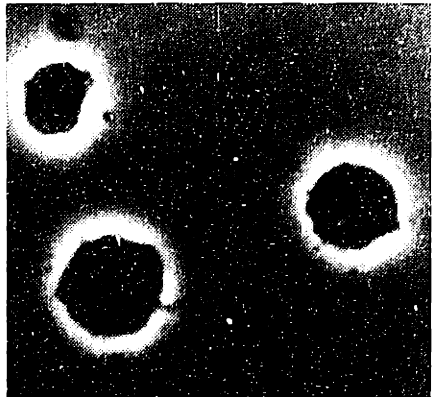
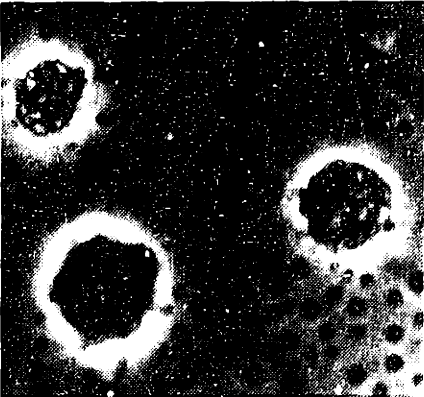
							<p>PRE-FREEZE</p> <p>TYPE 1, 12 K/min, $\Delta T^0 = .5$ K</p> <p>PRE-FREEZE</p> <p>TYPE 3, 374 K/min, $\Delta T^0 = 3.5$ K</p> <p>TYPE 3 DURING WARMING AT 5 K/min</p> <p>'DARK' CELLS PRE-FREEZE</p> <p>TYPE 4, 1240 K/min, $\Delta T^0 = 8.5$ K</p>
<p>TOP:</p>							
<p>MIDDLE:</p>							
<p>BOTTOM:</p>							

FIGURE 4.11 Summary of lymphocyte types

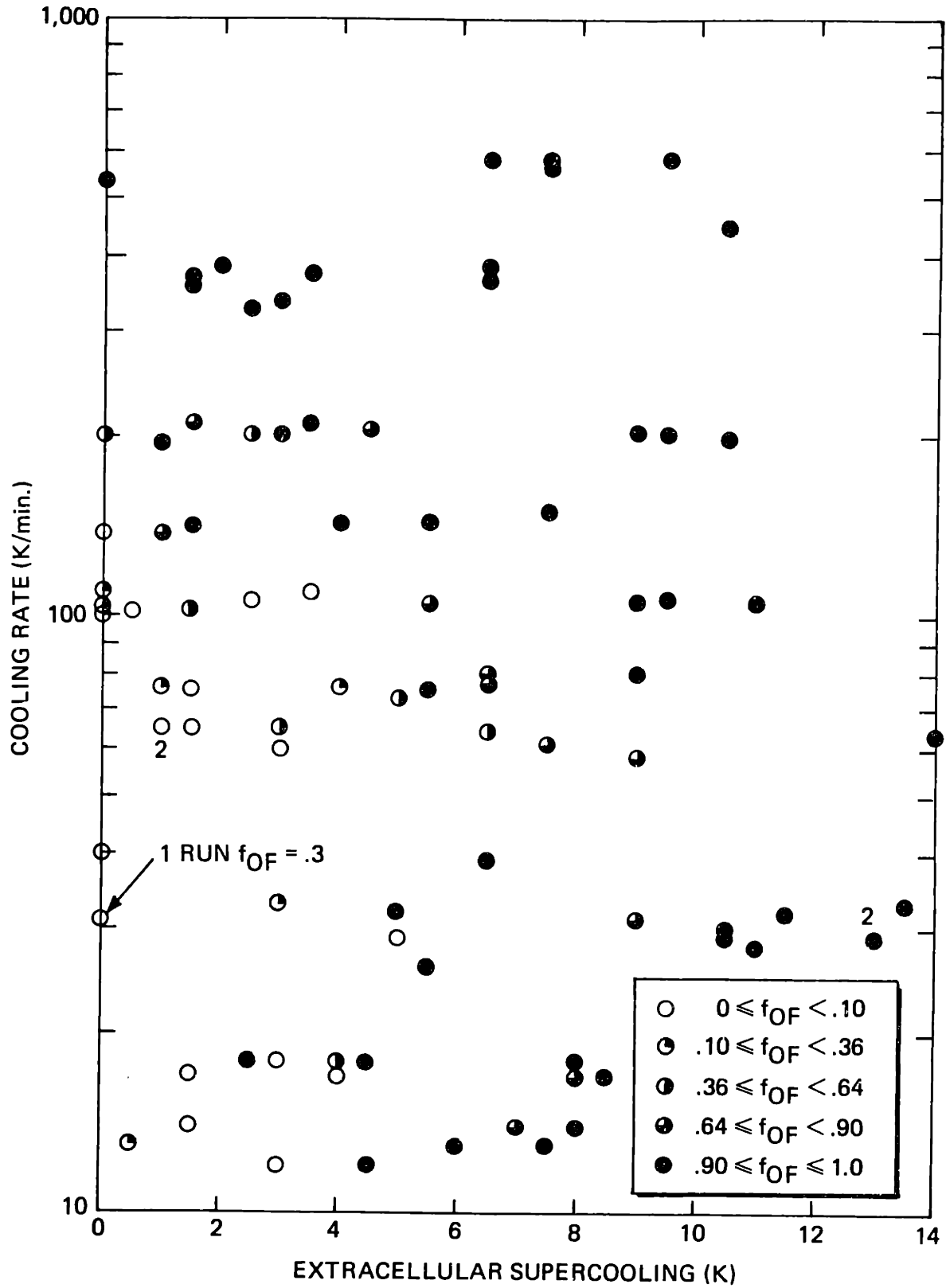


FIGURE 4.12 Summary of cryomicroscope lymphocyte observations; numbers next to data points refer to the number of runs at the indicated conditions, f_{OF} is the fraction of the cells in a given run with observable internal freezing

CHAPTER 5
DISCUSSION

5.1 Correlation of Theory with Experimental Results for Red Cells

The cooling rate dependence of observable internal freezing in red cells is shown from a variety of sources in Fig. 5.1. In addition to data from the present investigation for the 0-1 K supercooling range, 'sliced' from Fig. 4.7, experimental results are shown from Diller [20], Rapatz, Sullivan and Luyet [12] and Scheiwe, Nick and Körber [76]. Diller performed observations on a cryomicroscope; Rapatz et al. and Scheiwe et al. made post-thaw measurements of hemolysis on samples in capillaries. Only the supra-optimal cooling rate results are quoted from the latter two groups. All of the data were obtained with whole blood in ACD (anti-coagulant). Analytical curves are redrawn from Fig. 2.14 with $S_{Tf} = .5$ K and from Mazur [21]. The latter was calculated by taking the probability of intracellular freezing equal to 0 when the subcooling of the cell contents was less than 2 K or when cell volume was less than .1 of the original volume. Probability of intracellular freezing was set equal to 1 when internal subcooling exceeded 2 K and when volume was greater than .1 of the original volume. Since these criteria were applied to a cell with specific representative properties at an assumed freezing temperature of -10°C , a sharp transition from 0 to 1 probability of intracellular freezing, which is equated in this discussion to fraction observable intracellular freezing, would be expected.

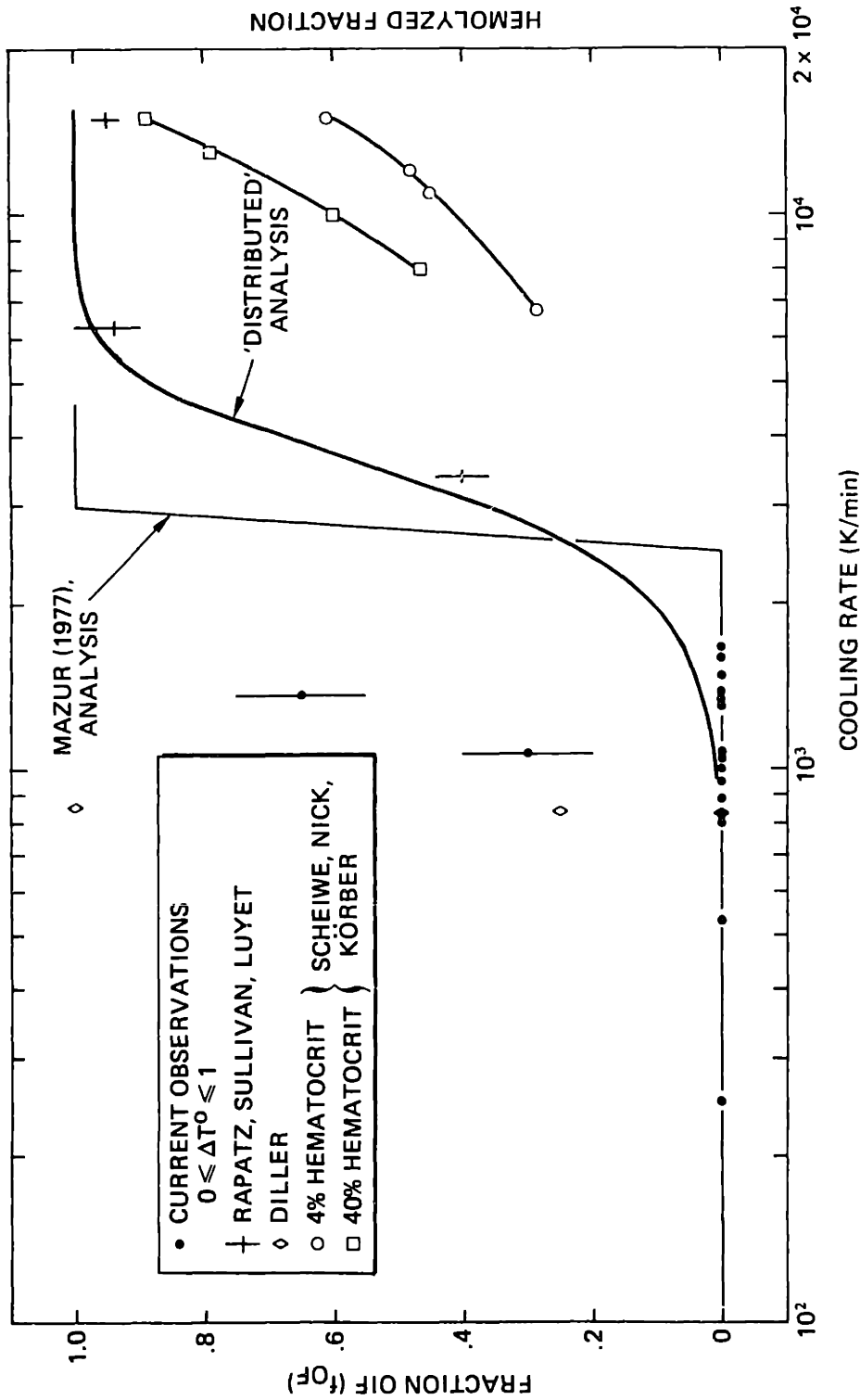


FIGURE 5.1 Comparison of red cell analytical and experimental results for effect of cooling rate on the cell fraction with observable internal freezing: data of Rapatz et al. and Scheiwe et al. are post-thaw hemolysis, current observations and data of Diller are cryomicroscope results, 'distributed' analysis is from section 2.5. Error bars on current observations at 1070 and 1370 K/min result from estimates of the fraction of type 3 and 4 cells.

The slope shown in this curve can not be reconciled with the stated freezing criteria. It should be noted that the above criteria are philosophically similar to those discussed in Sect. 2.4 as applied to individual cells in a population; each cell does or does not contain an observationally significant quantity of internal ice.

Other anomalies appear in Fig. 5.1. First, there is the discrepancy between the capillary hemolysis results; Schiewe et al. comment on this but do not offer an explanation. A strong possibility is the difference in procedures used to prevent supercooling. Seeding temperatures and thermal rebound duration were not the same in the two sets of experiments. Quantitative and qualitative disagreement between current observations and the earlier work of Diller may result from identification of different events as intracellular freezing and combined effects of instrumentation uncertainties. The distributed analysis is reasonably consistent with current data up to the highest cooling rates used in the experiments, with the exception of two runs at 1070 and 1370 K/min. Instrumentation-related temperature uncertainties, on the order of 1-2 K, discussed in Sect. 3.1 and Appendix E can account for these data. The close correspondence between the hemolysis data of Rapatz et al. and the curve from the analysis of Sect. 2.4 is probably fortuitous in light of the supercooling-rebound factors mentioned above as well as solution and warming rate effects in the hemolysis data. Allowances for these should be made in comparing hemolysis data to intracellular freezing results. For slow warming one expects capillary survival to be low-

er than that predicted by the analysis, assuming equivalence between OIF and lethality. The situation is clouded for the rapid warming experiments cited, in that some cells survive internal freezing; see Figs. 1.2 and 1.4. Recrystallization and the quantities of internal ice associated with damage by this mechanism must be studied further before intracellular freezing and survival results can be compared meaningfully in other than specific situations.

Data for the effect of extracellular supercooling on observable internal ice formation are compared in Fig. 5.2. Each of the three points shown from Diller [20] represents several experiments at a particular value of supercooling. The separate experimental points are not shown because the total ranges of cooling rates for 0 to 100% observable freezing are only ~ 10 K/min, smaller than the data points. Again, substantial qualitative and quantitative differences separate previous from current data. The point labeled Körber [77] was obtained from high speed movies of red cells at 1200 K/min in which $\sim 3/10$ cells showed evidence of internal freezing after supercooling of between 1.5 and 4 K. These observations are consistent with the current results.

The $f_{OF} = .1$ and $.9$ contour lines from Fig. 2.18 are 'flattened' onto the cooling rate, extracellular supercooling plane of Fig. 5.2. The analysis, performed with Table 2.2 values and with $T_f = -6^\circ\text{C}$ and $S_{Tf} = .5^\circ\text{C}$, fits the data fairly well. The predicted larger range of supercoolings for the transition from $f_{OF} = 0$ to $f_{OF} = 1$ at higher cooling rates is supported by the data, for example, at 1000 K/min. Al-

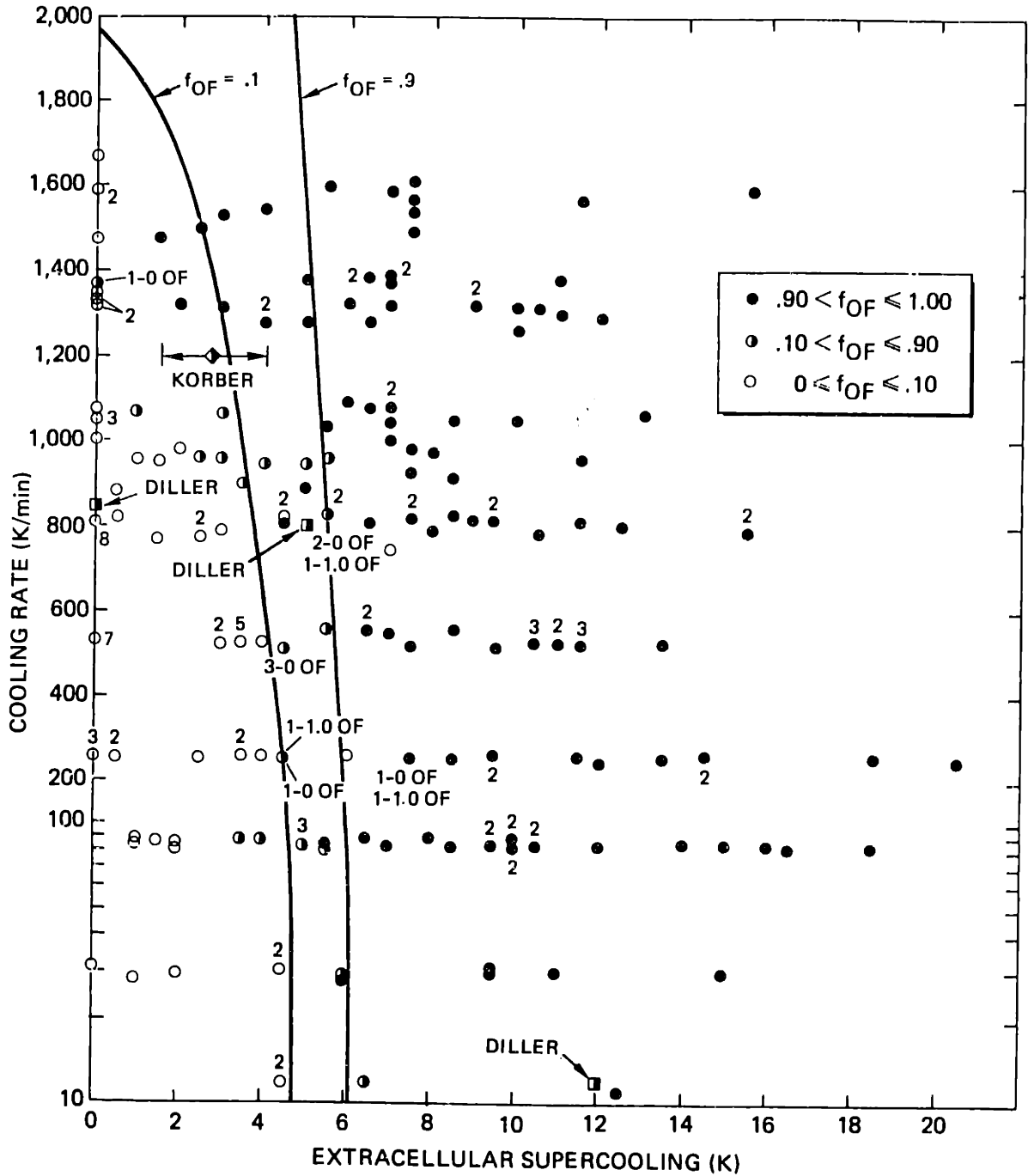


FIGURE 5.2 Comparison of red cell analytical and experimental results for effect of extracellular supercooling: curves labeled $f_{OF} = .1, .9$ are for the respective fractions of cells with observable internal freezing from the analysis of section 2.6

though conclusions should be avoided in assessing the correlation between theory and experiment at substantially higher cooling rates, in light of the instrumentation difficulties discussed previously, the general features of the model are confirmed.

Three observations support the assisted, membrane-related hypothesis for intracellular freezing. First, in the presence of external subcooling of at least 20 K, internal subcooling also occurs. This unequivocally indicates a lack of heterogeneous nucleation sites capable of inducing spontaneous internal freezing. Second, changes of appearance associated in Chapter 4 with internal freezing occur within two or three video fields or 34 to 51 ms after passage of the external ice front. This establishes the role of the cell environment in precipitating internal freezing. Third, apparent gaps and protrusions in cell surfaces and internal dendritic structures originating at one or more points on the surface, such as those of Fig. 4.4, argue for extracellular ice and membrane participation in internal freezing.

5.2 Correlation of Theory with Experimental Results for Lymphocytes

Distributed properties of human lymphocytes are summarized in Table 5.1. As was the case for red cells, the variations of permeability and activation energy result from experimental uncertainty and not from intrinsic distributions. These values are reasonable for a 'first-cut' analysis. The mean area listed is substantially larger due to membrane folds than that required to enclose the total cell volume. The standard deviation of area is estimated from error bars in reference [78]

TABLE 5.1

HUMAN LYMPHOCYTE PROPERTIES

PROPERTY	MEAN	STANDARD DEVIATION	SCALING, UNITS	SOURCE
K_{PR}	7.57	.33	$\times 10^{-13}$ cm ³ /dyne-s	[79]
A	2.6	.35	$\times 10^{-6}$ cm ²	[78]
N_{Wi}	5.29	1.30	$\times 10^{-12}$ moles	See text
E	14.1	1.6	kcal/mole	[79]
α	3.95	1.06	$\times 10^{-7}$ cm ⁵ /dyne-s-mole	Eqs. (2.26), (2.27)
T_f	-6	1	°C	See text

and in this case probably does reflect the area distribution. An initial mean volume of $138 \mu^3$ was estimated from optical microscopy diameter measurements on cells separated by the procedures of Table 3.2. Equation (2.17) was applied to calculate the mean initial water content using an initial ratio of water to total cell volume of .69. This ratio is obtained from the osmotically inactive volume fraction of .31 reported by Hempling [79]. The standard deviation of the initial water content was estimated from a flow cytometry histogram assuming intensity-volume proportionality and using Eq. (2.18). The flow cytometry technique involves single-file entrainment of cells in a laminar stream which interrupts a laser beam-detector pair [80]. The detector signal from thousands of cells forms a histogram of forward scattered light.

Appendix 0 discusses reported and present lymphocyte volume measurements and examines the intensity-volume proportionality assumption. Osmometric behavior is proposed as the basis for volume calibration of laser flow cytometry systems. The mean and standard deviation of the parameter, α , were calculated using the approximations of Eqs. (2.26) and (2.27). The freezing temperature mean and standard deviation were deduced from low cooling rate data in Fig. 4.10 using the logic of Sect. 2.6.

Results of analysis using the methods of Chapter 2 and the properties of Table 5.1 are shown for the effect of cooling rate in Fig. 5.3. The water content criterion for observable internal freezing, ϕ_{OF} , was increased to .9 because of the small volume change associated with

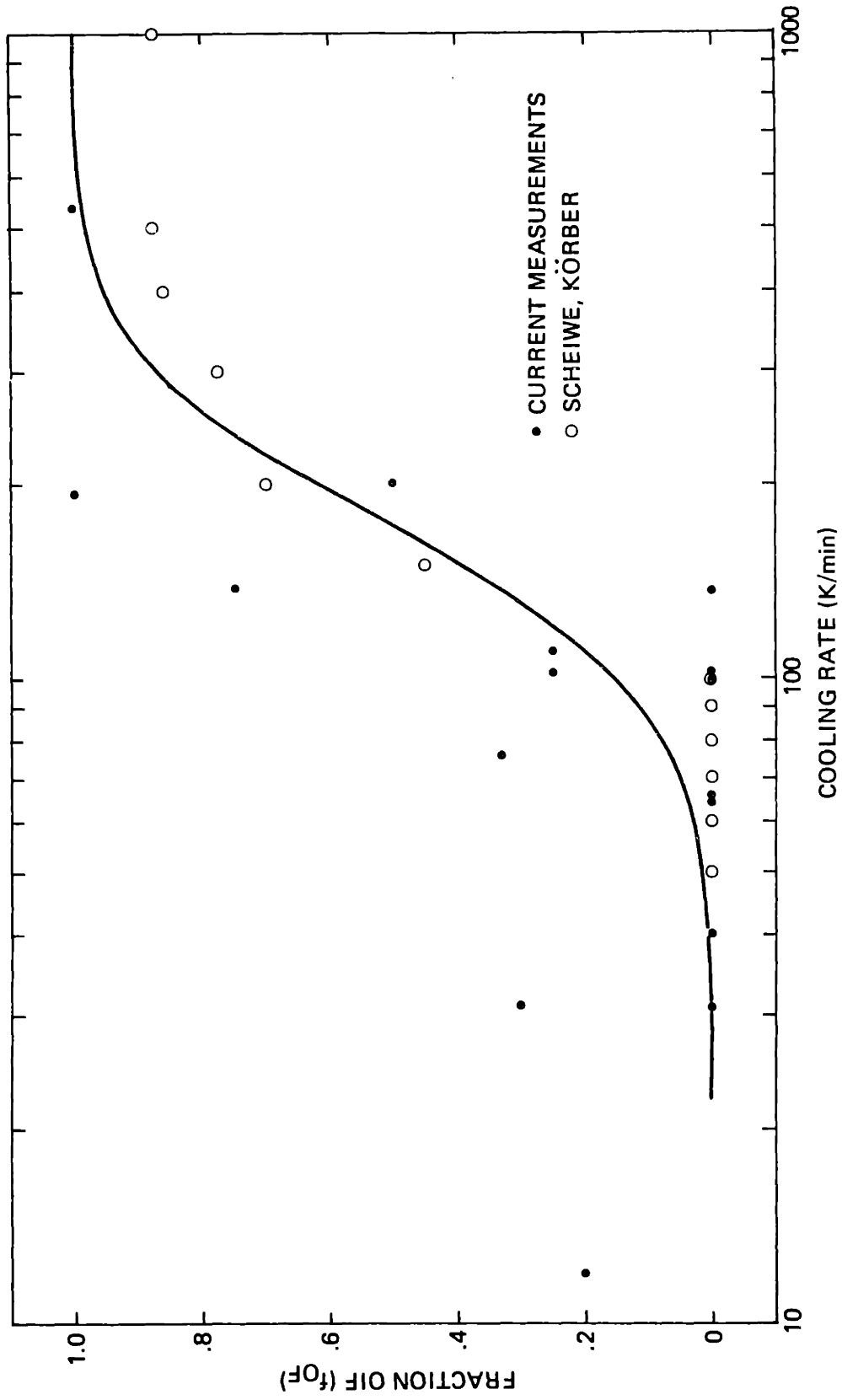


FIGURE 5.3 Comparison of lymphocyte analytical and experimental results for effect of cooling rate on the cell fraction with observable internal freezing: solid curve results from the distributed analysis

type 3 lymphocytes. Current experimental results with external supercooling in the 0-1 K range compare favorably to the theoretical curve. The recent results of Scheiwe and Körber [81], obtained during cooling, also compare favorably although questions arise concerning the definition of the intracellular freezing event. Scheiwe and Körber detected intracellular ice formation during cooling as sudden twitching without gray level change or as darkening in a range of temperatures near 243 K. The events characterized in Chapter 4 as intracellular freezing occur soon after passage of the external ice front at temperatures roughly 20 K higher than the phenomena observed by Scheiwe and Körber. Possible explanations for these differences include use of growth medium to suspend cells in the present experiments versus saline, used by Scheiwe and Körber, and effects of external ice growth velocities which are probably substantially higher in the present convective cooling stage experiments than in the previous conduction stage work.

Analytical results for the effect of extracellular supercooling, qualitatively similar to those of Fig. 2.17 for red cells, are shown in Fig. 5.4. The approximate factor of 20 reduction in cooling rates required to produce a specified fraction observable internal freezing reflects the order of magnitude lower α and factor of 4 higher activation energy for lymphocytes. The decreased slopes of the curves at low cooling rates, compared to Fig. 2.17, are caused by larger variance in the assumed distribution of cell freezing temperatures. These results combine with the cooling rate results of 0 supercooling, Fig. 5.3, to form the fraction observable freezing surface above the cooling rate,

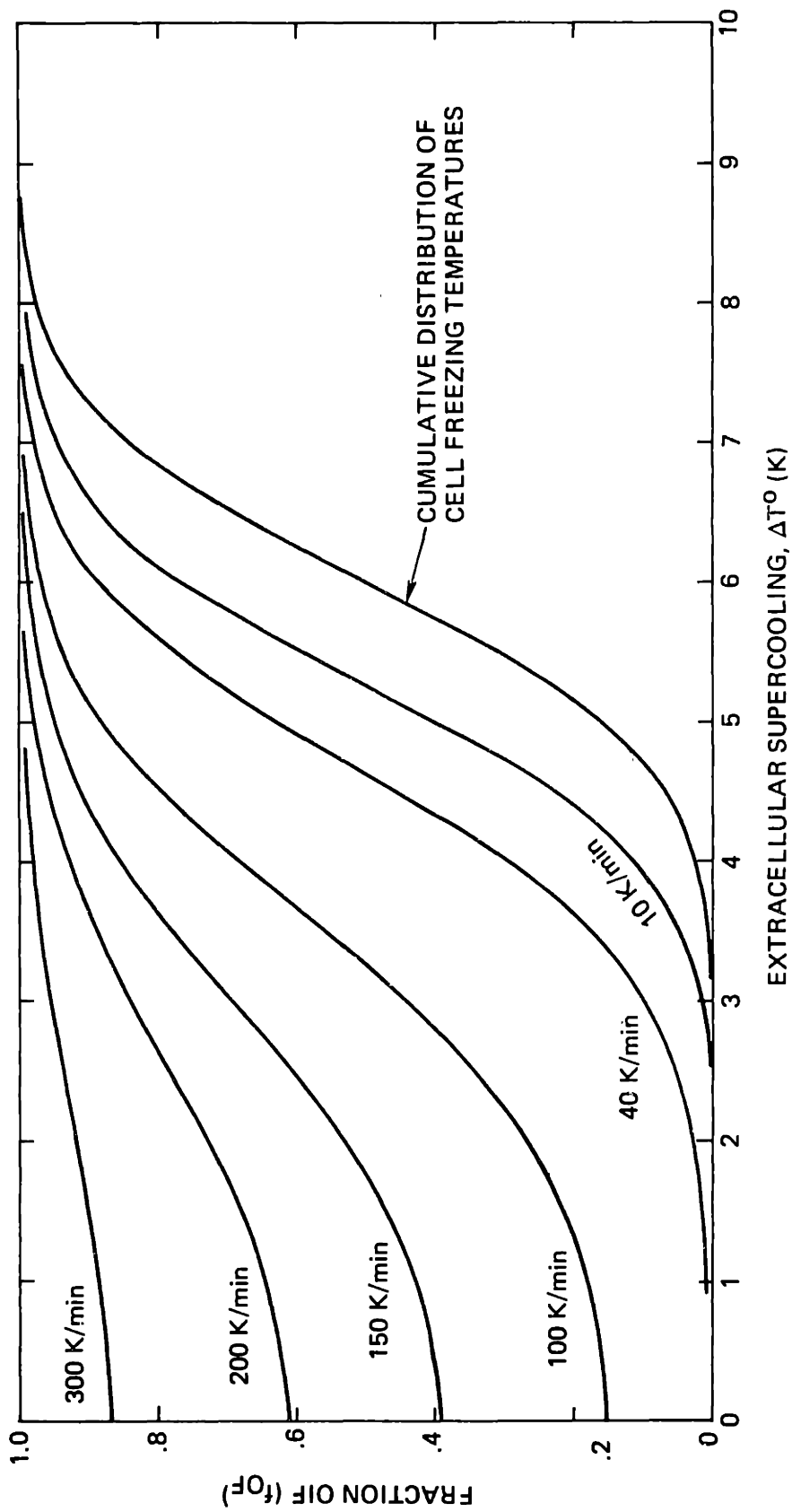


FIGURE 5.4 Fraction of lymphocytes with observable internal freezing: dependence on extracellular supercooling

extracellular supercooling plane in Fig. 5.5. This surface, as expected, resembles Fig. 2.18 for red cells.

The $f_{0F} = .1$ and $.9$ contours of Fig. 5.5 can be projected down onto the cooling rate, supercooling plane to illustrate the theoretical range of conditions for the transition from few to most cells with observable freezing, in a form directly comparable to experimental findings. Figure 5.6 shows the transition zone superimposed on the lymphocyte observations of Fig. 4.10. The theoretical curves accommodate the major features of the experimental results such as the region in the lower left of the figure with few observably frozen cells and the region to the right of the $f_{0F} = .9$ curve consisting of frozen cells, predominantly. Although the analysis can be fine-tuned to optimally fit the data by assigning different means and variances for the assumed freezing temperature distribution, increasing the number of cells observed or obtaining better estimates of the biophysical property distributions would be more productive exercises.

5.3 Summary

A schematic overview of the present work is shown in Fig. 5.7.

Highlights include:

- 1) introduction of distributions of cell properties in the analysis of water transport and intracellular freezing supported by:
 - a) statistical techniques for combining three out of four distributions of properties into a single distributed parameter,

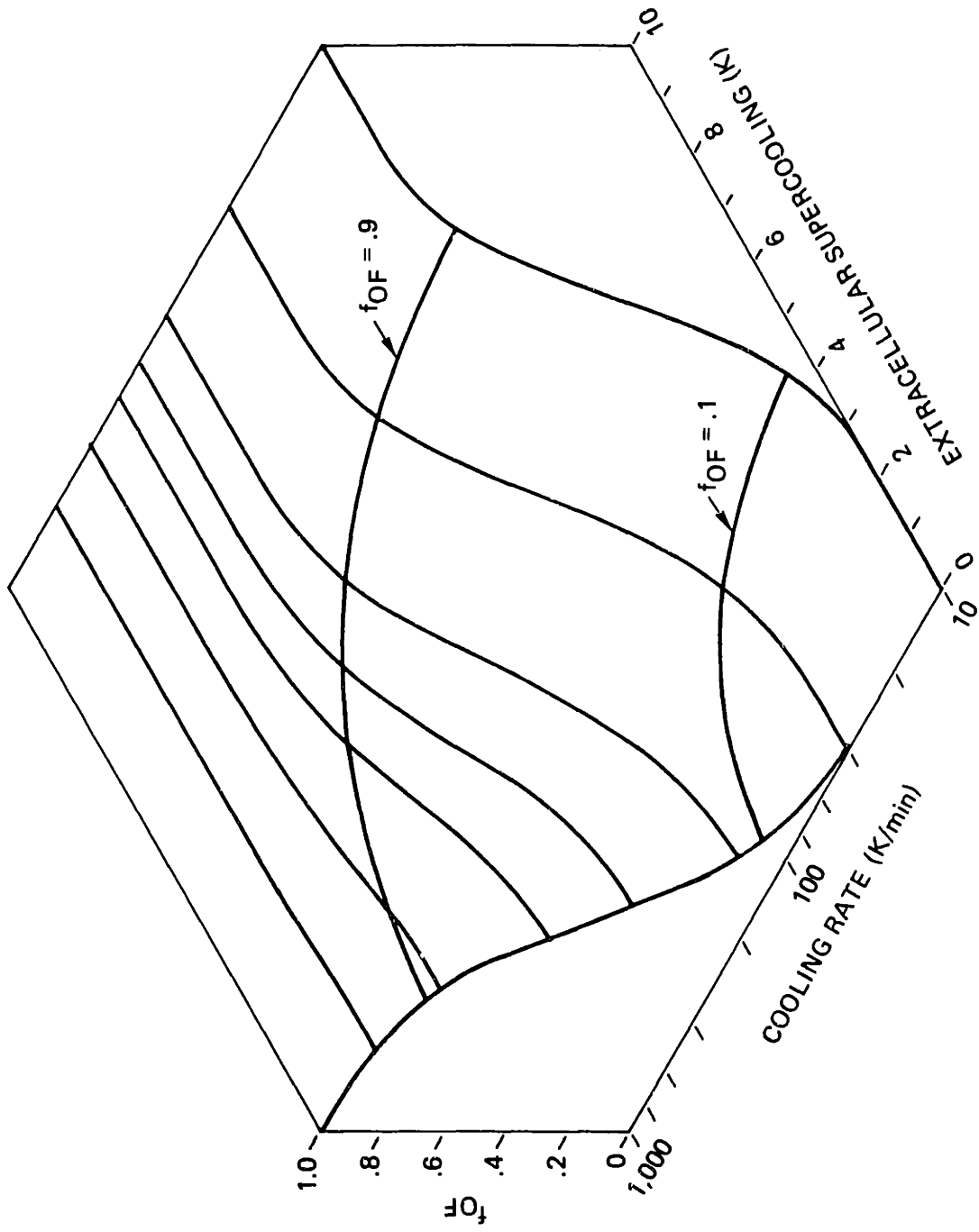


FIGURE 5.5 Fraction internal freezing surface above the cooling rate-extracellular supercooling plane for lymphocytes

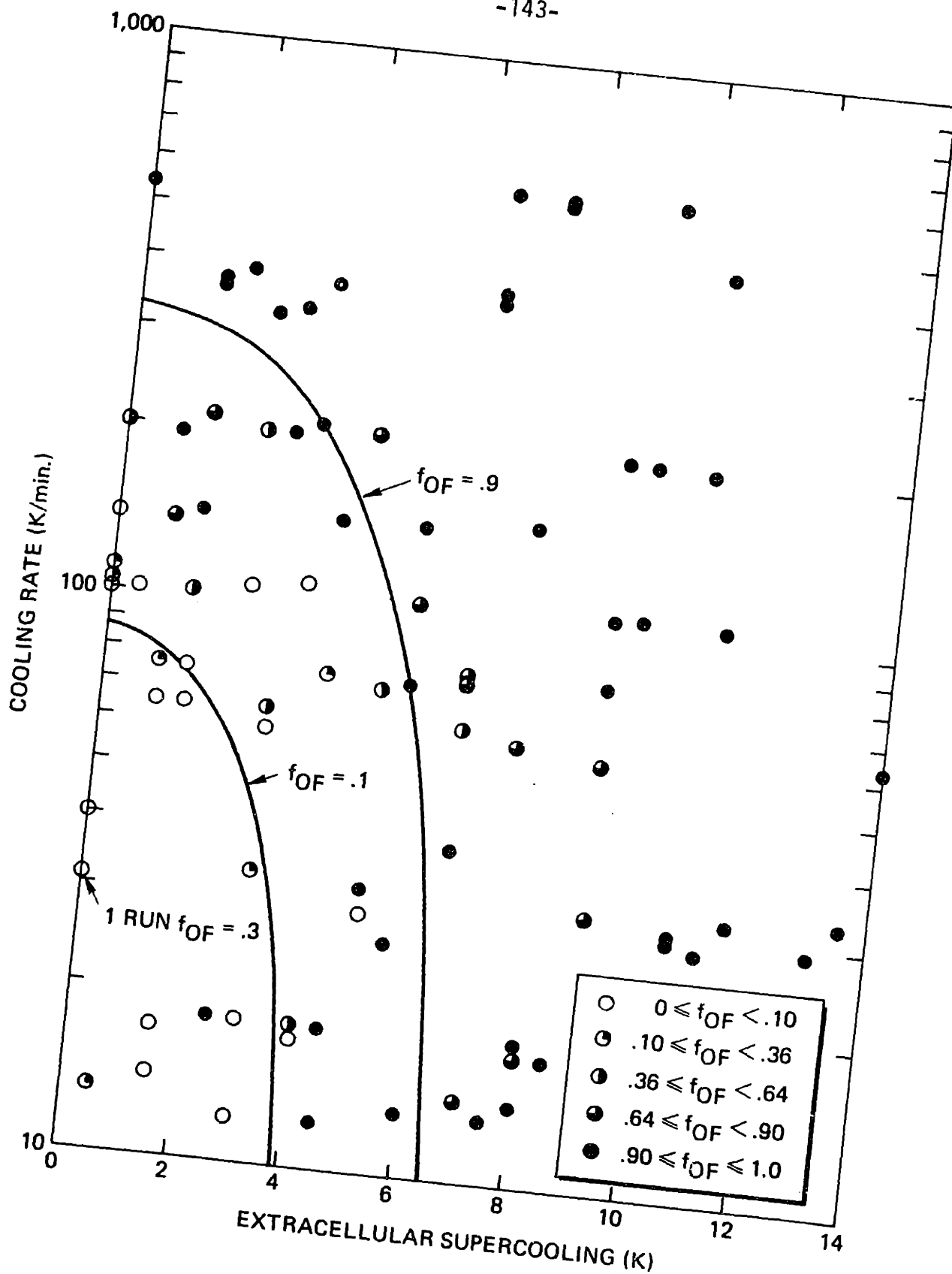


FIGURE 5.6 Comparison of lymphocyte analytical and experimental results for effect of extracellular supercooling

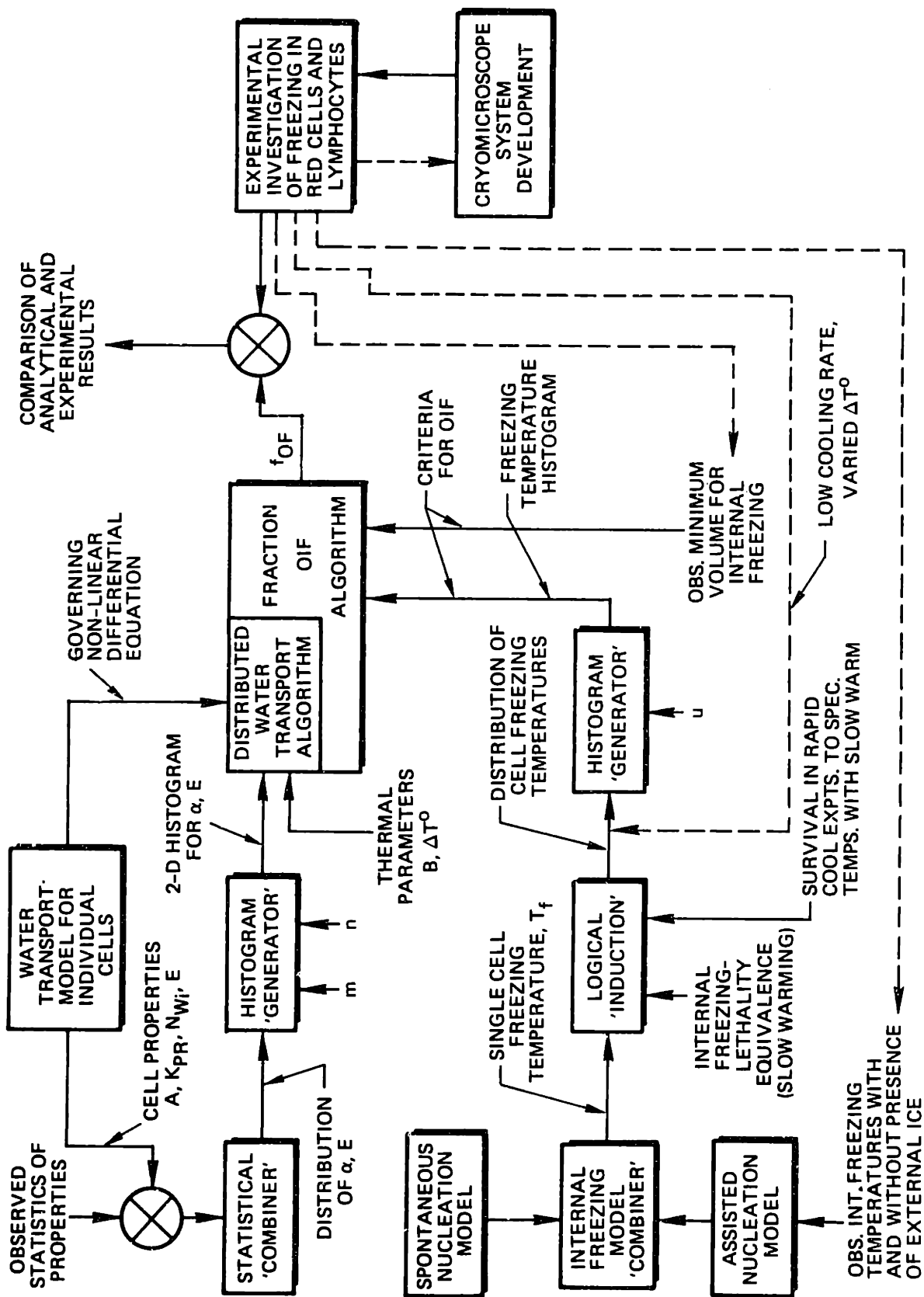


FIGURE 5.7 Schematic overview of the present work

- b) combination of the assisted and spontaneous models of internal freezing,
 - c) definition of two criteria for observable freezing in an individual cell: minimum water content and temperature below the cell freezing temperature,
 - d) elucidation of two experimental techniques for establishing the shape of the distribution of cell freezing temperatures: rapid cooling to sub-zero temperatures followed by slow warming, and slow cooling with varied extracellular supercooling,
- 2) numerical solutions for the fraction of human red cells and lymphocytes with internal freezing presented compactly in a surface above the cooling rate-extracellular supercooling plane,
- 3) experimental results for the fractions of red cell and lymphocyte populations with intracellular freezing over 10-1500 K/min cooling and with 0-20 K of supercooling,
- 4) cryomicroscope system improvements:
- a) construction of a hardwired digital reference signal generator providing high temperature rate nonlinear protocol capability,
 - b) addition of a microcomputer-software, reference generation option,
 - c) redesign of the thermal control loop to provide an order-of-magnitude bandwidth improvement over the previous system involving construction of a lead compensating controller, thermocouple amplifier, and analysis and/or measurement of most aspects of the cryomicroscope thermal control problem,
 - d) development of a 'first generation' automated nucleation controller to provide predetermined values of supercooling in the cell-suspending medium,

- e) development of a video annotation system to record temperature and time on each video field for facilitating data reduction and interpretation,
- 5) conclusions:
- a) the distributed cell freezing model agrees well with experimental observations of human red cells and lymphocytes for the effects of cooling rate and supercooling,
 - b) intracellular freezing in red cells and lymphocytes is mediated by membrane related, environmental factors.

5.4 Suggestions for Future Research

Several investigations are recommended to address issues arising in the present work: artifacts that may result from interactions between cells and glass coverslips might be studied by careful control and variation of the suspension thickness. Alternately, the degree of isolation between the cells and the glass might be affected by applying thin coatings of silicone or other biologically inert and immiscible materials to the glass. The rate of ice growth in the extracellular environment, which is related to cooling rate, supercooling and thermal gradients in the surface of the viewing window, may be the primary parameter in internal freezing, underlying the observed supercooling and cooling rate effects. Isolation of the ice growth effects to the extent allowed by the physics of the problem promises interesting results. Initial work along these lines has been discussed recently by Scheiwe and Körber. The intracellular events immediately following external ice propagation are not clear in stopped or slow frame video. Strobed photo-

micrography at greater than 100 frames/second would provide a clearer view of these events and could lead to an understanding of the detailed mechanisms and dynamics of internal freezing.

Future analytical work is required to incorporate CPA effects into the distributed freezing model. Another promising study is the prediction and test of 'optimal' cooling protocols for a given cell population. Some of the groundwork for this has been discussed previously [71].

APPENDIX A

DISTRIBUTION OF A FUNCTION OF RANDOM VARIABLES

The distribution of a function of several random variables such as $\alpha = K_{PR}A/N_{wi}$ can be found by a reversible transformation of random vectors [47, Appendix 2A]. The vector \underline{y} , containing functions whose distributions are required, is defined in terms of the vector \underline{x} , whose probability density functions are known:

$$\underline{y} \equiv \underline{f}(\underline{x}) \tag{A.1}$$

A reversible transformation exists if another set of functions \underline{g} can be found such that:

$$\underline{x} = \underline{g}(\underline{y}) = \underline{g}(\underline{f}(\underline{x})) \tag{A.2}$$

If the partial derivatives $\partial f_i/\partial x_j$ and $\partial g_i/\partial y_j$ exist for all i and j , then the $p_{\underline{y}}$'s can be related to the $p_{\underline{x}}$'s.

The cumulative probability, $F_{\underline{y}}$, is obtained first:

$$F_{\underline{y}}(\underline{\beta}) = \int_I p_{\underline{x}}(\underline{\alpha}) d\underline{\alpha} \tag{A.3}$$

The region of integration is given by:

$$I = \{ \underline{\alpha} : f_1(\underline{\alpha}) \leq \beta_1, f_2(\underline{\alpha}) \leq \beta_2 \dots f_K(\underline{\alpha}) \leq \beta_K \} \tag{A.4}$$

This is simplified by the change of variables:

$$\underline{\gamma} = \underline{f}(\underline{\alpha}) \quad (\text{A.5})$$

$$\underline{\alpha} = \underline{g}(\underline{\gamma}) \quad (\text{A.6})$$

Equation (A.3) becomes:

$$F_{\underline{\gamma}}(\underline{\beta}) = \int_{-\infty}^{\beta_1} \int_{-\infty}^{\beta_2} \cdots \int_{-\infty}^{\beta_K} p_{\underline{x}}[\underline{g}(\underline{\gamma})] |J_g(\underline{\gamma})| d\underline{\gamma} \quad (\text{A.7})$$

The Jacobian of the transformation of Eqs. (A.5) and (A.6) is defined as:

$$J_g(\underline{\gamma}) = \begin{vmatrix} J_{11} & J_{12} & \cdots & J_{1K} \\ J_{21} & J_{22} & \cdots & J_{2K} \\ \vdots & \vdots & \ddots & \vdots \\ J_{K1} & J_{K2} & \cdots & J_{KK} \end{vmatrix} \quad (\text{A.8})$$

The J's are calculated using:

$$J_{ij} = \frac{\partial g_i(\underline{\gamma})}{\partial \gamma_j} \quad \begin{array}{l} i = 1, 2, \dots, K \\ j = 1, 2, \dots, K \end{array} \quad (\text{A.9})$$

For a particular β , β_ℓ , the probability of Eq. (A.7) becomes:

$$F_{\underline{\gamma}^\ell}(\beta_\ell) = \int_{-\infty}^{\infty} \int_{-\infty}^{\infty} \cdots \int_{-\infty}^{\beta_\ell} \cdots \int_{-\infty}^{\infty} p_{\underline{x}}[\underline{g}(\underline{\gamma})] |J_g(\underline{\gamma})| d\underline{\gamma} \quad (\text{A.10})$$

The distribution function of the ℓ^{th} y , $p_{y\ell}$ is found by differentiating Eq. (A.10) with respect to β_ℓ :

$$\begin{aligned}
 p_{y\ell}(\beta_\ell) &= \frac{d}{d\beta_\ell} [F_{y\ell}(\beta_\ell)] \\
 &= \int_{-\infty}^{\infty} \int_{-\infty}^{\infty} \cdots \int_{-\infty}^{\infty} p_{\underline{x}} [g(\gamma_1, \gamma_2 \cdots \gamma_{\ell-1}, \gamma_\ell = \beta_\ell, \gamma_{\ell+1} \cdots \gamma_K) \\
 &\quad \cdot |J_g(\underline{\gamma})| d\gamma_1 d\gamma_2 \cdots d\gamma_{\ell-1}, d\gamma_{\ell+1} \cdots d\gamma_K
 \end{aligned}
 \tag{A.11}$$

For the function $y_3 = x_1 x_3 / x_2$, p_{y_3} is desired and $p_{\underline{x}}$'s are Gaussians:

$$p_{x_i} = \frac{1}{\sqrt{2\pi} S_{x_i}} e^{-\frac{(x_i - \bar{x}_i)^2}{2S_{x_i}^2}}
 \tag{A.12}$$

The functions \underline{y} and \underline{x} of Eqs. (A.1) and (A.2) become:

$$\begin{aligned}
 y_1 &= f_1(x_1, x_2, x_3) = x_1 \\
 y_2 &= f_2(x_1, x_2, x_3) = x_2 \\
 y_3 &= f_3(x_1, x_2, x_3) = \frac{x_1 x_3}{x_2}
 \end{aligned}
 \tag{A.13}$$

$$\begin{aligned}x_1 &= g_1(y_1, y_2, y_3) = y_1 \\x_2 &= g_2(y_1, y_2, y_3) = y_2 \\x_3 &= g_3(y_1, y_2, y_3) = \frac{y_3 y_2}{y_1}\end{aligned}\tag{A.14}$$

The change of variables of Eqs. (A.5) and (A.6) becomes:

$$\begin{aligned}\gamma_1 &= f_1(\underline{\alpha}) = \alpha_1 \\ \gamma_2 &= f_2(\underline{\alpha}) = \alpha_2 \\ \gamma_3 &= f_3(\underline{\alpha}) = \frac{\alpha_3 \alpha_1}{\alpha_2}\end{aligned}\tag{A.15}$$

$$\begin{aligned}\alpha_1 &= g_1(\underline{\gamma}) = \gamma_1 \\ \alpha_2 &= g_2(\underline{\gamma}) = \gamma_2 \\ \alpha_3 &= g_3(\underline{\gamma}) = \frac{\gamma_3 \gamma_2}{\gamma_1}\end{aligned}\tag{A.16}$$

The Jacobian, using Eqs. (A.8) and (A.9), becomes:

$$J_g(\underline{\gamma}) = \begin{vmatrix} 1 & 0 & 0 \\ 0 & 1 & 0 \\ -\frac{\gamma_3 \gamma_2}{\gamma_1^2} & \frac{\gamma_3}{\gamma_1} & \frac{\gamma_2}{\gamma_1} \end{vmatrix} = \frac{\gamma_2}{\gamma_1}\tag{A.17}$$

The probability distribution function for y_3 can now be obtained using Eqs. (A.11), (A.12) and (A.17):

$$p_{y_3}(\beta_3) = \int_{-\infty}^{\infty} \int_{-\infty}^{\infty} \frac{1}{\sqrt{(2\pi)^3} S_{x_1} S_{x_2} S_{x_3}} e^{-\left[\frac{(\gamma_1 - \bar{x}_1)^2}{2 S_{x_1}^2} - \frac{(\gamma_2 - \bar{x}_2)^2}{2 S_{x_2}^2} - \frac{\left(\frac{\beta_3 \gamma_2}{\gamma_1} - \bar{x}_3\right)^2}{2 S_{x_3}^2}\right]} \cdot (\gamma_2 / \gamma_1) d\gamma_1 d\gamma_2 \quad (\text{A.18})$$

Equation (A.18) must be integrated over the range of γ_1 and γ_2 for each value of β_3 in order to build the distribution p_{y_3} .

Simple rectangular rule numerical integrations of Eq. (A.18) were performed using Table A.1 values for the contributing distributions: x_1 , x_2 and x_3 . The limits of integration on γ_1 and γ_2 were:

$$(\bar{x}_1 - 4S_{x_1}) \leq \gamma_1 \leq (\bar{x}_1 + 4S_{x_1}) \quad (\text{A.19})$$

$$(\bar{x}_2 - 4S_{x_2}) \leq \gamma_2 \leq (\bar{x}_2 + 4S_{x_2}) \quad (\text{A.20})$$

The moments of the distribution $p_{y_3}(\beta_3)$ are defined by Eqs. (A.21) through (A.23) and can be found easily by numerical integration of p_{y_3} over β_3 :

$$M_0 \equiv \int p_{y_3}(\beta_3) d\beta_3 \rightarrow 1 \quad (\text{A.21})$$

$$M_1 \equiv E(y_3) = \bar{y}_3 = \int \beta_3 p_{y_3}(\beta_3) d\beta_3 \quad (\text{A.22})$$

TABLE A.1
CONTRIBUTING DISTRIBUTION PROPERTIES

VARIABLE , NOTATION		STANDARD		
TEXT	APP. A	MEAN	DEVIATION	UNITS
K_{PR}	x_1	1.45×10^{-11}	$.3 \times 10^{-11}$	$\text{cm}^3/\text{dyne-s}$
A	x_3	135×10^{-8}	16×10^{-8}	cm^2
$N_{Wi} V_W$	x_2	67×10^{-12}	10×10^{-12}	cm^3

$$M_2 \equiv S_{y_3}^2 = E(y_3^2) - E^2(y_3) = \int \beta_3^2 p_{y_3}(\beta_3) d\beta_3 - \bar{y}_3^2 \quad (\text{A.23})$$

The requirement of Eq. (A.21) applies for any probability distribution function. The results of the moment integrations are listed in Table A.2.

An alternate approach for finding the first and second moments of the function y_3 , does not require the density function, p_{y_3} . The relevant definitions are:

$$M_1 = E(y_3) = \bar{y}_3 = \iiint_{-\infty}^{\infty} y_3 p_{x_1} p_{x_2} p_{x_3} dx_1 dx_2 dx_3 \quad (\text{A.24})$$

$$M_2 = S_{y_3}^2 = E(y_3^2) - E^2(y_3) \quad (\text{A.25})$$

$$= \iiint_{-\infty}^{\infty} y_3^2 p_{x_1} p_{x_2} p_{x_3} dx_1 dx_2 dx_3 - \bar{y}_3^2$$

When the x 's are independent, Eqs. (A.24) and (A.25) reduce to

$$\begin{aligned} M_1 = E(y_3) = \bar{y}_3 &= \left(\frac{\bar{x}_1 \bar{x}_3}{x_2} \right) = \bar{x}_1 \bar{x}_3 \left(\frac{\bar{1}}{x_2} \right) \\ &= \bar{x}_1 \bar{x}_3 \left[\int_{-\infty}^{\infty} \frac{1}{x_2} p_{x_2} dx_2 \right] \end{aligned} \quad (\text{A.26})$$

$$M_2 = S_{y_3}^2 = (S_{x_1}^2 + \bar{x}_1^2)(S_{x_3}^2 + \bar{x}_3^2) \left[\int_{-\infty}^{\infty} \left(\frac{1}{x_2} \right)^2 p_{x_2} dx_2 \right] - \left[\bar{x}_1 \bar{x}_3 \left(\frac{1}{x_2} \right) \right]^2 \quad (\text{A.27})$$

A simple numerical integration is required for each of these moments. Results of the integrations are listed in Table A.2 for direct comparison to the moments calculated from the distribution, p_{y_3} .

The probability distribution p_{y_3} , $[p_{\alpha/V_W}]$, is shown in Fig. 2.1 compared to a Gaussian distribution for y_3 , $[\alpha/V_W]$, calculated using the mean and variance from Eqs. (A.26) and (A.27).

TABLE A.2
COMPARISON OF MOMENTS CALCULATED FROM
 p_{y_3} TO VALUES CALCULATED FROM y_3 DIRECTLY

	p_{y_3}	y_3	UNITS
M_0	.9998	1.000	
M_1	2.990×10^{-7}	2.991×10^{-7}	$[\text{cm}^2/\text{dyne-s}]$
M_2	$.7545 \times 10^{-14}$	$.7597 \times 10^{-14}$	$[\text{cm}^2/\text{dyne-s}]^2$

APPENDIX B
APPROXIMATIONS FOR THE FIRST AND SECOND
STATISTICAL MOMENTS OF A FUNCTION OF RANDOM VARIABLES
USING SERIES EXPANSIONS

The mean and variance of a function of random variables can be approximated by expanding the function in a power series around the means of the contributing random variables and performing the defining integrals for M_1 and M_2 term by term [48; p.212]. The general procedure will be illustrated below for functions of three random variables and then applied to the specific case of $g(X,Y,Z) = \frac{XY}{Z}$.

The first step required in expanding $g(X,Y,Z)$ in the vicinity of a point $X = a, Y = b, Z = c$, is to introduce the parameter t [82] such that:

$$\begin{aligned} X &= a + Jt \\ Y &= b + Kt \\ Z &= c + Lt \end{aligned} \tag{B.1}$$

with $0 \leq t \leq 1$.

The function, $G(t) = g(a + Jt, b + Kt, C + Lt)$, can be expanded in a Taylor series around the point $G(0) = g(a,b,c)$:

$$G(t) = G(0) + tG'(0) + \frac{t^2}{2!} G''(0) + \dots + \frac{t^n}{n!} G^{(n)}(0) \tag{B.2}$$

where $G'(t)$ is defined using chain rule as:

$$G'(t) = \frac{\partial G}{\partial X} \frac{dX}{dt} + \frac{\partial G}{\partial Y} \frac{dY}{dt} + \frac{\partial G}{\partial Z} \frac{dZ}{dt} \quad (B.3)$$

while noting that from Eq. (B.1):

$$\frac{dX}{dt} = J$$

$$\frac{dY}{dt} = K \quad (B.4)$$

$$\frac{dZ}{dt} = L$$

The n^{th} derivative of G with respect to t can be written based on Eqs. (B.3) and (B.4) generally as:

$$\frac{d^n}{dt^n} G(t) = \left(J^2 \frac{\partial}{\partial X} + K \frac{\partial}{\partial Y} + L \frac{\partial}{\partial Z} \right)^n g(X,Y,Z) \quad (B.5)$$

The expansion for $g(X,Y,Z)$ can now be obtained by letting $t=1$

$$\begin{aligned} g(X,Y,Z) &= g(a,b,c) + \left(J \frac{\partial g}{\partial X} + K \frac{\partial g}{\partial Y} + L \frac{\partial g}{\partial Z} \right)_{(a,b,c)} \\ &+ \frac{1}{2} \left(J^2 \frac{\partial^2 g}{\partial X^2} + K^2 \frac{\partial^2 g}{\partial Y^2} + L^2 \frac{\partial^2 g}{\partial Z^2} + 2JK \frac{\partial^2 g}{\partial X \partial Y} \right) \end{aligned} \quad (B.6)$$

Cont'd. on p.

$$\begin{aligned}
 & + 2JL \frac{\partial^2 g}{\partial X \partial Z} + 2KL \frac{\partial^2 g}{\partial Y \partial Z})_{(a,b,c)} \\
 & + \dots \frac{1}{n!} \left(J \frac{\partial}{\partial X} + K \frac{\partial}{\partial Y} + L \frac{\partial}{\partial Z} \right)^n g(X,Y,Z)_{(a,b,c)}
 \end{aligned} \tag{B.6}$$

with

$$\begin{aligned}
 J & = X - a \\
 K & = Y - b \\
 L & = Z - c
 \end{aligned} \tag{B.7}$$

The first moment or expectation of $g(X,Y,Z)$ can be obtained through term by term integration of the series in Eq. (B.6) in the integral [see Eq. (A.24)]:

$$M_1 = E(g) = \bar{g} = \int_{-\infty}^{\infty} \int \int g(X,Y,Z) p_{XYZ} dXdYdZ \tag{B.8}$$

where

$$p_{XYZ} = p_X p_Y p_Z ,$$

the joint probability distribution of the random variables X , Y and Z .

The result of the integration, retaining terms through the second derivative in Eq. (B.6) only, is:

$$M_1 = \bar{g} \cong g(a,b,c) + \frac{1}{2} \left(\frac{\partial^2 g}{\partial X^2} S_X^2 + \frac{\partial^2 g}{\partial Y^2} S_Y^2 + \frac{\partial^2 g}{\partial Z^2} S_Z^2 \right)_{(a,b,c)} \tag{B.9}$$

The variance of g can be estimated using the above result for the mean of g by applying the definition:

$$M_2 = S_g^2 = E(g^2) - E^2(g) \quad (B.10)$$

The expectation of $g^2(X,Y,Z)$ can be found by applying the substitution:

$$g^*(X,Y,Z) = g^2(X,Y,Z) \quad (B.11)$$

Equation (B.9) can now be applied directly for g^* :

$$(\bar{g}^*) = g^*(a,b,c) + \frac{1}{2} \left(\frac{\partial^2 g^*}{\partial X^2} S_X^2 + \frac{\partial^2 g^*}{\partial Y^2} S_Y^2 + \frac{\partial^2 g^*}{\partial Z^2} S_Z^2 \right) (a,b,c) \quad (B.12)$$

The partial derivatives of Eq. (B.12) must be expanded using Eq. (B.11) and the chain rule. The X derivative is:

$$\frac{\partial^2 g^*}{\partial X^2} = 2 \left(\frac{\partial g}{\partial X} \right)^2 + 2g \frac{\partial^2 g}{\partial X^2} \quad (B.13)$$

Similar expansions result for the Y and Z partials in Eq. (B.12). The first term of Eq. (B.10) can now be obtained by writing Eq. (B.12) in terms of g using Eqs. (B.11) and (B.13):

$$\begin{aligned} E(g^2) = (\bar{g}^2) &= g^2(a,b,c) + S_X^2 \left(g \frac{\partial^2 g}{\partial X^2} + \left(\frac{\partial g}{\partial X} \right)^2 \right) \\ &+ S_Y^2 \left(g \frac{\partial^2 g}{\partial Y^2} + \left(\frac{\partial g}{\partial Y} \right)^2 \right) \\ &+ S_Z^2 \left(g \frac{\partial^2 g}{\partial Z^2} + \left(\frac{\partial g}{\partial Z} \right)^2 \right) \Big|_{(a,b,c)} \end{aligned} \quad (B.14)$$

The second term in Eq. (B.10) is found by squaring Eq. (B.9) and deleting higher order terms:

$$E^2(g) = \bar{g}^2 = g^2(a,b,c) + g \frac{\partial^2 g}{\partial X^2} S_X^2 + g \frac{\partial^2 g}{\partial Y^2} S_Y^2 + g \frac{\partial^2 g}{\partial Z^2} S_Z^2 \Big|_{(a,b,c)} \quad (B.15)$$

Equations (B.14) and (B.15) combine to give M_2 in Eq. (B.10):

$$M_2 = S_g^2 = S_X^2 \left(\frac{\partial g}{\partial X} \right)^2 + S_Y^2 \left(\frac{\partial g}{\partial Y} \right)^2 + S_Z^2 \left(\frac{\partial g}{\partial Z} \right)^2 \Big|_{(a,b,c)} \quad (B.16)$$

For the specific function, $g(X,Y,Z) = \frac{XY}{Z}$, Eqs. (B.9) and (B.16) become:

$$M_1 = \bar{g} = \frac{\bar{X}\bar{Y}}{\bar{Z}} + \frac{\bar{X}\bar{Y}}{\bar{Z}^3} S_Z^2 \quad (B.17)$$

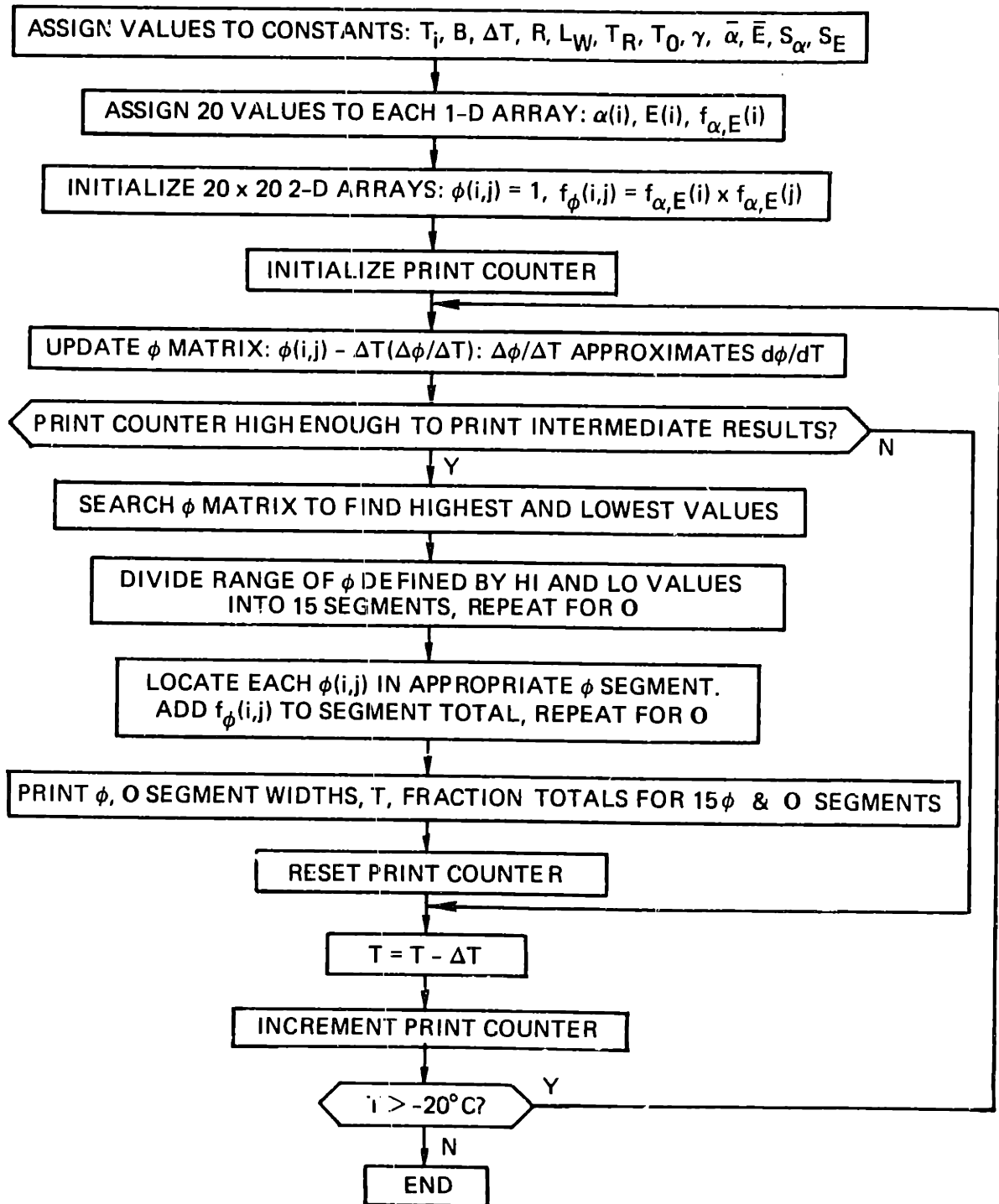
$$M_2 = S_g^2 = S_X^2 \left(\frac{\bar{Y}}{\bar{Z}} \right)^2 + S_Y^2 \left(\frac{\bar{X}}{\bar{Z}} \right)^2 + S_Z^2 \left(\frac{\bar{X}\bar{Y}}{\bar{Z}^2} \right)^2 \quad (B.18)$$

with

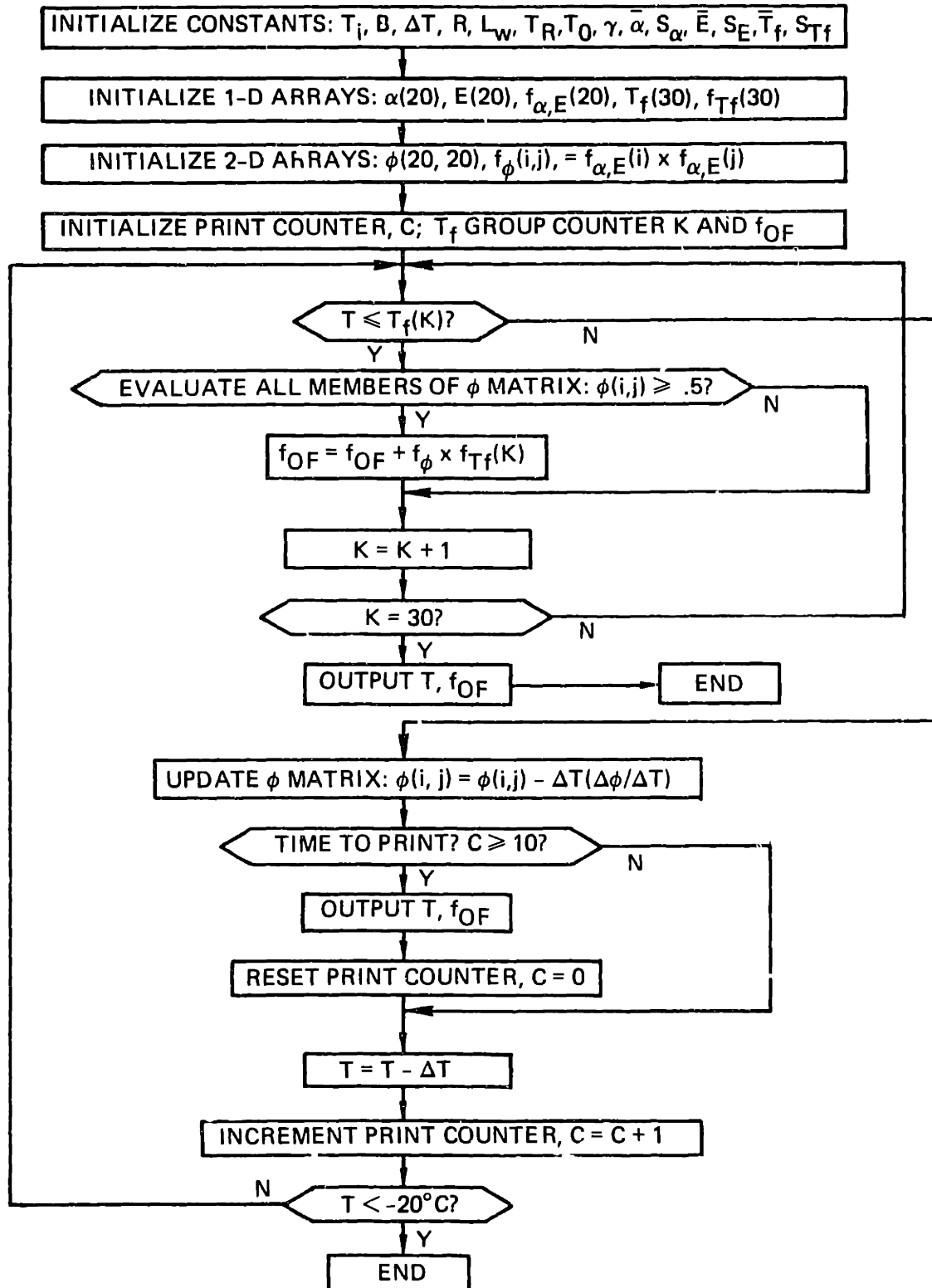
$$\begin{aligned} \bar{X} &= a \\ \bar{Y} &= b \\ \bar{Z} &= c \end{aligned} \quad (B.19)$$

Table A.1 values of \bar{X} , \bar{Y} , \bar{Z} , S_X , S_Y , S_Z for the RBC give $M_1 = 2.987$ and $M_2 = .6754$.

APPENDIX C FLOWCHART FOR DISTRIBUTED WATER TRANSPORT ANALYSIS



APPENDIX D FLOWCHART OF ALGORITHM FOR FINDING FRACTION OF CELLS THAT UNDERGO OBSERVABLE INTERNAL FREEZING



APPENDIX E
VIDEO INTERFACE

The primary method for noting the temperatures at which events occur in the microscope field of view is the chart recorder event marker. The recorder, a Hewlett Packard model 7100B with model 17502A thermocouple input module, draws a small mark at the edge of the chart when a footswitch is depressed or released. When thermal protocols involve temperature change rates on the order of 1000 K/min, the reaction time of the observer can introduce significant error between the temperature marked and the actual temperature at which an event occurs. A simple experiment was devised to measure observer reaction time using the same seating position and footswitch as that used during cryomicroscope studies. An assistant behind the observer closes switch 1 in Fig. E.1 causing the voltage across the resistor to go from zero to about 4 volts while lighting the diode. Releasing the foot pedal interrupts the current flow, and the measured voltage drops back to zero. The delay time is obtained directly from the screen of a storage oscilloscope. These times are listed in Table E.1 for 6 subjects including the author. Delay times of the order of .25 s result in systematic errors of ~4 K at temperature change rates of 1000 K/min with uncertainty of ~.5 K.

This source of temperature uncertainty can be removed by superimposing temperature information frame-by-frame on videotape during cryomicroscope investigations. Obvious advantages of this approach include relieving

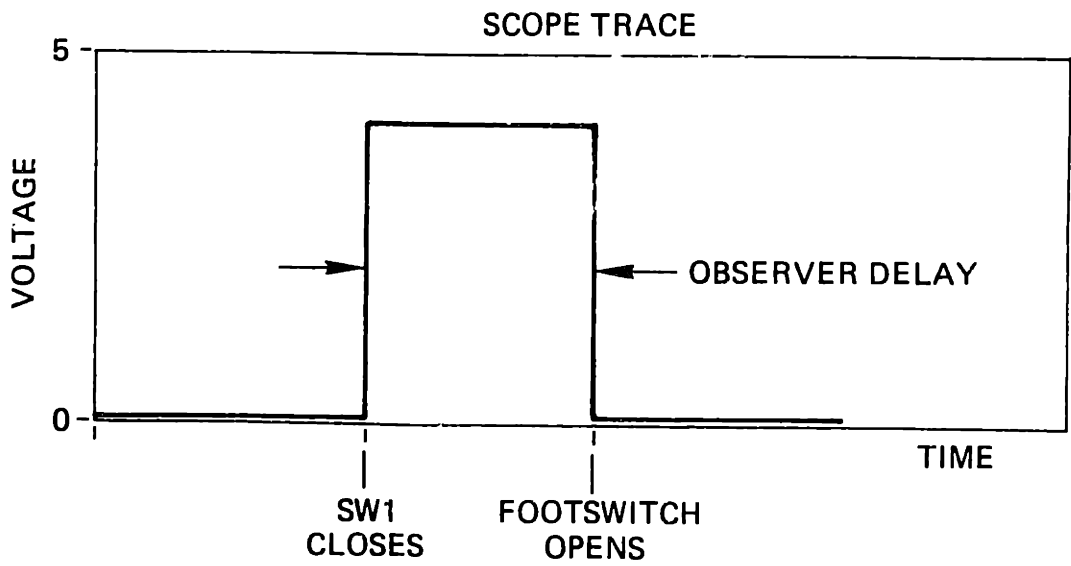
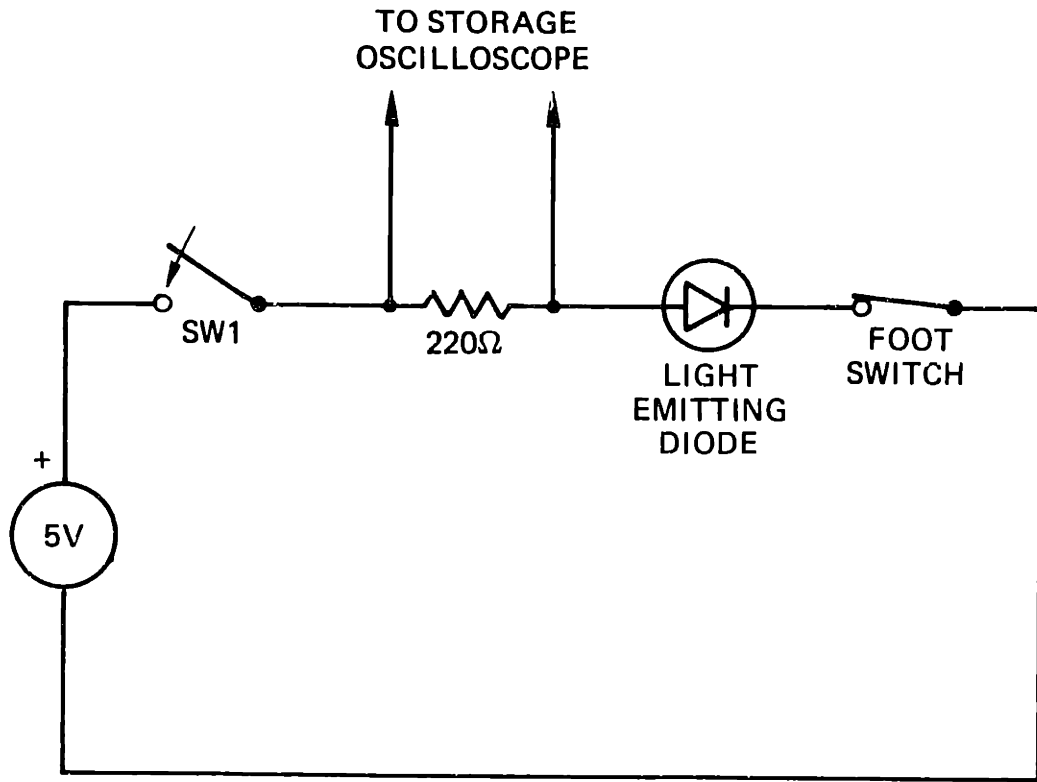


FIGURE E.1 Observer reaction time measurement

TABLE E.1

OBSERVER REACTION TIME MEASUREMENTS

SUBJECT	TIME \pm	STANDARD DEVIATION [SEC]	NO. TRIALS
1	.25	.03	50
2	.26	.04	25
3	.27	.05	20
4	.25	.04	25
5	.23	.01	9
6	.23	.03	25

the observer of a difficult task and streamlining data reduction and interpretation.

Hardware to superimpose temperature information on a video camera signal was designed and built by M.I.T. undergraduate electrical engineers Bob Schaefer and John English [70]. Later, a laboratory version of the instrument was constructed by Schaefer and the author. The system inputs include the camera video signal, horizontal and vertical sync signals, field counter reset, as well as amplified Type T (copper-constantan) thermocouple voltage corresponding to temperatures between 123.1 and 323.1 K. System output is the camera signal with 16 characters superimposed in the format $T = \text{ttt.t K}$; $F = \text{fffff}$. Since each video field has a duration of $\sim 1/60$ s, the 5-digit field counter provides ~ 28 minutes of timing before rolling over to 0 and starting again. Provisions are made internally to allow adjustment of the horizontal and vertical positions, and width of the displayed characters. A block diagram of the system is shown in Fig. E.2. The signal from the thermocouple amplifier, which ranges from 0 to 10 volts corresponding to the -200 to $+200^\circ\text{C}$ temperature range, is multiplied by a gain of 2.175 and offset by -3.919 v in the analog conditioner. The Analog Devices AD574 analog-to-digital converter is thus supplied with a 0 to 10 v input corresponding to 123.1 to 323.1 K. A conversion is initiated at the beginning of each field by the vertical sync pulse from the camera and is completed in sufficient time to update the temperature displayed in that field. The most significant 11 bits from the A/D converter, providing a resolution of $200 \text{ K}/2^{11}$

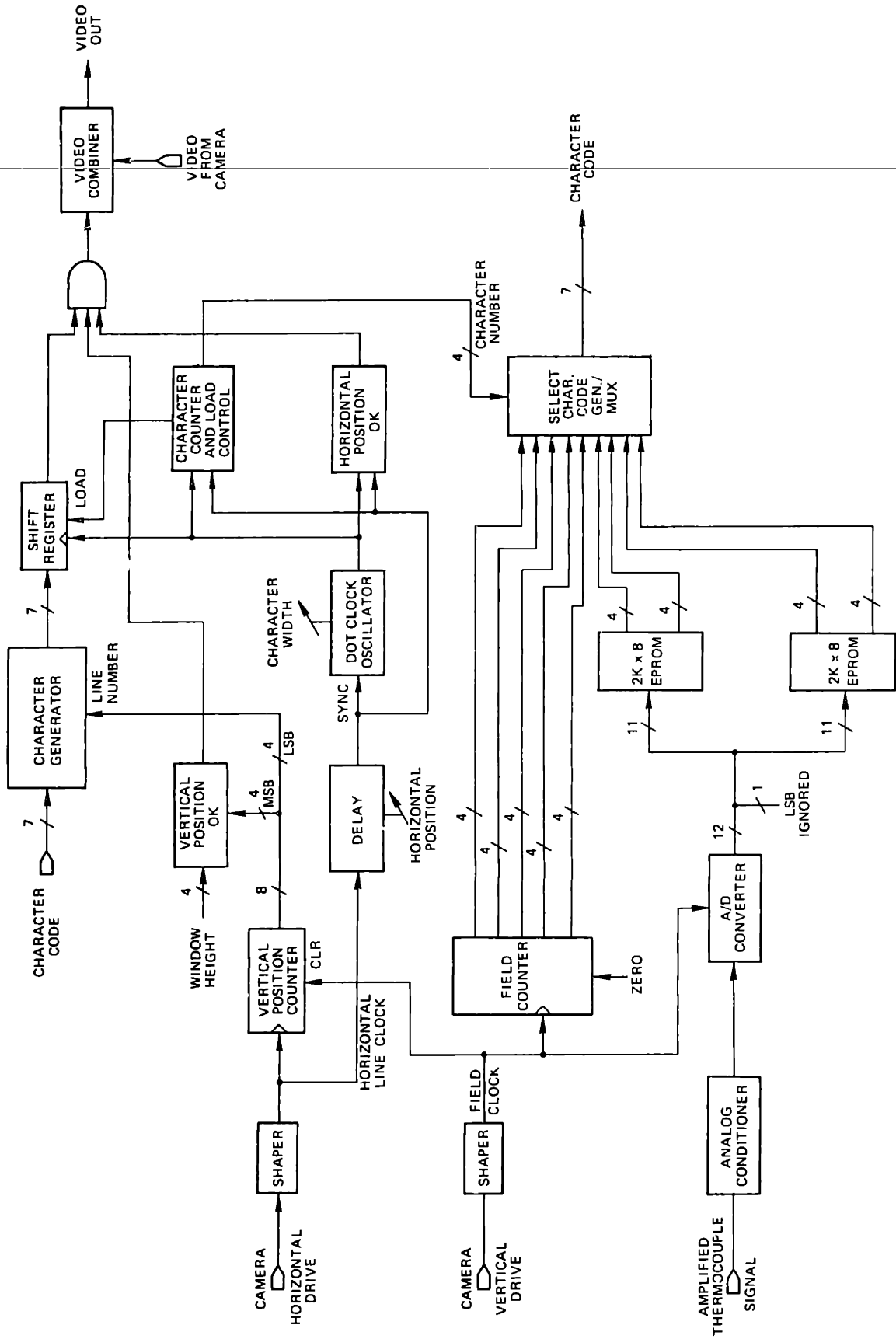


FIGURE E.2 Block diagram of video interface

or $\sim .1$ K, are used to address 2 $2K \times 8$ EPROM's. The EPROM's supply 4 4-bit binary coded decimal outputs corresponding to the 4 Kelvin temperature digits for each 11 bit address. Thermocouple linearization is performed by programming the EPROMs with exact temperatures at the 41 points listed in Table E.2 from the Omega type T thermocouple table [83], and with linearly interpolated temperatures for the (2048-41) points lying between the exact points. The maximum error resulting from this 40 segment piecewise linear approximation of the thermocouple behavior is less than the .1 K resolution of the A/D converter and temperature display. Five BCD digits from the 5 decade field counter, in addition to the 4 Kelvin digits, comprise the variable inputs to the character code generator-multiplexer. The multiplexer outputs seven bit ASCII code for the one-of-16 letters, punctuation symbols or variable digits specified by the 4-bit character number to the character generator, a Motorola MCM66710P ROM. This unit outputs 7 parallel bits for each of the nine lines of the characters to the shift register, which provides the 7 bits to a 3-input AND gate serially, at the 5-6.7 MHz dot clock rate. The AND gate only allows the character dots to be combined with the video signal during a window whose vertical extent is determined by the vertical position counter and O.K. vertical position circuits and whose horizontal extent is determined by the delay and O.K. horizontal position circuits.

A readable reference on video character generation is the SAMs publication: TV TYPEWRITER COOKBOOK [84].

TABLE E.2
THERMOCOUPLE LINEARIZATION END POINTS

<u>POINT</u>	<u>THERMOCOUPLE MILLIVOLTS WRT REF. AT 0°C</u>	<u>TEMP. [K]</u>
1	-4.648	123.1
2	-4.535	128.1
3	-4.419	133.1
4	-4.299	138.1
5	-4.177	143.1
6	-4.051	148.1
7	-3.923	153.1
8	-3.791	158.1
9	-3.656	163.1
10	-3.519	168.1
11	-3.378	173.1
12	-3.235	178.1
13	-3.089	183.1
14	-2.939	188.1
15	-2.788	193.1
16	-2.633	198.1
17	-2.475	203.1
18	-2.315	208.1
19	-2.152	213.1
20	-1.987	218.1
21	-1.819	223.1
22	-1.648	228.1
23	-1.475	233.1
24	-1.299	238.1
25	-1.121	243.1
26	-.940	248.1
27	-.757	253.1
28	-.571	258.1
29	-.383	263.1
30	-.193	268.1
31	0.000	273.1
32	.195	278.1
33	.391	283.1
34	.589	288.1
35	.789	293.1
36	.992	298.1
37	1.196	303.1
38	1.403	308.1
39	1.611	313.1
40	1.822	318.1
41	2.035	323.1

APPENDIX F
SUPERCOOLING CONTROLLER

Ice formation in the medium surrounding cells cooled on the cryo-microscope can occur after as much as 20°C supercooling. Some control of the degree of supercooling can be obtained by varying the position of the cell suspension and coverslip. This results from the temperature distribution in the viewing window surface; off-center positioning of the coverslip allows nucleation at the sample edge by substantially colder sections of the window. This effect could probably be calibrated for a range of thermal conditions and used to predetermine the supercooling.

An alternate approach for controlling external supercooling as an experimental variable is to induce nucleation at the proper time. A device which performs this task is shown schematically in Fig. F.1. Liquid nitrogen is self-pressurized in a small dewar and flows out when the control circuitry opens the solenoid valve. A small bolus of LN₂ strikes the edge of the coverslip and triggers nucleation with rapid ice formation throughout the suspension.

The electronic control circuitry is shown in Fig. F.2. The firing voltage is set on a 20 K Ω multiturn potentiometer. When the voltage from the thermocouple amplifier drops below the firing voltage, the first op-amp swings high. Voltage, v_1 , also swings high because the 100 μ F capacitor needs time to change its state of charge. The voltage,

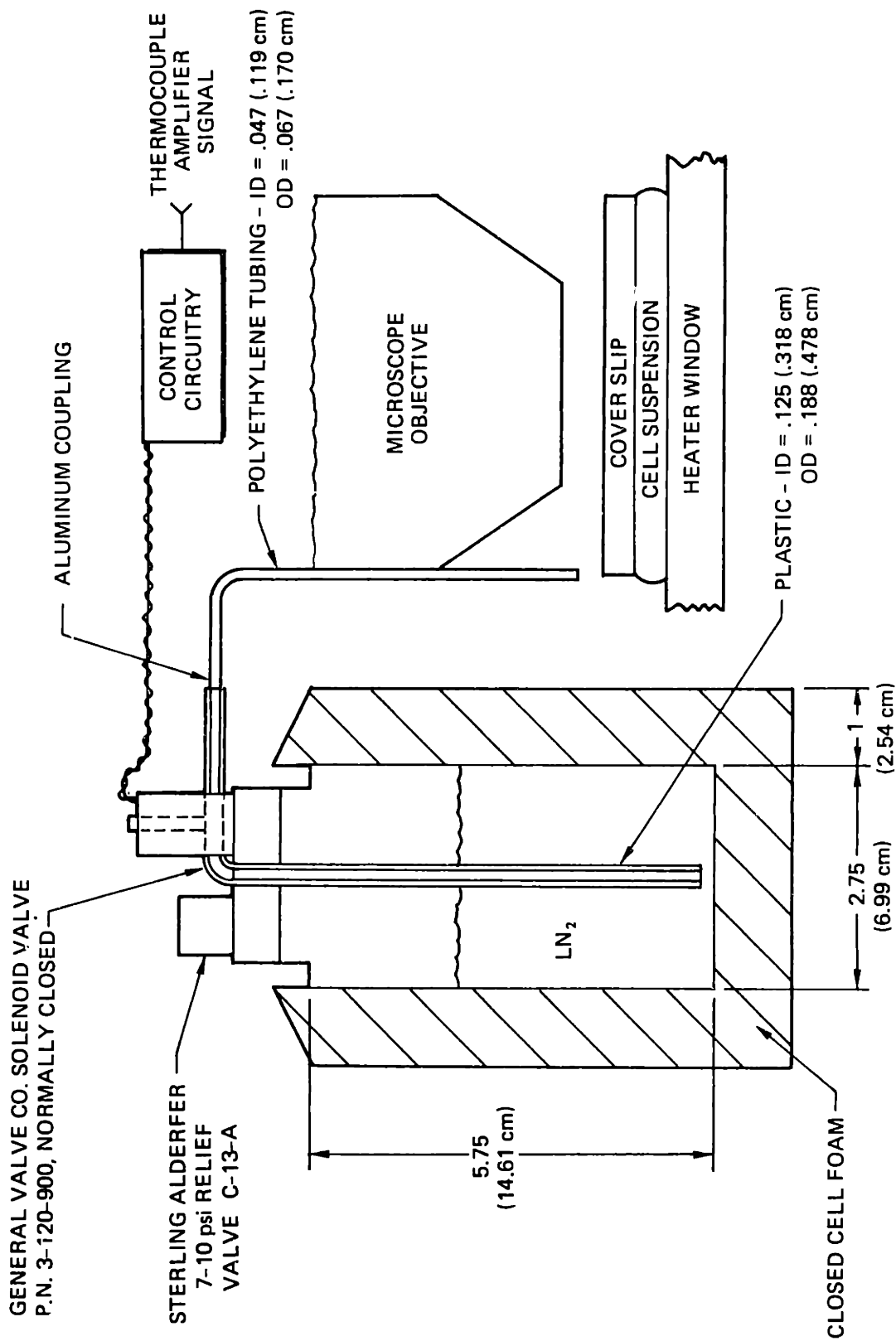


FIGURE F.1 Extracellular supercooling controller

v_1 , drops as C_1 charges following the function:

$$v_1 = 15e^{-\left(\frac{1}{R_1 C_1}\right)t} \quad (F.1)$$

The second op-amp also swings high when v_1 goes high and stays high until v_1 drops below the pulse period voltage, which can be adjusted on a 20 K Ω multiturn pot. The output of the second op-amp is divided in half and is used to drive a Darlington transistor pair which supplies the solenoid operating current. The pulse period is described by Eq. (F.2):

$$t_p = -R_1 C_1 \ln[v_F/15] \quad (F.2)$$

Voltages, v_1 and v_2 , are sketched in Fig. F.3. Pulse periods between 0.2 and 0.5 seconds are usually sufficient to induce nucleation.

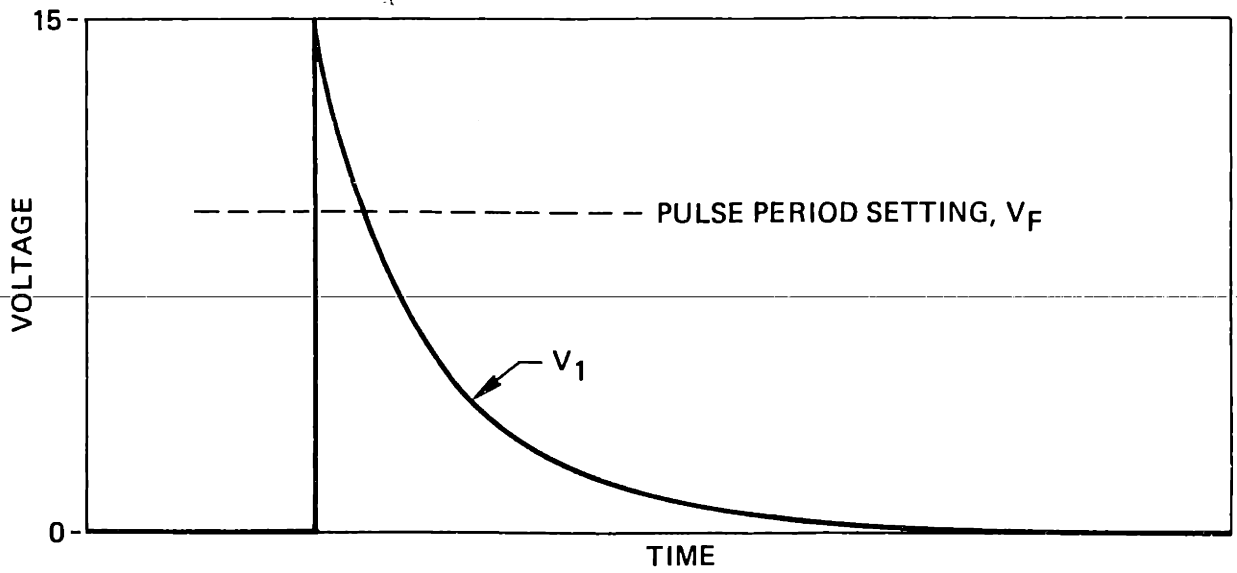
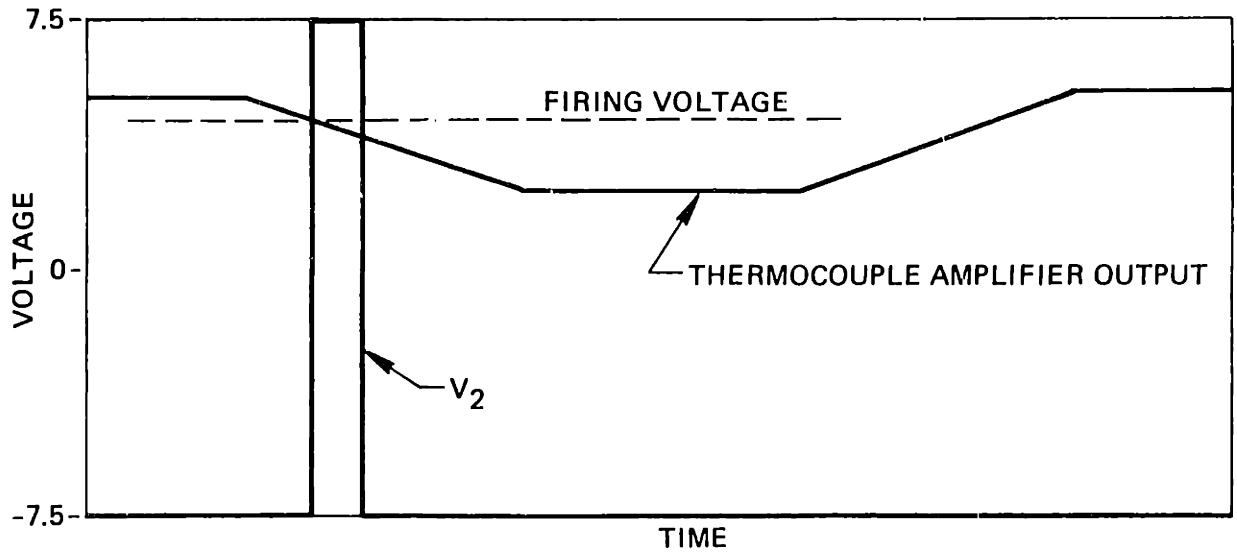


FIGURE F.3 Supercooling controller operating voltages

APPENDIX G
REFERENCE SIGNAL GENERATION

The reference signal generator provides a time-varying voltage analog of the desired thermal protocol. Three references that can be used with the temperature control loop are an analog integrator, a hardwired digital system and a programmable microprocessor system.

The only modifications required to use the analog integrator of Ushiyama [68] are removal of the power amplifier and addition of a lead to carry the reference signal to the new control loop. Initial switch settings should be: #1 on Reset, #2 on Offset Voltage, Integrate on Hold, #3 to Cool, Maximum Limit to I.C., and decade boxes and rotary switches as required to set cooling and warming rates. The voltage output of the initial condition potentiometer can be set with the aid of a digital voltmeter to obtain a proper starting temperature noting that $0^{\circ}\text{C} = 5\text{v}$ and $\Delta v/\Delta T \cong 25 \text{ mv}/^{\circ}\text{C}$ at 0°C . Setting the maximum limit switch to Initial Condition avoids the need to set a final temperature-voltage on the maximum limit potentiometer. The minimum temperature limit potentiometer should always be set for the desired minimum protocol temperatures. To initiate cooling, switches 1 and 2 are thrown to Subs. Activate and the Integrate switch moved from Hold. The temperature ramp stops when the minimum temperature is reached or when Hold is engaged. Linear warming proceeds by switching #3 to Warm and Integrate from Hold. The ramp stops when the Initial Condition is reached. Switches should then be returned to the initial settings starting with Hold.

The hardwired digital reference signal generator was developed to provide thermal protocol flexibility at high instantaneous temperature change rates [72]. In the binary representation chosen, all zeros correspond to -200°C or 0.000 V , and all ones to $+200^{\circ}\text{C}$ or $+10.000\text{ V}$. Ten bit word length gives 2^{10} discrete temperature values over the 400 K range or roughly $.4^{\circ}\text{C}$ resolution. Table G.1 lists binary and voltage equivalents of temperatures from -100°C to $+50^{\circ}\text{C}$ in $\sim 5^{\circ}\text{C}$ increments assuming an ideal, linear thermocouple. Figure G.1 shows the digital system block diagram. Data and addresses are entered on ten toggle switches; five pushbutton switches control the flow of information during programming and output phases of operation. The core of the reference system is the random access memory organized as $1024 (2^{10})$ 10 bit words. A string of words representing a list of temperatures is entered into memory during programming. During the output phase, the word list becomes available sequentially to the control loop through output registers and a digital-to-analog converter. A clock oscillator provides proper timing for the read-out process by controlling the counter, since the counter output is used to address the memory. Additional components in the system provide for stopping the clock automatically when the last memory location is reached, debouncing the switches to prevent erroneous logic signals, and displaying the current memory address and its contents.

Programming involves the following procedures and signal flows: the desired starting address for a protocol (usually 0000000000) is set on the entry switches and loaded into the counter using the load address

TABLE G.1

BINARY AND VOLTAGE EQUIVALENTS OF TEMPERATURE

TEMPERATURE [°C]	BINARY	VOLTAGE
-100.0	0100000000	2.500
- 95.3	0100001100	2.617
- 90.2	0100011001	2.744
- 85.2	0100100110	2.871
- 80.1	0100110011	2.998
- 75.0	0101000000	3.125
- 70.3	0101001100	3.242
- 65.2	0101011001	3.369
- 60.2	0101100110	3.496
- 55.1	0101110011	3.623
- 50.0	0110000000	3.750
- 44.9	0110001101	3.877
- 40.2	0110011001	3.994
- 35.2	0110100110	4.121
- 30.1	0110110011	4.248
- 25.0	0111000000	4.375
- 19.9	0111001101	4.502
- 15.2	0111011001	4.619
- 10.2	0111100110	4.746
- 5.1	0111110011	4.873
0.0	1000000000	5.000
5.1	1000001101	5.127
10.2	1000011010	5.254
15.2	1000100111	5.381
19.9	1000110011	5.498
25.0	1001000000	5.625
30.1	1001001101	5.752
35.2	1001011010	5.879
40.2	1001100111	6.006
44.9	1001110011	6.123
50.0	1010000000	6.250

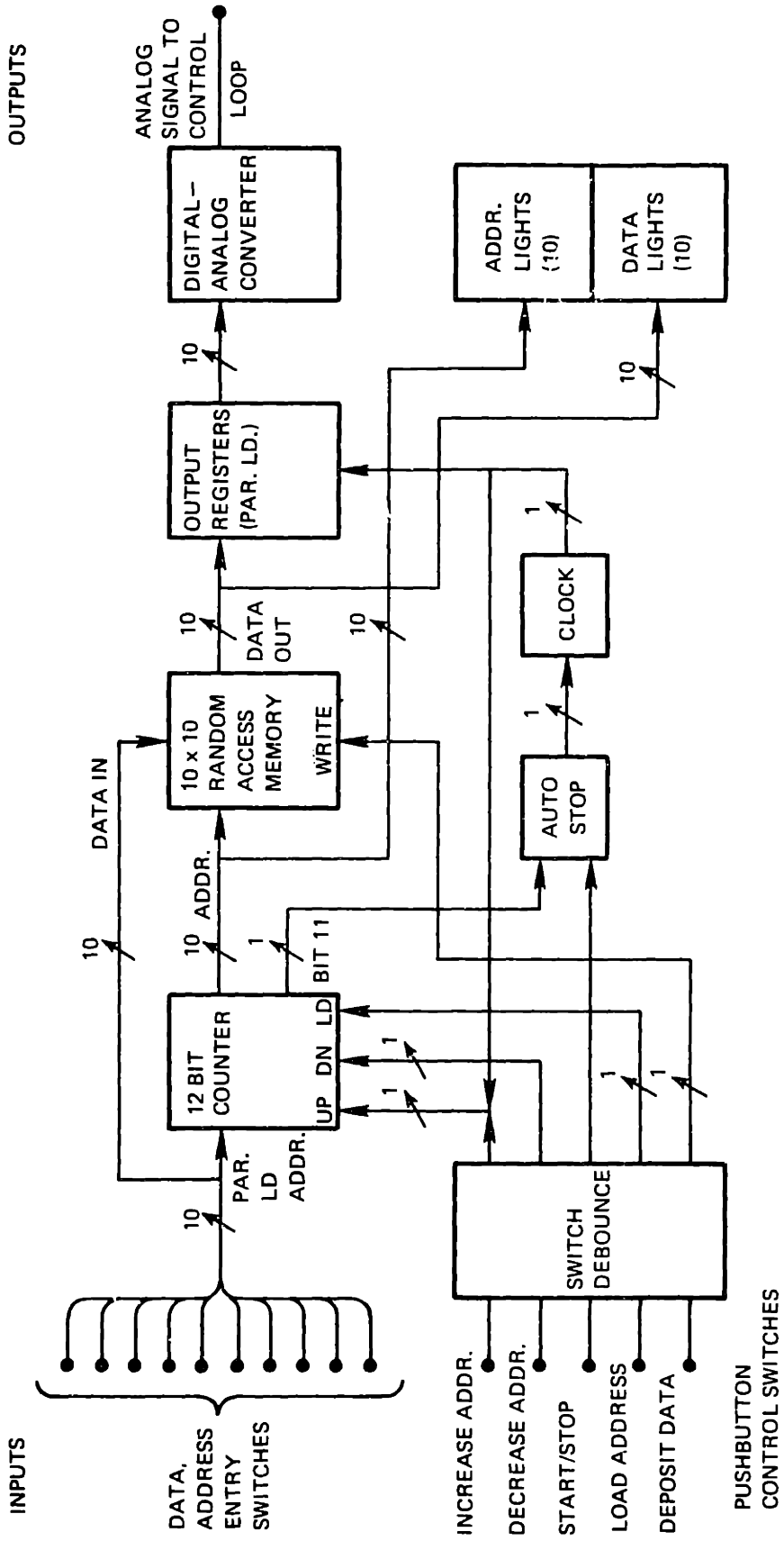


FIGURE G.1 Block diagram of hard-wired digital reference signal generator

pushbutton. This address is now available to the memory and is shown on the address lights. The contents of the address appear on the data lights. If the temperature represented by the 10 bit data word is incorrect, the new word is set on the entry switches and loaded into the same memory location using the deposit data pushbutton. This word now appears on the data lights. The address can be incremented using the increase address pushbutton, allowing the memory to be filled serially.

A thermal protocol is read out of memory to the analog system by the following steps: the starting address must be loaded using the load address switch and the clock started using the start/stop pushbutton. The counter increments on the rising edge of the clock pulse, giving time for the address and memory output to settle before the output registers are loaded on the falling edge of the clock signal. Once the registers are loaded with the contents of the new address, the digital-to-analog converter [DAC] has constant inputs until the next clock falling edge.

The DAC consists of an Analog Devices AD562 12 bit integrated circuit, of which only the 10 most significant bits are used, combined with an AD504 op-amp in a current-to-voltage configuration and a hybrid AD2700 10 volt precision reference. Calibration requires offset and gain trims which are performed by reading an all-zero location to the DAC and adjusting for 0.000 v and then by reading an all ones data word and adjusting for 10.000 v.

The time allotted for each temperature step, and therefore the instantaneous cooling rate, is determined by the clock oscillator which

consists of two 74LS123 monostables with 100 K Ω trimpots and capacitor connection blocks for setting period and duty cycles. The operating envelope of timing resistance and capacitance is shown in Fig. G.2 based on Eq. (G.1) [85]:

$$t_C = .45 R_P C_P \quad (G.1)$$

The clock is set for the required period by following the procedures: choose timing capacitance, C_P , roughly within the operating range; use approximately half of C_P for the duty cycle C_D ; adjust the trimpots with a frequency counter or oscilloscope as reference. Duty cycles of 50% are not necessary for proper system operation. Attainable clock rates of 1 Mhz provide nominal reference signals corresponding to 10⁷ K/min. The current thermal control loop is, of course, incapable of following such signals. A circuit schematic of the hardwired digital reference signal generator is shown in Fig. G.3.

The microprocessor-based reference signal generator utilizes a Tandy Corp. TRS-80 microcomputer with Level II BASIC and a custom interface assembled by Merte [73] and Rollins, Inc. of Lincoln, Massachusetts. The interface includes a multiplexed, 16 channel, 12 bit analog-to-digital converter (Analog Devices RTI-1220), 4 channel, 10 bit DAC (Analog Devices RTI 1221) counter-timer, printer control, and relay driver. A reference signal can be generated by software in conjunction with the counter-timer and one channel of the DAC. A program that performs linear cooling and warming, and constant temperature holds is flowcharted in Fig.

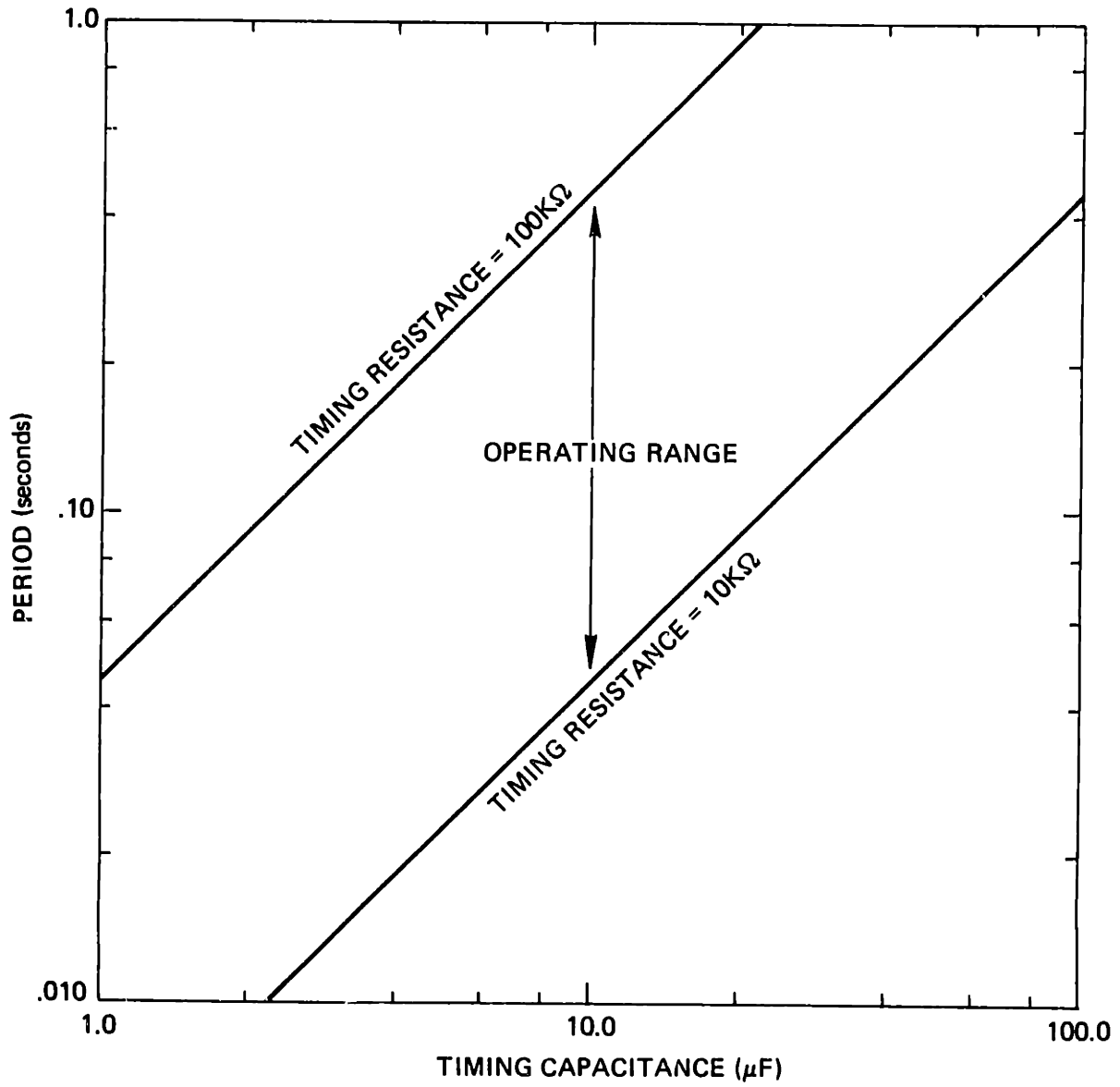


FIGURE G.2 Digital reference clock period dependence on timing resistance and capacitance

G.4. The program starts in a manual mode that allows the user to enter an initial temperature that can be modified easily prior to defining the desired thermal protocol. The conversion of this centigrade temperature to the proper form with output to the DAC is performed by the output voltage subroutine. Although this subroutine was written for an ideal, linear thermocouple, linearizing look-up tables or functions can be used.

Protocols with up to 20 straight segments are next entered serially by segment time and final temperature. The first segment starts at the manual mode initial temperature, $T(0)$ and ends at $T(1)$ within time, $SGTM(1)$. Holds are performed by programming equivalent starting and ending temperatures for a segment. After all of the segments have been keyed in, the program waits for the input "GO" before executing the protocol.

Execution begins by initializing the counters and determining the sign and magnitude of the temperature change for the first segment. The number of $.5^{\circ}\text{C}$ steps, $NSTPS$, that will be used to approximate a linear change between the segment endpoint temperatures is determined next. If $NSTPS$ is zero, a hold is performed for the duration of the first segment, after which the segment count, N , is incremented. The delay subroutine that executes the hold, contains a loop that keeps reading the timers and comparing the elapsed time to the required delay. The time resolution of the entire program is limited by the delay loop execution time of $\sim .1$ s. If $NSTPS$ is greater than or equal to 1, the program calculates the time required for each step, $SPTM$, and enters a loop that alternately

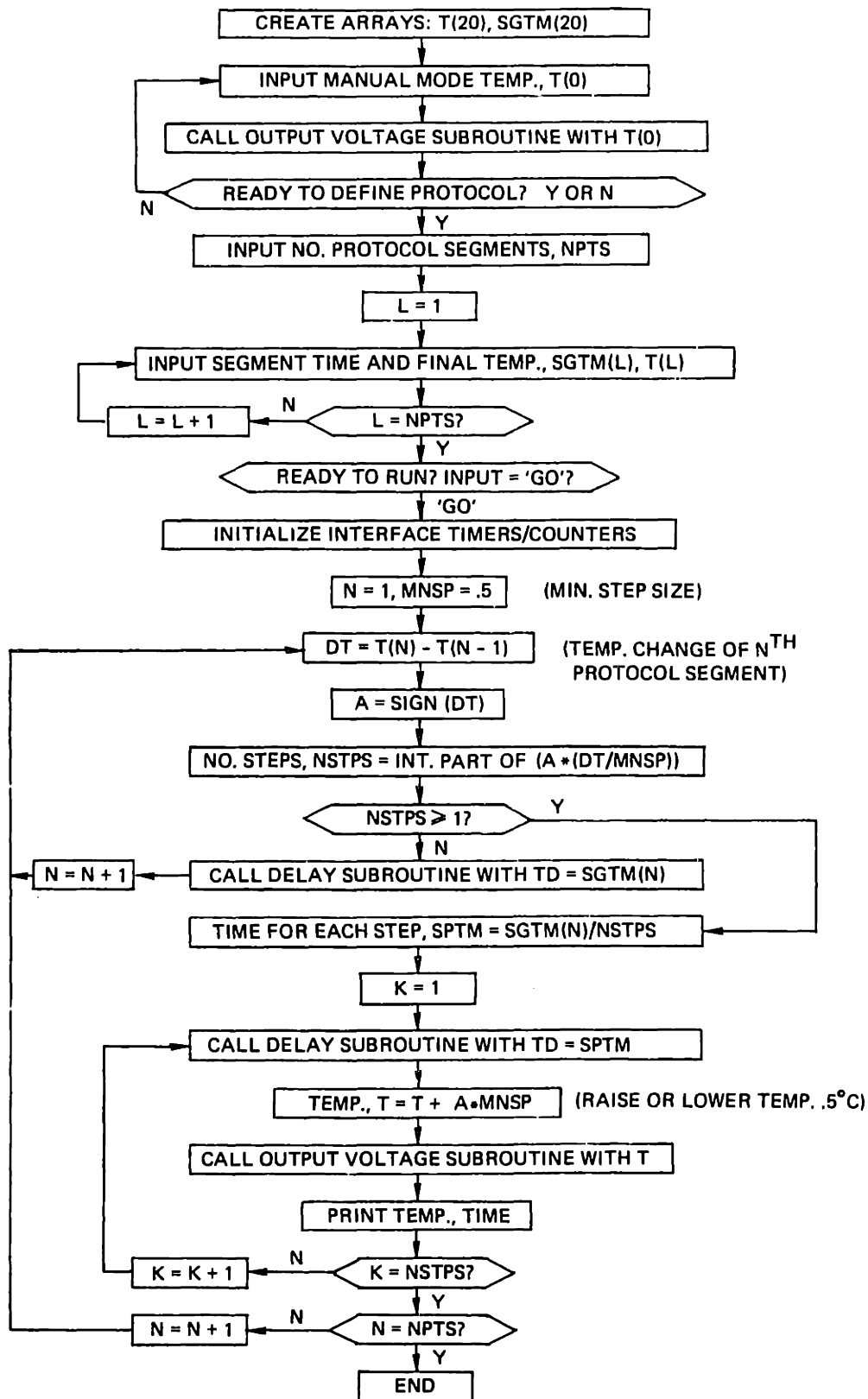


FIGURE G.4 Program flowchart for microcomputer reference signal generation

delays SPTM and outputs the temperature, raised or lowered by the step size. The temperature and time are printed on the monitor during the loop, providing timely progress information. When all NSTPS are executed, the program goes to the next segment while incrementing the segment counter.

The program can be interrupted in mid-stream using the TRS-80 'Break' key, and continued by typing CONT, ENTER. Changes in the program can be made by hitting 'Break' then RUN, ENTER. This starts the program over, allowing entry of a new protocol while the DAC maintains the temperature that had been attained when the Break key was pressed.

Temperature change rates up to about 60°C/min can be executed before timing errors from the delay subroutine become serious.

APPENDIX H

BANDWIDTH REQUIRED FOR THE THERMAL CONTROL SYSTEM

A guideline for the required thermal control system bandwidth can be obtained by considering the offset error illustrated in Fig. H.1, resulting from a ramp-reference input to a second order system. The steady-state offset can be expressed in terms of ramp magnitude, b_R , damping ratio, ζ , and system natural frequency, F_n , which is essentially equivalent to bandwidth [86]:

$$T_E = \frac{b_R \zeta}{\pi F_n \cdot 60} \quad (H.1)$$

The error is shown in Fig. H.2 as a function of bandwidth, with $\zeta = 1$, and temperature change rates of 20,200, and 2000°C/min. The bandwidth must be at least 10 Hz to restrict the error to 1°C or less.

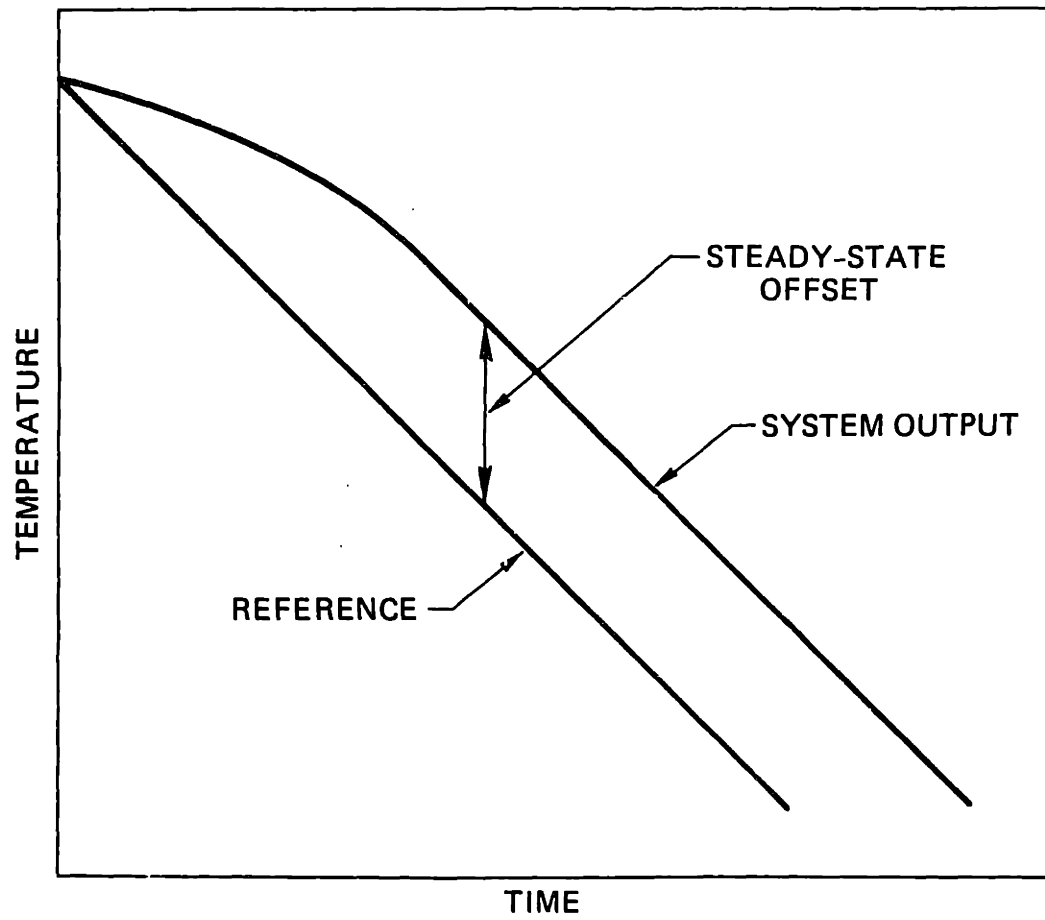


FIGURE H.1 Control system error for a ramp reference input

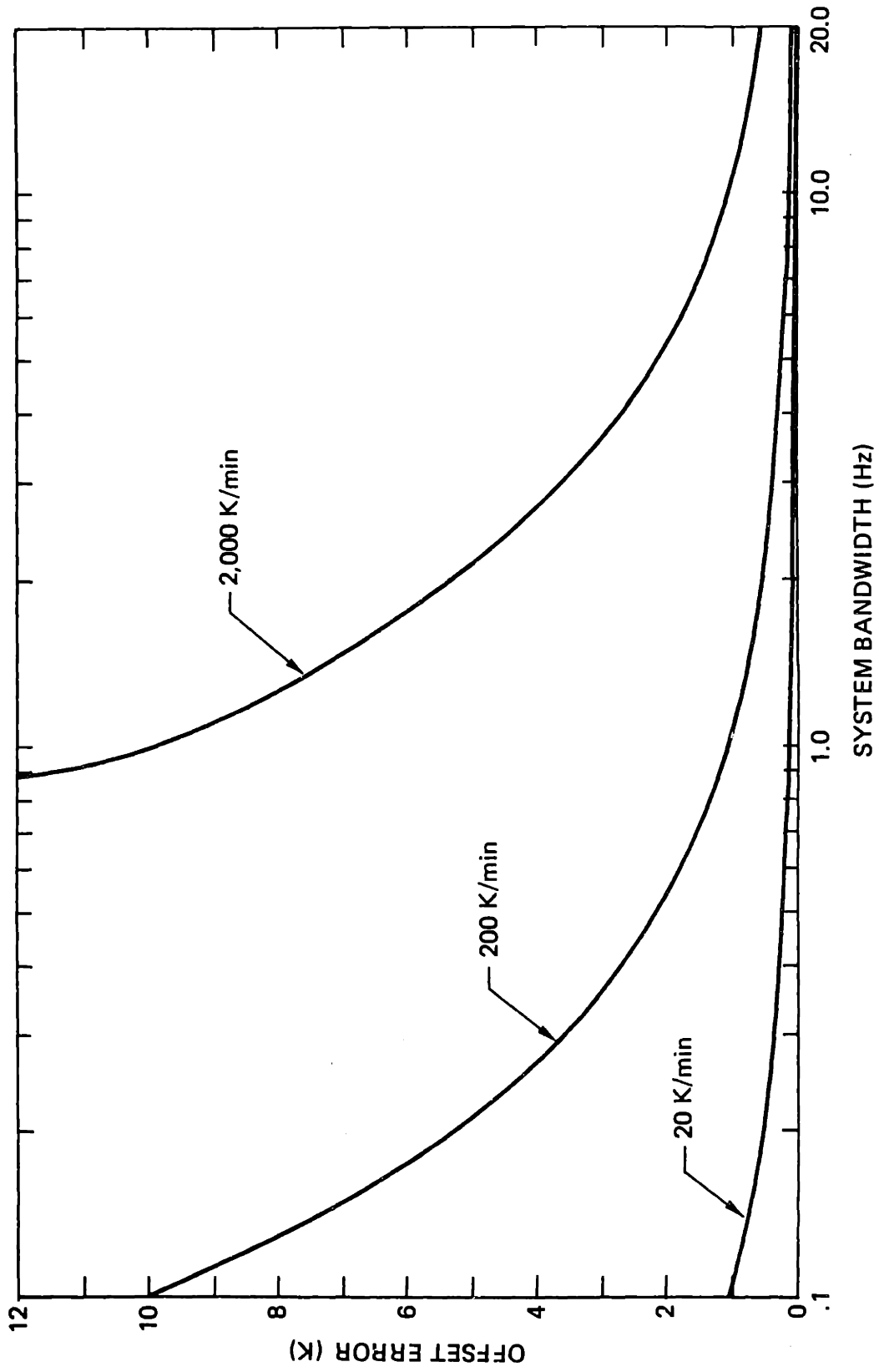


FIGURE H.2 Error for a ramp reference input: dependence on bandwidth and temperature change rate

APPENDIX I
COOLANT SUPPLY

The coolant supply provides dry nitrogen gas at flow rates ranging up to 18 lb/hr with temperatures as low as $\sim -170^{\circ}\text{C}$. The flow path schematic of Fig. I.1 shows the main components including the LN_2 -boil-off source, 0-25 psig regulator, manual control valve, viewing stage, and heat exchanger built by Diller [67]. The stream exhausts into the microscope environmental chamber where it maintains a slight positive pressure and thereby prevents water condensation on the stage. This overall arrangement was particularly convenient at the Cryogenic Engineering Laboratory due to the availability of boil-off from a large LN_2 storage tank.

Since the primary determinants of supply performance are flow rates and steam temperatures as functions of valve and regulator settings, measurements of these quantities were undertaken. Room temperature flows were determined using the parallel combination of a Fischer and Porter 'Flowrator' Tube #B4-21-10/27 with $\frac{1}{2}$ GSUT, 48AT60 float, and a Datametrics Model 800-LM mass flowmeter with model 1000-10K transducer. When flow rates exceeded the maximum of ~ 3.8 SCFM for the F and P rotameter, the additional flow was bypassed to the Datametrics transducer using the valve at the transducer outlet. Dependence of standard volume flow rate, with the control valve fully open, on regulator outlet pressure is shown in Fig. I.2. A representative Reynolds number for the flow based on a rate of 1 SCFM, tubing diameter of $\sim .021$ feet and density and viscosity from Table I.1 at 300 K is shown in Eq. (I.1):

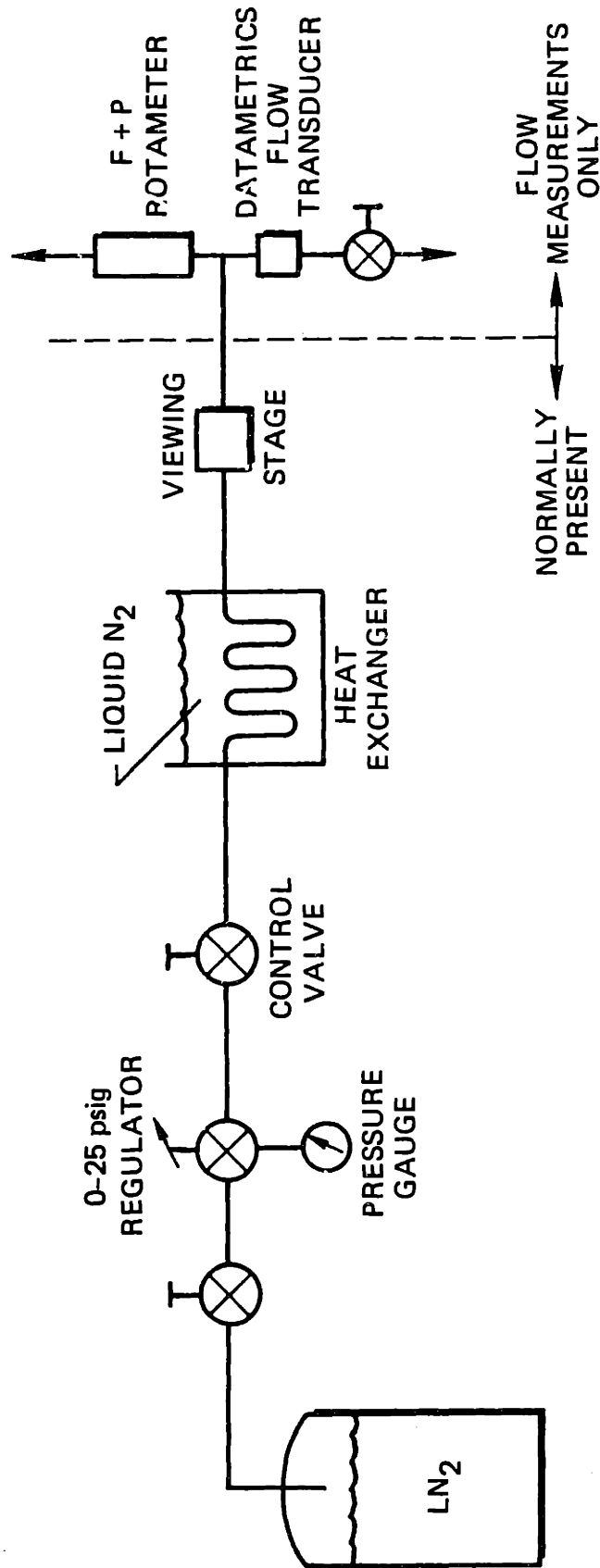


FIGURE I.1 Coolant supply flow schematic

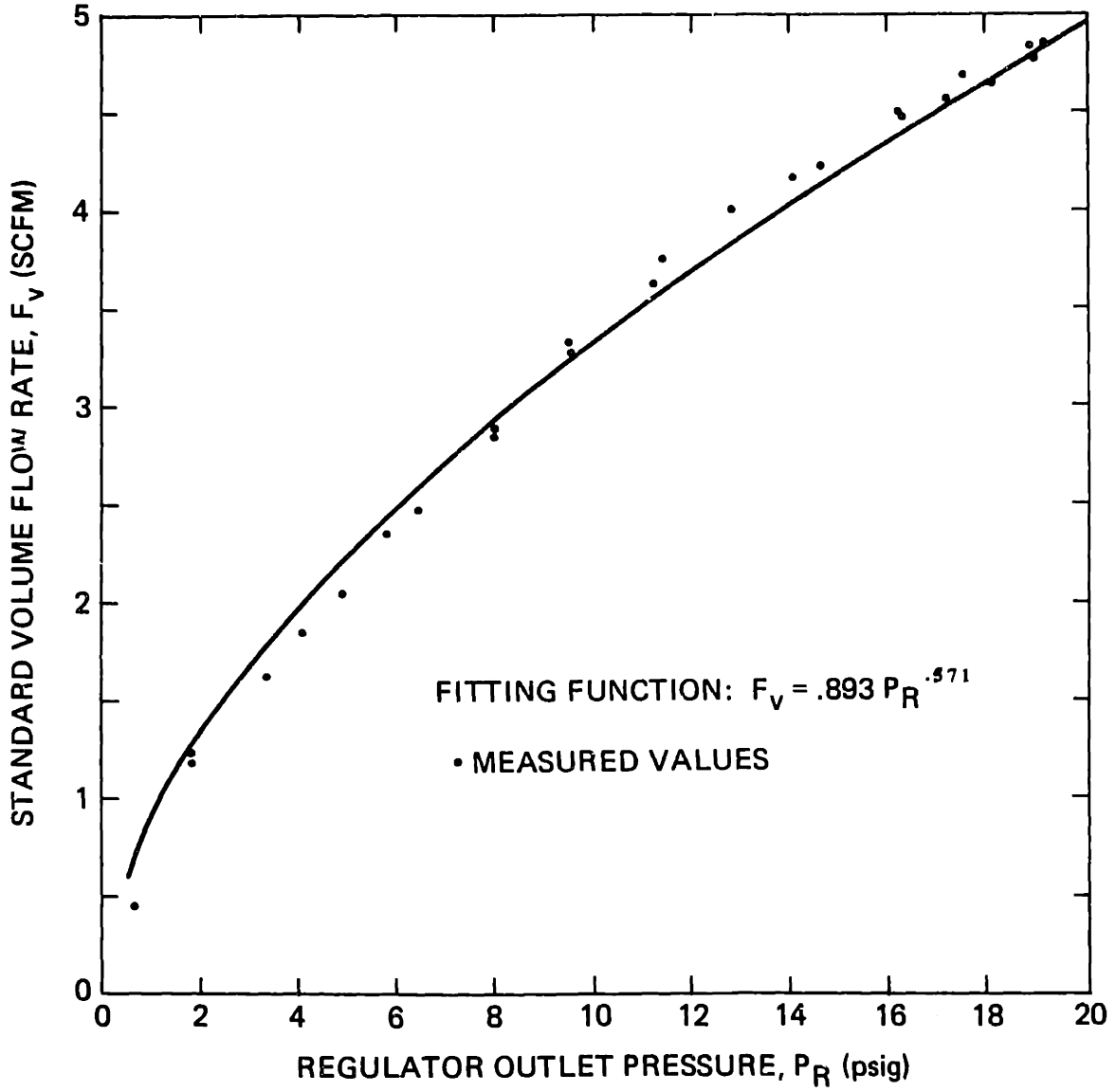


FIGURE I.2 Flow dependence on regulator outlet pressure

TABLE I.1
DENSITIES AND VISCOSITIES
OF NITROGEN GAS BETWEEN 100 and 300 K

T [K]	ρ [lbm/ft ³]	μ [lbm/hrft]	K_s [watt/cm-K]
100	.218	.0166	$.940 \times 10^{-4}$
150	.143	.0244	1.39×10^{-4}
200	.107	.0313	1.82×10^{-4}
250	.0853	.0376	2.23×10^{-4}
300	.0711	.0432	2.61×10^{-4}

$$\begin{aligned}
 \text{Re} &= \frac{\rho V D_F}{\mu} = \frac{4\rho(VA_F)}{\pi \mu D_F} \\
 &= \frac{4(.0711 \frac{\text{lbm}}{\text{ft}^3})(1 \frac{\text{ft}^3}{\text{min}})(60 \frac{\text{min}}{\text{hr}})}{(.0432 \frac{\text{lbm}}{\text{hrft}}) \pi(.021 \text{ ft})} \\
 &= 5980
 \end{aligned} \tag{I.1}$$

Since the laminar-to-turbulent transition occurs around $\text{Re} = 2000$ to 3000 , the coolant stream can, in general, be considered turbulent. The friction factor defined in Eq. (I.2), can be approximated for turbulent flow [87;p.59] as in Eq. (I.3):

$$f \equiv \frac{\Delta P}{4(L/D_F)(\rho V^2/2)} \tag{I.2}$$

$$f \approx \frac{.08}{\text{Re}^{.25}} \tag{I.3}$$

The flow velocity and therefore the volume flow rate can be expressed in terms of the pressure drop by combining Eqs. (I.2) and (I.3) where for room temperature flows, ρ and μ can be lumped in the constant C :

$$F_V = VA_F = C \Delta P^{1/1.75} \tag{I.4}$$

The pressure drop is equal to the regulator outlet, gauge pressure since the stream outlet is at 1 atm. The observed results correlate well with Eq. (I.4) when $C = .893$.

The dependence of volume flow on control valve position is shown in Fig. I.3 for regulator outlet pressures of 5, 10 and 15 psig. The non-dimensional flow rate is defined in Eq. (I.5) where the maximum flows obtained at each pressure are shown in Fig. I.2:

$$\hat{F}_V = \frac{F_V}{F_{Vmax}} \Big|_{P_R} \quad (I.5)$$

The experimental points lie close to the fitting function:

$$\begin{aligned} \hat{F}_V &= .768 \theta_V \quad 0 \leq \theta_V < .875 \\ \hat{F}_V &= 1 - e^{-1.27\theta_V} \quad .875 \leq \theta_V \leq 4.0 \end{aligned} \quad (I.6)$$

Figure I.3 also shows the flow rates obtained with the heat exchanger removed from the flow path for a regulator outlet pressure of 10 psig. These flows were normalized to the maximum flow obtained with the heat exchanger in the path and with $P_R = 10$ psig.

The steady-state stream temperature measured at the inlet to the stage, is shown in Fig. I.4 for mass flows between 3 and 18 lbm/hr. The function of Eq. (I.7) fits the data fairly well:

$$T_a - T_s = 190(1 - e^{-.129\dot{m}'}) \quad (I.7)$$

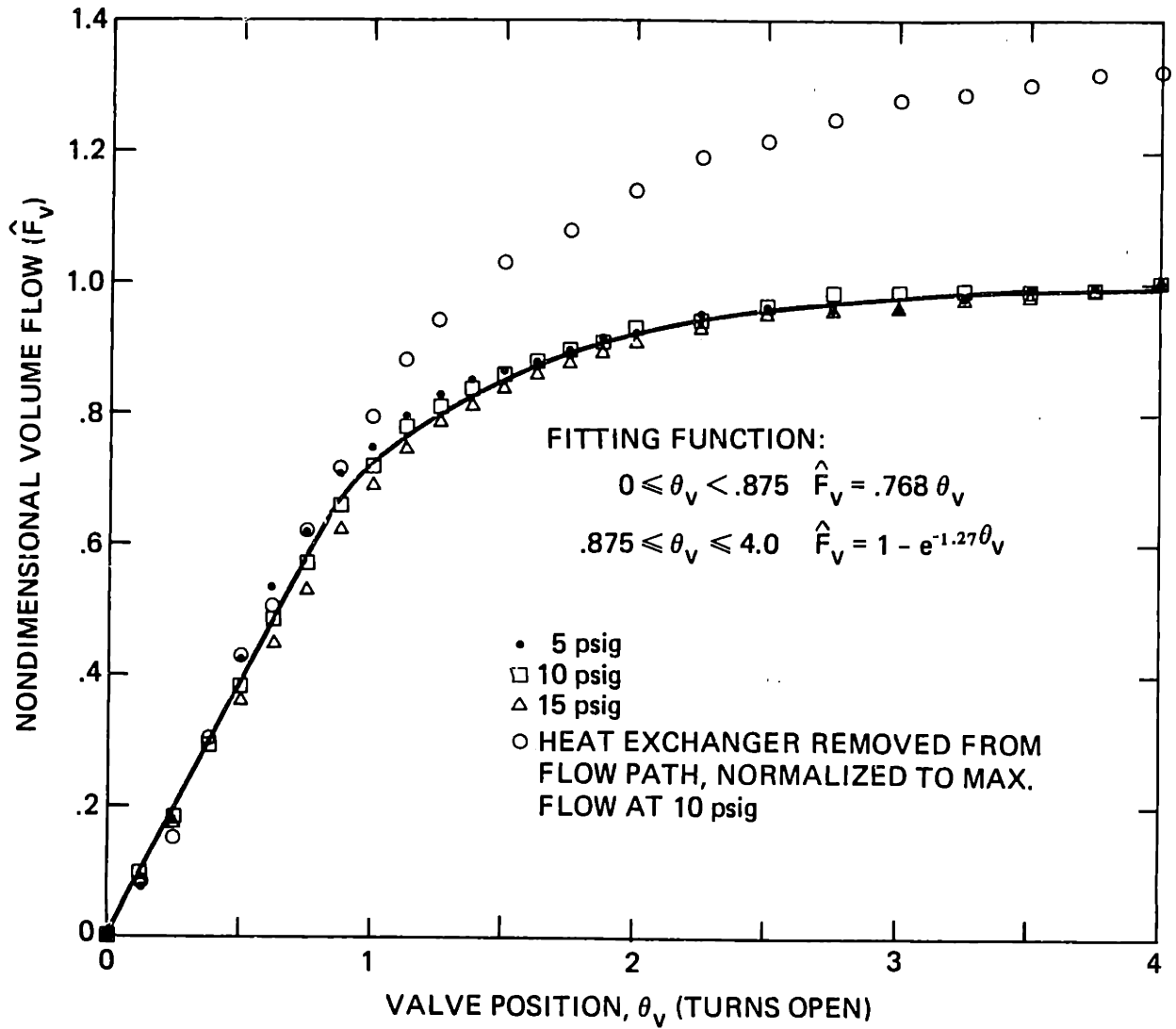


FIGURE I.3 Flow dependence on control valve position

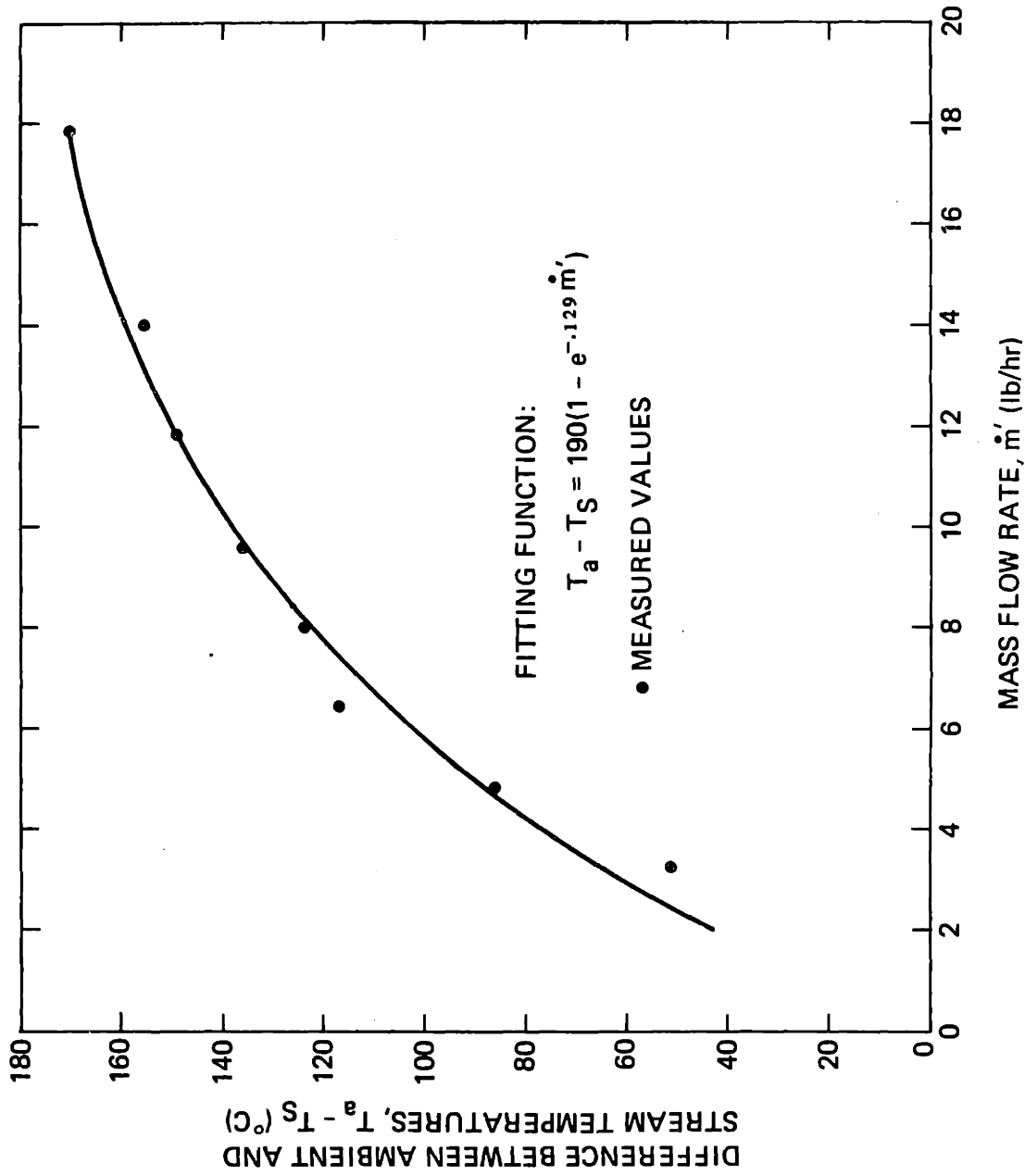


FIGURE I.4 Stream temperature dependence on mass flow

The mass flow that would be obtained for an ambient temperature stream at a particular set of valve and pressure settings, Eq. (I.8), has been corrected for temperature-dependent density and viscosity changes in the results shown.

$$\dot{m} = \rho_a \cdot 60 \cdot \hat{F}_V(\theta_V) \cdot .893(P_R)^{.571} \quad (I.8)$$

The temperature correction is effected by calculating a new driving pressure for the flow which reflects the changed flow resistance in the heat exchanger.

$$P'_R = P_R + \Delta P_{HE} - \Delta P'_{HE} \quad (I.9)$$

The new heat exchanger pressure drop depends on the ratio of pressure drops for equivalent mass flows at different temperatures:

$$\Delta P'_{HE} = \left(\frac{\Delta P_C}{\Delta P_a} \right) \Delta P_{HE} \quad (I.10)$$

The dependence of the general pressure drop on other flow variables is found by combining Eqs. (I.2) and (I.3) and the definition of Reynolds number:

$$\Delta P \propto \rho^{-.75} \mu^{.25} V^{1.75} \quad (I.11)$$

If the equivalent ambient and low temperature mass flows are defined as:

$$\dot{m} = \rho_a V_a A_F = \rho_c V_c A_F \quad (I.12)$$

then the ratio of pressure drops using Eq. (I.11) becomes:

$$\frac{\Delta P_c}{\Delta P_a} = \frac{\rho_a \mu_c^{.25}}{\rho_c \mu_a^{.25}} \quad (I.13)$$

The pressure difference across the heat exchanger at ambient temperature can be found by considering first, the ratio of the flow without the heat exchanger to that with the heat exchanger shown in Fig. I.5. The flow-ratio data points calculated from Fig. I.3 fit the empirical function:

$$\frac{F_v \text{ NO HE}}{F_v} = .125 \theta_v^{.72} + 1.0 \quad (I.14)$$

Since the flow without the heat exchanger is larger than that with the heat exchanger at a given driving pressure, $\Delta P = P_R$, removing the heat exchanger has the same effect as increasing the driving pressure. The increased, or effective driving pressure for the flow is related to the measured driving pressure and flow ratio by combining Eqs. (I.11) and (I.14) while noting that F_v is defined as VA_F :

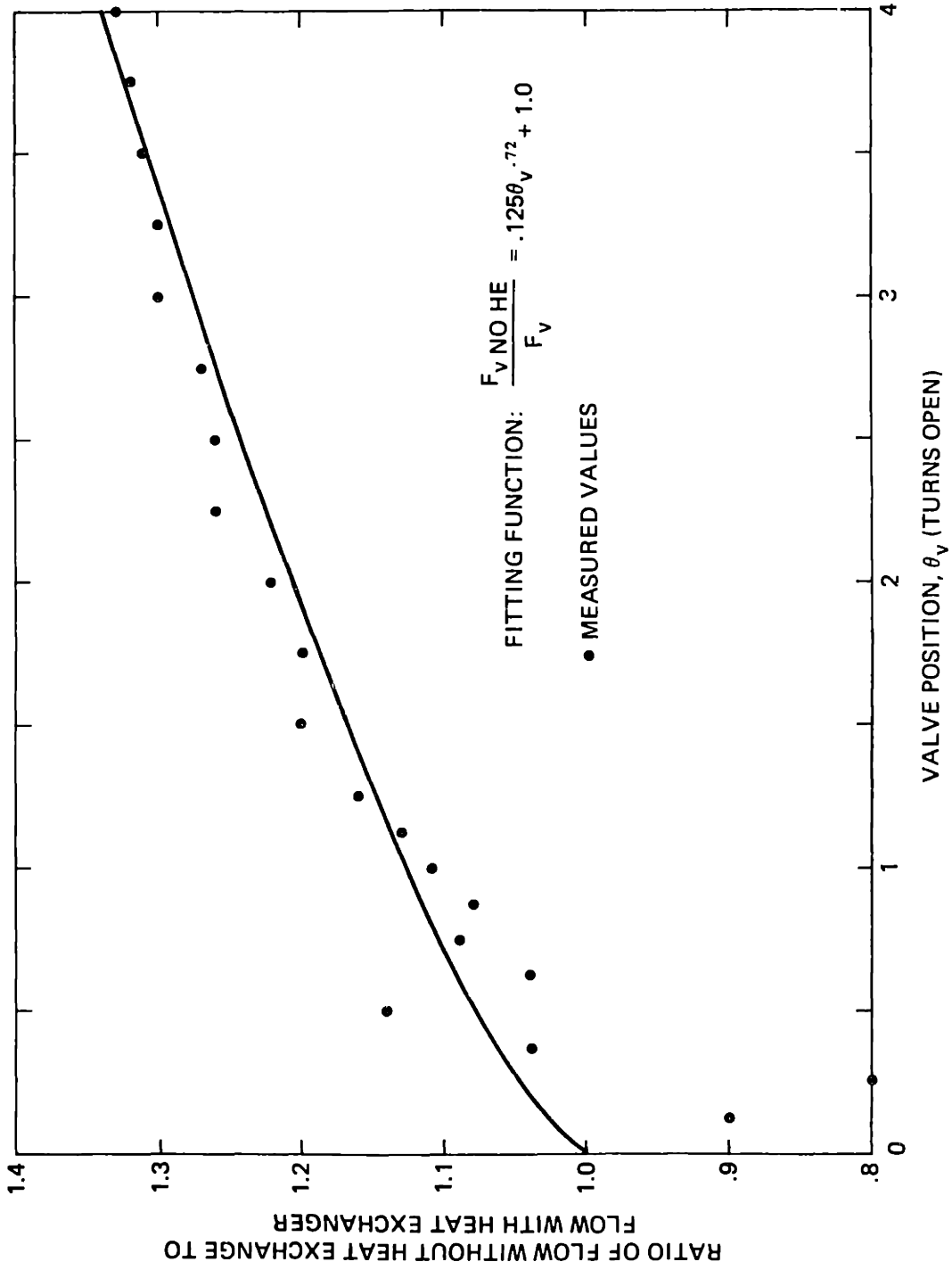


FIGURE I.5 Ratio of flow without heat exchanger to flow with heat exchanger: dependence on valve position

$$\frac{\Delta P_{EFF}}{P_R} = \left(\frac{F_V}{F_V} NO HE \right)^{1.75} = (.125 \theta_V^{.72} + 1.0)^{1.75} \quad (I.15)$$

The heat exchanger pressure drop can now be estimated as:

$$\begin{aligned} \Delta P_{HE} &= \Delta P_{EFF} - P_R \\ &= P_R [(.125 \theta_V^{.72} + 1.0)^{1.75} - 1] \end{aligned} \quad (I.16)$$

Equations (I.8), (I.9), (I.10), (I.13) and (I.16) are combined in Eq. (I.17), which provides the corrected mass flow as a function of valve position, regulator outlet pressure and stream temperature through density and viscosity:

$$\dot{m}' = \rho_a \cdot 60 \cdot \hat{F}_V(\theta) \cdot .893 [P_R (1 + [(.125 \theta_V^{.72} + 1.0)^{1.75} - 1] [1 - \frac{\rho_a}{\rho_c} \left(\frac{\mu_c}{\mu_a} \right)^{.25}])]^{.571} \quad (I.17)$$

The valve position term in Eq. (I.17) is calculated from Eq. (I.6). Values of ρ from [88] and μ from [89] are listed in Table I.1 for temperatures between 100 and 300 K.

In summary, the dependence of coolant supply ambient temperature flows on regulator outlet pressure and control valve settings has been measured. Correlation of the pressure dependence data with an expression derived from turbulent-flow friction factors is excellent. Heat exchanger

outlet stream temperatures were measured for a range of mass flow rates. Analysis is provided for calculating the low-temperature stream flow rates from control valve position, regulator outlet pressure and stream temperature.

APPENDIX J
SPECIMEN VIEWING STAGE

The specimen viewing stage is the heart of the cryomicroscope. Stages built during the past decade for the M.I.T. cryomicroscope [67,68,90,69,91] are characterized by the type of specimen that can be controlled thermally, mechanical and electrical design details, optical performance, and thermal slew rate capability.

Two stages that were considered for the present work were those of McGrath [69,19] and Ushiyama [68]. These differ primarily in the respective use of conductive and convective heat transfer mechanisms for cooling the sample, as well as the use of glued versus clamped heater attachment methods. Both stages were capable of meeting performance requirements but the convection stage was chosen because it seemed to offer higher reliability. Thermal stresses, which are minimized in the convection stage by use of O-ring seals and mercury electrical contacts, tended to delaminate glued discs from the conduction stage.

Thermal performance of the convection stage was measured or analyzed in the areas of steady-state heater power requirements, frequency response, temperature gradients and thermal slew rate capability. The mechanical layout of the stage is shown in Fig. J.1. The stage consists of a flow passage for cold N_2 gas between two optical windows. The upper window contains the thermocouple installation as well as a tin oxide electrically conductive coating. The upper disc is sandwiched between O-rings and held

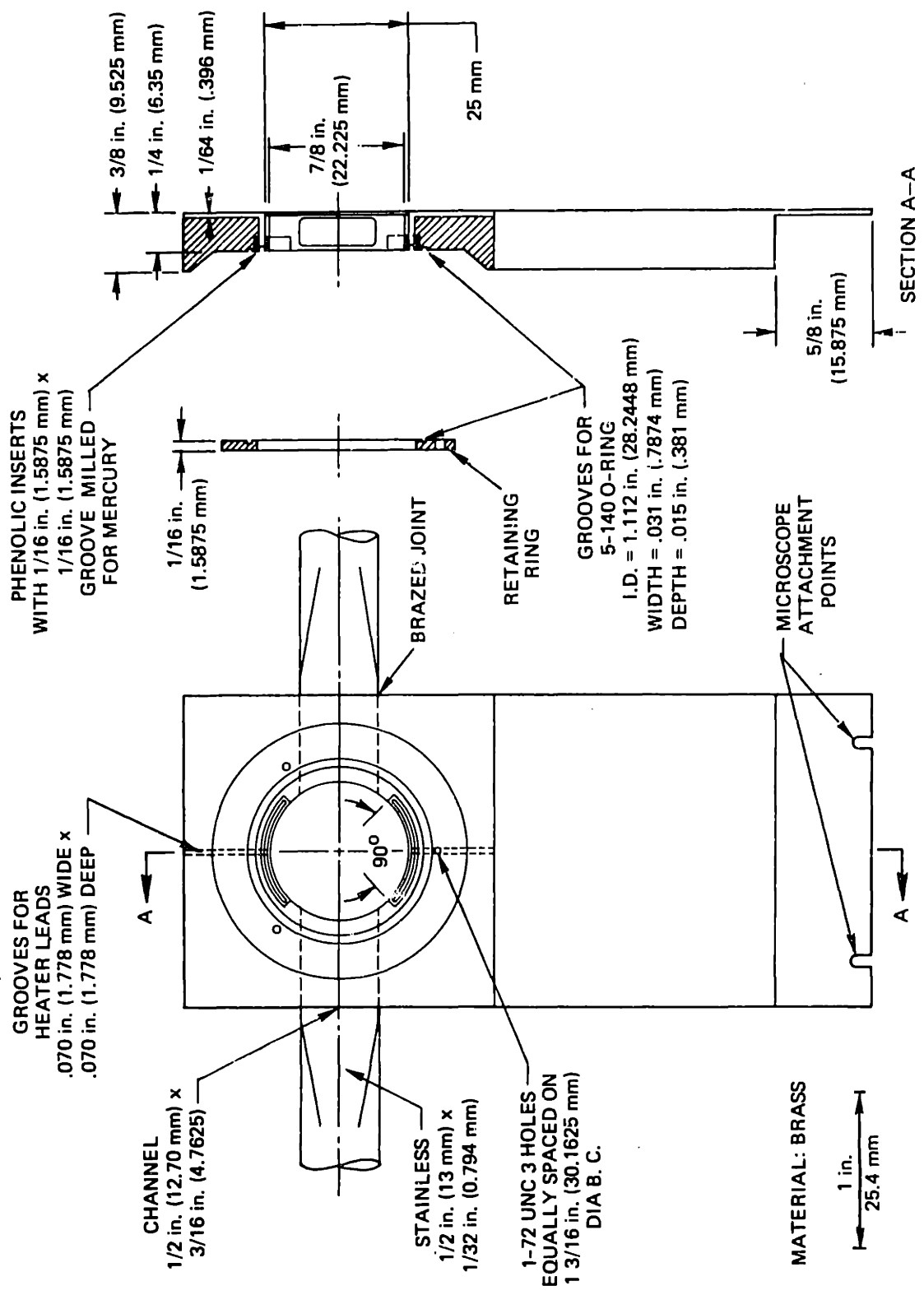


FIGURE J.1 Specimen viewing stage

in place against the mercury power connections by a retaining ring. One to two μl of cell suspension can be retained on top of the heater disc with a coverslip.

An enlarged cross section of the heater and the corresponding lumped parameter heat transfer model are shown in Fig. J.2. Positive heat flow directions are indicated by the arrows. The time rate of change of window temperature depends on electrical dissipation and convective heat transfer terms:

$$M_T \frac{dT_w}{dt} = \dot{Q}_R - \dot{Q}_S \quad (\text{J.1})$$

Equation (J.1) reduces to (J.2) for steady-state conditions:

$$\dot{Q}_R - \dot{Q}_S = 0 \quad (\text{J.2})$$

The convection term depends on the heat transfer coefficient [87, Chap. 5] and the window-stream temperature difference:

$$\dot{Q}_S = hA_w(T_w - T_s) \quad (\text{J.3})$$

Heater power required to maintain steady disc temperatures above the stream temperature was measured for a range of flow rates with and without liquid nitrogen in the heat exchanger by varying the input voltage to the power amplifier incrementally. Heater power was computed using:

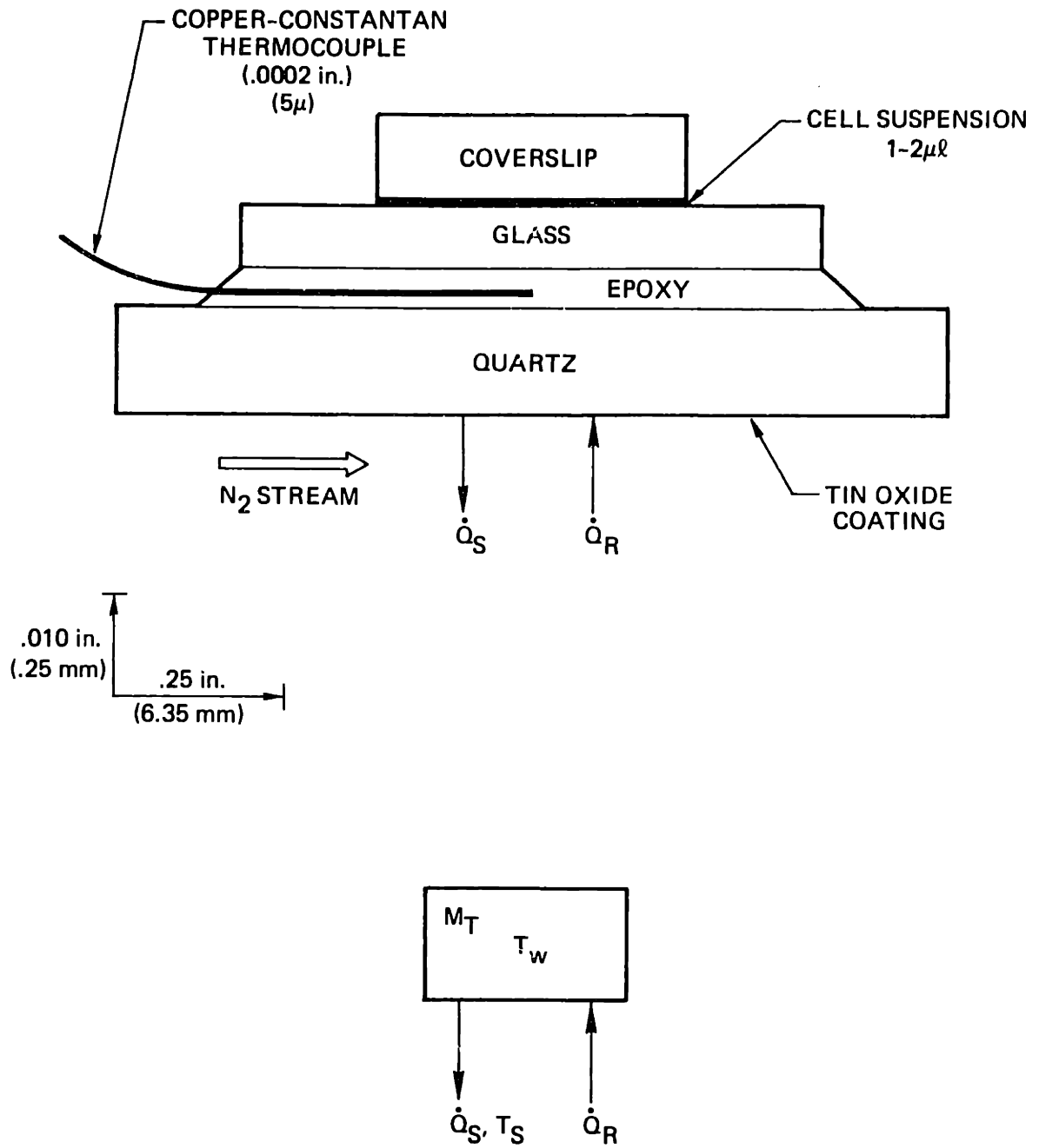


FIGURE J.2 Heater window cross section and corresponding lumped parameter heat transfer model

$$\dot{Q}_R = \frac{v_H^2}{R_H} \quad (J.4)$$

Measured results are shown for the cases of ambient temperature and cold streams in Figs. J.3 and J.4. The values for cold streams do not go through zero power as expected from Eq. (J.4), due to probable heat-leaks from the body of the stage to the window by conduction. Heat transfer coefficients can be found directly from the slopes of the curves in these figures assuming an effective area of 4.9 cm², and are listed in Table J.1. Nusselt numbers [87; Chaps. 7,8] computed with $D_F = .95$ and the observed values of h are shown in Fig. J.5 as a function of Reynolds number, which is calculated from the mass flow rate using:

$$Re = \frac{4\dot{m}}{\pi D_F \mu} \quad (J.5)$$

The viscosities and thermal conductivities used in the computations are listed in Table I.1 from [89]. A good fit to the data is the function:

$$\frac{hD_F}{K_{TS}} = .458 Re^{.643} \quad (J.6)$$

A complementary approach to Eq. (J.1) for describing the dynamics of the heater is the Laplace transform/block diagram representation [86; Chaps. 2,4] of Fig. J.6. The overall transfer function relating thermocouple output voltage to resistive heating and stream temperature is given by Eq. (J.7) where the window time constant, τ_w , is the ratio of

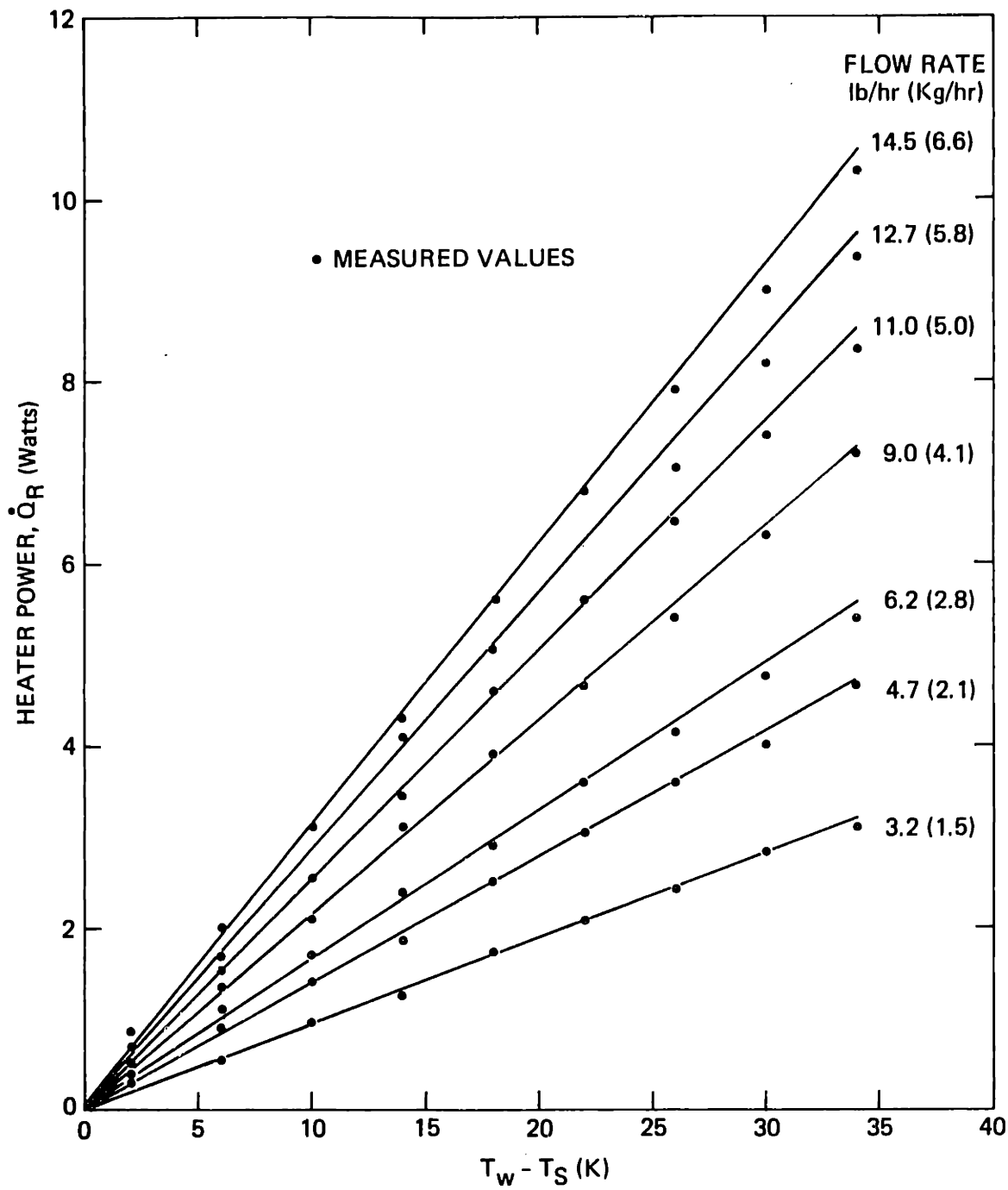


FIGURE J.3 Heater power dependence on window-stream temperature difference for an ambient temperature stream

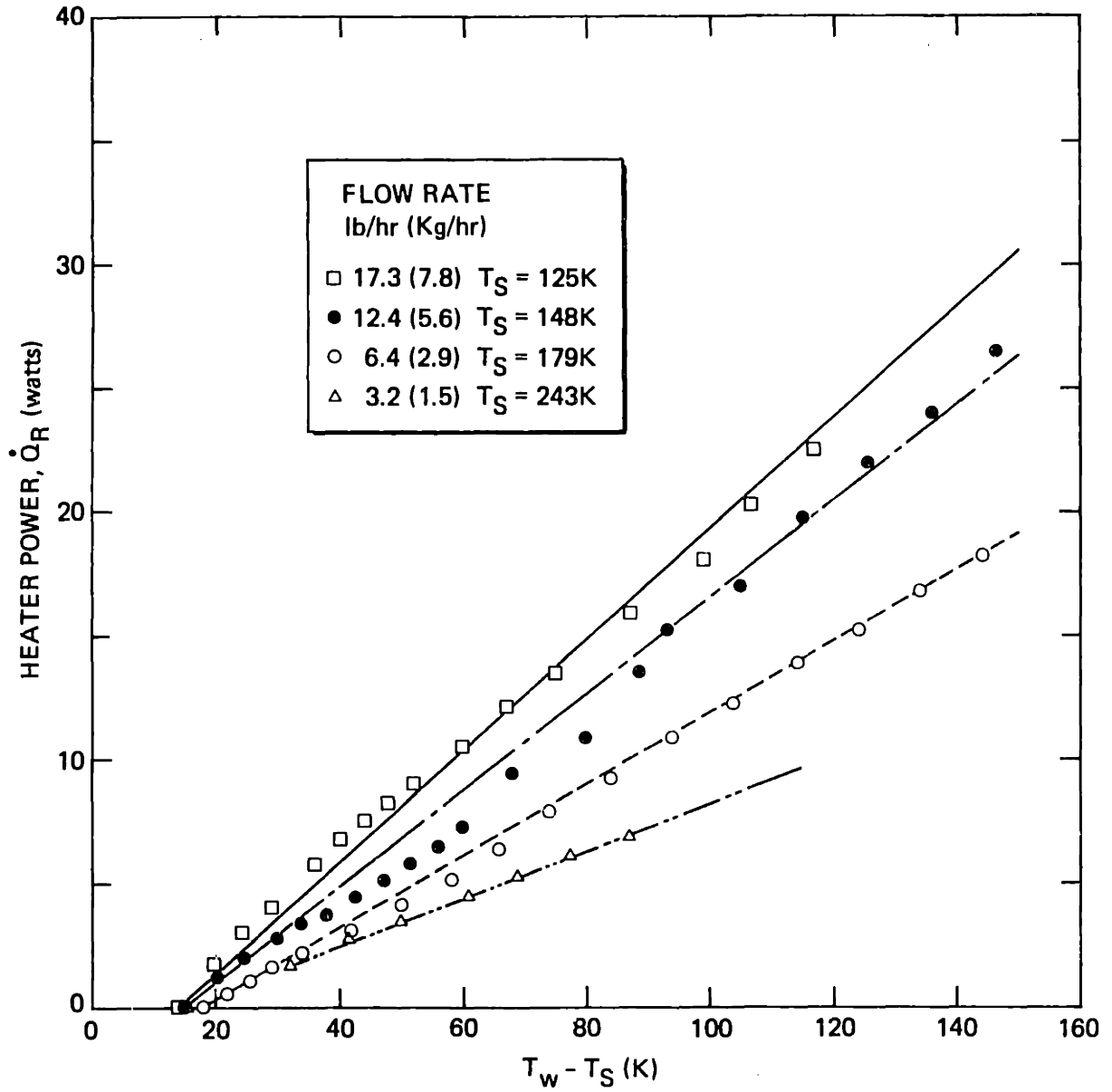


FIGURE J.4 Heater power dependence on window-stream temperature difference for cold streams

TABLE J.1

SUMMARY OF MEASURED HEAT TRANSFER COEFFICIENTS

MASS FLOW, \dot{m} [lb/hr]	AMBIENT-STREAM TEMP. DIFFERENCE [K]	HEAT TRANSFER COEFFICIENT, h [watts/cm ² -K]
3.2	0	1.91×10^{-2}
4.7	0	2.84×10^{-2}
6.2	0	3.33×10^{-2}
9.0	0	4.35×10^{-2}
11.0	0	5.13×10^{-2}
12.7	0	5.77×10^{-2}
14.5	0	6.31×10^{-2}
3.2	55	1.96×10^{-2}
6.4	119	2.96×10^{-2}
12.4	150	3.98×10^{-2}
17.3	173	4.59×10^{-2}

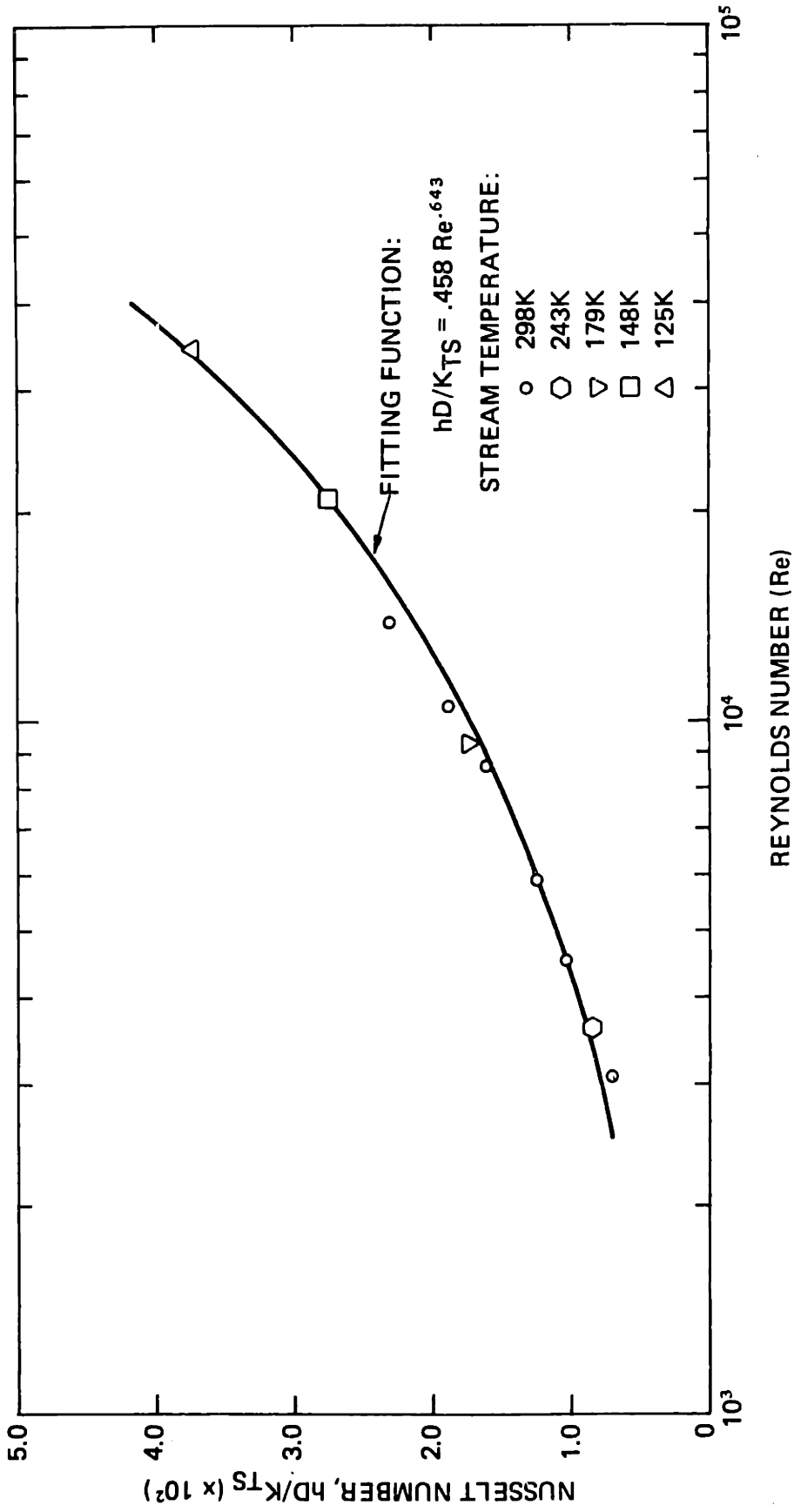


FIGURE J.5 Dependence of Nusselt number on Reynolds number

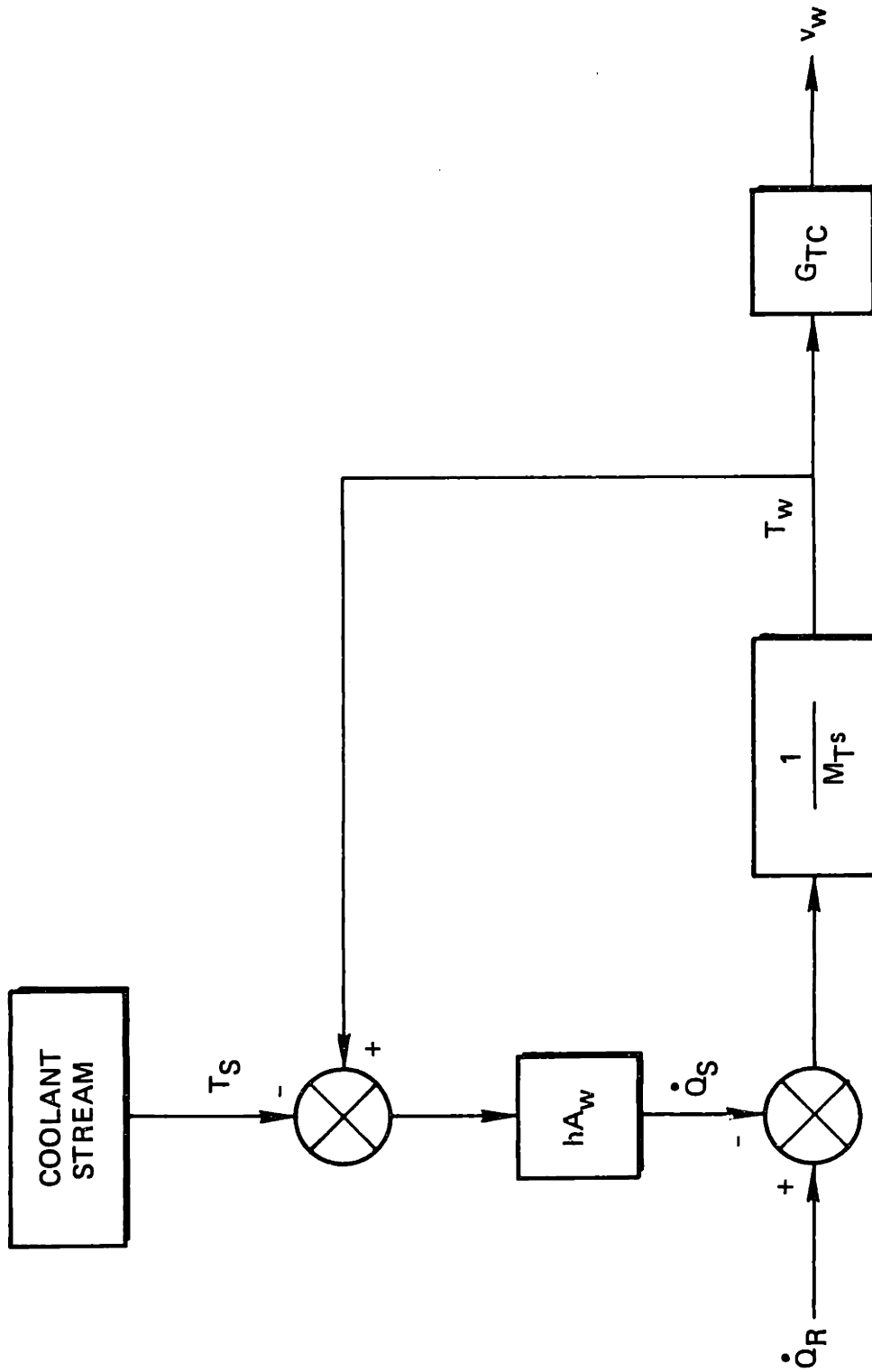


FIGURE J.6 Block diagram of heater window

the thermal mass to the heat transfer coefficient area product:

$$v_w = G_{TC} T_w = G_{TC} \left(\frac{\dot{Q}_R}{hA_w} + T_s \right) \frac{1}{\tau_w s + 1} \quad (J.7)$$

The complications attending the dependences of h , τ_w and T_s on mass flow rate can be avoided by operating at fixed values of flow. With fixed h and τ_w , the dynamics depend entirely on input power. The transfer function relating output voltage to input power is obtained from the first term of Eq. (J.7):

$$v_w / \dot{Q}_R = \frac{G_{TC}}{hA_w} \left(\frac{1}{\tau_w s + 1} \right) \quad (J.8)$$

The magnitude ratio and phase shift of this transfer function are given in Eqs. (J.9) and (J.10):

$$|G_w| = \left| \frac{v_w}{\dot{Q}_R} \right| = \frac{|G_{TC}|}{hA_w} \frac{1}{\sqrt{(2\pi F \tau_w)^2 + 1}} \quad (J.9)$$

$$\phi_w = \angle \left(\frac{v_w}{\dot{Q}_R} \right) = -\tan^{-1}(2\pi F \tau_w) \quad (J.10)$$

The time constant of the window can be estimated by first estimating its thermal mass. Table J.2 lists the volumes and specific heats of the window layers shown in Fig. J.2. The resulting estimate of .291 joules/K is used to compute the range of values of τ_w shown in Table J.3. The

TABLE J.2
ESTIMATED THERMAL MASS OF THE HEATER WINDOW

LAYER	THICKNESS [cm]	VOLUME [cm ³]	MASS [gm]	SPECIFIC HEAT [cal/gm K]	M _T THERMAL MASS [cal/K]
QUARTZ	.025	6.08×10 ⁻²	.161	.18	2.90×10 ⁻²
EPOXY	.011	2.67×10 ⁻²	3.21×10 ⁻²	.2	6.42×10 ⁻³
GLASS	.015	3.65×10 ⁻²	9.48×10 ⁻²	.199	1.89×10 ⁻²
GLASS	.020	2.93×10 ⁻²	7.61×10 ⁻²	.199	1.52×10 ⁻²
TOTAL					6.95×10 ⁻² (.291 [Joules/K])

TABLE J.3

EXPECTED RANGE OF WINDOW TIME CONSTANT

MASS FLOW, \dot{m} [lb/hr]	AMBIENT- STREAM TEMPERATURE DIFFERENCE [K]	HEAT TRANSFER COEFFICIENT, h [watts/cm ² -K]	TIME CONSTANT τ_w [s]	F _{-3db} [hz]
3	60	2.0×10^{-2}	3.0	.054
6	100	3.0×10^{-2}	2.0	.080
18	170	5.0×10^{-2}	1.2	.13

frequency at which the response is attenuated by $\sqrt{2}$ (3db) and phase shifted by 45° can be determined from Eq. (J.9) as written below, and is also shown in Table J.3. The time constant is typically ~ 2 s with $F_{-3db} = .08$ hz.

$$F_{-3db} = \frac{1}{2\pi\tau_w} \quad (J.11)$$

The frequency response of 2 heater windows was measured under a range of flow conditions. A Hewlett-Packard model 3300A function generator with model 3304 A sweep/offset plug-in supplied sinusoidal 2-10 v p.p. signals to the power amplifier (described in Appendix K). The oscillating signals were superimposed on a sufficiently large DC level to maintain the heater at $\sim -30^\circ\text{C}$. The window thermocouple output voltage was amplified with signal conditioning circuitry described in Appendix L, and displayed concurrently on an oscilloscope with the input signal allowing calculation of overall window, power amplifier and thermocouple amplifier, gain and phase shift.

The data are shown in Fig. J.7. Over the .01-10 hz frequency range, the power amplifier and thermocouple amplifier phase shifts are zero and the gains remain constant, thus effectively providing the frequency response of the window. The single-pole model of Eq. (J.9) is shown normalized to the magnitude at .01 hz and shifted down 7.5 db. The single pole phase lag of Eq. (J.10) is also shown. Substantial, unexpected phase shift occurs at frequencies above $\sim .4$ hz. The data conform to a damped

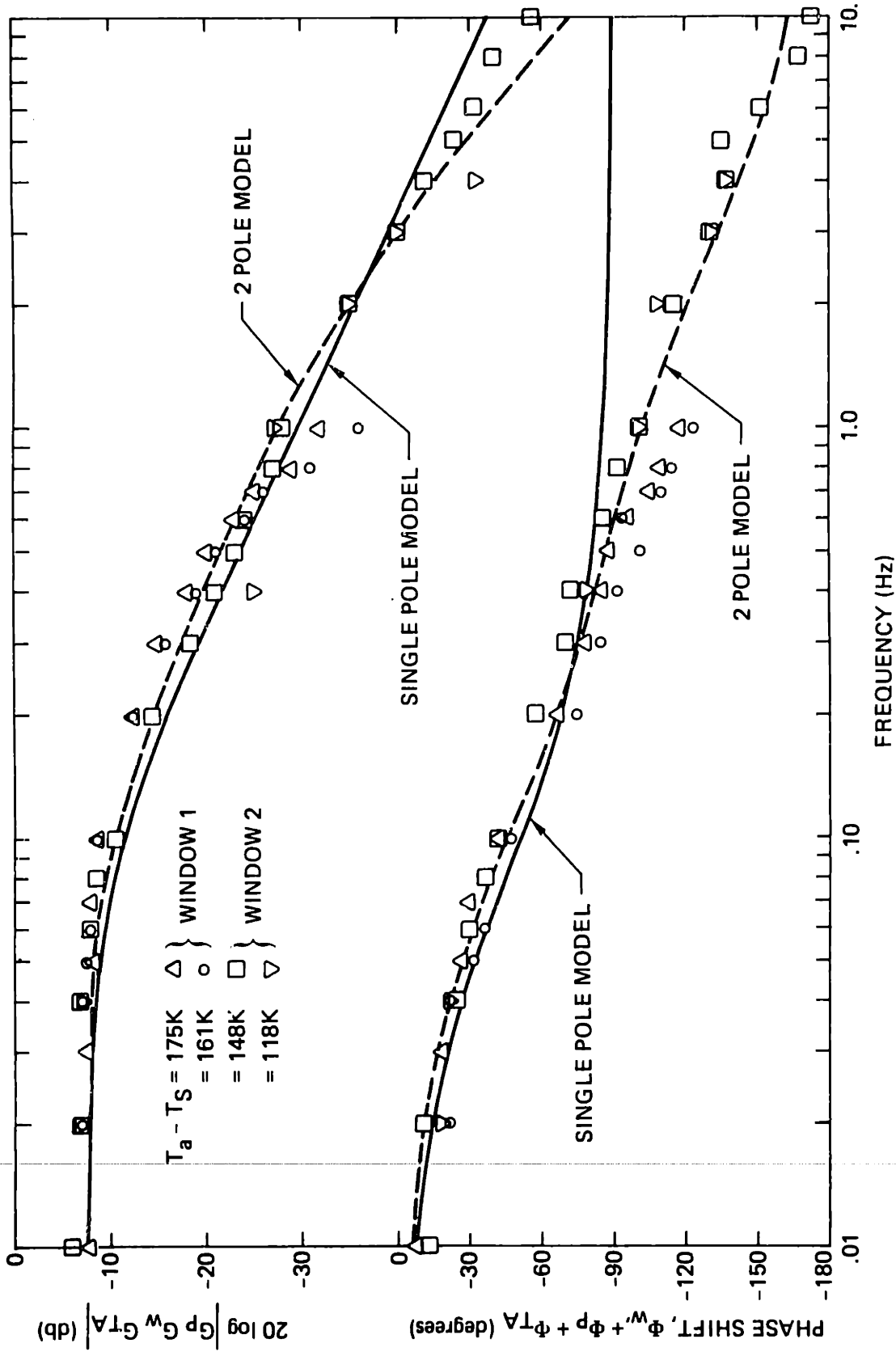


FIGURE J.7 Heater window frequency response

2-pole model with time constants of 1.6 s (.1 hz) and .0529 s (3 hz):
 In the absence of a complete heat transfer model to explain the additional dynamics, it is reasonable to assign one time constant to the window thermal mass and one to the thermocouple. If typical power amplifier and thermocouple amplifier gains of 4.1 and 688, used in these tests, are factored out, the overall window transfer function can be expressed as:

$$G_w \equiv \frac{V_w}{\dot{Q}_R} = G_{MT} G_{TC} \tag{J.12}$$

$$= \left[\frac{1}{hA_w} \left(\frac{1}{\tau_w s + 1} \right) \right] \left(\frac{K_{TC}}{\tau_{TC} s + 1} \right)$$

The constant, K_{TC} , is $\sim 36.4 \mu\text{V/K}$ (see Appendix L).

The thermal gradients in the surface of the viewing window are a potential source of instrumentation error. The magnitude of these gradients can be estimated from the fin approximation of the viewing window shown in Fig. J.8. The window is assumed to have uniform electrical heat input and convective heat removal. The outer edge of the circular window is assumed to be in intimate thermal contact with an environment at the stream temperature. The energy balance for the differential element can be written as:

$$K_w \delta \frac{d}{dr} \left(r \frac{dT_w}{dr} \right) + h(T_w - T_s)r + \frac{\dot{Q}_R}{A_w} r = 0 \tag{J.13}$$

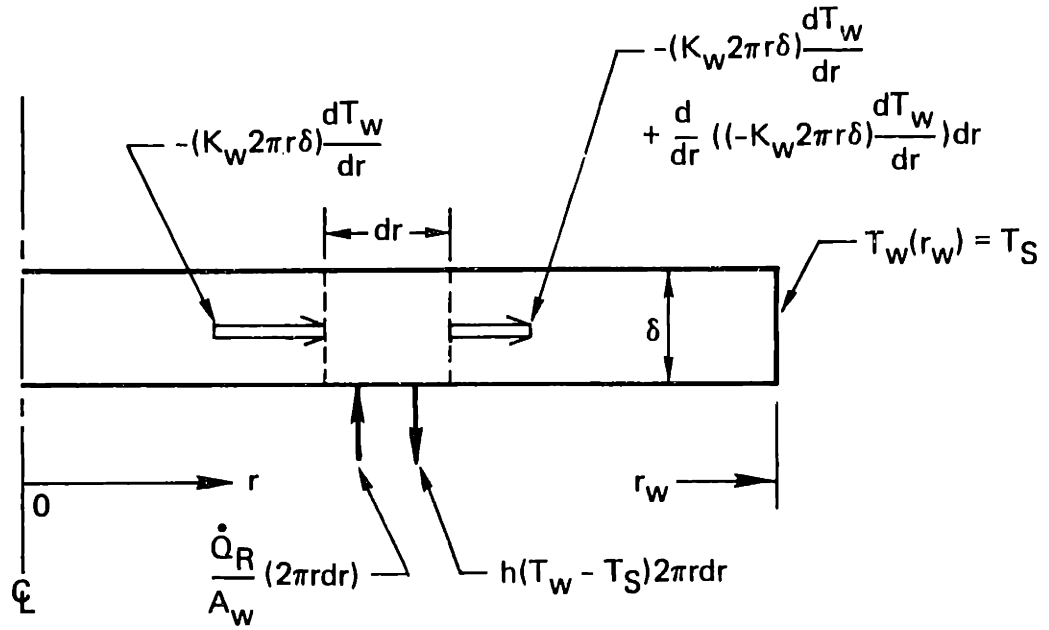


FIGURE J.8 Fin approximation of the viewing window

If \hat{T} , m_1 and m_2 are defined by Eqs. (J.14) through (J.16), then Eq. (J.13) can be expressed in the standard form of (J.17) subject to the boundary conditions of Eqs. (J.18) and (J.19):

$$\hat{T} \equiv T_w - T_s \quad (J.14)$$

$$m_1 \equiv \frac{\dot{Q}_R}{A_w K_w \delta} \quad (J.15)$$

$$m_2^2 \equiv \frac{h}{K_w \delta} \quad (J.16)$$

$$\frac{d}{dr} \left(r \frac{d\hat{T}}{dr} \right) - m_2^2 r \left(\hat{T} - \frac{m_1}{m_2^2} \right) = 0 \quad (J.17)$$

$$\hat{T}(0) = \text{Finite} \quad (J.18)$$

$$\hat{T}(r_w) = 0 \quad (J.19)$$

The solution to Eq. (J.17) consists of modified Bessel functions of order zero [98]:

$$\hat{T}(r) = \frac{m_1}{m_2^2} + C_1 I_0(m_2 r) + C_2 K_0(m_2 r) \quad (J.20)$$

Routine application of the boundary conditions gives the constants C_1 and C_2 :

$$C_1 = -\frac{m_1}{m_2} \frac{1}{I_0(m_2 r_w)} \quad (J.21)$$

$$C_2 = 0 \quad (J.22)$$

The solution, therefore, is:

$$T_w(r) - T_s = \frac{\dot{Q}_R}{hA_w} \left(1 - \frac{I_0(m_2 r)}{I_0(m_2 r_w)} \right) \quad (J.23)$$

The radial temperature distribution of Eq. (J.23) is shown in Fig. J.9 with $\dot{Q}_R = 10,20$ watts, $A_w = 4.9$ cm², $K_w = 8.8 \times 10^{-3}$ watts/cm K [glass; 87], $h = 3.0 \times 10^{-2}$ watts/cm²K, $r_w = 1.25$ cm and $\delta = .051$ cm (cover-slip is not included). Tabulated values [99] for the modified Bessel function, I_0 , were used.

Gradients within a .05 cm microscope field of view, typical for the present investigations, are expected to be less than .2 K at radial positions out to .5 cm on the window. At positions as far out as .7 cm the temperature difference across the field of view is expected to be less than .5 K. Radial displacement of the observed field and the measurement/control thermocouple must be greater than ~.5 cm to produce .5 K error, assuming an axial location for either the thermocouple or the field of view.

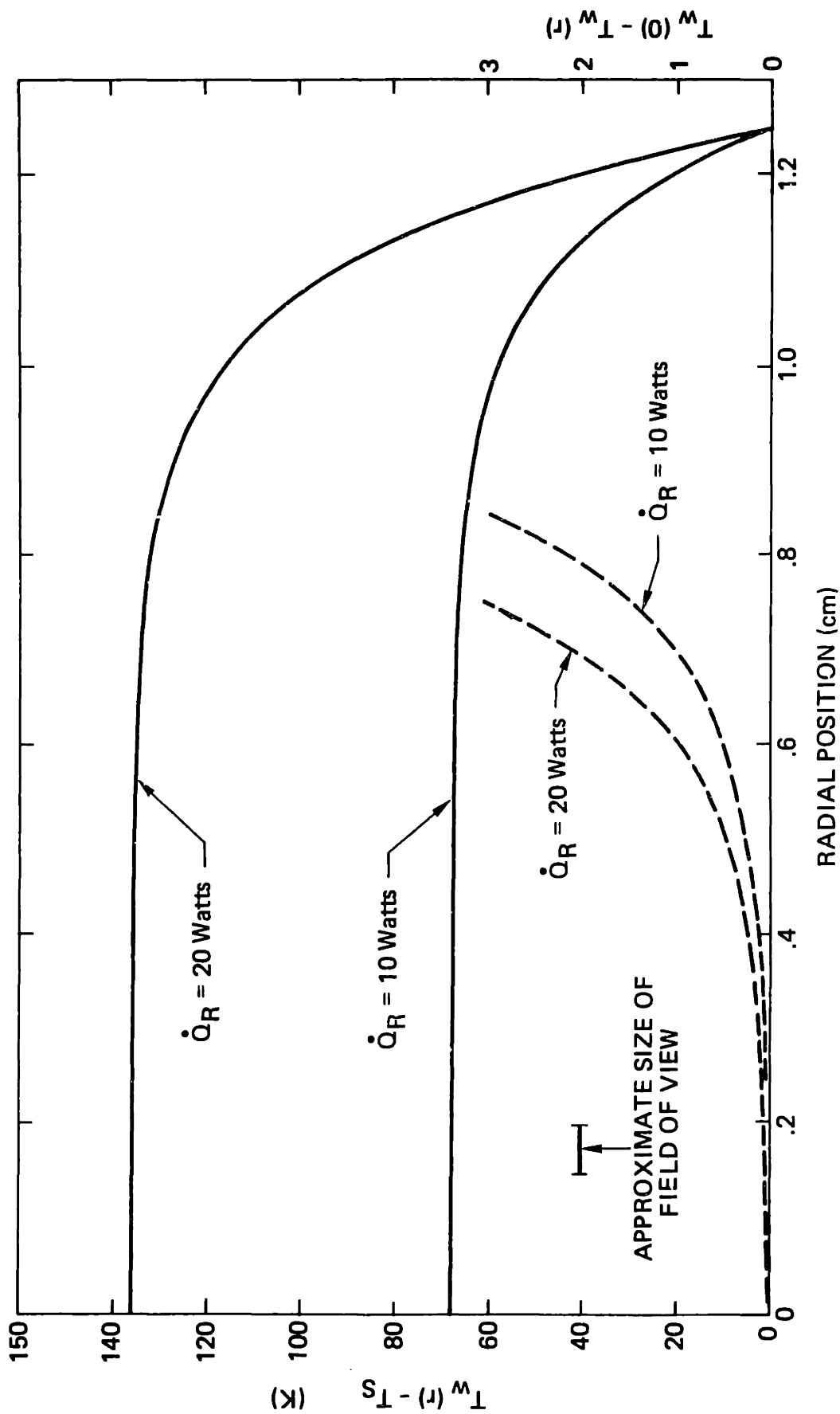


FIGURE J.9 Radial temperature distribution in the viewing window

The slew rate capability of the stage is the maximum cooling rate that can be obtained when heater power is switched off. Assuming first order response, the governing equation is (J.1) with $\dot{Q}_R = 0$ and \dot{Q}_S given in Eq. (J.3), subject to the initial condition:

$$T_w(0) = T_{wi} \quad (J.24)$$

The solution for the window temperature is:

$$T_w(t) = (T_{wi} - T_s)e^{-t/\tau_w} + T_s \quad (J.25)$$

The maximum cooling rate between the initial temperature and a final window temperature above the stream temperature is defined as:

$$B_{\max} = \frac{T_{wi} - T_{wf}}{t_f} \quad (J.26)$$

The minimum time, t_f , to reach the final temperature, T_{wf} , can be found by solving Eq. (J.25) for t_f :

$$t_f = -\tau_w \ln \left[\frac{T_{wf} - T_s}{T_{wi} - T_s} \right] \quad (J.27)$$

Values of the maximum cooling rate from Eqs. (J.26) and (J.27) with $\tau_w = 1.6$ s are shown in Fig. J.10 for window temperature drops of 25, 50 and 100 K as a function of the initial window-stream temperature differ-

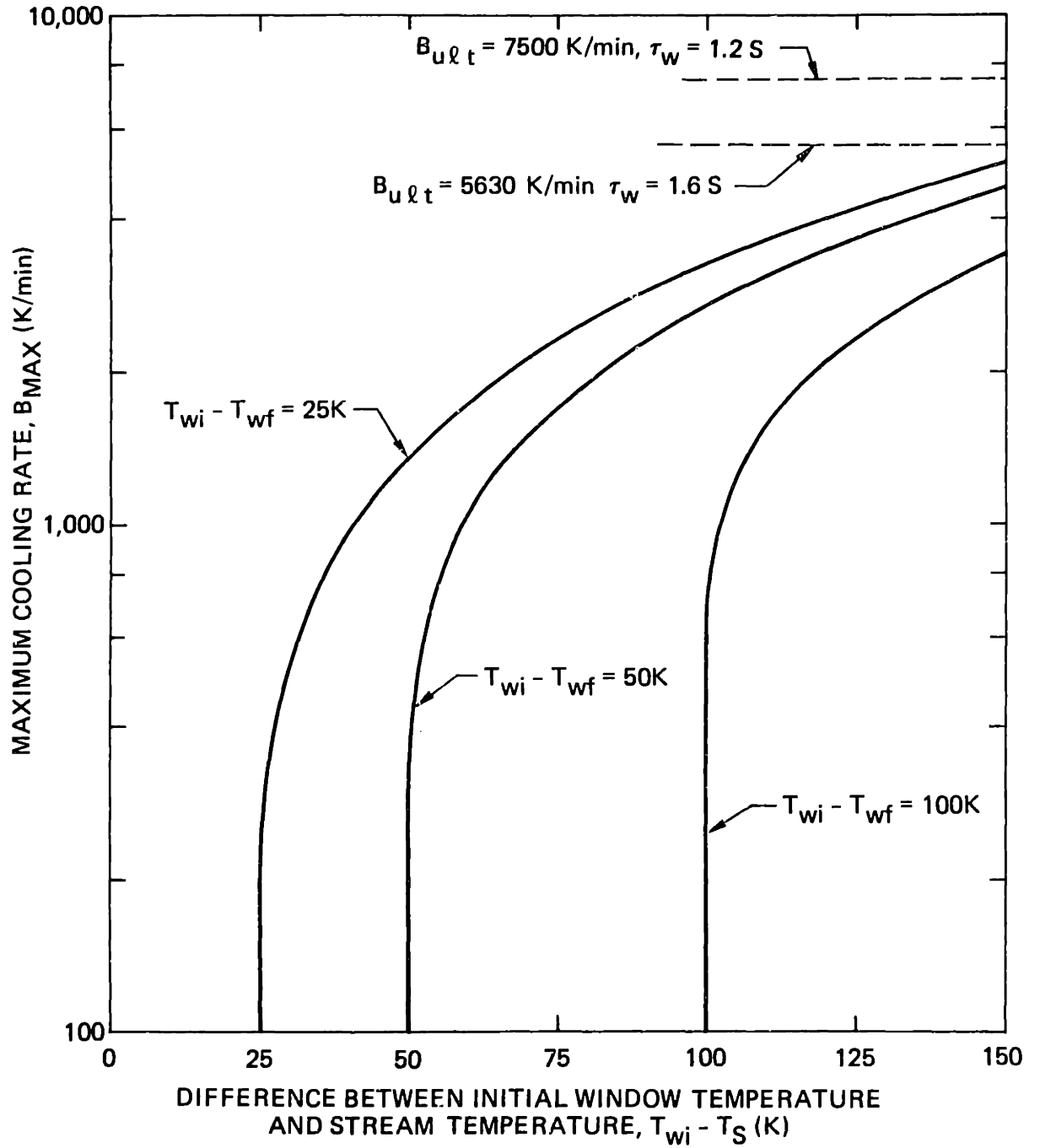


FIGURE J.10 Maximum cooling rate capability of the viewing stage

ence. Substantial cooling rates can be obtained with stream temperatures only a few degrees lower than the final window temperature. If the initial-to-final window temperature change is 50 K, for example, a stream temperature 10 K lower than the final window temperature is sufficient to provide >1000 K/min cooling capability. The ultimate cooling rate attainable is given by the initial slope of the response:

$$B_{ult} \equiv - \frac{dT_w}{dt} = \frac{T_{wi} - T_s}{\tau_w} \quad (J.28)$$

This is 5630 K/min with an initial-stream temperature difference of 150 K and with $\tau_w = 1.6$ s .

APPENDIX K
POWER AMPLIFIER CHARACTERISTICS

The power amplifier must supply a maximum of approximately 40 watts to the heater window in the band from DC to less than 20 hz. Window-to-window variations of the tin-oxide heating-layer resistance complicates the amplifier's task. The current design, shown in Fig. K.1, uses the Darlington transistor pair, on heat sinks, originally described by Diller [67]. Operational amplifier feedback and safety cut-off circuits have been added to linearize voltage transfer characteristics, facilitate gain changes and reduce the risk of heater burn-out. Current flowing in the Darlington pair causes voltage, v_H , to appear across the heater while v_E appears on the ballast. A fraction of the latter voltage, determined by the R_3, R_4 divider, is fed back to the op-amp and compared to the input. If the v_E fraction is too low, the op-amp output increases, resulting in greater current flow, i_2 , and hence greater v_E . The safety circuit compares an adjustable set voltage to the thermocouple amplifier output. If the temperature signal exceeds the set-point, the comparator swings high, an NPN transistor shorts the amplifier input to ground, and current, i_2 , in the load is forced to zero. Figure K.1 also shows the adjustable-output DC supply for the heater.

The voltage transfer behavior of the amplifier is derived by noting that the op-amp makes v^- equal to the input voltage, v_C , within its linear range of operation. The voltage across the ballast resistor is

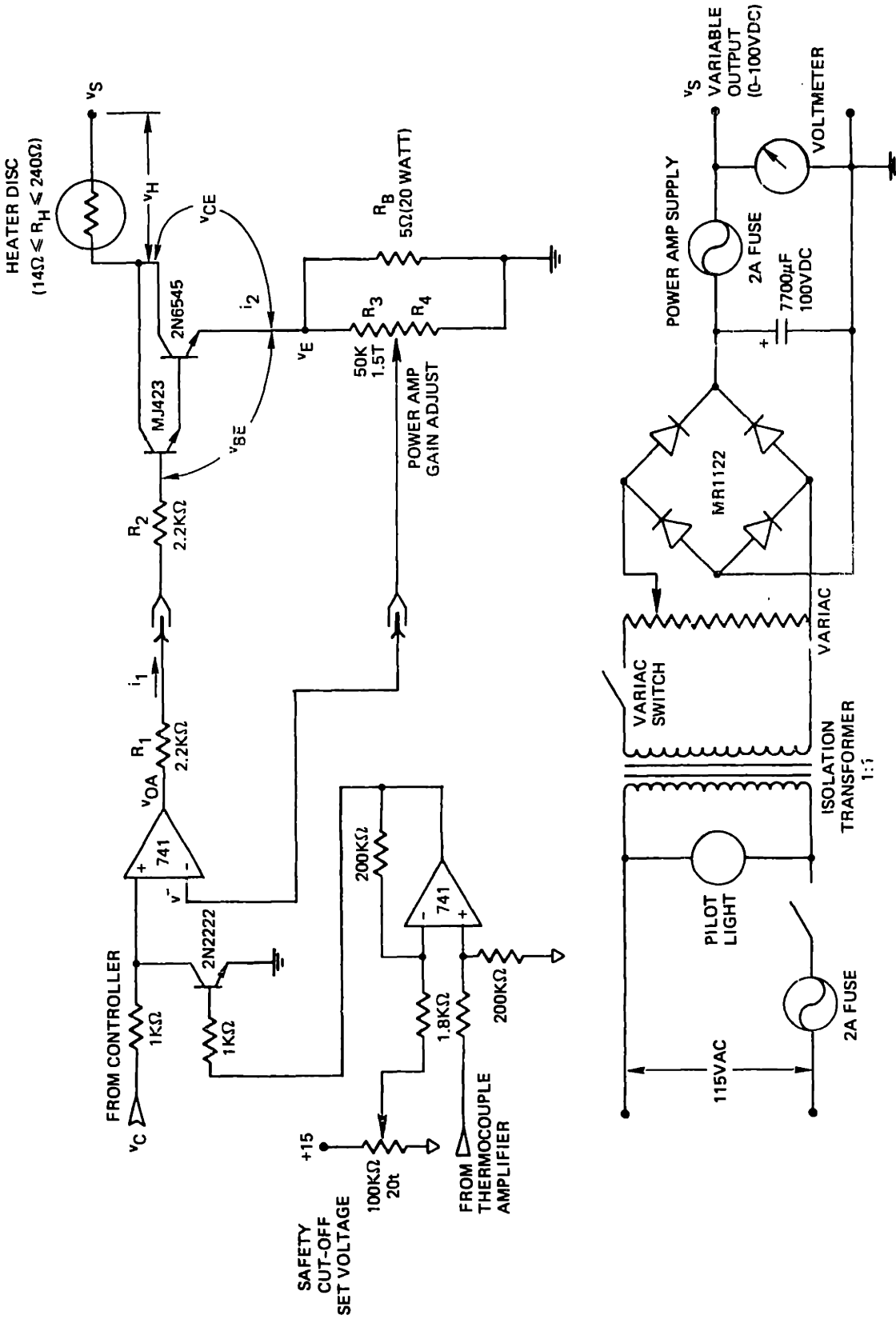


FIGURE K.1 Power amplifier circuit schematic

related to the inverting input voltage by the gain-adjust voltage divider:

$$v_E = v^- \left[\frac{R_4}{R_3 + R_4} \right] \quad (K.1)$$

Because essentially the same current flows in both the load and ballast resistors, the output and ballast voltages are related by Eq. (K.2):

$$v_H = v_E \left[\frac{R_H}{R_B} \right] \quad (K.2)$$

The above observations are combined in Eq. (K.3) which defines the voltage gain:

$$K_{VP} \equiv \frac{v_H}{v_C} = \left(\frac{R_H}{R_B} \right) \left(\frac{R_4}{R_3 + R_4} \right) \quad (K.3)$$

This linear voltage transfer characteristic was confirmed by measurements.

Output power is constrained by one of three factors, depending on the heater resistance and supply voltage setting. At relatively high heater resistances power is limited by the maximum voltage that can be applied to the load. This voltage is expressed in Eq. (K.4) which assumes zero resistance in the transistor for the full-on condition:

$$v_{H,max} = \left(\frac{R_H}{R_H + R_B} \right) v_S \quad (K.4)$$

The maximum power that can be dissipated in the heater is:

$$Q_{R,max} = v_{H,max}/R_H \quad (K.5)$$

Equations (K.4) and (K.5), combined, are shown in Fig. K.2 for supply voltage settings of 50 and 100 volts. The amplifier can supply 90 watts to a typical 100 ohm heater for a supply at 100 v but only 24 watts to the same heater at a voltage setting of 50 v. The maximum power normally required for operation, 40 watts, can be supplied to heaters with up to 240 ohms resistance at a supply setting of 100 v. Amplifier maximum output current is one of the factors constraining power delivered to relatively low resistance loads. This current, in the present amplifier design, is actually limited by the op-amp output voltage and the resistances, R_1 and R_2 . The maximum voltage that can appear across the ballast depends on the op-amp maximum output voltage, the drop across R_1 and R_2 , and the Darlington base-to-emitter drop:

$$v_{E,max} = v_{OA,max} - i_1(R_1 + R_2) - v_{BE} \quad (K.6)$$

The currents, i_1 and i_2 , are related by the overall current gain of the Darlington pair:

$$i_1 = i_2/h_{FE} \quad (K.7)$$

The maximum current in the load produces the drop across the ballast:

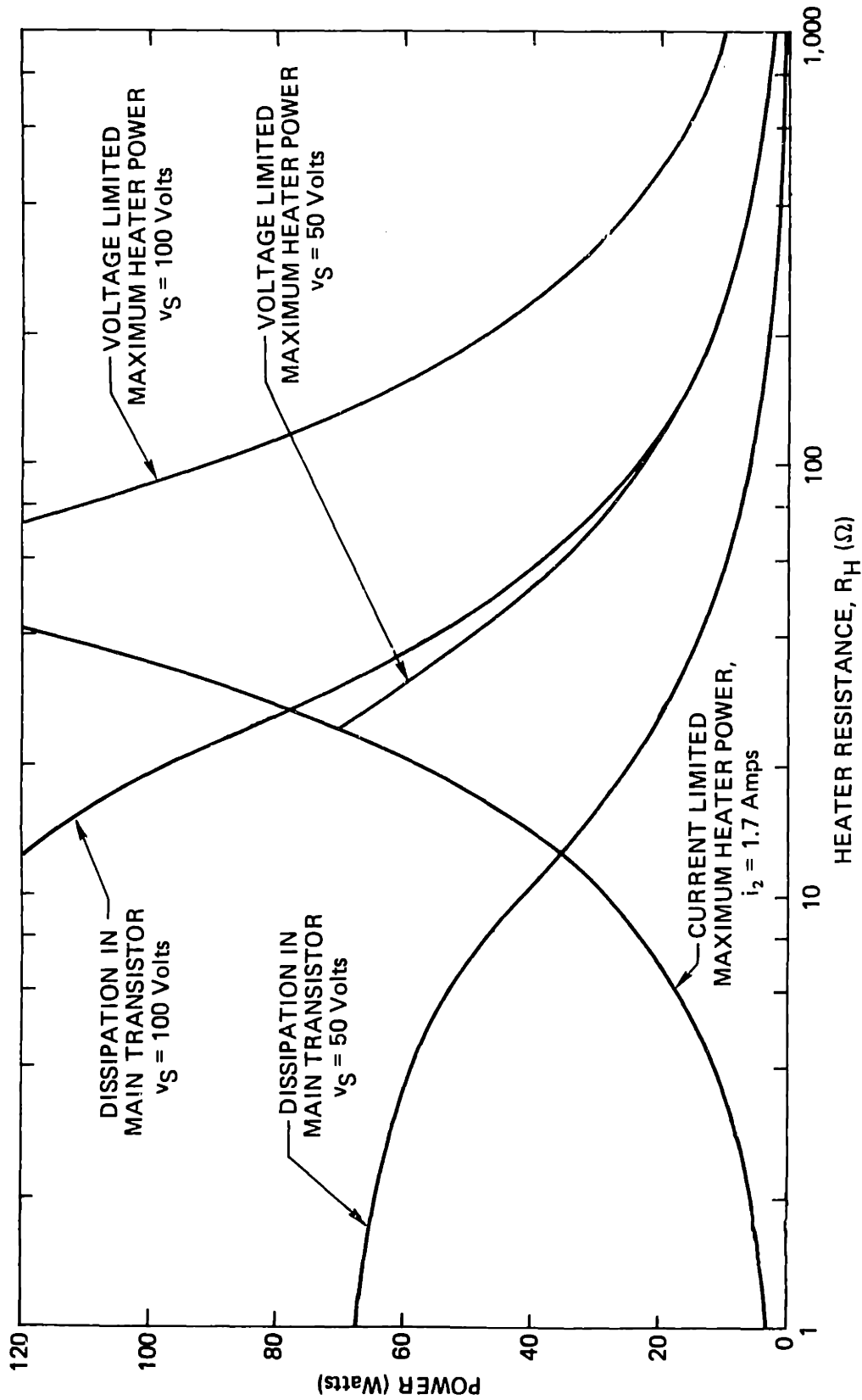


FIGURE K.2 Heater power and transistor dissipation: dependence on resistance and supply voltage

$$i_{2,\max} = v_{E,\max}/R_B \quad (\text{K.8})$$

Equations (K.6) through (K.8) can be combined to eliminate v_B and i_1 , and solved for $i_{2,\max}$:

$$i_{2,\max} = \frac{V_{OA,\max} - v_{BE}}{R_B + \frac{R_1 + R_2}{h_{FE}}} \quad (\text{K.9})$$

The maximum current is ~1.7 amps using measured current gain of 2400, $R_1 + R_2 = 4.4 \text{ K}\Omega$, measured v_{BE} for the pair of 1.3 v, $R_B = 5 \text{ ohm}$, and maximum op-amp output of 13 volts. The low-resistance maximum power can be expressed in terms of the maximum amplifier output current as:

$$\dot{Q}_{R,\max} = i_{2,\max}^2 R_H \quad (\text{K.10})$$

This equation is shown in Fig. K.2 with $i_{2,\max} = 1.7 \text{ amps}$. The requisite 40 watts for normal operation can be supplied to heaters with greater than 14 ohm resistance.

A third factor that can potentially restrict amplifier operation is the power dissipated in the main current-carrying transistor of the Darlington pair. This power goes as the load current times the voltage dropped across the transistor:

$$P_T = i_2 v_{CE} \quad (\text{K.11})$$

The voltage across the transistor depends on the supply voltage, load current and heater plus ballast resistance:

$$v_{CE} = v_S - i_2(R_H + R_B) \quad (K.12)$$

Transistor power dissipation becomes:

$$P_T = v_S i_2 - i_2^2(R_H + R_B) \quad (K.13)$$

For currents below 1.7 amps the maximum dissipation in the transistor occurs at a current level given in Eq. (K.14), found by setting the derivative of P_T in Eq. (K.13) with respect to i_2 , equal to 0:

$$i_2 = v_S/2(R_H + R_B) \quad (K.14)$$

Dissipation in the transistor, Eq. (K.13), is shown in Fig. K.2 with current given by Eq. (K.14) up to 1.7 amps and then constant at 1.7 amps, for supply settings of 50 and 100 v. Dissipation of 100 watts can be tolerated, but as a rule, the maximum should not exceed 50 watts. This implies that for heater resistances below 45 ohm, supply voltage should be below 100 v. A supply setting of 50 volts is more than sufficient to provide 40 watts to heaters below 45 ohms and reduces the transistor dissipation significantly.

An important quantity for overall control loop design is the change

in output power corresponding to a change of input voltage. For operation below 40 watts with heaters between 14 and 240 ohms, power dissipated in the heater goes as Eq. (K.15):

$$\dot{Q}_R = K_{VP}^2 v_C^2 / R_H \quad (K.15)$$

The incremental change of heater power with input voltage is found by differentiating Eq. (K.15):

$$K_{Pi} = \frac{d\dot{Q}_R}{dv_C} = \frac{2 K_{VP}^2 v_C}{R_G} \quad (K.16)$$

At 40 watts the incremental heater power becomes:

$$K_{Pi} \Big|_{\dot{Q}_R=40} = \frac{12.7 K_{VP}}{\sqrt{R_H}} \quad (K.17)$$

A reasonable, linearized power-amplifier transfer-function magnitude can be defined as the average incremental power:

$$\begin{aligned} |G_P| &= \frac{K_{Pi} \Big|_{\dot{Q}_R=0} + K_{Pi} \Big|_{\dot{Q}_R=40}}{2} \\ &= .5 \left(\frac{12.7 K_{VP}}{\sqrt{R_H}} \right) \end{aligned} \quad (k.18)$$

The measured frequency response of the current power amplifier with op-amp feedback is compared to that of the previous configuration in Fig.

K.3. The frequency response of both versions is far beyond the requirements of the thermal control system.

In summary, a circuit is described that supplies 40 watts to a purely resistive load in the band from DC to 20 hz; measured bandwidth is 3×10^4 hz. The linear relation between input and output voltage is derived and verified. Three limitations on power are defined as functions of heater resistance: maximum output current, maximum voltage across the load and power dissipation in the main transistor. A linearized transfer function is defined for use in overall control system analysis.

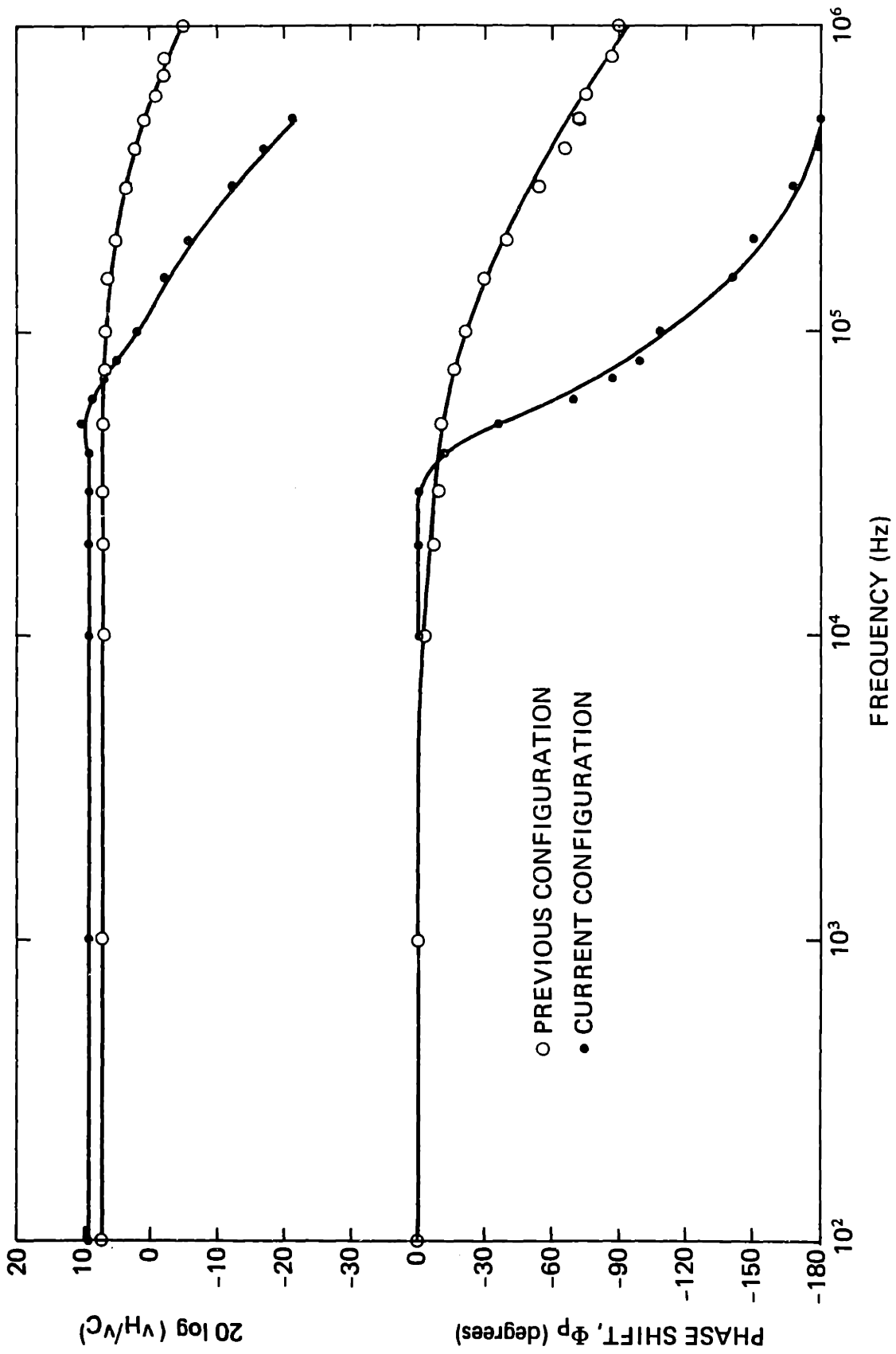


FIGURE K.3 Power amplifier frequency response

APPENDIX L
THERMOCOUPLE AMPLIFICATION

Two thermocouple amplifiers have been evaluated for the thermal control system: an HP model 7100B strip chart recorder with type 17502A thermocouple input module, used in the previous system [68], and a signal conditioning module based on an Analog Devices AD522 instrumentation amplifier. The thermocouple amplifier must provide 25 mv/K centered at 5.00 v corresponding to inputs of $\sim 40 \mu\text{v/K}$ centered at 0°C . Bandwidth of 20 hz is desirable.

The HP unit internally linearizes the thermocouple EMF such that pen movement is proportional to temperature over the operating range of -200°C to $+200^\circ\text{C}$. Output is taken from a retransmitting potentiometer mechanically linked to the pen drive. A 10.0 v supply to the pot provides the 0.0 to 10.0 v swing over the range of travel. Accuracy of the recorder is specified [74] to be within 0.5% of the reading or $\pm 1^\circ\text{C}$, whichever is greater.

The thermocouple signal conditioning module schematic is shown in Fig. L.1. Thermocouple wiring is provided to allow use of the HP recorder in parallel with the signal conditioner. Thermoelectric voltage for copper-constantan [83] is shown in Fig. L.2. A straight line with slope of $36.4 \mu\text{v/K}$ fits the data well from -60 to $+10^\circ\text{C}$. Amplifier gain of 688 gives an output of 25 mv/K with less than 1 K linearization error over this range. An adjustable voltage offset is summed with the 522 output such that the overall output is 5.000 v at 0°C . Drift at the

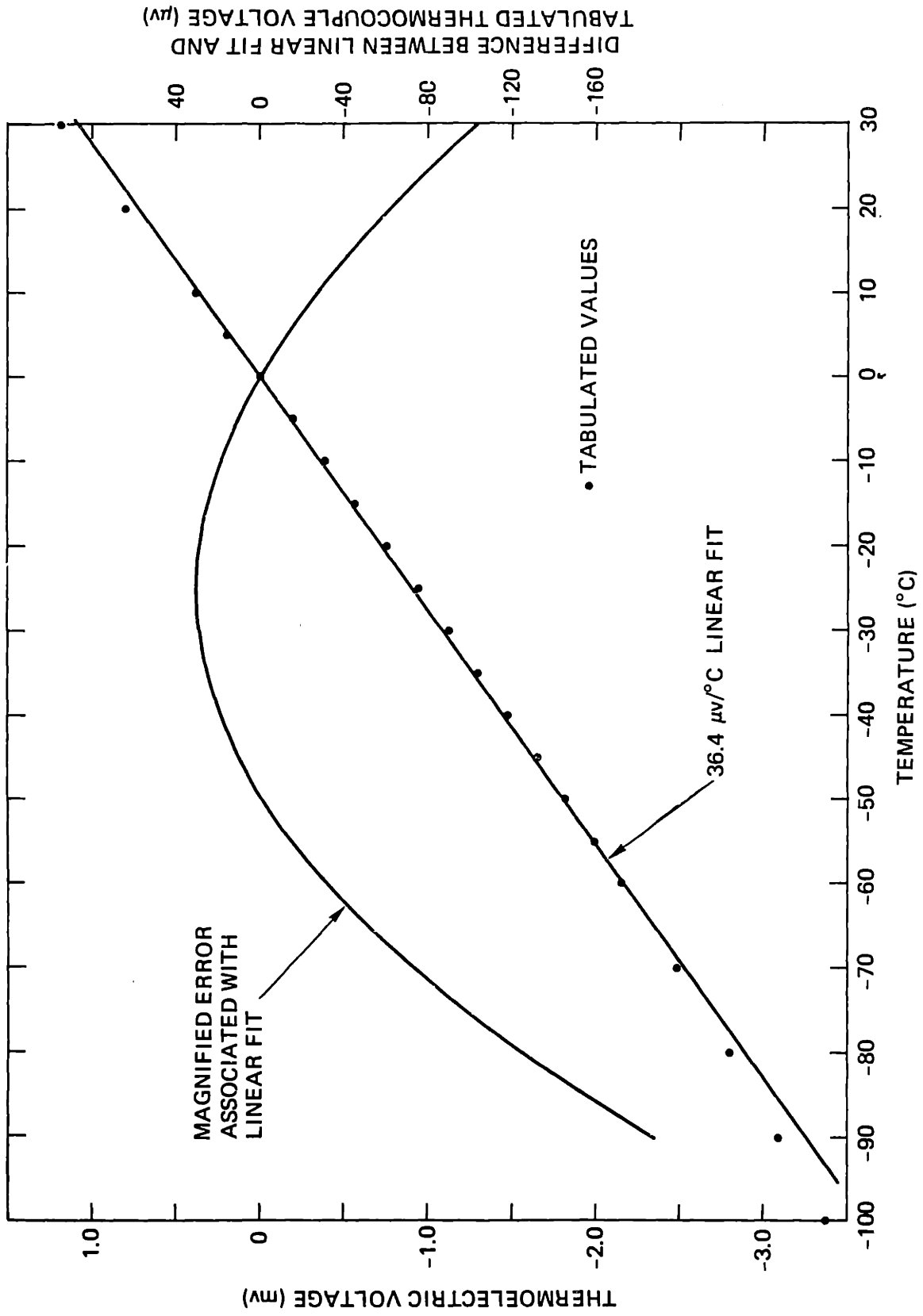


FIGURE L.2 Copper-constantan thermoelectric voltage

output is on the order of 0.5 mv/hour or less than 10 mv per day. Noise in a bandwidth of 25 hz is less than 2 mv peak-to-peak corresponding to temperature uncertainty of .08 K. Calibration of the signal conditioning module involves the following procedures:

1. Short inputs using switch provided, and set offset to 5.000 v using a digital meter on the output.
2. Place measuring thermocouple in LN₂ while keeping reference TC in ice bath. Adjust gain to obtain a reading at the output of: 5.000 v + -5.539 mv × 668 = 1.189 v.

Input offset voltage of the AD522 is multiplied by the gain setting, requiring readjustment of the module offset when the gain is changed. Steps (1) and (2) will normally have to be repeated once or twice.

Measured frequency response of the 2 thermocouple amplifiers is shown in Fig. L.3. The gain data were normalized to the respective gains at .1 hz. A two-pole critically damped model [86] with gain and phase shift in Eqs. (L.1) and (L.2) is a fair approximation to the chart recorder response. Frequency response of the signal conditioning module, essentially flat out to 100 hz, conforms to a single pole model with time constant of 6.37×10^{-4} s. The module's bandwidth is about 2 orders of magnitude higher than that of the HP recorder.

$$\frac{|G_{TA}(F)|}{|G_{TA}(.1)|} = \frac{1}{\sqrt{\left(1 - \left(\frac{F}{5.5}\right)^2\right)^2 + \left(\frac{2F}{5.5}\right)^2}} \quad (L.1)$$

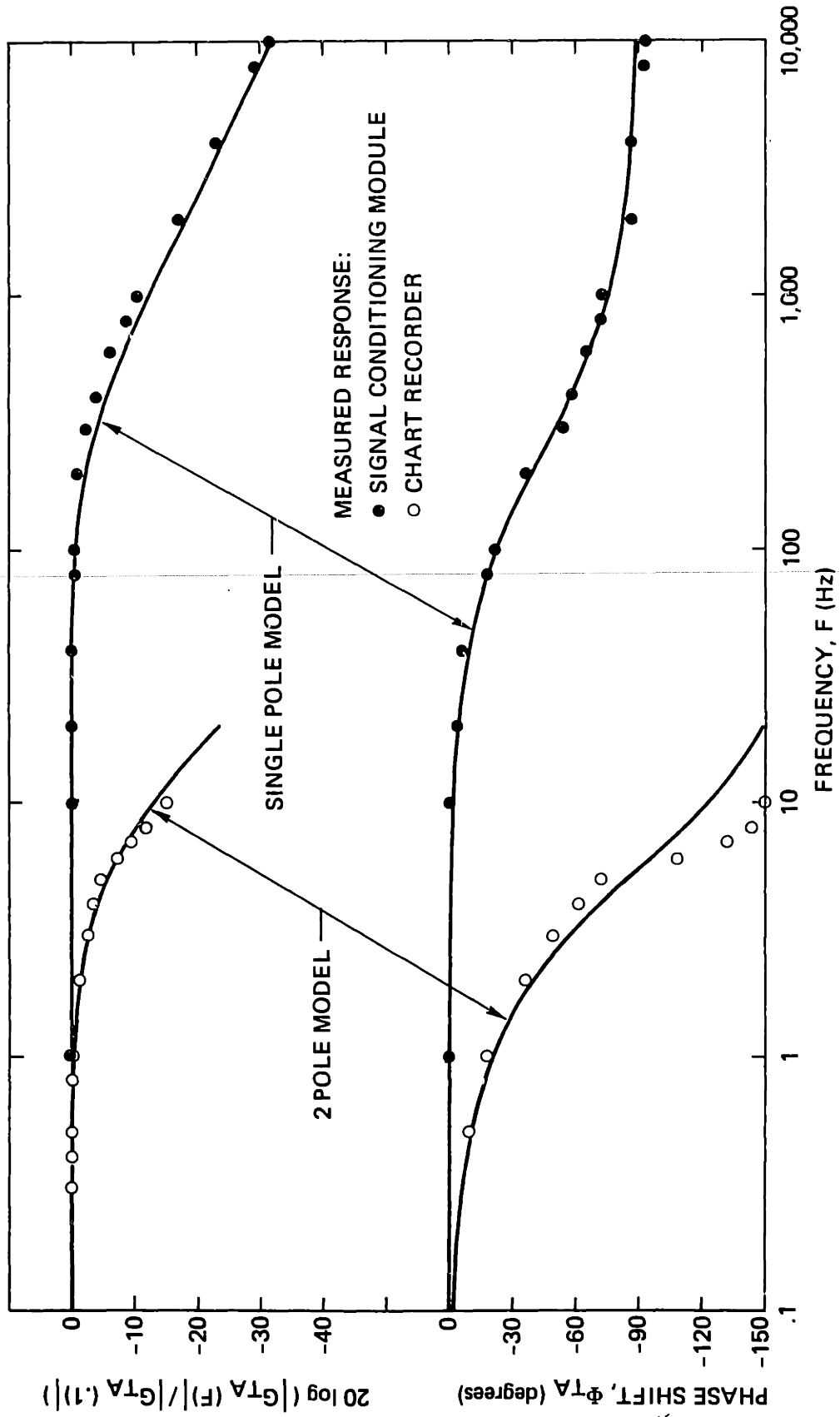


FIGURE L.3 Frequency response of the chart recorder and signal conditioning module

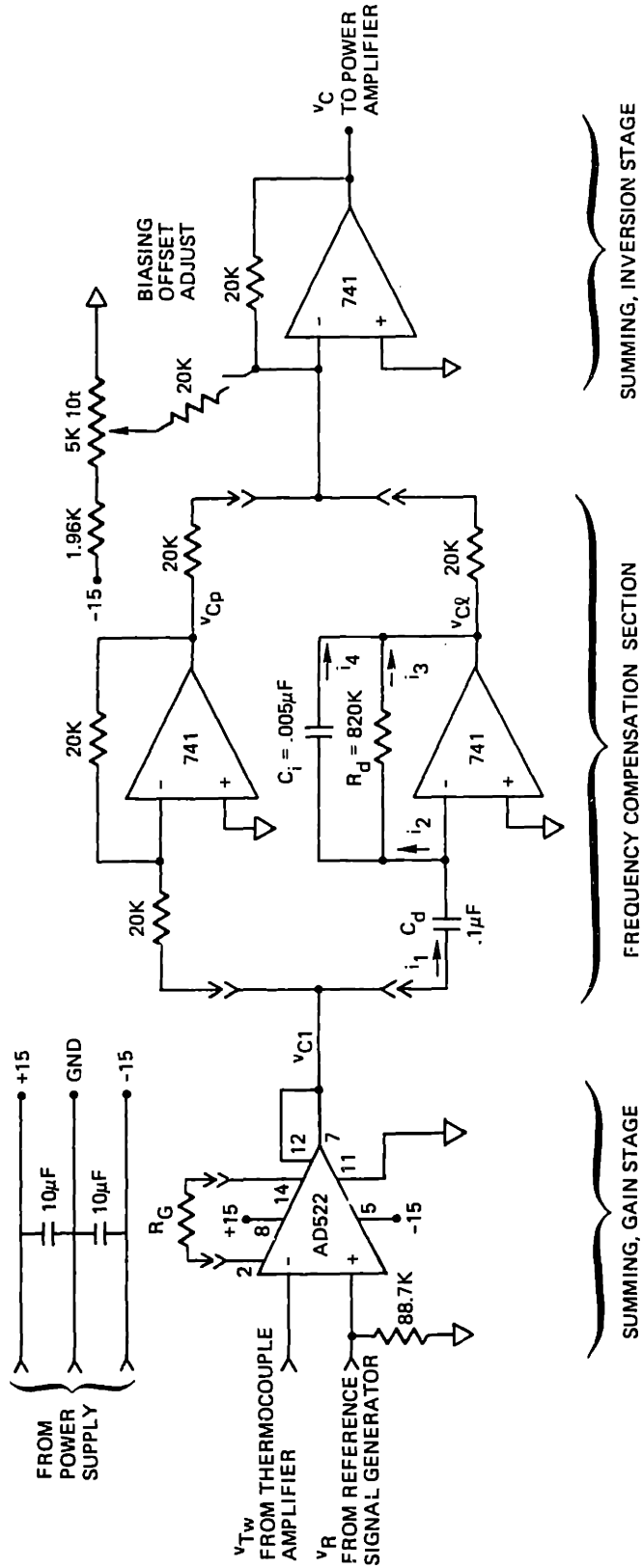
$$\phi_{TA} = - \tan^{-1} \left[\frac{2F/5.5}{\left(1 - \left(\frac{F}{5.5}\right)^2\right)} \right] \quad (L.2)$$

APPENDIX M
LEAD COMPENSATING CONTROLLER

The controller transfer function must be tailored to provide desired overall thermal control system performance. High gain is incorporated to increase system bandwidth and reduce steady state error but must be counterbalanced by addition of phase lead to maintain sufficient stability margin [86]. Controller gains of order 1000 are possible provided phase lead compensates for lag introduced by the heater window above $\sim .2$ hz. The circuit built to perform these tasks is organized in three subsections shown in Fig. M.1. A summing and gain stage utilizes an Analog Devices AD522 hybrid instrumentation amplifier to determine the instantaneous control system error, the difference between the reference signal and the measured temperature. The instrumentation amplifier is used because of its high common-mode rejection which permits distinction of millivolt level differences between signals averaging several volts. The gain of the AD522 can be set over a range of roughly 1-1000 with a single resistor according to the nominal equation:

$$|G_{C1}| = K_{C1} = \frac{V_{C1}}{(V_R - V_{TW})} = 1 + 2 \times 10^5 / R_G \quad (M.1)$$

Phase shift of the first controller stage, ϕ_{C1} , is zero over a frequency band much wider than that of interest for thermal control.



NOTE: ALL FIXED RESISTORS 1% METAL FILM

FIGURE M.1 Controller circuit schematic

The second section of the controller consists of proportional and phase-lead compensating circuits. The transfer function of the proportional circuit is simply:

$$\frac{v_{CP}}{v_{C1}} = -1 \quad (M.2)$$

The transfer function of the compensating leg can be derived by first applying Kirchoff's current law at the op-amp inverting input, assuming negligible input bias current:

$$i_1 = i_2 \quad (M.3)$$

The currents in the feedback paths must sum to i_2 :

$$i_2 = i_3 + i_4 \quad (M.4)$$

The current, i_1 , is related to the input capacitance and voltage changes by:

$$i_1 = C_d \frac{d v_{C1}}{dt} = C_d v_{C1} s \quad (M.5)$$

The op-amp makes the inverting input a virtual ground over its linear range of operation, assuming negligible input offset voltage. This allows current in the resistive feedback path to be expressed as:

$$i_3 = \frac{0 - v_{C\ell}}{R_d} \quad (M.6)$$

Current in the capacitive feedback path goes as Eq. (M.7):

$$i_4 = C_i \frac{d(0 - v_{C\ell})}{dt} = -C_i v_{C\ell} s \quad (M.7)$$

Equations (M.3) through (M.7), combined, are the voltage transfer function:

$$\frac{v_{C\ell}}{v_{C1}} = - \frac{R_d C_d s}{1 + R_d C_i s} \quad (M.8)$$

The proportional and phase-lead transfer functions, Eqs. (M.2) and (M.8), sum to form the transfer function of the second section of the controller:

$$\begin{aligned} G_{C2} &= \frac{(v_{Cp} + v_{C\ell})}{v_{C1}} \\ &= - \left[\frac{1 + s(R_d C_d + R_d C_i)}{1 + R_d C_i s} \right] \end{aligned} \quad (M.9)$$

The third section of the controller sums the two second stage legs and inverts the signal:

$$G_{C3} = \frac{v_C}{v_{Cp} + v_{C\ell}} \quad (M.10)$$

As was the case for the first controller stage, phase shift can be considered zero. An offset voltage can be added to the controller output for test purposes.

The overall transfer function of the controller is the product of the subsection functions in Eqs. (M.1), (M.9) and (M.10):

$$G_C = \frac{v_C}{(v_R - V_{TW})} = K_{C1} \left[\frac{1 + s(R_d C_d + R_d C_i)}{1 + R_d C_i s} \right] \quad (M.11)$$

The magnitude and phase of G_C become:

$$|G_C| = K_{C1} \frac{\sqrt{1 + [2\pi F(R_d C_d + R_d C_i)]^2}}{\sqrt{1 + (2\pi F R_d C_i)^2}} \quad (M.12)$$

$$\phi_C = \tan^{-1}[2\pi F(R_d C_d + R_d C_i)] - \tan^{-1}(2\pi F R_d C_i) \quad (M.13)$$

Equations (M.12) and (M.13) are compared to measured values in Fig. M.2 using $R_d = 820 \text{ K}\Omega$, $C_d = 0.1 \text{ }\mu\text{F}$, $C_i = 0.005 \text{ }\mu\text{F}$ and $G_{C1} = 1$. The theoretical phase shift and gain conform well to the measurements.

The effects of controller gain and phase lead on control loop performance are considered in Appendix N.

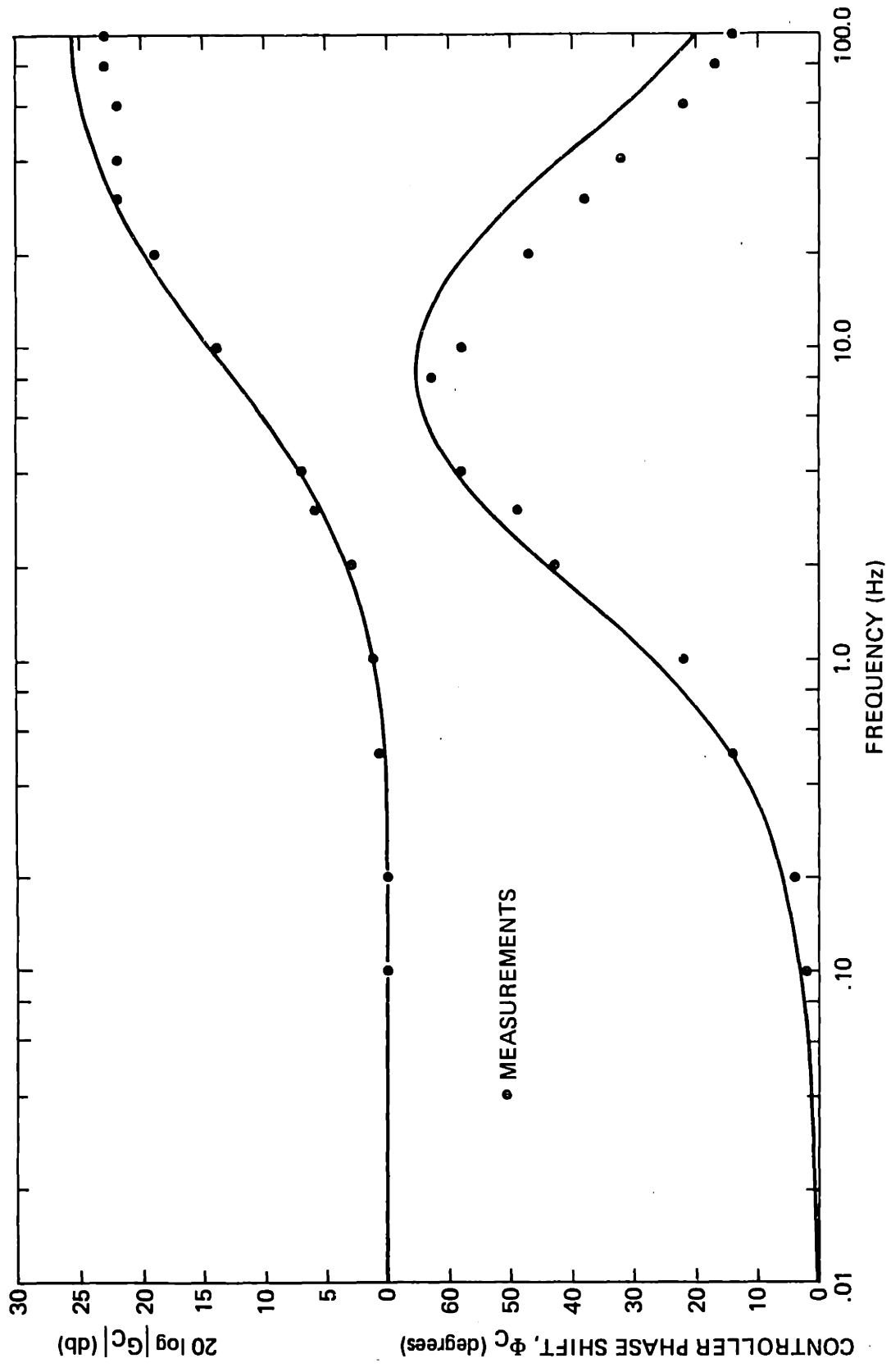


FIGURE M.2 Controller frequency response

APPENDIX N
THERMAL CONTROL LOOP PERFORMANCE

Overall thermal control loop performance can be evaluated in terms of steady-state error between measured and reference temperatures, and frequency response including bandwidth and the stability criteria of gain margin and phase margin.

Error is defined as the difference between the reference and feedback voltages:

$$v_e = v_R - v_{Tw} \quad (N.1)$$

The window temperature-equivalent voltage can be related to the system reference and stream temperature inputs using block diagram manipulation techniques [86; Ch. 4] and Figs. 3.2 and J.6:

$$v_{Tw} = v_R \left(\frac{G_{OL}}{G_{OL} + 1} \right) + T_S \left(\frac{hA_w G_w G_{TA}}{G_{OL} + 1} \right) + C_{TA} \left(\frac{1}{G_{OL} + 1} \right) \quad (N.2)$$

The third term in Eq. (N.2) results from the 5.0 volt offset added by the thermocouple amplifier. The open loop transfer function, G_{OL} , is the product of the contributing functions:

$$G_{OL} = G_C G_p G_w G_{TA} \quad (N.3)$$

These functions are summarized in Table N.1 for the previous and present control systems. Note that the controller transfer function must be idealized to separate the subtraction stage from the gain stages. Typical previous and current values of the transfer function constants are listed in Table N.2. The control system error, expressed as the combination of Eqs. (N.1) and (N.2), becomes:

$$v_e = v_R \left(1 - \frac{G_{OL}}{G_{OL} + 1} \right) - T_S \left(\frac{h_A G_w G_{TA}}{G_{OL} + 1} \right) - C_{TA} \left(\frac{1}{G_{OL} + 1} \right) \quad (N.4)$$

TABLE N.1
SUMMARY OF THERMAL CONTROL LOOP COMPONENT TRANSFER FUNCTIONS

Component	T.F. Def.	Previous Transfer Function	Previous Transfer Function
Controller	$G_C = \frac{V_C}{V_R}$	K_{C1}	$K_{C1} \left(\frac{1 + s[R_d C_d + R_d C_i]}{1 + R_d C_i s} \right)$
Power Amplifier	$G_p = \frac{Q_R}{V_C}$	$\left(\frac{12.7}{2} \right) \frac{K_{VP}}{\sqrt{R_H}}$	$\left(\frac{12.7}{2} \right) \frac{K_{VP}}{\sqrt{R_H}}$
Viewing Window	$G_W = \frac{V_W}{Q_R}$	$\frac{K_{TC}}{hA_W} \left(\frac{1}{\tau_W s + 1} \right) \left(\frac{1}{\tau_{TC} + 1} \right)$	$\frac{K_{TC}}{hA_W} \left(\frac{1}{\tau_W s + 1} \right) \left(\frac{1}{\tau_{TC} + 1} \right)$
Thermocouple Amplifier	$G_{TA} = \frac{V_{TW}}{V_W}$	$\frac{K_{TA}}{\frac{s^2}{(2\pi F_n)^2} + \frac{s}{\pi F_n} + 1}$	$\frac{K_{TA}}{\tau_{TA} s + 1}$

TABLE N.2
TYPICAL VALUES OF TRANSFER FUNCTION CONSTANTS

Constant	Previous System	Current Value
K_{C1} [v/v]	50	393
$R_d C_d$ [s]	--	8.2×10^{-2}
$R_d C_i$ [s]	--	4.1×10^{-3}
K_{VP} [v/v]	12.5	6.8
R_H [ohms]	~500	34
K_{TC} [v/°C]	36.4×10^{-6}	36.4×10^{-6}
h @ $T_s = -75^\circ\text{C}$ [watts/cm ² K]	3.0×10^{-2}	3.0×10^{-2}
h @ $T_s = -145^\circ\text{C}$	5.0×10^{-2}	5.0×10^{-2}
A_w [cm ²]	4.9	4.9
τ_w [s]	1.6	1.6
τ_{TC} [s]	.053	.053
K_{TA} [v/v]	688	688
F_n [hz]	5.5	5.5
τ_{TA} [s]	--	6.37×10^{-4}
G'_{OL} [v/v] (stream at -75°C)	30.2	496
G'_{OL} [v/v] (stream at -145°C)	19.1	298

The steady-state error can be found by superimposing the contributions resulting from step inputs for each term in Eq. (N.4) as s goes to zero:

$$v_{e,ss} = \lim_{s \rightarrow 0} s \left(\frac{v_R}{s} \right) \left(1 - \frac{G_{OL}}{G_{OL} + 1} \right) - s \left(\frac{T_S}{s} \right) \left(\frac{h_A G_w G_{TA}}{G_{OL} + 1} \right) - s \left(\frac{C_{TA}}{s} \right) \left(\frac{1}{G_{OL} + 1} \right) \quad (N.5)$$

The limit of G_{OL} as s goes to zero is written below using the component transfer functions:

$$\lim_{s \rightarrow 0} G_{OL} = G'_{OL} = K_{C1} \left(\frac{12.7}{2} \right) \frac{K_{VP}}{\sqrt{R_H}} \frac{K_{TC}}{h_A w} K_{TA} \quad (N.6)$$

The steady-state error, therefore, becomes:

$$v_{e,ss} = v_R \left(1 - \frac{G'_{OL}}{G'_{OL} + 1} \right) - T_S \frac{K_{TC} K_{TA}}{G'_{OL} + 1} - C_{TA} \left(\frac{1}{G'_{OL} + 1} \right) \quad (N.7)$$

The steady-state error of Eq. (N.7) is shown for the present system in Fig. N.1 using the component values listed in Table N.2. The error is less than .6 K for extreme input stream conditions and is less than .2 K for typical conditions. Under similar conditions the steady-state error of the previous system would be several K. These large errors were avoided previously by manually switching an integrator into the loop during the

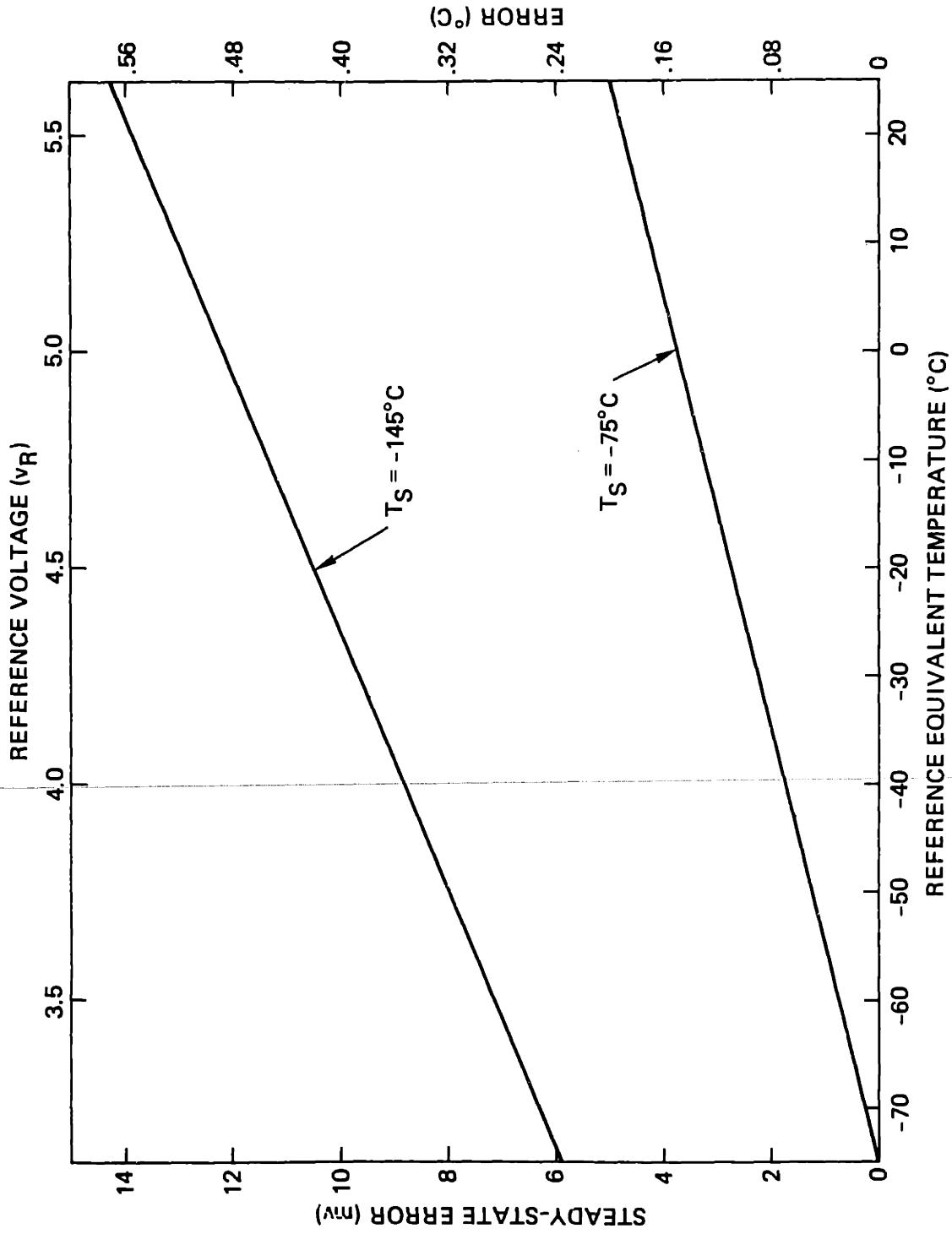


FIGURE N.1 Thermal control system steady-state error dependence on reference and stream temperatures

'hold' mode of operation, effectively reducing the steady-state error to zero. This approach results in difficult operation if accurate holds are required during cooling at rates greater than ~ 1 K/s as well as reduced stability margins for the loop due to additional phase lag.

The open loop frequency response of the thermal control system is determined by the open loop transfer function, G_{OL} , of Eq. (N.3). The magnitude and phase shift of this function are given below for the previous system in Eqs. (N.8) and (N.9) and for the present system in Eqs. (N.10) and (N.11) using the contributing transfer functions listed in Table N.1:

$$|G_{OL}|_{\text{(previous system)}} = G'_{OL} \left[\frac{1}{\sqrt{\left(1 - \left(\frac{F}{F_n}\right)^2\right)^2 + \left(\frac{2F}{F_n}\right)^2}} \right] \quad (N.8)$$

$$\times \left[\frac{1}{\sqrt{(1 + (2\pi \tau_w F)^2)(1 + (2\pi \tau_{TC} F)^2)}} \right]$$

$$\begin{aligned} \phi_{OL}(\text{previous system}) &= -\tan^{-1} \left[\frac{(2F/F_n)}{\left(1 - \left(\frac{F}{F_n}\right)^2\right)} \right] - \tan^{-1} [2\pi \tau_w F] \\ &\quad - \tan^{-1} [2\pi \tau_{TC} F] \end{aligned} \quad (N.9)$$

$$\begin{aligned}
 |G_{OL}|_{\text{(present system)}} &= G_{OL}' \frac{\sqrt{1 + [2\pi F(R_d C_d + R_d C_i)]^2}}{\sqrt{1 + (2\pi F R_d C_i)^2}} \frac{1}{\sqrt{(2\pi F \tau_{TA})^2 + 1}} \\
 &\times \frac{1}{\sqrt{(1 + (2\pi \tau_w F)^2)(1 + (2\pi \tau_{TC} F)^2)}}
 \end{aligned}
 \tag{N.10}$$

$$\begin{aligned}
 \phi_{OL} \text{(present system)} &= \tan^{-1}(2\pi F(R_d C_d + R_d C_i)) - \tan^{-1}(2\pi F R_d C_i) \\
 &\quad - \tan^{-1}(2\pi F \tau_{TA}) - \tan^{-1}(2\pi F \tau_w) - \tan^{-1}(2\pi \tau_{TC} F)
 \end{aligned}
 \tag{N.11}$$

Values from Table N.2 in Eqs. (N.7) through (N.10) give the open loop frequency response curves shown in Figs. N.2 and N.3. Relative stability of a control loop is indicated by the phase and gain margins. The phase margin is the angle by which the open loop phase shift leads -180° at the frequency where the gain drops below 1 (0 db). The gain margin is the attenuation present at the frequency where the phase lag exceeds 180 degrees. Stability is generally ensured when the phase margin is $30-60^\circ$ and when the gain margin is greater than 6 db. The previous system was marginally stable with phase margin of 14° and gain margin of 3 db. The present system exhibits substantially higher relative stability with a 30 degree phase margin and 12 db gain margin.

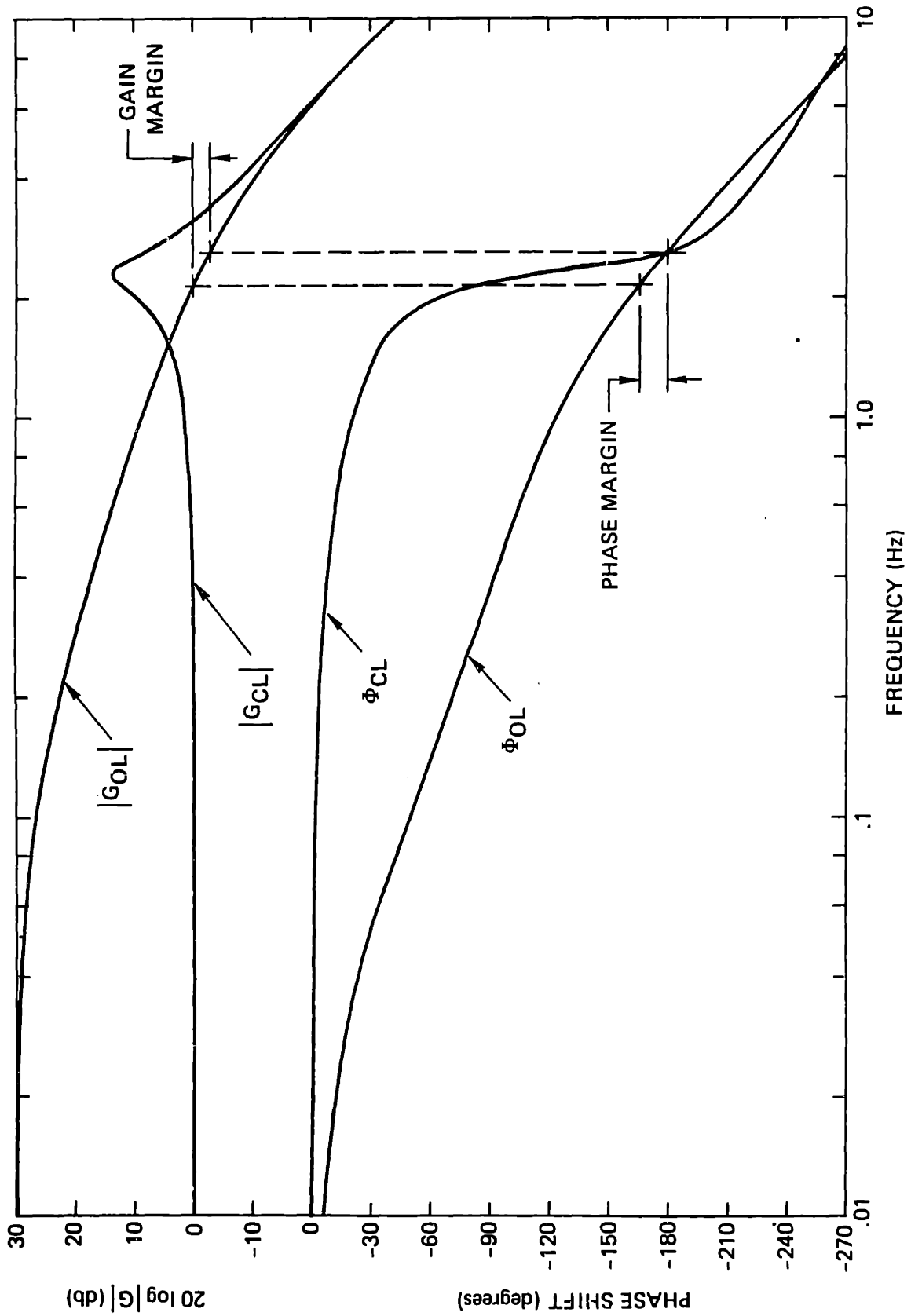


FIGURE N.2 Open and closed loop frequency response of previous thermal control system

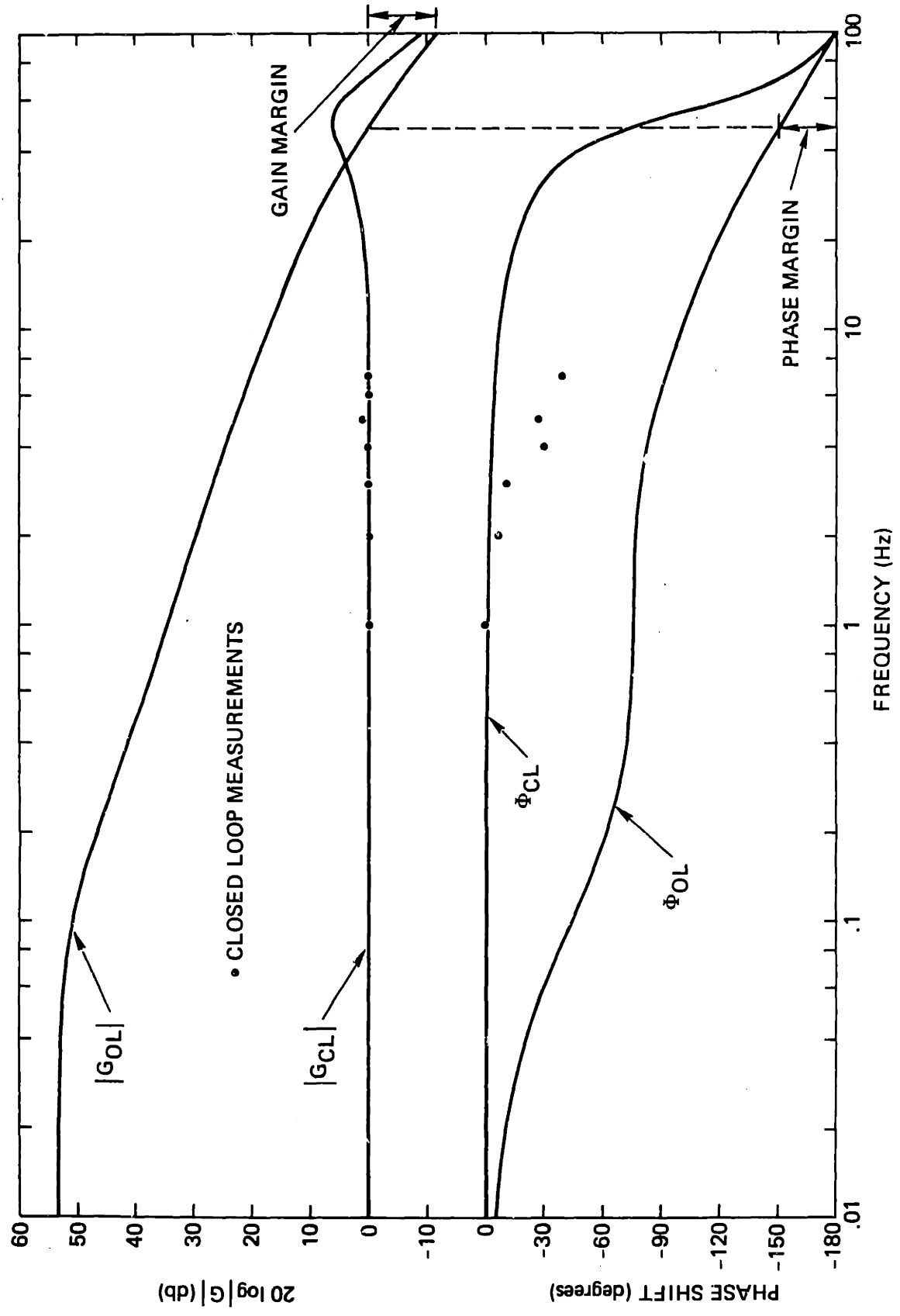


FIGURE N.3 Open and closed loop frequency response of present thermal control system

The bandwidth of the thermal control system can be determined from the closed loop transfer function defined in Eq. (N.12):

$$G_{CL} = \frac{G_{OL}}{G_{OL} + 1} \quad (N.12)$$

The magnitude of the closed loop transfer function is defined as:

$$|G_{CL}| \equiv \frac{|G_{OL}|}{|G_{OL} + 1|} \quad (N.13)$$

The closed loop phase shift is given by the open loop phase shift minus the phase shift corresponding to the denominator of Eq. (N.12):

$$\phi_{CL} = \phi_{OL} - \angle(G_{OL} + 1) \quad (N.14)$$

The latter phase shift can be defined in terms of the imaginary and real parts of the complex function, $G_{OL} + 1$:

$$\angle(G_{OL} + 1) \equiv \tan^{-1} \frac{\text{Im}(G_{OL} + 1)}{\text{Re}(G_{OL} + 1)} \quad (N.15)$$

The imaginary part of the complex function, G_{OL} , is unaffected by the addition of 1, allowing the identity:

$$\text{Im}(G_{OL} + 1) = \text{Im}(G_{OL}) \quad (N.16)$$

The imaginary part of G_{OL} is related to the magnitude and phase of G_{OL} by:

$$\text{Im}(G_{OL}) = |G_{OL}| \sin \phi_{OL} \quad (\text{N.17})$$

The real part of $(G_{OL} + 1)$ is simply the real part of $(G_{OL}) + 1$:

$$\text{Real}(G_{OL} + 1) = \text{Real}(G_{OL}) + 1 \quad (\text{N.18})$$

The real part of G_{OL} can be related trigonometrically to the magnitude and phase of G_{OL} as was done for the imaginary part:

$$\text{Real}(G_{OL}) = |G_{OL}| \cos \phi_{OL} \quad (\text{N.19})$$

Equations (N.14) through (N.19) can now be combined to obtain the closed loop phase shift:

$$\phi_{CL} = \phi_{OL} - \tan^{-1} \left(\frac{|G_{OL}| \sin(\phi_{OL})}{|G_{OL}| \cos(\phi_{OL}) + 1} \right) \quad (\text{N.20})$$

For the previous system, using the contributing functions in Table N.1, Eq. (N.13) becomes (N.21) after considerable manipulation:

(previous system)

$$|G_{CL}| = \frac{G'_{OL}}{\sqrt{\left(G'_{OL} + \frac{F^4 4\pi^2 \tau_W \tau_{TC}}{F_n^2} - F^2 \left[4\pi^2 \tau_W \tau_{TC} + \frac{4\pi \tau_W}{F_n} + \frac{4\pi \tau_{TC}}{F_n} + \frac{1}{F_n^2} \right] + 1 \right)^2 + \left(-F^3 \left[\frac{8\pi^2 \tau_W \tau_{TC}}{F_n} + \frac{2\pi \tau_W}{F_n^2} + \frac{2\pi \tau_{TC}}{F_n^2} \right] + F \left[2\pi \tau_W + 2\pi \tau_{TC} + \frac{2}{F_n} \right] \right)^2}} \quad (N.21)$$

Equations (N.20) and (N.21) are shown in Fig. N.2 for the previous system making use of Eqs. (N.8), (N.9) and values from Table N.2. The expected closed loop bandwidth is approximately 3 hz.

Similarly, for the present system Eq. (N.13) becomes (N.22) which is shown in Fig. N.3 with phase shift of Eq. (N.20) using Eqs. (N.10), (N.11) and Table N.2 values:

$$|G_{CL}| = \frac{G'_{OL} \sqrt{1 + (2\pi F(R_d C_d + R_d C_i))^2}}{\sqrt{\left[G'_{OL} + F^4 16\pi^4 R_d C_i \tau_{TA} \tau_W \tau_{TC} + 1 - F^2 4\pi^2 (\tau_W \tau_{TC} + R_d C_i (\tau_W + \tau_{TC} + \tau_{TA})) + \tau_{TA} \tau_W + \tau_{TA} \tau_{TC} \right]^2 + \left(-F^3 8\pi^3 (R_d C_i (\tau_W \tau_{TC} + \tau_{TA} \tau_W + \tau_{TA} \tau_{TC}) + \tau_{TA} \tau_W \tau_{TC}) + F 2\pi (G'_{OL} (R_d C_d + R_d C_i) + \tau_W + \tau_{TC} + R_d C_i + \tau_{TA}) \right)^2}} \quad (N.22)$$

The expected bandwidth is ~80 hz. Measured closed loop magnitude was flat out to 7 hz but unexpected phase lag was present. The actual bandwidth of the system is probably substantially greater than 10 hz even with the additional phase lag but higher frequency measurements were not performed. These measurements are difficult due to the need for small sinusoidal input amplitude which is a direct consequence of finite slew rate capability of the stage. The maximum time-rate-of-change of a sinusoidal input signal at a frequency, F , with amplitude $\frac{1}{2} v_{R,pp}$ is:

$$\left(\frac{d(\frac{1}{2} v_{R,pp} \sin(2\pi Ft))}{dt} \right)_{\max} = \pi F v_{R,pp} \quad (N.23)$$

To avoid clipping, this voltage change rate should not exceed that corresponding to the slew rate capability, B_{\max} , yielding the following limit on the allowable input voltage swing:

$$v_{R,pp} \leq \frac{B_{\max} \cdot 25}{60 \cdot \pi \cdot F} \text{ [mv]} \quad (N.24)$$

This equation is shown in Fig. N.4 for assumed maximum slew rates of 2000 and 4000 K/min with experimental points categorized by no clipping, moderate clipping or massive nonlinearity of the output waveforms. Based on a typical window-stream temperature difference of ~90 K during these measurements, maximum slew rate should be in the 3000 K/min range (see Appendix J); this is confirmed by the observed incidence of clipping. The maximum allowable input voltage swing under these conditions is less than 2 K at 10 hz.

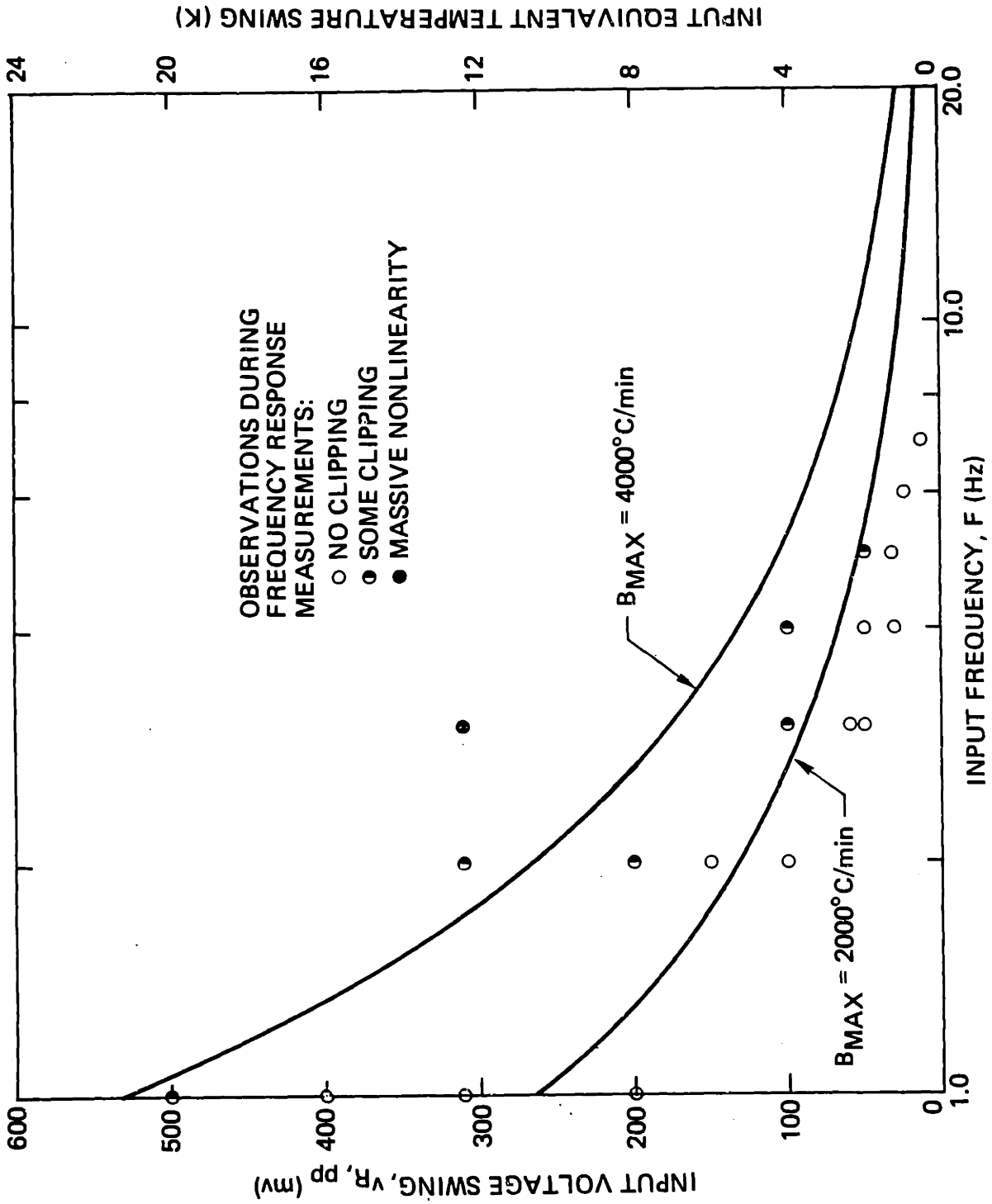


FIGURE N.4 Slew rate limits on allowable input voltage swing to the thermal control loop

These slew rate limitations combined with roughly 2 mv of electrical noise referred to the controller input cause a practical upper limit of control system bandwidth in the 10 - 20 hz range. Improvements in useful bandwidth are contingent on increased heat transfer capability of the stage and/or reduced thermal mass of the viewing window.

APPENDIX 0
HUMAN LYMPHOCYTE VOLUME

Mean volume and the variance of the volume distribution are important parameters in cell freezing simulations. For human lymphocytes, a sampling of the reported means ranges from $120 \mu^3$ [78], to $280 \mu^3$ [79], as shown in Table 0.1. Because of the wide range of values and the likelihood that different separation techniques result in different populations, diameter measurements were performed using optical microscopy on cells separated at MGH by the same procedures as were used during the cryomicroscope studies. Cells suspended in .290 osm solutions had a mean volume of $138 \mu^3$, assuming sphericity.

Standard deviation of assumed normal volume distributions are also listed in Table 0.1. The first group of values listed were estimated from graphed distributions in the articles cited; the other values were obtained by the author from light microscopy diameter measurements and flow cytometry forward-scattered light histograms. The means and variances of volume were computed from the means and standard deviations of diameters using Eqs. (0.1) and (0.2) which were derived using Eqs. (B.9) and (B.16):

$$\bar{V} \approx V(\bar{D}_C) + \frac{1}{2} \frac{\partial^2 V}{\partial D_C^2} S_D^2 \Big|_{\bar{D}_C} = \frac{\pi}{6} \bar{D}_C^3 + \frac{\pi}{2} \bar{D}_C S_D^2 \quad (0.1)$$

$$S_V^2 \approx S_D^2 \left(\frac{\partial V}{\partial D_C} \right)^2 \Big|_{\bar{D}_C} = S_D^2 \frac{\pi^2}{4} \bar{D}_C^4 \quad (0.2)$$

TABLE 0.1
SUMMARY OF LYMPHOCYTE VOLUME MEASUREMENTS

MEAN VOLUME \bar{V}	CELL COUNT	NORMALIZED STANDARD DEV. $\hat{S}_V = S_V/\bar{V}$	METHOD	CONDITIONS	REFERENCE
120	2×10^2 (SECTIONS)	.4	TEM STEREOLOGY	.300 osm	[78], S_V approx. from diameter dis- tribution
197	4.7×10^4	.15	COULTER	PBS	[92]
250	8×10^3	.2	COULTER	SALINE	[93]
210	--	--	COULTER	.286 osm	[94]
280	5×10^4	--	COULTER	.315 osm	[79]
138	40	.38	OPTICAL MICROSCOPY	.290	
--	6×10^3	.17	LASER FLOW CYTOMETRY	.290	

An Ortho Diagnostic Systems Inc., Spectrum 111 laser flow cytometer was used to obtain histograms of forward scattered light, such as that of Fig. 0.1a for cells in .290 osm saline. The identity of the population causing the lower peak in the bimodal distribution of forward scattered light, is not known. The standard deviation listed in Table 0.1 is obtained from the Spectrum 111 computer report, Fig. 0.1b, by normalizing the listed standard deviation to the mean forward scattered light signal. This assumes a linear relationship between forward-scattered light intensity and cell volume. The validity of this assumption is considered below, based on reported studies and on preliminary calibration measurements.

The dependence of forward scattered light intensity on cell volume has been determined analytically and experimentally by Mullaney et al. [95,96,97]. The light intensity was found to vary linearly with cell volume for scattering angles between .5 and 2°. For a detector that accepts scattered light at greater angles, such as that of the Ortho Spectrum 111, intensity is not a simple function of volume. Unfortunately, calibration of the instrument using plastic microspheres of known sizes is not workable, due to the nonlinear dependence of the scattered light intensity on particle index of refraction, relative to the suspending medium. The known, osmometric behavior of lymphocytes and other cells, suggests a potentially effective approach for calibrating large-angle, flow cytometers. The method involves performing scattered light measurements on similar cell populations in solutions with a range of osmolalities. For cells obeying the Boyle-Van't Hoff law, volume is proportional

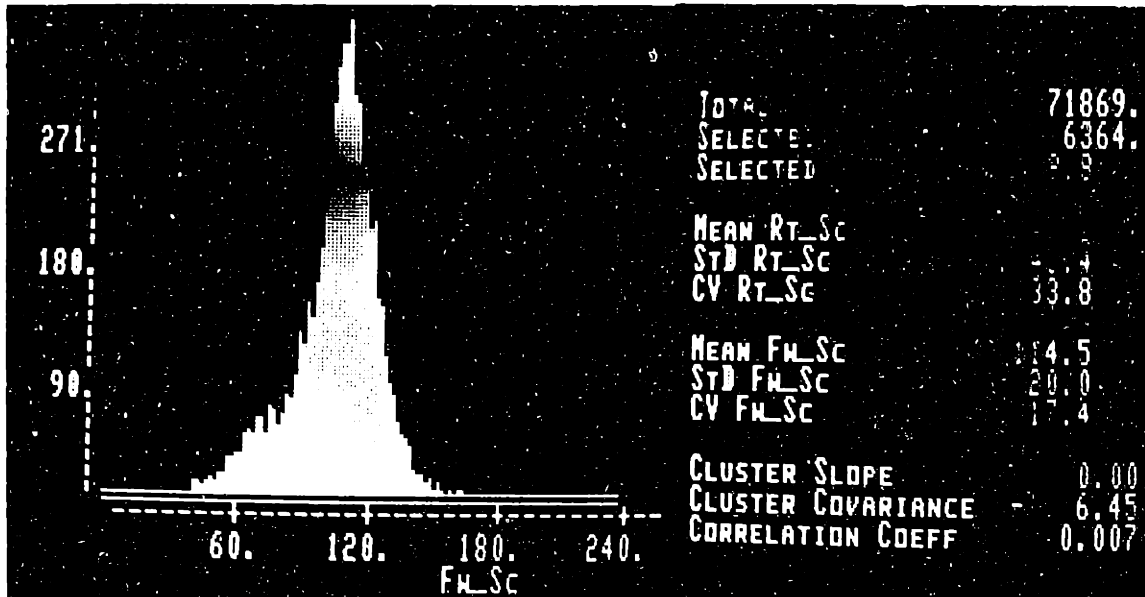


FIGURE 0.1a

FIGURE 0.1b

FIGURE 0.1a Laser flow cytometry histogram of forward-scattered light, lymphocytes in .290 osm saline

FIGURE 0.1b Ortho Spectrum 111 computer report

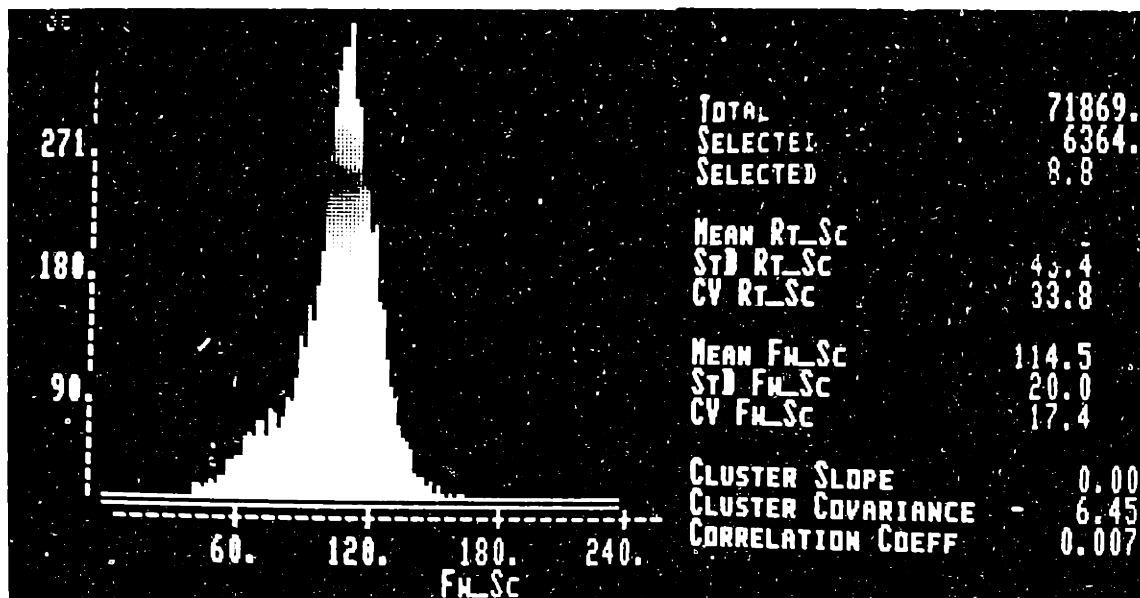


FIGURE 0.1a

FIGURE 0.1b

FIGURE 0.1a Laser flow cytometry histogram of forward-scattered light, lymphocytes in .290 osm saline

FIGURE 0.1b Ortho Spectrum 111 computer report

to $1/\text{osmolality}$; intensity, measured as a function of osmolality, can therefore be related to volume. An independent measurement must be performed to establish the mean cell size in one of the solutions.

Normalized mean cell volumes from a preliminary optical microscopy study by the author are shown in Fig. 0.2 at 4 osmolalities ranging from .290 to 1.0 osm. Additional values of cell volume, from the literature cited, are shown normalized to respective mean volumes at .290 osm. This method of presentation allows comparison of the osmotic properties without the need to reconcile disparities in the cited mean volumes. The solid line from Hempling [79], is at least squares fit of several measurements with .99 correlation coefficient. The data confirm osmometric ideality for human lymphocytes over the range, .1 to 1 osm.

The normalized mean forward scattered light intensity is shown in Fig. 0.3 as a function of ideal volume for the 4 solutions considered. The intensity varies linearly with volume over the .65 to 1.0 range. Significant departure from linearity occurs below .6 fractional volume. The effect of the nonlinearity is to 'stretch' the sub-mean side of the forward scattering histogram to the left. In the histogram of Fig. 0.1a, the effect should be present at signal levels below ~ 103 in Fw_Sc units. The histogram can be corrected by moving the cell counts at lower signal levels to the right by an amount which brings the normalized signal level to the dashed line in Fig. 0.3. Cells counted at ~ 80 Fw_Sc units, for example, would shift to ~ 100 Fw_Sc units. Accurate corrections of the histogram require more cytometry measurements on cells in hyper- and

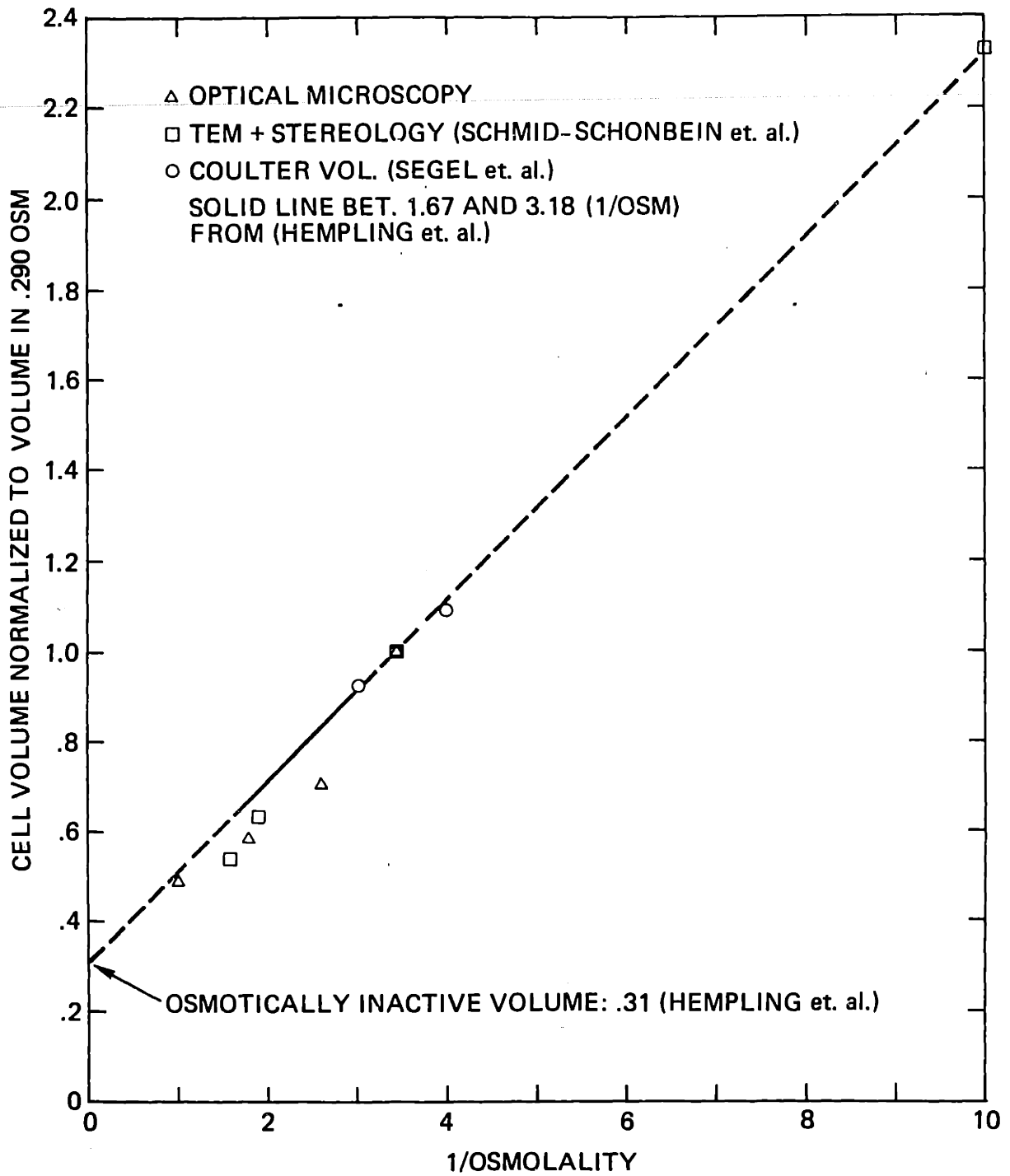


FIGURE 0.2 Osmometric behavior of human lymphocytes

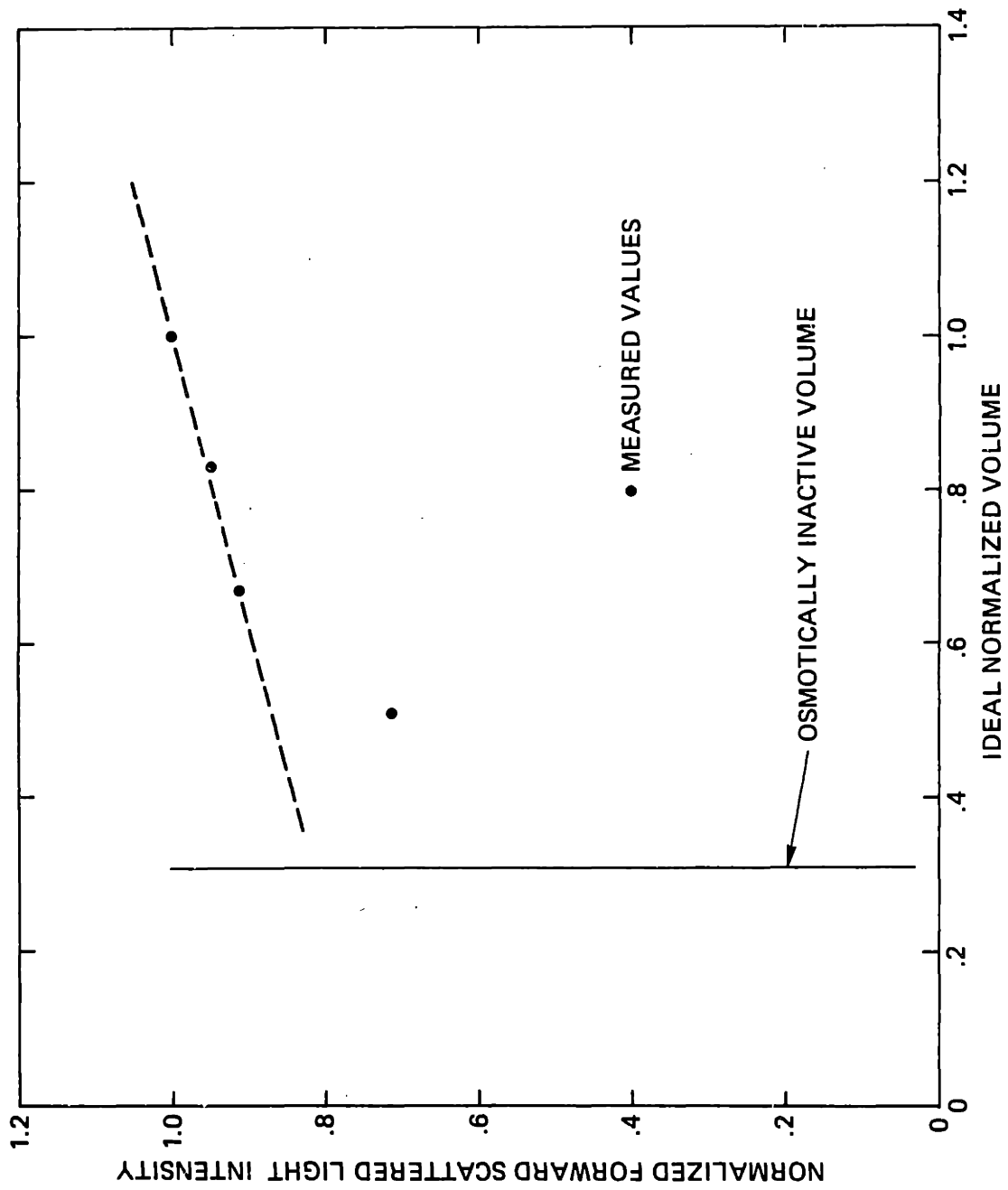


FIGURE 0.3 Flow cytometer forward scattered light dependence on lymphocyte volume

hypo-osmotic solutions in order to better define the shape of the curve relating normalized intensity to volume. Table 0.2 summarizes the results of the optical microscopy and flow cytometry studies.

The assumptions required in performing an osmometric calibration of the flow cytometer are: osmometric behavior of the cells is ideal or at least reproducibly nonideal, and relative indices of refraction between cells and suspending medium do not change with salinity.

To summarize, human lymphocyte mean volume and standard deviations of volume distributions are reviewed briefly; optical microscopy volume measurements are reported; standard deviation is estimated from flow cytometry measurements; lymphocyte osmometric behavior is reviewed and compared to current volume measurements; a method for calibrating flow cytometers using osmometric behavior is described.

TABLE 0.2
OPTICAL MICROSCOPY AND FLOW CYTOMETRY MEASUREMENTS

OSMOLALITY	$\frac{1}{\text{OSMOLAL.}}$	OPT. MICR. NORMALIZED	NORMALIZED FORWARD SCAT.	IDEAL VOLUME
[osm/Kg]	[Kg/osm]	Vol./# Cells	Light/# Cells	
.290	3.45	1.0 ± .4/42	1.00 ± .17/6400	1.00
.385	2.60	.71 ± .19/26	.948 ± .19/5700	.830
.556	1.80	.59 ± .11/14	.913 ± .20/4300	.670
1.0	1.0	.50 ± .15/32	.710 ± .24/2300	.510

REFERENCES

- [1] Huggins, C.E., Blood Preservation by Freezing, in Biomedical Physics and Biomaterials Science, ed. by H.E. Stanley, M.I.T. Press, Cambridge, 1972, pp. 191-205.
- [2] Doebbler, G.F., Rowe, A.W., Rinfret, A.P., Freezing of Mammalian Blood and its Constituents, in Cryobiology, ed. by H.T. Meryman, Academic Press, London, 1966, pp. 407-450.
- [3] Meryman, H.T., Review of Biological Freezing, in Cryobiology, ed. by H.T. Meryman, Academic Press, London, 1966, pp. 1-114.
- [4] Leibo, S.P., Mazur, P., Methods for the Preservation of Mammalian Embryos by Freezing, in Methods in Mammalian Reproduction, ed. by J.C. Daniel, Jr., pp. 179-201, Academic Press, N.Y., 1978.
- [5] Mazur, P., Schmidt, J., Interactions of Cooling Velocity, Temperature, and Warming Velocity on the Survival of Frozen and Thawed Yeast, Cryobiol. 5, 1-17, 1968.
- [6] Mazur, P., Farrant, J., Leibo, S.P., Chu, E.H.Y., Survival of Hamster Tissue Culture Cells after Freezing and Thawing, Cryobiology 6, 1-9, 1969.
- [7] Leibo, S.P., Farrant, J., Mazur, P., Hanna, M.G. Jr., Smith, L.H., Effects of Freezing on Marrow Stem Cell Suspensions: Interactions of Cooling and Warming Rates in the Presence of PVP, Sucrose, or Glycerol, Cryobiology 6, 315-332, 1970.
- [8] Miller, R.H., Mazur, P., Survival of Frozen-Thawed Human Red Cells as a Function of Cooling and Warming Velocities, Cryobiology 13, 404-414, 1976.
- [9] Mazur, P., Leibo, S.P., Farrant, J., Chu, E.H.Y., Hanna, M.G. Jr., Smith, L.H., Interactions of Cooling Rate, Warming Rate and Protective Additive on the Survival of Frozen Mammalian Cells, in The Frozen Cell, ed. by G.E.W. Wolstenholme and M. O'Connor, J.A. Churchill, London, 1970, pp. 69-85.
- [10] Mazur, P., Physical and Chemical Basis of Injury in Single-Celled Micro-organisms Subjected to Freezing and Thawing, in Cryobiology, ed. by H.T. Meryman, Academic Press, London, 1966, pp. 213-315.

- [11] Meryman, H.T., Williams, R.J., Douglas, J., Freezing Injury from Solution Effects and Its Prevention by Natural or Artificial Cryoprotection, *Cryobiology* 14, 287-302, 1977.
- [12] Rapatz, G., Sullivan, J.J., Luyet, B., Preservation of Erythrocytes in Blood Containing Various Cryoprotective Agents, Frozen at Various Rates, and Brought to a Given Final Temperature, *Cryobiology* 5, 18-25, 1968.
- [13] Mazur, P., Causes of Injury in Frozen and Thawed Cells, *Fed. Proc. Amer. Soc. Exp. Biol.* 24, S175-S182, 1965.
- [14] Mazur, P., *Cryobiology: The Freezing of Biological Systems*, *Science* 168, 939-949, 1970.
- [15] Lovelock, J.E., The Haemolysis of Human Red Blood-Cells by Freezing and Thawing, *Biochem. Biophys. Acta*, 10, 414-426, 1953.
- [16] Farrant, J., Morris, G.J., Thermal Shock and Dilution Shock as the Causes of Freezing Injury, *Cryobiology* 10, 134-140, 1973.
- [17] McGrath, J.J., The Kinetics and Thermodynamics of Human Erythrocyte Freeze-Thaw Damage at Sub-Optimal Cooling Rates, M.I.T. Ph.D. Thesis, January, 1977.
- [18] Leibo, S., Fundamental Cryobiology of Mouse Ova and Embryos, from The Freezing of Mammalian Embryos, Ciba Foundation Symposium 52 (New Series) 1977, Elsevier/Excerpta Medical North-Holland.
- [19] McGrath, J., Cravalho, E., An Experimental Comparison of Intracellular Ice Formation and Freeze-Thaw Survival of HeLa S-3 Cells, *Cryobiol.* 12, 540-550, 1975.
- [20] Diller, K.R., Intracellular Freezing: Effect of Extracellular Supercooling, *Cryobiology* 12, 480-485, 1975.
- [21] Mazur, P., The Role of Intracellular Freezing in the Death of Cells Cooled at Supraoptimal Rates, *Cryobiology* 14, 251-272, 1972.
- [22] Mazur, P., Kinetics of Water Loss from Cells at Subzero Temperatures and the Likelihood of Intracellular Freezing, *J. Gen. Physiol.* 47, 347-369, 1963.

- [23] Mansoori, G.A., Kinetics of Water Loss from Cells at Subzero Centigrade Temperatures, *Cryobiology* 12, 34-45, 1975.
- [24] Silvaes, O.M., Cravalho, E.G., Toscano, W.M., Huggins, C.E., The Thermodynamics of Water Transport from Biological Cells During Freezing, *J. Heat Transfer*, Nov. 1975, 582-588.
- [25] Levin, R.L., Cravalho, E.G., Huggins, C.E., Effect of Hydration on the Water Content of Human Erythrocytes, *Biophys. J.* 16, 1411-1426, 1976.
- [26] Levin, R.L., Cravalho, E.G., Huggins, C.E., A Membrane Model Describing the Effect of Temperature on the Water Conductivity of Erythrocyte Membranes at Subzero Temperatures, *Cryobiology* 13, 415-429, 1976.
- [27] Levin, R.L., Cravalho, E.G., Huggins, C.E., The Concentration Polarization Effect in a Multicomponent Electrolyte Solution-The Human Erythrocyte, *J. Theor. Biol.* 71, 225-254, 1978.
- [28] Levin, R.L., Cravalho, E.G., Huggins, C.E., Effect of Solution Non-Ideality on Erythrocyte Volume Regulation, *Biochem. Biophys. Acta* 465, 179-190, 1977.
- [29] Pushkar, N.S., Itkin, Y.A., Bronstein, V.L., Gordiyenko, E.A., Kozmin, Y.V., On the Problem of Dehydration and Intracellular Crystallization during Freezing of Cell Suspensions, *Cryobiology* 13, 147-152, 1976.
- [30] Lynch, M.E., Diller, K.E., An Irreversible Thermodynamic Model of Cell Freezing, *Proc. 10th Annual Pittsburgh Conf. Inst. Soc. Am.*, April, 1979.
- [31] Silvaes, O.M., A Thermodynamic Model of Water and Ion Transport Across Cell Membrane During Freezing and Thawing: The Human Erythrocyte, M.I.T. Ph.D. Thesis, October, 1974.
- [32] Hua, T.C., Cravalho, E.G., Jiang, L., The Temperature Difference Across the Membrane During Freezing and Its Effects on Water Transport, *Cryo-Letters*, 3, 255-264, 1982.
- [33] Ling, G.R., Tien, C.L., An Analysis of Cell Freezing and Dehydration, *J. Ht. Trans.*, August, 1970, 393-398.
- [34] Toscano, W.M., Cravalho, E.G., Silvaes, O.M., Huggins, C.E., The Thermodynamics of Intracellular Ice Nucleation in the Freezing of Erythrocytes, *J. Heat Transfer*, August, 1975, 326-332.

- [35] Cosman, M.D., Moussa, N.A., Cravalho, E.G., Huggins, C.E., A Dimensionless Criterion for Ice Formation in Cells, Abstract in Cryobiology 14, 711, 1977.
- [36] DeGroot, S.R., Mazur, P., Non-Equilibrium Thermodynamics, North-Holland, Amsterdam-London, 1969.
- [37] Katchalsky, A., Curran, P.F., Non-Equilibrium Thermodynamics in Biophysics, Harvard University Press, Cambridge, MA. 1965, Partic. Ch. 10.
- [38] Denbigh, K., The Principles of Chemical Equilibrium, Cambridge University Press, 1971, Chapter 8.
- [39] Papanek, T.H., The Water Permeability of the Human Erythrocyte In the Temperature Range +25°C to -10°C, M.I.T. Ph.D. Thesis, January 1978.
- [40] Rich, G.T., Sha'afi, R.I., Romualdez, A. and Solomon, A.K., Effect of Osmolality on the Hydraulic Permeability Coefficient of Red Cells, J. Gen. Physiol. 52, 941-954, 1968.
- [41] Papanek, T.H., An Apparatus to Measure Red Cell Permeability at Low Temperature, M.I.T. S.M. Thesis, May, 1975.
- [42] Blum, R.M., and Forster, R.E., The Water Permeability of Erythrocytes, Biochem. Biophys. Acta 203, 1970, 410-423.
- [43] Farmer, R.E.L. and Macey, R.I., Perturbation of Red Cell Volume: Rectification of Osmotic Flow, Biochem. Biophys. Acta 196, 1970, 53-65.
- [44] Vieira, F.L., Sha'afi, R.I. and Solomon, A.K., The State of Water in Human and Dog Red Cell Membranes, J. Gen. Physiol. 55, 1970, 451-466.
- [45] Evans, E., Fung, Y-C., Improved Measurements of the Erythrocyte Geometry, Microvasc. Res. 4, 1972, 335-347.
- [46] Savitz, D., Sidel, V.W., Solomon, A.K., Osmotic Properties of Human Red Cells, J. Gen. Physiol. 48, 1964, 79-94.
- [47] Wozencraft, J.M., Jacobs, I.M., Principles of Communication Engineering, John Wiley & Sons, Inc., New York, 1965.
- [48] Papoulis, A., Probability, Random Variables, and Stochastic Processes, McGraw-Hill Book Company, New York, 1965.

- [49] Asahina, E., Intracellular Freezing and Frost Resistance in Egg-Cells of the Sea Urchin, *Nature* 191, 1263-1265, 1961.
- [50] Morris, G., McGrath, J., Intracellular Ice Nucleation and Gas Bubble Formation in Spirogyra, *Cryo-Letters* 2, 341-352, 1981.
- [51] Leibo, S., McGrath, J., Cravalho, E., Microscopic Observation of Intracellular Ice Formation in Unfertilized Mouse Ova as a Function of Cooling Rate, *Cryobiol.* 15, 257-271, 1978.
- [52] Mazur, P., Physical and Temporal Factors Involved in the Death of Yeast at Subzero Temperatures, *Biophys. J.* 1, 247-264, 1961.
- [53] Mazur, P., The Role of Cell Membranes in the Freezing of Yeast and Other Single Cells, *Annals New York Academy of Sciences* 125, 658-676, 1965.
- [54] Rasmussen, D.H., Macaulay, M.N. and MacKenzie, A.P., Supercooling and Nucleation of Ice in Single Cells, *Cryobiology* 12, 328-339, 1975.
- [55] Wood, G.R., Walton, A.G., Kinetics of Ice Nucleation from Water and Electrolyte Solutions, Research and Development Progress Report No. 500, U.S. Dept. of The Interior, 1969.
- [56] Rasmussen, D.H., MacKenzie, A.P., Effect of Solute on Ice-Solution Interfacial Free Energy; Calculation from Measured Homogeneous Nucleation Temperatures, in Water Structure at the Water-Polymer Interface, H.H.G. Jellinek, ed., Plenum Press, New York, 126-145, 1972.
- [57] Uhlmann, D.R., Chalmers, B., The Energetics of Nucleation, *Industrial and Engineering Chemistry*, 57, 19-31, 1965.
- [58] Hoffman, J.D., Thermodynamic Driving Force in Nucleation and Growth Processes, *J. Chem. Phys.*, 29, 1192-1193, 1958.
- [59] Fletcher, N.H., Size Effect in Heterogeneous Nucleation, *J. Chem. Phys.* 29, 572-576, 1958.
- [60] Fletcher, N.H., Nucleation by Crystalline Particles, *J. Chem. Phys.* 38, 237-240, 1963.
- [61] Solomon, A.K., Characterization of Biological Membranes by Equivalent Pores, *J. Gen. Physiol.* 51, 335S-364S, 1968.

- [62] Jackson, K.A., Chalmers, B., Freezing of Liquids in Porous Media with Special Reference to Frost Heave in Soils, J. Appl. Phys. 29, 1178-1181, 1958.
- [63] Shimada, K., Asahina, E., Visualization of Intracellular Ice Crystals Formed in Very Rapidly Frozen Cells at -27°C, Cryobiol. 12, 209-218, 1975.
- [64] Ferguson, J., The Thermodynamics of the Freezing and Thawing of Biological Cells, M.S. Thesis, Cornell Univ., May, 1980.
- [65] Farrant, J., Walter, C., Heather Lee, McGann, L., Use of Two-Step Cooling Procedures to Examine Factors Influencing Cell Survival Following Freezing and Thawing, Cryobiology 14, 273-286, 1977.
- [66] Mazur, P., Rhian, M., Mahlandt, B., Survival of Pasteurella Tularensis in Gelatin-Saline After Cooling and Warming at Subzero Temperatures, Arch. of Biochem. and Biophys. 71, 1957, 31-51.
- [67] Diller, K.R., A Microscopic Investigation of Intracellular Ice Formation in Frozen Human Erythrocytes, M.I.T. Sc.D. Thesis, June, 1972.
- [68] Ushiyama, M., Volumetric Changes in Saccharomyces Cerevisiae During Freezing at Constant Cooling Velocities, S.M.M.E. Thesis, M.I.T., September 1973.
- [69] McGrath, J.J., The Dynamics of Freezing and Thawing Mammalian Cells: The HeLa Cell, M.I.T. S.M. Thesis, February, 1974.
- [70] English, J., Schaefer, B., Superimposing Data on a Video Signal, M.I.T. Introductory Digital Systems Laboratory, Course Project, May, 1981.
- [71] Cosman, M.D., Cravalho, E.G., Optimal Cooling Protocols for Cryopreservation of Individual Cells, Abstract in Cryobiology 15, 705-705, 1978.
- [72] Cosman, M.D., Cravalho, E.G., Huggins, C.E., An Electronic Cryomicroscope Temperature Controller, Abstract in Cryobiology 16, 613, 1979.
- [73] Merte, K.E., A Digitally Controlled Experimental Apparatus for Cryogenic Preservation of the Rat Heart, S.M. Thesis, M.I.T., August, 1979.

- [74] Hewlett-Packard, Operating and Service Manual: Model 17502A Input Module, Pasadena, CA., 1967.
- [75] Canham, P.B., Burton, A.C., Distribution of Size and Shape in Populations of Normal Human Red Cells, Circulation Research 22, 405-422, 1968.
- [76] Scheiwe, M.W., Nick, H.E., Körber, C., An Experimental Study on the Freezing of Red Blood Cells With and Without Hydroxyethyl Starch, Cryobiology 19, 461-477, 1982.
- [77] Körber, C., Private correspondence, November, 1979.
- [78] Schmid-Schonbein, G.E., Shih, Y.Y., Chien, S., Morphometry of Human Leukocytes, Blood 56, 866-875, 1980.
- [79] Hempling, H.G., Thompson, S., Dupre, A., Osmotic Properties of Human Lymphocyte, J. Cell. Physiol. 93, 293-302, 1977.
- [80] Horan, P.K., Wheelless, L.L. Jr., Quantitative Single Cell Analysis and Sorting, Science 198, 149-157, 1977.
- [81] Scheiwe, M.W., Körber, C., Basic Investigations on the Freezing of Human Lymphocytes, Cryobiology, in press.
- [82] Thomas, G.B., Calculus and Analytic Geometry, Addison-Wesley, Reading, Mass., 1968, Chapter 18.
- [83] Omega Engineering Inc., 1979 Temperature Measurement Handbook, Stamford, Connecticut.
- [84] Lancaster, D., TV Typewriter Cookbook, Howard W. Sams & Co., Inc., Indianapolis, Ind., 1976.
- [85] Texas Instruments, Inc., The TTL Data Book for Design Engineers, Dallas, Texas, 6,76-6,82, 1976.
- [86] Ogata, K., Modern Control Engineering, Prentice-Hall, Inc., Englewood Cliffs, N.J., Chs. 6, 9, 1970.
- [87] Rohsenow, W.M., Choi, H.Y., Heat, Mass, and Momentum Transfer, Prentice-Hall, Inc., Englewood Cliffs, N.J., 1961.
- [88] Stobridge, T.R., NBS Technical Note 129: The Thermodynamic Properties of Nitrogen from 64 to 300°K Between 0.1 and 200 Atmospheres, U.S. Dept. of Commerce Off. of Tech. Services, Washington, D.C., January, 1962, p. 30-31.

- [89] Scott, R.B., Cryogenic Engineering, D. Van Nostrand Co., Inc., Princeton, N.J., 1959, p. 280.
- [90] Hrycaj, T.M., The Effects of Freezing on the Microcirculation of the Hamster Cheek Pouch, M.I.T. S.M. Thesis, 1975.
- [91] Fleischaker, D., Stability of a Propagating Phase Boundary: A Cryogenic Experimental Study, M.I.T. S.M. Thesis, 1978.
- [92] Ben-Sasson, S., Patinkin, D., Grover, N.B., Doljanki, F., Electrical Sizing of Particles in Suspensions IV. Lymphocytes, J. Cell. Physiol. 84, 205-214, 1974.
- [93] Westring, D.W., Ladinsky, J.L., Feick, P., Meyer, L.M., The Volume Distribution of Human Lymphocytes, Proc. Soc. Exp. Biol. Med. 131, 1077-1083, 1969.
- [94] Segel, G.B., Cokelet, G.R., Lichtman, M.A., The Measurement of Lymphocyte Volume: Importance of Reference Particle Deformability and Counting Solution Tonicity, Blood 57, 894-899, 1981.
- [95] Mullaney, P.F., Van Dilla, M.A., Coulter, J.R., Dean, P.N., Cell Sizing: A Light Scattering Photometer for Rapid Volume Determination, Rev. Sci. Instr. 40, 1029-1032, 1969.
- [96] Mullaney, P.F., Dean, P.N., The Small Angle Light Scattering of Biological Cells: Theoretical Considerations, Biophys. J. 10, 764-772, 1970.
- [97] Mullaney, P.F., Crowell, J.M., Salzman, G.C., Martin, J.C., Hiebert, R.D., Goad, C.A., Pulse-Height Light-Scatter Distributions Using Flow-Systems Instrumentation, J. Histochem. Cytochem. 24, 298-304, 1976.
- [98] Arpaci, V.S., Conduction Heat Transfer, Addison-Wesley, Reading, Mass., 1966, Ch. 3.
- [99] Abramowitz, M. and Segun, I., eds., Handbook of Mathematical Functions, Dover Publications, Inc., New York, 1965, Table 9.8.